



**HAL**  
open science

# Multifunctional Rare Earth Vanadate Nanoparticles: Luminescent Labels, Oxidant Sensors and Magnetic Resonance Imaging Contrast Agents

Markus Schoeffel

► **To cite this version:**

Markus Schoeffel. Multifunctional Rare Earth Vanadate Nanoparticles: Luminescent Labels, Oxidant Sensors and Magnetic Resonance Imaging Contrast Agents. Materials Science [cond-mat.mtrl-sci]. Ecole Polytechnique X, 2012. English. NNT: . pastel-00688113

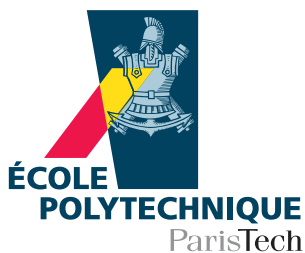
**HAL Id: pastel-00688113**

**<https://pastel.hal.science/pastel-00688113>**

Submitted on 16 Apr 2012

**HAL** is a multi-disciplinary open access archive for the deposit and dissemination of scientific research documents, whether they are published or not. The documents may come from teaching and research institutions in France or abroad, or from public or private research centers.

L'archive ouverte pluridisciplinaire **HAL**, est destinée au dépôt et à la diffusion de documents scientifiques de niveau recherche, publiés ou non, émanant des établissements d'enseignement et de recherche français ou étrangers, des laboratoires publics ou privés.



## THESE

présentée pour obtenir le grade de

**DOCTEUR DE L'ÉCOLE POLYTECHNIQUE**

Spécialité : Physique

par

**Markus SCHÖFFEL**

# **Multifunctional Rare Earth Vanadate Nanoparticles: Luminescent Labels, Oxidant Sensors and Magnetic Resonance Imaging Contrast Agents**

Soutenue publiquement le 22 mars 2012 devant le jury composé de

Prof. Stéphane PETOUD	CNRS Orléans	Président
Prof. Olivier TILLEMENT	Université Lyon 1	Rapporteur
Dr. Claire WILHELM	Université Paris 7	Rapporteur
Dr. Caroline ROBIC	Guerbet France	Examineur
Dr. Thierry GACOIN	Ecole Polytechnique	Examineur
Dr. Isabelle MAURIN	Ecole Polytechnique	Examineur
Dr. Antigoni ALEXANDROU	Ecole Polytechnique	Directrice de thèse



There's plenty of room at the  
bottom.

---

*(Title of the talk given by  
Richard Feynman at the  
annual meeting of the  
American Physical Society on  
December 29th, 1959.)*



# Acknowledgments

I would like to express my deep and sincere gratitude to my supervisor Antigoni Alexandrou for hosting me in her group at the *Laboratoire d'Optique et Biosciences* (LOB) at the *Ecole Polytechnique* (EP). She gave me the possibility to work on the fascinating interface between physics, chemistry, and biology. I appreciated greatly the freedom she gave me during my research but also that she sometimes limited my ambitions spreading too large and brought me back to my subject. Her wide knowledge, encouraging and personal guidance have provided an excellent basis for the present PhD thesis. I wish to express my warm and sincere thanks to Cédric Bouzigues also from the LOB who co-supervised my thesis especially concerning the topics of biological applications of nanoparticles in general and hydrogen peroxide detection in particular. His comprehensive experience in this area allowed to design experiments properly and to solve encountered problems quickly.

I am deeply grateful to Isabelle Maurin from the *Laboratoire de Physique de la Matière Condensée* (LPMC) at the EP who always found the time to answer my questions concerning X-ray diffraction and magnetism. Without her help, many of the results concerning the material characterization would not have been obtained and many conclusions would not exist. The detailed and constructive comments after the proofreading of the manuscript were of great value for me.

It is difficult to overstate my gratitude to Thierry Gacoin and Jean-Pierre Boilot from the LPMC for the unique opportunity to synthesize and characterize myself the materials in their laboratory and, more importantly, for the fact that I could benefit from pioneering and extensive know-how in the field. It was this collaboration that enabled me to combine applications of nanoparticles to biology with the conception and characterization of nanoparticles with expanded functionalities.

I do not want to miss the opportunity to express my gratefulness to the other members of the jury for their huge effort to evaluate this work. I want in particular thank Olivier Tillement and Claire Wilhelm who have accepted the labor intensive mission to be the reviewers of the manuscript. Their helpful comments have shown to me the enormous work they have accomplished and allowed to improve the manuscript. I am grateful to Stéphane Petoud for being the president of the jury and to Caroline Robic for her feedback from the point of view of a researcher in industry.

I am indebted to many colleagues who made contributions to this work. The study dealing with the influence of the nanoparticles on proton relaxation would not have been possible without the collaboration with Olivier Clément, and the assistance by Laetitia Pidial and Gwennhael Autret from the *Laboratoire de Recherche en Imagerie* at the *Paris Centre de recherche Cardiovasculaire*. I am thankful for the

---

measurements on the clinical MRI system, for giving me access to the relaxometer as well as the fruitful discussions and helpful advice. I highly appreciated the introduction to the relaxation time measurement procedure given by Florence Gazeau from the *Laboratoire Matière et Systèmes Complexes* at the *Université Paris 7*. Pierre Levitz from the LPMC found despite his tight schedule the time to perform on his special equipment frequency-dependent measurements on proton relaxation. The obtained data were of great utility for the comprehension of the effects linked to Eu-doping. François Devreux also from the LPMC showed me how to carry out gas adsorption measurements. The results constituted an important element in the understanding of the morphology of the nanoparticles.

I would like to thank numerous former and current PhD students of the LPMC: Geneviève Mialon acquainted me with the field of colloidal nanoparticle synthesis. Charlotte Vichery helped me perform the measurements on the SQUID magnetometer and indicated to me the right conversions when I was lost between cgs and SI unit systems. Blaise Fleury always had a helpful solution if something went wrong with a synthesis. Amélie Revaux introduced me to the experimental techniques necessary for my teaching subject.

I am grateful to the former PhD students of LOB Silvan Türkcan and Thanh Liêm Nguyễn. They familiarized me with the microscopy setup, explained to me the programs for data analysis and showed me how to culture cells and put nanoparticles inside without killing them all.

It was a pleasure to work with my kind and helpful colleagues at the LOB. I would like to especially thank my office colleagues Yannick Goulam Houssen, Thanh Liêm Nguyễn, Byung-Kuk Yoo, Silvan Türkcan, Gaël Latour and Rachid Rezgui for making these three years so enjoyable.

A special thank you goes to my wife Maria Quanz for her enormous support.

# Contents

<b>Abstract</b>	<b>XIII</b>
<b>Résumé</b>	<b>XV</b>
<b>Zusammenfassung</b>	<b>XVII</b>
<b>List of Figures</b>	<b>XXII</b>
<b>List of Tables</b>	<b>XXIII</b>
<b>Introduction</b>	<b>1</b>
Nanotechnology for biological imaging and therapy . . . . .	1
Rare earth vanadate nanoparticles . . . . .	2
Positioning of this work . . . . .	4
<b>1 Synthesis and characterization of bulk rare earth vanadates</b>	<b>7</b>
1.1 Synthesis of bulk gadolinium vanadate . . . . .	7
1.1.1 Solid state synthesis . . . . .	7
1.1.2 Synthesis by coprecipitation . . . . .	9
1.1.3 Experimental protocol . . . . .	10
1.1.3.1 Ceramic method . . . . .	10
1.1.3.2 Coprecipitation and thermal treatment . . . . .	10
1.1.4 Results and discussion . . . . .	11
1.2 Characterization by X-ray diffraction . . . . .	12
1.2.1 Crystal structure . . . . .	12
1.2.2 Experimental protocol . . . . .	13
1.2.3 Results and discussion . . . . .	13
1.2.3.1 Identity . . . . .	13
1.2.3.2 Purity . . . . .	14
1.2.3.3 Stoichiometry . . . . .	16
1.3 Characterization of the magnetic properties . . . . .	20
1.3.1 Paramagnetism . . . . .	20
1.3.2 Long range antiferromagnetic order . . . . .	21
1.3.3 Cooperative magnetic effects in GdVO <sub>4</sub> . . . . .	22
1.3.4 Experimental protocol . . . . .	23
1.3.5 Results and discussion . . . . .	23
1.4 Conclusion . . . . .	25

<b>2</b>	<b>Synthesis and characterization of rare earth vanadate nanoparticles</b>	<b>27</b>
2.1	Synthesis of nanoparticles . . . . .	27
2.1.1	Nanoparticle formation by coprecipitation . . . . .	27
2.1.2	Nanoparticle formation control by complexation . . . . .	29
2.1.3	Stabilization of colloids . . . . .	30
2.1.3.1	Van der Waals attraction . . . . .	30
2.1.3.2	Electrostatic repulsion . . . . .	30
2.1.3.3	Kinetic stabilization . . . . .	31
2.1.3.4	Steric repulsion . . . . .	32
2.1.4	Experimental protocol . . . . .	34
2.1.4.1	Reactant preparation . . . . .	34
2.1.4.2	Synthesis by normal route . . . . .	34
2.1.4.3	Citrate synthesis route . . . . .	35
2.1.4.4	Synthesis of core-shell nanoparticles . . . . .	35
2.1.4.5	Purification . . . . .	36
2.1.4.6	Size selection . . . . .	37
2.2	Surface modification of nanoparticles . . . . .	38
2.2.1	Silica coating . . . . .	38
2.2.2	Functionalization . . . . .	39
2.2.3	Experimental protocol . . . . .	41
2.2.3.1	Silica coating of the nanoparticles . . . . .	41
2.2.3.2	Functionalization . . . . .	42
2.2.3.3	Analysis of the surface modifications . . . . .	42
2.2.4	Results and discussion . . . . .	43
2.3	Vanadate concentration . . . . .	45
2.3.1	Quantification by UV absorption . . . . .	46
2.3.2	Colorimetric quantification . . . . .	47
2.3.3	Experimental protocol . . . . .	48
2.3.3.1	Reactant preparation . . . . .	48
2.3.3.2	Calibration graph . . . . .	49
2.3.3.3	Sample quantification . . . . .	49
2.3.3.4	Synthesis yield determination . . . . .	50
2.3.4	Results and discussion . . . . .	50
2.3.4.1	Molar extinction coefficient . . . . .	50
2.3.4.2	Error in vanadate quantification . . . . .	51
2.3.4.3	Influence of the rare earth . . . . .	52
2.3.4.4	Synthesis yield . . . . .	52
2.4	Stability . . . . .	54
2.4.1	Toxicology of nanoparticle decomposition products . . . . .	54
2.4.1.1	Rare earth ions . . . . .	54
2.4.1.2	Vanadate . . . . .	55
2.4.2	Colorimetric rare earth quantification . . . . .	57
2.4.3	Experimental protocol . . . . .	58
2.4.3.1	Preparation of xylenol orange solution . . . . .	58
2.4.3.2	Preparation of rare earth solutions . . . . .	58
2.4.3.3	Determination of the calibration equation . . . . .	58

2.4.3.4	Quantification of free rare earths in nanoparticle dispersions . . . . .	59
2.4.4	Results and discussion . . . . .	59
2.4.4.1	Calibration equation . . . . .	59
2.4.4.2	Rare earth leaching from nanoparticles . . . . .	62
2.5	Particle size . . . . .	64
2.5.1	Experimental protocol . . . . .	64
2.5.2	Results and discussion . . . . .	64
2.5.3	Comparison to electron microscopy data . . . . .	66
2.6	Microstructural analysis of X-ray data . . . . .	68
2.6.1	Theoretical considerations . . . . .	68
2.6.1.1	Coherence length . . . . .	69
2.6.1.2	Williamson-Hall analysis . . . . .	69
2.6.1.3	Anisotropic broadening . . . . .	70
2.6.2	Experimental protocol . . . . .	72
2.6.2.1	Data acquisition . . . . .	72
2.6.2.2	Manual Williamson-Hall analysis . . . . .	72
2.6.2.3	Automated microstructural analysis . . . . .	72
2.6.3	Results and discussion . . . . .	73
2.6.3.1	Crystal structure . . . . .	73
2.6.3.2	Spherical crystallite model . . . . .	74
2.6.3.3	Non-spherical crystallite model . . . . .	75
2.7	Specific surface . . . . .	80
2.7.1	Experimental protocol . . . . .	80
2.7.2	Results and discussion . . . . .	81
2.8	Magnetic properties of Gd-containing nanoparticles . . . . .	83
2.8.1	Finite size effects in nanomaterials . . . . .	83
2.8.2	Experimental protocol . . . . .	84
2.8.3	Results and discussion . . . . .	84
2.9	Conclusion . . . . .	86
<b>3</b>	<b>Rare earth vanadate nanoparticles as optical hydrogen peroxide sensor</b>	<b>89</b>
3.1	Luminescence of rare earth vanadates . . . . .	89
3.1.1	Electronic structure of lanthanides . . . . .	89
3.1.2	Electronic excitations and energy levels . . . . .	90
3.1.3	Radiative transitions . . . . .	92
3.1.3.1	Free rare earth ions . . . . .	92
3.1.3.2	Rare earth ions in a crystal . . . . .	92
3.1.4	Non-radiative transitions . . . . .	94
3.1.4.1	Multiphonon relaxation . . . . .	95
3.1.4.2	Energy transfer . . . . .	95
3.1.5	Optical properties of $Y_{1-x}Eu_xVO_4$ materials . . . . .	96
3.1.6	Luminescence spectra and quantum yield . . . . .	99
3.1.6.1	Excitation- and emission spectra . . . . .	100
3.1.6.2	Luminescence quantum yield . . . . .	101

3.2	Hydrogen peroxide detection . . . . .	102
3.2.1	Hydrogen peroxide in living organisms . . . . .	102
3.2.1.1	Hydrogen peroxide as a cellular second messenger . . . . .	102
3.2.1.2	Generation of hydrogen peroxide by NADPH oxidases . . . . .	103
3.2.1.3	Regulation of NADPH oxidases . . . . .	105
3.2.2	Hydrogen-peroxide mediated signaling pathways . . . . .	106
3.2.2.1	Switching on the signaling cascade . . . . .	106
3.2.2.2	Switching off the signaling cascade . . . . .	107
3.2.2.3	Hydrogen peroxide regulation of growth, proliferation and apoptosis . . . . .	109
3.2.3	Techniques for the measurement of hydrogen peroxide . . . . .	110
3.2.3.1	Nonreversible molecular probes . . . . .	110
3.2.3.2	Reversible probes . . . . .	115
3.2.3.3	Europium-doped inorganic nanoparticles . . . . .	117
3.2.4	Experimental protocol . . . . .	120
3.2.4.1	Luminescence microscopy setup . . . . .	120
3.2.4.2	Sample preparation for nanoparticle observation . . . . .	120
3.2.4.3	Nanoparticle response to hydrogen peroxide . . . . .	122
3.2.4.4	Cell culture . . . . .	122
3.2.4.5	Loading cells with nanoparticles . . . . .	123
3.2.4.6	In vivo hydrogen peroxide monitoring . . . . .	124
3.2.4.7	Data analysis . . . . .	125
3.2.5	Results and discussion . . . . .	126
3.2.5.1	Kinetics of photoreduction and reoxidation . . . . .	126
3.2.5.2	Intracellular hydrogen peroxide production . . . . .	126
3.3	Conclusion . . . . .	129
<b>4</b>	<b>Rare earth vanadate nanoparticles as multimodal contrast agent</b>	<b>133</b>
4.1	Magnetic resonance imaging . . . . .	133
4.1.1	Magnetic relaxation . . . . .	134
4.1.2	Bloembergen-Purcell-Pound relaxation theory . . . . .	135
4.2	Contrast and contrast agents . . . . .	136
4.2.1	Contrast generating mechanisms . . . . .	136
4.2.1.1	Contrast from chemical shift . . . . .	137
4.2.1.2	$T_1$ contrast . . . . .	137
4.2.1.3	$T_2$ contrast . . . . .	138
4.2.1.4	Proton density contrast . . . . .	138
4.2.2	Contrast enhancing agents . . . . .	138
4.2.2.1	Mode of action . . . . .	138
4.2.2.2	Types and design . . . . .	139
4.2.3	Paramagnetic relaxation enhancement . . . . .	140
4.2.3.1	Inner-sphere relaxivity . . . . .	141
4.2.3.2	Outer-sphere relaxivity . . . . .	143
4.2.4	Clinically approved contrast agents . . . . .	143
4.2.4.1	Gd-containing positive contrast agents . . . . .	144
4.2.4.2	Other positive contrast agents . . . . .	146

4.2.4.3	Negative contrast agents . . . . .	146
4.2.5	New positive, inorganic and nanostructured contrast agents . .	149
4.2.6	Nanoparticles as multimodal agents for imaging and therapy .	151
4.2.6.1	Coupling of MRI and optical imaging . . . . .	152
4.2.6.2	Coupling of MRI and positron emission tomography or single-photon emission computed tomography . .	153
4.2.6.3	Coupling of MRI and X-ray computed tomography .	154
4.2.6.4	Coupling of MRI and ultrasonography . . . . .	154
4.2.6.5	Coupling of MRI and chemotherapy . . . . .	155
4.2.6.6	Coupling of MRI and neutron-capture therapy . . . .	155
4.3	Materials and methods . . . . .	156
4.3.1	Sample preparation . . . . .	156
4.3.2	Measurement of relaxation times . . . . .	156
4.3.3	Relaxivity data analysis . . . . .	157
4.3.4	Nuclear magnetic resonance dispersion spectroscopy . . . . .	157
4.3.5	Response to hydrogen peroxide . . . . .	158
4.4	Results and discussion . . . . .	158
4.4.1	Relaxation times at 20 MHz . . . . .	158
4.4.2	Frequency-dependent relaxation times . . . . .	163
4.4.3	Luminescence . . . . .	165
4.4.4	Hydrogen peroxide detection . . . . .	166
4.5	Conclusion . . . . .	169
	<b>Summarizing discussion and outlook</b>	<b>171</b>
<b>A</b>	<b>Theory of characterization methods</b>	<b>175</b>
A.1	X-ray powder diffraction . . . . .	175
A.1.1	Bragg-Brentano parafofocussing geometry . . . . .	175
A.1.2	Technical data of the X-ray diffractometer . . . . .	176
A.1.3	Calibration for instrumental aberrations . . . . .	177
A.1.4	Correction factor for sample eccentricity . . . . .	177
A.1.5	Profile shape function . . . . .	178
A.1.6	Determination of the instrumental resolution . . . . .	180
A.1.7	Material for resolution calibration . . . . .	181
A.1.8	Rietveld refinement . . . . .	182
A.1.9	Debye-Waller factor . . . . .	183
A.1.10	Algorithm for Rietveld refinement . . . . .	183
A.1.11	Agreement factors . . . . .	184
A.1.12	Crystal structure refinement of GdVO <sub>4</sub> samples . . . . .	185
A.2	Magnetism and magnetometry . . . . .	186
A.2.1	Quantum numbers . . . . .	186
A.2.2	Paramagnetism . . . . .	187
A.2.3	Magnetic susceptibility . . . . .	189
A.3	Dynamic light scattering . . . . .	191
A.3.1	Scattering experiment . . . . .	191
A.3.2	Hydrodynamic diameter . . . . .	191

A.3.3	Size averages . . . . .	193
A.4	Scanning electron microscopy . . . . .	195
A.4.1	General considerations . . . . .	195
A.4.2	Experimental protocol . . . . .	196
A.5	Gas adsorption . . . . .	197
A.5.1	Adsorption isotherms . . . . .	197
A.5.2	Brunauer-Emmett-Teller theory . . . . .	197
A.6	Luminescence spectroscopy . . . . .	199
A.6.1	Quantum yield . . . . .	199
A.6.2	Acquisition of luminescence spectra . . . . .	200
A.6.3	Quantum yield determination . . . . .	200
A.6.4	Instrument calibration . . . . .	201
A.7	Nuclear magnetic resonance . . . . .	202
A.7.1	Nuclear spin . . . . .	202
A.7.2	Interaction spin–magnetic field . . . . .	203
A.7.3	Macroscopic magnetization . . . . .	204
A.7.4	Resonant energy absorption . . . . .	205
A.7.5	Signal detection . . . . .	206
A.7.6	Pulse sequences . . . . .	206
A.7.7	Image formation . . . . .	208
<b>B</b>	<b>Crystallographic and magnetic properties of selected rare earth com- pounds</b>	<b>211</b>
	<b>Bibliography</b>	<b>216</b>

# Abstract

Multimodal imaging techniques are of great interest due to the wealth of information they provide. This thesis is devoted to the development and characterization of nanoparticles which can be applied as luminescent probes, for oxidant detection and as contrast agents in magnetic resonance imaging. The work is based on previous studies on  $Y_{0.6}Eu_{0.4}VO_4$  nanoparticles which show strong, non-blinking and stable luminescence. Time and space resolved optical oxidant detection is feasible after reversible photoreduction of  $Eu^{3+}$  to  $Eu^{2+}$  and reoxidation by *e. g.*  $H_2O_2$ . This oxidation is detectable by a modification of the luminescence properties.

The incorporation of paramagnetic  $Gd^{3+}$  confers proton relaxation enhancing properties to the system. We synthesized nanoparticles of either 10 nm or 40 nm diameter and of the compositions  $GdVO_4$  and  $Gd_{0.6}Eu_{0.4}VO_4$  as well as core-shell systems containing a  $Y_{0.6}Eu_{0.4}VO_4$  core and a  $GdVO_4$  shell with 40 nm total diameter. X-ray microstructural analysis in combination with dynamic light scattering and electron microscopy enabled us to propose a model for the relationship between the shape of the nanoparticles and the crystallites contained in them. Complexometric titration indicated that rare earth leaching is negligible making this type of nanoparticles well suited for *in vivo* applications. We demonstrated that even after substitution of  $Y^{3+}$  by  $Gd^{3+}$ , the nanoparticles retain the ability of  $H_2O_2$  detection by luminescence modulation. Temperature and magnetic field dependent measurements of the magnetization of  $Gd_{0.6}Eu_{0.4}VO_4$  nanoparticles confirmed the paramagnetic behavior according to a Curie-Weiss law in the temperature range from 290 K down to 5 K. We found that the proton relaxivity of  $GdVO_4$  and  $Gd_{0.6}Eu_{0.4}VO_4$  nanoparticles of 10 nm diameter as well as of the core-shell nanoparticles is higher than that of the commercial chelate compound Dotarem<sup>®</sup>. Nuclear magnetic resonance dispersion spectroscopy showed higher proton relaxivities for nanoparticles made up from  $Gd_{0.6}Eu_{0.4}VO_4$  than from pure  $GdVO_4$ .

The present data suggest that rare earth vanadate nanoparticles containing simultaneously Gd and Eu are very promising candidates for applications as *in vivo* multifunctional probe. This system might also be useful as a target in gadolinium neutron capture therapy or for positron emission tomography.



# Résumé

Les techniques d'imagerie multimodale peuvent apporter une grande richesse d'information. Cette thèse est consacrée au développement et à la caractérisation de nanoparticules qui peuvent être utilisées en tant que marqueurs luminescents, pour la détection d'oxydants et comme agents de contraste pour l'imagerie à résonance magnétique. Ces travaux sont basés sur des études précédentes concernant des nanoparticules de composition  $Y_{0,6}Eu_{0,4}VO_4$ , qui présentent une forte luminescence stable sans clignotement. La détection optique d'oxydants résolue temporellement et spatialement se base sur la photoréduction réversible d' $Eu^{3+}$  vers  $Eu^{2+}$  et la réoxydation d' $Eu^{2+}$  vers  $Eu^{3+}$  induite par exemple par  $H_2O_2$ . Cette oxydation est détectable suite à une modification des propriétés de luminescence.

L'incorporation de  $Gd^{3+}$  paramagnétique permet l'accélération de la relaxation de l'aimantation des protons. Nous avons synthétisé des nanoparticules de 10 nm et 40 nm de diamètre de composition  $GdVO_4$  et  $Gd_{0,6}Eu_{0,4}VO_4$ , ainsi que des systèmes cœur-coquille contenant un cœur de  $Y_{0,6}Eu_{0,4}VO_4$  et une coquille de  $GdVO_4$  avec un diamètre total de 40 nm. L'analyse microstructurale par rayons X combinée avec la diffusion dynamique de la lumière et la microscopie électronique à balayage nous a permis de proposer un modèle liant la forme des nanoparticules à celle des cristallites les composant. La titration complexométrique a indiqué que le taux de relargage de terres rares est négligeable, ce qui rend envisageable l'utilisation de nanoparticules de ce type pour des applications *in vivo*. Nous avons démontré que les nanoparticules conservent, même après substitution de  $Y^{3+}$  par  $Gd^{3+}$ , la capacité de détecter  $H_2O_2$  par une modification de leur luminescence. Des mesures de l'aimantation des nanoparticules  $Gd_{0,6}Eu_{0,4}VO_4$  en fonction du champ et de la température ont confirmé leur comportement paramagnétique conforme à une loi de Curie-Weiss dans une gamme de température allant de 290 K à 5 K. Nous avons trouvé que la relaxivité par rapport aux protons induite par les nanoparticules  $GdVO_4$  et  $Gd_{0,6}Eu_{0,4}VO_4$  d'un diamètre de 10 nm est plus importante que pour le composé commercial chélaté Dotarem<sup>®</sup>. Des mesures de dispersion de relaxation magnétique nucléaire ont indiqué une relaxivité plus élevée pour les nanoparticules composées de  $Gd_{0,6}Eu_{0,4}VO_4$  par rapport à celles de  $GdVO_4$ .

Les données actuelles indiquent que les nanoparticules de vanadate de terres rares contenant simultanément Gd et Eu sont des candidats prometteurs pour une application *in vivo* en tant que sonde multifonctionnelle. Ce système pourrait également être utile comme cible pour la thérapie par capture de neutrons utilisant les ions de gadolinium ou pour la tomographie par émission de positrons.



# Zusammenfassung

Multimodale bildgebende Verfahren sind von hohem Interesse da sie einen großen Informationsreichtums zur Verfügung stellen. Diese Doktorarbeit ist der Entwicklung und Charakterisierung von Nanopartikeln gewidmet, welche als lumineszierende Marker, zur Detektion von Oxidanzien und als Kontrastmittel für die Magnetresonanztomographie verwendet werden können. Die Arbeit basiert auf vorherigen Studien bezüglich  $Y_{0,6}Eu_{0,4}VO_4$  Nanopartikeln, welche eine starke und stabile Lumineszenz ohne Blinken zeigen. Diese ermöglichen eine zeitlich und räumlich aufgelöste optische Detektion von Oxidanzien durch reversible Photoreduktion von  $Eu^{3+}$  zu  $Eu^{2+}$  und Rückoxidation von  $Eu^{2+}$  zu  $Eu^{3+}$  mit z. B.  $H_2O_2$ . Diese Oxidation kann aufgrund der Veränderung der Lumineszenzeigenschaften detektiert werden.

Das Einfügen von paramagnetischem  $Gd^{3+}$  verleiht dem System protonenrelaxationsverstärkende Eigenschaften. Wir synthetisierten Nanopartikel von entweder 10 nm oder 40 nm Durchmesser und mit den Zusammensetzungen  $GdVO_4$  und  $Gd_{0,6}Eu_{0,4}VO_4$  wie auch Kern-Schale Systeme bestehend aus einem  $Y_{0,6}Eu_{0,4}VO_4$  Kern und einer  $GdVO_4$  Schale mit einem Gesamtdurchmesser von 40 nm. Mikrostrukturelle Röntgenanalyse zusammen mit dynamischer Lichtstreuung und Elektronenmikroskopie erlaubten es uns, ein Modell des Zusammenhanges zwischen der Form eines Nanopartikels und derjenigen der Kristallite, die es aufbauen, vorzuschlagen. Eine komplexometrische Titration ergab, dass die Freisetzung von seltenen Erden vernachlässigbar ist und bestätigte die Eignung dieses Types von Nanopartikeln für *in vivo* Anwendungen. Wir zeigten dass selbst nach der Substitution von  $Y^{3+}$  durch  $Gd^{3+}$  die Eigenschaft der Nanopartikel, durch Lumineszenzmodulation  $H_2O_2$  zu Detektieren, erhalten bleibt. Temperatur- und magnetfeldabhängige Messungen der Magnetisierung von  $GdVO_4$  Nanopartikeln bestätigten das paramagnetische Verhalten gemäß eines Curie-Weiss Gesetzes im Temperaturbereich von 290 K bis zu 5 K. Wir stellten fest, dass die Protonenrelaxivität von  $GdVO_4$  Nanopartikeln von 10 nm Durchmesser wie auch von Kern-Schale Nanopartikeln höher ist, als die der kommerziellen Chelatverbindung Dotarem<sup>®</sup>. Die Spektroskopie der Dispersion der kernmagnetischen Resonanz zeigte höhere Protonenrelaxivitäten für Nanopartikel aus  $Gd_{0,6}Eu_{0,4}VO_4$  verglichen mit solchen aus  $GdVO_4$ .

Die vorliegenden Daten deuten darauf hin, dass Seltenerdvanadat-Nanopartikel, die gleichzeitig Gd und Eu enthalten, sehr aussichtsreiche Kandidaten als multifunktionelle *in vivo* Sonden sind. Dieses System könnte auch für die Gadolinium-Neutroneneinfangtherapie oder für die Positronenemissionstomographie nützlich sein.



# List of Figures

1.1	Photograph of bulk GdVO <sub>4</sub> powder from different synthesis methods	11
1.2	Crystal structure of YVO <sub>4</sub>	12
1.3	Comparison of the diffraction pattern of GdVO <sub>4</sub> from coprecipitation with thermal treatment and from the ceramic method	14
1.4	Comparison of the diffraction patterns of GdVO <sub>4</sub> obtained by the ceramic method with those of the precursor oxides	16
1.5	Rietveld refinement of the X-ray diffraction data for GdVO <sub>4</sub> samples obtained by both synthesis pathways	18
1.6	Susceptibility of an antiferromagnet	22
1.7	Molar susceptibility of bulk GdVO <sub>4</sub> as a function of the temperature	23
1.8	Magnetic moment of Gd <sup>3+</sup> in bulk GdVO <sub>4</sub> as a function of the magnetic field	25
2.1	Nucleation-growth models for the synthesis of uniform nanoparticles	28
2.2	Structure formula of the citrate molecule	29
2.3	Electric double layer on the surface of a nanoparticle	31
2.4	Interplay between electrostatic repulsion and van der Waals attraction	32
2.5	Schematic view of steric repulsion between particles	33
2.6	Interplay between steric repulsion and van der Waals attraction	33
2.7	Hydrolysatation and condensation of sodium metasilicate	39
2.8	Silication of rare earth vanadate nanoparticles	40
2.9	Structure formula of the APTES molecule	40
2.10	Functionalization of silica coated rare earth vanadate nanoparticles	41
2.11	Infrared spectra of pristine, silica coated and APTES functionalized Y <sub>0.6</sub> Eu <sub>0.4</sub> VO <sub>4</sub> nanoparticles	43
2.12	Zeta potential of pristine, silica coated and APTES functionalized Y <sub>0.6</sub> Eu <sub>0.4</sub> VO <sub>4</sub> nanoparticles	44
2.13	Number average size distribution of pristine, silica coated and APTES functionalized Y <sub>0.6</sub> Eu <sub>0.4</sub> VO <sub>4</sub> nanoparticles	45
2.14	UV-VIS spectrum of silica coated Y <sub>0.6</sub> Eu <sub>0.4</sub> VO <sub>4</sub> nanoparticles	46
2.15	Hypothetical trigonal-bipyramidal structure of the monoperoxovanadium(V) complex	48
2.16	Absorbance of calibration samples for the colorimetric determination of orthovanadate	50
2.17	Calibration curve for the colorimetric determination of orthovanadate	51
2.18	X-ray structure of the Mg <sup>2+</sup> -ADP-orthovanadate complex in the myosin ATPase domain	56
2.19	Structure formula of the ADP-orthovanadate complex	57

2.20	Structure formula of the xylenol orange molecule . . . . .	57
2.21	Absorbance of the xylenol orange – rare earth complex . . . . .	60
2.22	Calibration curve for the colorimetric determination of free rare earths . . . . .	61
2.23	Temporal evolution of the absorption spectrum of xylenol orange due to rare earth leaching . . . . .	62
2.24	Temporal evolution of the free rare earth concentration . . . . .	63
2.25	SEM micrographs of silica coated GdVO <sub>4</sub> nanoparticles . . . . .	67
2.26	X-ray diffraction patterns of bulk and nanoparticulate GdVO <sub>4</sub> . . . . .	73
2.27	Williamson-Hall plot for GdVO <sub>4</sub> nanoparticles . . . . .	74
2.28	Coherence length for GdVO <sub>4</sub> nanoparticles . . . . .	75
2.29	Microstructural analysis of the X-ray data for GdVO <sub>4</sub> nanoparticles . . . . .	76
2.30	Reconstruction of the crystallite shape . . . . .	78
2.31	3D view of the crystallite shape . . . . .	79
2.32	Formation of nanoparticles from crystallites . . . . .	80
2.33	Nitrogen adsorption isotherm for silica coated GdVO <sub>4</sub> nanoparticles . . . . .	81
2.34	BET analysis of the nitrogen adsorption data for silica coated GdVO <sub>4</sub> nanoparticles . . . . .	82
2.35	Molar susceptibility of Gd <sub>0.6</sub> Eu <sub>0.4</sub> VO <sub>4</sub> <sup>cit</sup> nanoparticles as a function of the temperature . . . . .	84
2.36	Magnetic moment of Gd <sup>3+</sup> in GdVO <sub>4</sub> <sup>cit</sup> and in Gd <sub>0.6</sub> Eu <sub>0.4</sub> VO <sub>4</sub> <sup>cit</sup> nanoparticles as a function of the magnetic field . . . . .	85
3.1	Dieke energy level structure for trivalent rare earth ions in LaF <sub>3</sub> . . . . .	93
3.2	Pathways of non-radiative RE <sup>3+</sup> deexcitation . . . . .	94
3.3	Non-radiative transitions with energy trapping inside the crystal . . . . .	96
3.4	Excitation and emission spectra for bulk Y <sub>0.95</sub> Eu <sub>0.05</sub> VO <sub>4</sub> . . . . .	97
3.5	Mechanism of Eu <sup>3+</sup> luminescence in a rare earth vanadate matrix . . . . .	98
3.6	Energy diagram of Eu <sup>3+</sup> luminescence in a rare earth vanadate matrix . . . . .	99
3.7	Luminescence excitation and emission spectrum for Y <sub>0.6</sub> Eu <sub>0.4</sub> VO <sub>4</sub> nanoparticles . . . . .	100
3.8	H <sub>2</sub> O <sub>2</sub> generation by NOX-type transmembrane enzymes . . . . .	104
3.9	Architecture of the active gp91phox/NOX2 complex . . . . .	105
3.10	The H <sub>2</sub> O <sub>2</sub> cycle inside the cell . . . . .	107
3.11	Conformational change induced by intramolecular disulfide linkage . . . . .	108
3.12	H <sub>2</sub> O <sub>2</sub> mediated signaling pathways in endothelial cells . . . . .	109
3.13	Hydrogen peroxide detection using Amplex Red . . . . .	111
3.14	Hydrogen peroxide detection using dichloro-dihydrofluorescein . . . . .	111
3.15	Hydrogen peroxide detection by deprotection of a fluorescein boronate derivative . . . . .	112
3.16	Hydrogen peroxide detection by deprotection of a coumarin boronate derivative . . . . .	112
3.17	Hydrogen peroxide detection by deprotection of a fluorescein sulfonate derivative . . . . .	113
3.18	Hydrogen peroxide detection by photoinduced electron transfer . . . . .	114
3.19	Hydrogen peroxide detection by emission wavelength shift . . . . .	114
3.20	Reversible molecular probe for hydrogen peroxide detection . . . . .	115

3.21	Europium complex for reversible hydrogen peroxide detection . . . . .	115
3.22	Reversible hydrogen peroxide detection using HyPer . . . . .	116
3.23	Excitation and emission spectra of $Y_{0.6}Eu_{0.4}VO_4$ nanoparticles before and after photoreduction . . . . .	118
3.24	Cyclic photoreduction and reoxidation of a single $Y_{0.6}Eu_{0.4}VO_4$ nanoparticle . . . . .	118
3.25	Concentration-dependent luminescence recovery of $Y_{0.6}Eu_{0.4}VO_4$ nanoparticles . . . . .	119
3.26	Luminescence microscopy setup . . . . .	121
3.27	Luminescence of silica coated $Y_{0.6}Eu_{0.4}VO_4$ nanoparticles detected individually . . . . .	127
3.28	Luminescence of silica coated $Y_{0.6}Eu_{0.4}VO_4$ nanoparticles in ensemble detection . . . . .	128
3.29	White-light transmission image of a vascular smooth muscle cell . . .	129
3.30	Individually detected silica coated $Y_{0.6}Eu_{0.4}VO_4$ nanoparticle as a cellular hydrogen peroxide sensor . . . . .	130
4.1	Magnetic resonance and relaxation . . . . .	134
4.2	Rotational correlation times dependent relaxation times according to the BPP theory . . . . .	136
4.3	Mode of action of a contrast agent . . . . .	139
4.4	Multiple contributions to the overall relaxivity . . . . .	140
4.5	Structure of clinically approved contrast agents based on a tetraazacyclododecanetetraacetic acid ligand . . . . .	146
4.6	Structure of clinically approved contrast agents based on a diethylenetriaminepentaacetic acid ligand . . . . .	147
4.7	Structure of mangafodipir trisodium . . . . .	148
4.8	Relaxation times for Dotarem <sup>®</sup> . . . . .	159
4.9	Relaxation times for $Gd_{0.6}Eu_{0.4}VO_4^{cit}$ nanoparticles . . . . .	160
4.10	Comparison of the NMRD profiles for several Gd-containing nanoparticles . . . . .	163
4.11	NMRD profiles for three clinically approved $Gd^{3+}$ contrast agents . .	164
4.12	Luminescence emission spectrum for $Gd_{0.6}Eu_{0.4}VO_4$ nanoparticles . .	165
4.13	$Gd_{0.6}Eu_{0.4}VO_4$ nanoparticles as hydrogen peroxide sensors in ensemble detection . . . . .	167
4.14	$Y_{0.6}Eu_{0.4}VO_4/GdVO_4$ core-shell nanoparticles as hydrogen peroxide sensors in ensemble detection . . . . .	168
A.1	Bragg-Brentano parafocussing geometry . . . . .	175
A.2	Data acquisition in Bragg-Brentano geometry . . . . .	177
A.3	Displacement of the reflection positions of silicon . . . . .	178
A.4	Integral breadth of the Bragg peaks of calibration samples . . . . .	181
A.5	Comparison of the integral breadths of the Bragg peaks for silicon and bulk $GdVO_4$ . . . . .	182
A.6	Geometry of a scattering experiment . . . . .	192
A.7	Dependency of the average particle size on the weighting method . . .	194

A.8 Contrast through secondary electron emission . . . . .	195
A.9 Polymers used for surface coating for SEM observation . . . . .	196
A.10 Main types of gas physisorption isotherms, according to the IUPAC classification . . . . .	198
A.11 Structure formula of rhodamine 6G hydrochloride . . . . .	199
A.12 Emission spectrum of rhodamine 6G . . . . .	201
A.13 Calibration curve for the quantum yield determination . . . . .	202
A.14 Zeeman splitting of the nuclear energy niveaus in a static magnetic field . . . . .	204
A.15 Larmor precession of a nuclear spin in a static magnetic field . . . . .	205
A.16 Effect of an electromagnetic pulse on the magnetization vector . . . . .	206
A.17 NMR signal detection . . . . .	207
A.18 Inversion recovery pulse sequence . . . . .	207
A.19 CPMG pulse sequence . . . . .	208
A.20 Transverse relaxation time measurement . . . . .	208
A.21 MRI scanner gradient magnets . . . . .	209
A.22 Pulse and gradient timing during image acquisition . . . . .	210

# List of Tables

1.1	Peak positions and intensities for GdVO <sub>4</sub> . . . . .	15
1.2	Sample stoichiometry derived from elemental analysis . . . . .	16
1.3	Parameters obtained from Rietveld refinement . . . . .	19
2.1	Molar extinction coefficients for aqueous solutions of trichloromonoper- oxovanadium(V) in the presence of rare earth ions . . . . .	51
2.2	Yield of nanoparticle syntheses by the normal and citrate route . . . . .	53
2.3	Fit parameters for the quantification of free rare earth ions . . . . .	61
2.4	Nanoparticle sizes obtained from dynamic light scattering . . . . .	65
2.5	Nanoparticle size analysis . . . . .	67
2.6	Parameters obtained from the microstructural analysis . . . . .	77
3.1	Electronic configurations of rare earth ions used in this study . . . . .	90
3.2	Energy scales of different interactions encountered in solid rare earth compounds . . . . .	91
3.3	Selection rules for transitions in lanthanide ions in a crystal . . . . .	94
3.4	Luminescence quantum yields for nanoparticle dispersions . . . . .	101
3.5	Characteristic data for cellular ROS species . . . . .	103
4.1	FDA approved Gd-containing contrast agents in the USA . . . . .	144
4.2	Approved Gd-containing contrast agents in the EU . . . . .	145
4.3	Physical constants of main contrast agents . . . . .	145
4.4	Approved negative contrast agents . . . . .	148
4.5	Physical constants of negative contrast agents . . . . .	149
4.6	New nanoparticulate positive contrast agents . . . . .	151
4.7	Imaging and therapeutic techniques and their targeting component . . . . .	152
4.8	Relaxivities for rare earth vanadate nanoparticles . . . . .	161
B.1	Crystal structure of selected REXO <sub>4</sub> . . . . .	212
B.2	Magnetic properties of selected REXO <sub>4</sub> . . . . .	214



# Introduction

## Nanotechnology for biological imaging and therapy

Currently, nanotechnologies enjoy great popularity in many scientific domains. In particular, nanoobjects are of special interest for biological imaging and therapy. The use of nanoparticles allows to tailor a probe for the intended application and to incorporate the functionalities needed. Biological and medical imaging applications rely mainly on luminescence and magnetic resonance imaging so that a nanoparticle suited for such applications should possess convenient luminescence and magnetic properties. Chemo- and radiotherapy are widely used potent therapy methods for which nanoparticles can be used beneficially if they are able to carry a drug to a specific target or if they possess a radiosensitizing effect.

A large variety of luminescent nanoobjects for imaging has been proposed. Exogenously introduced organic fluorophores or endogenously genetically encoded fluorescent proteins are well documented but they suffer from rapid photobleaching (Goldys, 2009) and have therefore a limited application range for biological processes which have to be studied on long time scales in the minute to hour range. Semiconductor fluorescent nanocrystals have a high quantum yield and photostability but studies of biological molecules labeled with a single quantum dot may be hindered by the blinking of these particles (Michalet *et al.*, 2005). Potential cytotoxicity and a complex surface modification chemistry constrain further their applications. Newer developments include luminescent nanodiamonds (Chang *et al.*, 2008) or composites made up from inorganic nanoparticles conjugated to organic fluorophores (Burns *et al.*, 2006). Rare earth doped nanoparticles exhibit interesting optical properties and low cytotoxicity that make them ideal candidates for biological luminophores (Bouzigues *et al.*, 2011). Their promising photophysical properties include high photostability, no blinking, narrow emission lines, long lifetimes and simple surface functionalization procedures. They have additionally the potential to detect oxidants in a time- and space-resolved manner.

Another widely used imaging technique especially in the human body is magnetic resonance imaging (Westbrook and Kaut, 1998) where the different relaxation times of the protons in water depending on the environment are used to reconstruct an image. Contrast can significantly be increased and scanning times reduced when administering a contrast agent containing paramagnetic ions. Clinically approved contrast agents contain  $Gd^{3+}$  ions bound to an organic chelator so that liberation of toxic  $Gd^{3+}$  ions is prevented. Incorporation of gadolinium ions in nanoparticles would allow for high local concentrations, increased relaxivity values, long circulation times and negligible leaching rates.

The combination of different imaging techniques is of great interest as more and

complementary information can be obtained in the same time. Multimodal imaging and sensing can contribute to more efficient and less time-consuming medical examinations rendering possible the use of less xenobiotic substances and a cost reduction.

One of the major topics in chemotherapy is the toxicity of the administered drug (Perry, 2007). Targeting allows to reduce unwanted side effects on healthy parts of the organism and can deliver the active principle at a high concentration to the region or the organ to treat. For a target-oriented delivery of the active compound, the latter has to be conjugated with an addressing moiety (Hillery *et al.*, 2001). Strategies often involve the packing of the active compound in a biodegradable polymer containing the address sequence. However, conjugation of drugs to nanoparticles which can be observed with the imaging techniques cited above adds the possibility to track the drug and to monitor the release process. Special forms of radiotherapy such as neutron capture therapy use the radiation produced by an internal target in the body (Alessio, 2011). Nanoparticles open up the possibility to combine imaging and therapy as the image-yielding compound and the target for the nuclear reaction may be incorporated in one and the same object.

## Rare earth vanadate nanoparticles

Multifunctional rare earth vanadate nanoparticles can be used for biological imaging and therapy. Luminescent rare earth vanadate and phosphate nanoparticles have been developed in the *Laboratoire de Physique de la Matière Condensée* (LPMC) at the *Ecole Polytechnique* and their properties have been studied thoroughly. Several applications including oxidant detection and single particle tracking have been demonstrated by the *Laboratoire d'Optique et Biosciences* (LOB). In the following, we will give a short chronological summary of the studies carried out at the LPMC and LOB laboratories and devoted to this type of nanomaterials in the two laboratories where this thesis work was performed:

- Huignard (2001) developed two aqueous synthesis protocols for the production of lanthanide-doped yttrium vanadate  $\text{YVO}_4$  nanoparticles of either 10 nm or 40 nm diameter.  $\text{Eu}^{3+}$  doping of the matrix material yielded a strong luminophore emitting in the red spectral region. It was shown that the synthesized nanoparticles can be functionalized by adding a silica layer onto their surface. Characteristic material parameters were reported and the optical properties as well as the mechanism of luminescence of  $\text{Eu}^{3+}$ -doped  $\text{YVO}_4$  were studied in a comprehensive manner.
- Buissette (2004) adapted the colloidal synthesis protocol to produce rare earth phosphates.  $(\text{La,Ce,Tb})\text{PO}_4$  nanoparticles of 5 nm diameter presenting green luminescence emission were described. It was shown that the cerium ions can be protected from oxidation by growing a crystalline  $\text{LaPO}_4$  layer on the core nanoparticles. These core-shell composites could further be covered with a silica layer for functionalization. The feasibility of white luminescence emission was demonstrated using mixtures of  $\text{Eu}^{3+}$ -doped  $\text{YVO}_4$  with  $(\text{Ce,Tb})\text{PO}_4$  and

CePO<sub>4</sub>. The incorporation of these nanoparticles in silica yielded transparent and luminescent layers.

- Giaume (2006) studied the method of surface functionalization by a two step process in which first a silica layer is added and then an organic layer. Conditions for different surface functionalization reactions were reported and detailed analysis of the obtained organic surface as well as its reactivity for coupling reactions were provided. The size and shape of nanoparticles with and without a silica layer was determined by electron microscopy with good statistics due to a large number of analyzed particles.
- Casanova (2008) analyzed the physics of the photoinduced bleaching process in Eu<sup>3+</sup>-doped YVO<sub>4</sub> nanoparticles. It was discovered that the photobleaching is due to a reduction of the Eu<sup>3+</sup> ions which is reversible upon adding an oxidant like hydrogen peroxide. This finding opened the way for the application of such nanoparticles as an optical hydrogen peroxide sensor. The response of single nanoparticles to hydrogen peroxide was studied and the detection of endogenously produced hydrogen peroxide was shown in cells. Furthermore, tracking of nanoparticles coupled to the bacterial  $\epsilon$ -toxin was demonstrated.
- Mialon (2009) investigated the crystallinity of Eu<sup>3+</sup>-doped YVO<sub>4</sub> nanoparticles. It was shown that polycrystalline particles obtained from the colloidal synthesis can be treated thermally after their embedding in a solid silica matrix in order to avoid coalescence so that monocrystalline particles can be recovered. Optical properties before and after annealing as well as in different solvents and with changing Eu-doping levels were studied. An upconversion process in ytterbium- and erbium-codoped nanoparticles was described and analyzed.
- Nguyen (2009) used Eu<sup>3+</sup>-doped YVO<sub>4</sub> nanoparticles for the detection of hydrogen peroxide with temporal resolution. The characterization of the luminescence response to different hydrogen peroxide concentrations allowed to calibrate the nanoparticles as a quantitative sensor. The hydrogen peroxide production in cells after stimulation of the latter with a signaling molecule was shown using internalized nanoparticles. The temporal resolution enabled the characterization of different signaling pathways and their interplay. The versatility of the nanoparticles for the elucidation of cellular signaling pathways was demonstrated.
- Türkcan (2010) employed Eu<sup>3+</sup>-doped YVO<sub>4</sub> nanoparticles as a luminescent probe linked to peptidic pore-forming toxins. Single molecule tracking of the receptor-bound labeled toxins by luminescence microscopy allowed to investigate the receptor motion on the cell membrane. It was shown that the toxin receptors undergo confined diffusion in stable domains of the cell membrane. These domains were demonstrated to be lipid rafts. Introduction of receptor-bound nanoparticle-labeled toxins into a microfluidic channel enabled the application of a force to the receptor and to study its behavior under non-equilibrium conditions.

## Positioning of this work

The aim of the present thesis was to further develop the system of rare earth vanadate nanoparticles so that it can accommodate additional functionalities. During this task, we could rely on the comprehensive knowledge concerning the synthesis and the luminescence properties of the system. A promising approach consisted in rendering the particles detectable for magnetic resonance imaging.  $\text{Gd}^{3+}$  ions are effective proton relaxation enhancing agents and due to the chemical similarity of rare earths, the synthesis of gadolinium-containing rare earth vanadate nanoparticles was possible using the protocols developed previously. Various architectures of the nanoparticles are possible. The gadolinium ions may either be mixed with the europium ions so that the luminescent and relaxation enhancing properties are concentrated in one phase or the core-shell principle may be revisited so that a luminescent phase is combined with a relaxation enhancing phase. In both cases, it has to be verified if the luminescence properties and the ability to detect hydrogen peroxide are retained. The presence of gadolinium in the nanoparticles opens up simultaneously the possibility for therapeutic applications. These topics will be discussed in the manuscript as follows:

1. The present study is devoted to multifunctional nanoparticles, however, the first chapter will deal with the synthesis as well as the crystallographic and magnetic properties of bulk rare earth vanadates, in particular those of  $\text{GdVO}_4$ . The knowledge of the properties of the bulk material is crucial for several characterizations of the nanoparticles. We will discuss the advantages and drawbacks of two methods for the synthesis of the bulk material. The products were analyzed thoroughly and especially concerning the aspects of purity and stoichiometry. The magnetic character conferred to the compound by incorporation of  $\text{Gd}^{3+}$  ions was characterized to be able to assess later in the manuscript the influence of the finite size of the nanoparticles on this property.
2. The second chapter deals with the synthesis and characterization of nanoparticles. We will review the basics of the colloidal chemistry process which allows the formation of nanoparticles of either about 10 nm or 40 nm diameter. The stability aspects of aqueous nanoparticle dispersions will be discussed and the possibility of nanoparticle coating with a silica layer which can also serve as a base for the functionalization with reactive organic groups will be presented. As the exact knowledge of the concentration of rare earth or vanadate ions contained in the particles is of crucial importance for their application in magnetic resonance imaging, special attention is paid to their quantification. Both free rare earth and vanadate ions are toxic to animals and humans, therefore the determination of the stability of the particles, in particular the ion leaching rates, is necessary. Perhaps the most important question when dealing with nanoobjects is their size and shape. We will therefore discuss the methods of dynamic light scattering and scanning electron microscopy which allow for determination of the size of a nanoobject. These techniques are complementary to the microstructural analysis of the X-ray diffraction pattern obtained for the nanoparticles. We will present the corresponding

analysis and make an attempt to provide a model in order to explain the relationship between one crystallite and one nanoparticle. This model will be completed by gas adsorption measurements aiming to determine the specific surface of the nanoparticles. The last section will be devoted to magnetic measurements on the nanoparticles.

3. We will start the third chapter with an overview of the luminescence properties of rare earth ions. The optical properties of  $\text{Eu}^{3+}$ -doped  $\text{YVO}_4$  materials follow and we will then discuss the results of the quantum yield determination on nanoparticles of various compositions. The next section will be devoted to the cellular role of hydrogen peroxide as a second messenger, its endogenous production and an overview of signaling pathways involving hydrogen peroxide. We will then review intracellular techniques for detection of hydrogen peroxide and put hereby the focus on the properties of Eu-doped rare earth nanoparticles. Finally, the results of *in vitro* measurements concerning the photoreduction and luminescence recovery of individual nanoparticles as well as of ensembles of nanoparticles will be discussed and data on *in vivo* detection of hydrogen peroxide will be presented. These data confirm previously obtained results and show the reproducibility of the oxidant detection properties for successive syntheses.
4. The fourth chapter will deal with the application of Gd-containing rare earth vanadate nanoparticles as contrast agents in magnetic resonance imaging. For this purpose, we will first review the relaxation mechanisms in nuclear magnetic resonance and discuss the parameters influencing them. Contrast and contrast enhancing mechanisms will be discussed and an overview of the currently clinically approved contrast agents will be given. We will furthermore present newer developments in contrast agent design which are mainly based on nanoparticles. A summary of the multimodal aspects of imaging will complete the theory part. We will then present and discuss the results concerning the relaxation times at fixed and variable magnetic field of various designs of rare earth vanadate nanoparticles. The last section will deal with the luminescence properties of Gd-containing rare earth vanadate nanoparticles as well as their response to hydrogen peroxide thus demonstrating the multifunctional properties of these nanoparticles.



# Chapter 1

## Synthesis and characterization of bulk rare earth vanadates

The present chapter deals with bulk rare earth vanadate materials. Although the intended applications require that the material is used in form of nanoparticles, it is important to study thoroughly the properties of the bulk material before investigating additional finite size effects. The knowledge of parameters derived from the bulk material is of crucial importance for the characterization of the nanoparticles. We will start with the description of two different synthesis routes for the production of gadolinium vanadate. Comparative characterization of the two obtained samples allows the assessment of their quality. One synthesis protocol is simple and rapid but it is possible that it does not result in the needed quality while the other can produce a high quality compound but at the expense of a time-consuming procedure. As a pure and stoichiometric  $\text{GdVO}_4$  compound must be guaranteed, we will pursue with a comprehensive characterization of the obtained products by X-ray diffraction. The last section of the chapter will be devoted to the study of the magnetic properties conferred to the material by incorporation of paramagnetic gadolinium ions. The obtained data will be compared in the next chapter to those obtained for the nanoparticles and will allow to determine the influence of the finite size on the magnetism.

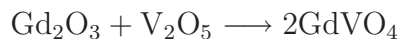
### 1.1 Synthesis of bulk gadolinium vanadate

Synthesis of bulk rare earth vanadates and in particular of gadolinium vanadate may be performed by two different methods. The intended material can either be produced by a solid state synthesis at high temperature or by first employing the colloidal chemistry route for precipitating the material from soluble salt solutions in water and followed by a thermal treatment in order to increase the particle size.

#### 1.1.1 Solid state synthesis

Inorganic solids are most commonly prepared by the ceramic method consisting of mixing and heating of solid precursors so that they react to form the desired compound (Smart and Moore, 2005). Generally, one takes stoichiometric amounts of the precursors, which are ground finely to the smallest particle size possible and then heated for several hours in a furnace. Applied to the particular case

of gadolinium vanadate, the most facile reaction scheme is to produce  $\text{GdVO}_4$  as the sum of gadolinium oxide  $\text{Gd}_2\text{O}_3$  and vanadium pentoxide  $\text{V}_2\text{O}_5$ :



The ceramic method demands a high temperature, essential to provide the activation energy so that the highly coordinated ions can leave their lattice position and diffuse over long distances. Lower temperatures often render the reaction impossible or unreasonably slow. However, this high temperature may cause problems concerning the stability of the precursors or the product. In the general case, the ceramic method is a solid state synthesis and the reaction temperature does not reach the melting temperature of any of the precursors or products but is ideally about two-thirds of them. In our special case, this condition cannot be fulfilled due to the large difference in the melting temperatures of vanadium pentoxide and gadolinium oxide.  $\text{V}_2\text{O}_5$  melts already at  $681^\circ\text{C}$  (Lide, 2008) whereas  $\text{Gd}_2\text{O}_3$  needs to be heated to  $2339^\circ\text{C}$  (Lide, 2008) for fusion. A temperature well below  $700^\circ\text{C}$  would extremely slow down the synthesis as the diffusion process is the time limiting step. Diffusion can be facilitated by small grain sizes and thorough mixing but a high temperature remains still necessary.

Working with vanadium pentoxide in the liquid phase may cause problems due to volatility and decomposition of this compound. Boussières *et al.* (1958) reported that  $\text{V}_2\text{O}_5$  has a non-negligible vapor pressure at high temperatures. They measured a value of 12 hPa at  $1200^\circ\text{C}$  meaning that prolonged heating at temperatures in this range results in a loss of  $\text{V}_2\text{O}_5$ . Milan (1929) has measured the dissociation pressure of vanadium pentoxide. At  $1125^\circ\text{C}$ , they have determined an oxygen partial pressure of 235 hPa and an amount of 4.7 mol %  $\text{VO}_2$  produced by reduction of  $\text{V}_2\text{O}_5$ . The authors state that the decomposition is reversible as long as the oxygen is not removed. However, the oxygen partial pressure in air is only 211 hPa and thus smaller than the partial pressure from the oxygen originating from  $\text{V}_2\text{O}_5$  decomposition. A reaction in an open system results therefore in a net oxygen loss and production of  $\text{VO}_2$ . We note that the resulting compound  $\text{VO}_2$  has a melting point of  $1967^\circ\text{C}$  (Lide, 2008) and that one reobtains the conditions of a real solid state reaction upon reduction of  $\text{V}_2\text{O}_5$  to  $\text{VO}_2$ .

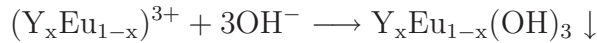
Unfortunately, the literature is ambiguous on the question if, and in the affirmative case how, stoichiometric  $\text{GdVO}_4$  can be prepared by the ceramic method. Cook and Cashion (1979) reported that mixing stoichiometric amounts of  $\text{Gd}_2\text{O}_3$  and  $\text{V}_2\text{O}_5$  results after sintering in a product containing a few percent of unreacted gadolinium oxide. Sage (2006) stated that an about 2% excess of  $\text{V}_2\text{O}_5$  is necessary in order to compensate its volatility. On the other hand, Schwarz (1963) explained that problems due to evaporation and reduction of  $\text{V}_2\text{O}_5$  can be circumvented when controlling carefully the reaction conditions. They reported that a slow heating of the mixture between the rare earth oxide and  $\text{V}_2\text{O}_5$  up to  $950^\circ\text{C}$  over a period of 4 h prevents fusion of  $\text{V}_2\text{O}_5$  which has still not reacted. This behavior may be interpreted by the initial formation of  $\text{GdVO}_4$  at the surface of  $\text{V}_2\text{O}_5$  grains. As this compound has a melting point of about  $1800^\circ\text{C}$  (Higuchi *et al.*, 2004), the vapor pressure of  $\text{V}_2\text{O}_5$  is reduced and the latter remains in the solid state. The authors

report that after this slow heating ramp, the end temperature can be increased to 1100 °C without the risk of oxygen loss. Also higher end temperatures have been reported. Gaur and Lal (1983) prepared GdVO<sub>4</sub> from Gd<sub>2</sub>O<sub>3</sub> and V<sub>2</sub>O<sub>5</sub> at temperatures of about 1250 °C and using two firing cycles. However, they do not state the heating ramp.

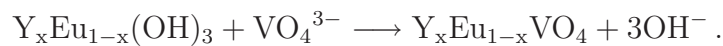
Based on these literature data, a thorough characterization of the obtained sample is required. The compound will be analyzed by X-ray diffraction in order to exclude any contamination. Possible impurity phases could involve unreacted Gd<sub>2</sub>O<sub>3</sub> due to a partial evaporation of the reaction partner V<sub>2</sub>O<sub>5</sub> or the parasitic phase GdVO<sub>3</sub> formed by reduction of GdVO<sub>4</sub>. It is also possible to obtain a non-stoichiometric GdVO<sub>4</sub> phase with vacancies on the vanadium and oxygen sites due to evaporation and reduction of V<sub>2</sub>O<sub>5</sub>.

### 1.1.2 Synthesis by coprecipitation

Huignard *et al.* (2000) have studied the synthesis of Eu-doped yttrium vanadate nanoparticles at ambient temperature by coprecipitation from soluble yttrium and europium nitrate and sodium orthovanadate salts. Although we focus on bulk material in this chapter and not on nanoparticles, the general findings, with exception made to the conditions for size control, are transposable to the present case. The authors have shown that the reaction strongly depends on the pH and that yttrium orthovanadate can only be obtained in a narrow pH range between 12.5 and 13.0. The reaction involves in a first step the precipitation of the kinetically favored hydroxide Y<sub>x</sub>Eu<sub>1-x</sub>(OH)<sub>3</sub>



which, in a second step, reacts with orthovanadate to form thermodynamically stable Y<sub>x</sub>Eu<sub>1-x</sub>VO<sub>4</sub>



In very alkaline conditions with pH > 13, yttrium and europium hydroxides are precipitated and cannot react with orthovanadate. An acidic pH favors the formation of condensed vanadate species and the production of a rare earth orthovanadate is not feasible.

We note that Huignard (2001) has only investigated the properties of aqueous Y<sup>3+</sup> and Eu<sup>3+</sup> ions and not those of other trivalent rare earth solutions, but Chang and Mao (2007) have also obtained Gd(OH)<sub>3</sub> by a colloidal hydrothermal method using a soluble Gd<sup>3+</sup> salt and NaOH at pH 13. Holleman *et al.* (1995) states generally that all rare earth hydroxides are not soluble in water and only soluble in acids. These data suggest that the synthesis conditions derived from Y<sup>3+</sup> and Eu<sup>3+</sup> solutions can also be applied to Gd<sup>3+</sup>.

For the synthesis of a bulk reference material, we are not interested in a well-defined particle size so that a careful control of the growth process is not necessary. The solution method has the advantage that it is carried out at ambient temperature and circumvents any possible problem linked to the high temperature

solid state synthesis described in section 1.1.1. However, a drawback resides in the fact that one may obtain only little extended crystalline regions comprising defects due to the rapid precipitation of  $\text{GdVO}_4$  upon combination of the precursor solutions. Mialon *et al.* (2008) have shown that the crystallinity of yttrium vanadate nanoparticles can be significantly increased by thermal treatment at temperatures of  $900^\circ\text{C}$  and above. We can use a similar process for increasing the crystallite size in a  $\text{GdVO}_4$  precipitate. This two step synthesis process starting with coprecipitation followed by thermal treatment is more time consuming than the direct synthesis *via* the ceramic method but problems arising from the use of  $\text{V}_2\text{O}_5$  are avoided.

## 1.1.3 Experimental protocol

### 1.1.3.1 Ceramic method

We synthesized bulk gadolinium vanadate  $\text{GdVO}_4$  by a high temperature solid state synthesis based on the protocol presented by Gaur and Lal (1983) and using the heating rate given by Schwarz (1963). 0.03 mol (10.875 g) powdered  $\text{Gd}_2\text{O}_3$  (purity 99.99%,  $M_W = 362.50$  g/mol, Strem Chemicals) and 0.03 mol (5.456 g) powdered  $\text{V}_2\text{O}_5$  (spectrographically standardized,  $M_W = 181.88$  g/mol, Johnson Matthey) are ground and mixed intimately in a agate mortar. The obtained powder is poured into an alumina crucible with alumina lid and placed in an oven. The thermal treatment cycle consists in a heating ramp at 4 K/min to  $1250^\circ\text{C}$  and a subsequent plateau of 10 h. The oven is allowed to cool down to ambient temperature without temperature control. The obtained brown-grey powder is ground in the agate mortar and then placed again in the alumina crucible. A second thermal cycle is performed under identical conditions as the first one yielding a red-brown product. The reaction yield is determined based on the mass of the final powder product after grinding.

### 1.1.3.2 Coprecipitation and thermal treatment

Gadolinium vanadate  $\text{GdVO}_4$  bulk material is also prepared by coprecipitation from solution. For this purpose, sodium orthovanadate  $\text{Na}_3\text{VO}_4$  (purity 99.9%,  $M_W = 183.91$  g/mol, Alfa Aesar) is dissolved in ultrapure water with a specific resistance of at least  $18.2 \text{ M}\Omega \cdot \text{cm}$  to a final concentration of 0.1 M. The pH of the solution is verified using a pH meter and is adjusted if necessary to the range 12.5–13.0 by adding 1 M sodium hydroxide (Merck). The solution is then filtered through a  $0.22 \mu\text{m}$  vacuum filter system (Corning) in order to remove nonsoluble impurities.  $\text{Gd}(\text{NO}_3)_3 \cdot 6\text{H}_2\text{O}$  (purity 99.9%,  $M_W = 451.36$  g/mol, Alfa Aesar) is dissolved in ultrapure water to a final concentration of 0.1 M and is used as prepared. We note that  $\text{GdCl}_3$  can equally be employed under otherwise unchanged conditions.

A volume of 0.1 M  $\text{Na}_3\text{VO}_4$  solution is placed in a recipient and stirred vigorously at ambient temperature. The same volume of 0.1 M  $\text{Gd}(\text{NO}_3)_3$  solution is poured into the recipient and the stirring is maintained for 30 min. We note that the synthesis can also be performed using solutions with a concentration of 0.2 M in order to reduce the reaction volume.

The precipitate is isolated by successive centrifugation-redispersion cycles. The

dispersion is spun at 26,323 g for 20 min. The supernatant is discarded and the precipitate recovered in a glass flask. Complete redispersion is achieved in about 80 mL ultrapure water under stirring for several hours. Plastic recipients should not be used as prolonged stirring may contaminate the nanoparticle dispersion with plastic particles difficult to remove. The initial suspension can be highly concentrated in this step by a factor of 10 to 20 facilitating and speeding up all further purification steps. The centrifugation-redispersion cycles are repeated 3 to 5 times depending on the concentration factor and until a conductivity of the dispersion below  $100 \mu\text{S}/\text{cm}$  is reached. In the last centrifugation step, the precipitate is not redispersed but placed in a recipient and dried overnight at  $100^\circ\text{C}$ . The obtained product is ground to a fine white powder and the reaction yield is determined based on the mass of the final powder product after grinding.

The crystallite size in the  $\text{GdVO}_4$  powder is increased by thermal treatment. The sample is placed in an alumina crucible and subjected to a temperature program consisting in a 2 h ramp to  $900^\circ\text{C}$  and a 10 h step at this temperature. All annealing reactions are conducted in an oxidizing air atmosphere.

#### 1.1.4 Results and discussion

$\text{GdVO}_4$  bulk material was produced by the ceramic method as well as by coprecipitation and subsequent thermal treatment. Synthesis yields reached 95 % in the case of the ceramic method and about 75 % for the coprecipitation pathway. The yields of the coprecipitation reaction are generally lower and differ from one to another synthesis although the same protocol was employed. This finding can be explained by the fact that purification demands several centrifugation and redispersion steps with a slight loss of material during each step.

The visual comparison of the two thermally treated powders and the precursor from the precipitation reaction shows a significant difference in color (fig. 1.1). The powder obtained from room temperature coprecipitation is white to slightly



**Figure 1.1: Photograph of bulk  $\text{GdVO}_4$  powder from different synthesis methods.** Samples were obtained from coprecipitation at room temperature (left, sample MS20), from coprecipitation and subsequent thermal treatment at  $900^\circ\text{C}$  (middle, MS11) and from the ceramic method at  $1250^\circ\text{C}$  (right, MS8).

yellow. After thermal treatment at  $900^\circ\text{C}$ , this powder darkens its color to become yellow-ochre. In contrast, the product from the ceramic method is red-brown. This

difference in the color can be explained by either a non-stoichiometry of the product or by a second parasitic phase. The following section will therefore be devoted to a X-ray study in order to elucidate further this question.

## 1.2 Characterization by X-ray diffraction

### 1.2.1 Crystal structure

Most of the phosphates, arsenates and vanadates as well as chromates of rare earths crystallize in the tetragonal zircon structure (Schwarz, 1963) having the space group  $I4_1/amd$  (no. 141, Hahn (2005)). This structure is in particular found for  $YVO_4$  (fig. 1.2) and  $GdVO_4$ . One unit cell contains four formula units

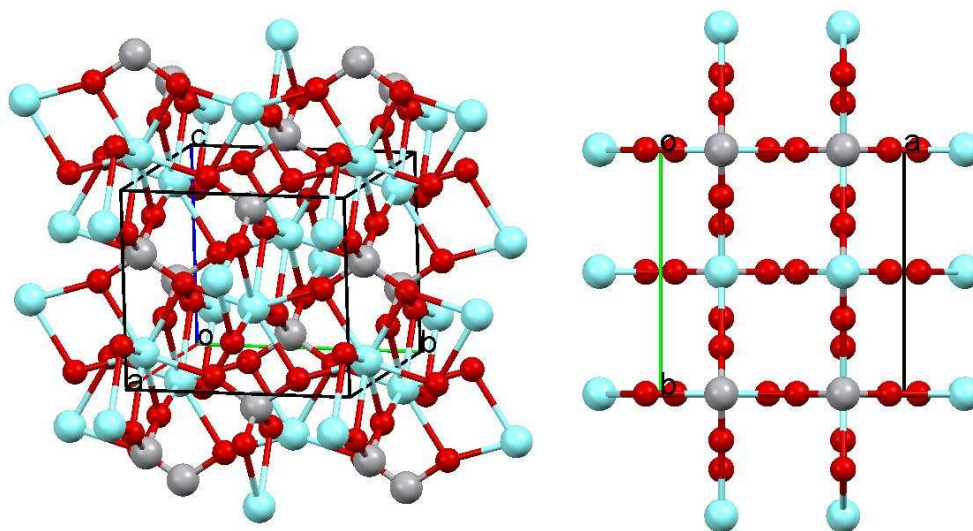


**Figure 1.2: Crystal structure of  $YVO_4$ .** Atoms are drawn to 0.25 of their respective van-der-Waals radius and sticks are 0.1 Å thick. Oxygen atoms are shown in red, vanadium atoms in grey and yttrium atoms in light blue. Left drawing: 3D view of the structure. Right drawing: Projection of the structure along the crystallographic  $c$ -axis visualizing the chains of  $[VO_4]$  tetrahedra and  $[YO_8]$  distorted dodecahedra. Crystallographic data is from Broch (1933) deposited in the crystallographic information file (CIF) 1011156 on the Crystallography Open Database (Grazulis *et al.*, 2009).

of  $YVO_4$ . These are organized so that along the crystallographic  $c$ -axis,  $[VO_4]$  tetrahedra containing the vanadium atom in their center alternate with  $[YO_8]$  polyhedra made up from a central yttrium atom and oxygen atoms in their corners. The two types of polyhedra are interconnected by edge sharing resulting in isolated  $[VO_4]$  tetrahedra. We note that the  $[YO_8]$  polyhedra are distorted dodecahedra in which the yttrium ion occupies a non-centrosymmetric crystallographic site with  $D_{2d}$  symmetry. This distortion is due to the presence of two different sets of Y–O bond lengths. While 4 Y–O bonds measure 2.30 Å, the 4 others are longer and measure 2.43 Å (Guillot-Noël *et al.*, 1998). This property is of crucial importance for the luminescence of  $Eu^{3+}$  ions introduced as dopants in the host structure and

occupying the crystallographic site of the  $Y^{3+}$  ion. We will discuss this topic in section 3.1.

It is interesting to note that many rare earth vanadates show a low temperature Jahn-Teller distortion of their tetragonal structure to an orthorhombic geometry (tab. B.1). However, such a crystallographic transition has neither been found for  $YVO_4$  (Elliott *et al.*, 1972) nor for  $GdVO_4$  (Cashion *et al.*, 1969).

## 1.2.2 Experimental protocol

A comprehensive description of the X-ray diffraction technique as well as a detailed discussion of the applied corrections is given in appendix section A.1. In brief, data acquisition is performed on a X-ray powder diffractometer in Bragg-Brentano geometry using Cu  $K_\alpha$  radiation at a wavelength of  $\lambda = 1.5418 \text{ \AA}$ . A  $2\theta$  range from  $10^\circ$  to  $75^\circ$  is used for routine measurements or up to  $130^\circ$  for measurements employed in Rietveld refinement. A step width of  $0.005^\circ$  is defined for  $GdVO_4$  samples and of  $0.01^\circ$  for the  $Gd_2O_3$  and  $V_2O_5$  precursors. The integration time per angular step is set to 100 s except for the  $GdVO_4$  sample from coprecipitation and thermal treatment where a diffraction pattern with a high signal-to-noise ratio was acquired using an integration time of 500 s.

## 1.2.3 Results and discussion

### 1.2.3.1 Identity

We have recorded the X-ray powder diffraction patterns of bulk  $GdVO_4$  obtained by the ceramic method and from coprecipitation and thermal treatment at  $900^\circ\text{C}$ . The results are shown for comparison in fig. 1.3. A perfect agreement of the two diffraction patterns is found indicating that both synthesis pathways were able to produce the same compound. A detailed analysis of the peak profiles (data not shown) confirmed that the peak widths are almost identical for the two samples. This finding signifies that a material with the same crystallite size may be obtained either by the ceramic method at  $1250^\circ\text{C}$  or from coprecipitation and annealing at  $900^\circ\text{C}$ . We can therefore compare in the following these two samples to verify if the applied conditions during the synthesis of  $GdVO_4$  from  $Gd_2O_3$  and  $V_2O_5$  were appropriate to avoid evaporation of  $V_2O_5$  and the formation of a non-stoichiometric compound as discussed in section 1.1.1.

The identity of the material can readily be assessed by comparing the X-ray diffraction pattern of  $GdVO_4$  obtained by coprecipitation and thermal treatment to the peak list for  $GdVO_4$  reported by Swanson *et al.* (1967). Table 1.1 lists the obtained peak positions and intensities together with those from the literature. The comparison shows generally a good agreement between the measured and the literature values although the difference is somewhat bigger for the (211), (112) and (220) peaks. This proves that the synthesized product is made up from  $GdVO_4$ . The material obtained from the ceramic method displays a likewise good agreement with the literature values (data not shown). However, as the visual comparison of the samples obtained by the two synthesis pathways (fig. 1.1) showed different colors,

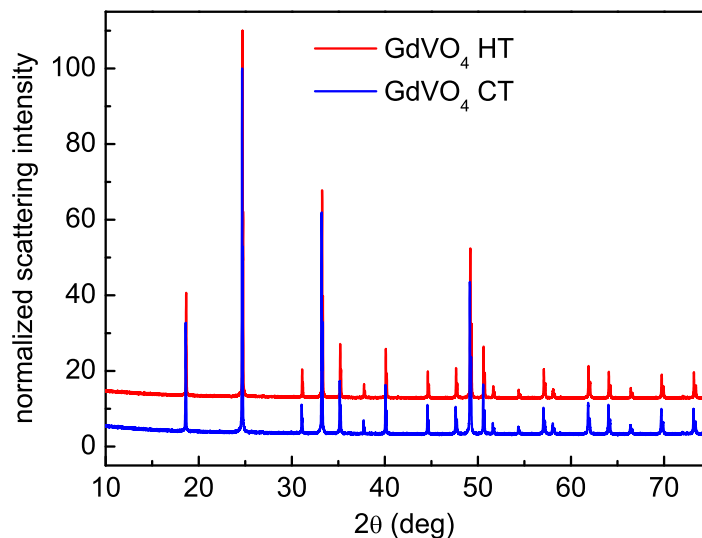


**Figure 1.3: Comparison of the diffraction pattern of  $\text{GdVO}_4$  from coprecipitation with thermal treatment and from the ceramic method.** Data were normalized to the most intense peak. HT stands for the diffraction data of the compound produced by the high temperature ceramic method and CT for that obtained from coprecipitation and successive thermal treatment with the highest annealing temperature being  $900^\circ\text{C}$ . HT data are shifted upwards for better visualization.

we have now to decide whether this effects is due to impurities in the material or due to a non-stoichiometry of the  $\text{GdVO}_4$  compound.

### 1.2.3.2 Purity

Phase purity has been assessed by comparison of the diffraction profile of  $\text{GdVO}_4$  to those of the precursors  $\text{Gd}_2\text{O}_3$  and  $\text{V}_2\text{O}_5$ . The corresponding patterns are displayed in fig. 1.4 for the  $\text{GdVO}_4$  sample synthesized by the ceramic method. We find that none of the peaks of  $\text{Gd}_2\text{O}_3$  nor  $\text{V}_2\text{O}_5$  is visible. The inset in fig. 1.4 shows that there is not even a small contribution from the precursors at the position of their most intense peaks. The ceramic method is able to produce a high purity compound with crystallized impurities smaller than the detection level of the X-ray analysis. The latter can be estimated by calculation of the instrument level of detection  $\delta$  within a 99.95 % confidence level. Rousseau (2001) devised the expression

$$\delta = \frac{4.65}{I(X)} \sqrt{\frac{I_b}{t_c}} \quad (1.1)$$

where  $I(X)$  is the count rate over background per percent of the substance of interest X,  $I_b$  is the background count rate in the diffractogram of the product  $\text{GdVO}_4$  in the region of interest ( $1400\text{s}^{-1}$ ) and  $t_c$  is the counting time per detector position, here 100 s. The count rates  $I(X)$  for  $\text{V}_2\text{O}_5$  and  $\text{Gd}_2\text{O}_3$  were calculated from the non-normalized diffractograms (graphs not shown) and yielded values of  $I(\text{V}_2\text{O}_5) = 230\text{s}^{-1}$  and  $I(\text{Gd}_2\text{O}_3) = 90\text{s}^{-1}$ , respectively. With eq. 1.1, we obtain an instrument level of detection for  $\text{V}_2\text{O}_5$  of 0.07 % and for  $\text{Gd}_2\text{O}_3$  of 0.2 %. As we

**Table 1.1: Peak positions and intensities for GdVO<sub>4</sub>.** Data are displayed for GdVO<sub>4</sub> synthesized by coprecipitation and thermal treatment at 900 °C (sample MS11). Integrated intensities  $I$  are normalized to the most intense reflection in the diffractogram, the (200) peak. The peak indicated with \* is splitted and arises from reflections corresponding to the (431) and (501) planes.

$h$	$k$	$l$	measured		Swanson <i>et al.</i> (1967)	
			$2\theta$ (deg)	$I$ (%)	$2\theta$ (deg)	$I$ (%)
1	0	1	18.600	30	18.601	30
2	0	0	24.661	100	24.667	100
2	1	1	31.067	9	31.091	12
1	1	2	33.209	66	33.227	75
2	2	0	35.156	20	35.148	25
2	0	2	37.714	4	37.716	4
3	0	1	40.061	14	40.072	12
1	0	3	44.575	9	44.590	10
3	2	1	47.611	12	47.611	12
3	1	2	49.135	58	49.152	55
4	0	0	50.566	16	50.581	16
2	1	3	51.601	4	51.611	6
4	1	1	54.341	3	54.351	4
4	2	0	57.045	13	57.060	12
0	0	4	58.053	3	58.047	6
3	3	2	61.845	16	61.859	16
2	0	4	64.028	11	64.041	14
*			66.388	5	66.399	6
2	2	4	69.713	10	69.720	10
5	1	2	73.175	13	73.179	12
4	4	0	74.314	3	74.331	2

do not observe any peak in the diffractogram of the synthesized product, impurities resulting from the precursor oxides must be smaller than these levels of detection. The cumulative impurities are therefore smaller than 0.3% equivalent with a purity of GdVO<sub>4</sub> higher than 99.7%. This result does not confirm the observation made by Cook and Cashion (1979) of several percent unreacted Gd<sub>2</sub>O<sub>3</sub> in the product, when starting from stoichiometric amounts of the reactants.

The quality of the GdVO<sub>4</sub> sample prepared by coprecipitation and annealing at 900 °C can be assessed by the same procedure as non-reacted Gd(NO<sub>3</sub>)<sub>3</sub> and Na<sub>3</sub>VO<sub>4</sub> salts should form the corresponding oxides at high temperatures. The comparison of the diffraction pattern of this GdVO<sub>4</sub> sample to that of the sample from the ceramic method (fig. 1.3) shows that the peak positions and intensities superpose perfectly. No parasitic reflections can be found. Absolute background count rates at constant integration time per angular step were comparable to those for the sample

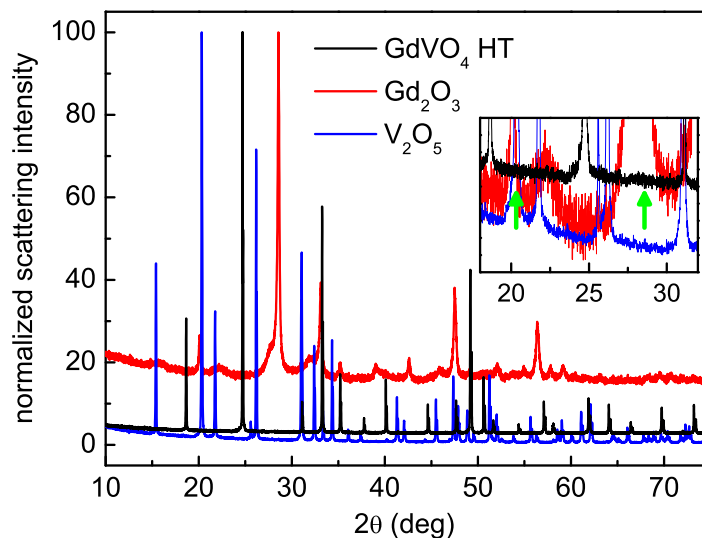


**Figure 1.4: Comparison of the diffraction patterns of  $\text{GdVO}_4$  obtained by the ceramic method with those of the precursor oxides.** The graph shows the diffractograms of the three compounds normalized to their most intense peak. The inset depicts the region of small scattering angles in detail. The green arrows mark the position of the most intense peak of  $\text{V}_2\text{O}_5$  (left arrow) and  $\text{Gd}_2\text{O}_3$  (right arrow), respectively. Diffractograms in the inset have been shifted in intensity after normalization for better visualization.

obtained by the ceramic method. We may therefore estimate the purity with respect to another crystalline phase to be also at least 99.7%.

### 1.2.3.3 Stoichiometry

We have used three approaches to elucidate the stoichiometry of the  $\text{GdVO}_4$  sample from the ceramic method. In a first step, the composition of the sample was determined by inductively coupled plasma atomic emission spectroscopy. This measurement was carried out by the *Service Central d'Analyse* of the *CNRS*. The obtained percentages are displayed in tab. 1.2. The data confirms clearly the

**Table 1.2: Sample stoichiometry derived from elemental analysis.** Data were obtained from the *Service Central d'Analyse* of the *CNRS* as mass percentage. CT refers to sample MS11 and HT to sample MS8. Data for sample MS11 is the average from two measurements. The standard deviation of this measurement performed twice serves as an estimation of the error for all measurements.

sample	mass %		atoms per formula unit	
	Gd	V	Gd	V
CT 900 °C	57.2 ± 0.5	19.0 ± 0.1	0.990 ± 0.009	1.013 ± 0.007
HT 1250 °C	57.4 ± 0.5	18.9 ± 0.1	0.994 ± 0.009	1.009 ± 0.007

1 : 1 stoichiometry between Gd and V. We can therefore deduce that the used

synthesis conditions did not result in a loss of  $V_2O_5$ . This observation supports that the controlled and slow heating rate of 4 K/min used during our synthesis, which corresponds to that reported by Schwarz (1963), is necessary and sufficient to prevent fusion and subsequent evaporation of  $V_2O_5$ . We note that the determination of the oxygen content is not possible by elemental analysis and an oxygen loss due to reduction cannot be excluded.

In a second approach, we have searched for the compound  $GdVO_3$  which is in principle obtainable by reduction of  $GdVO_4$  (Sage, 2006) and presents also the the 1 : 1 stoichiometry between Gd and V. As  $GdVO_3$  crystallizes in an orthorhombic structure (Pickardt *et al.*, 1988), specific peaks would be visible in a mixed compound composed of  $GdVO_4$  and  $GdVO_3$ . However, the analysis of the diffractogram showed that the latter contains exclusively peaks which can be attributed to  $GdVO_4$  (tab. 1.1). We may therefore conclude that no  $GdVO_3$  impurity is present above the instrumental limit of detection which can be estimated to be in the order of 0.1 % for the most intense peak of  $GdVO_3$  at  $2\theta = 32.940^\circ$  as given in the International Centre for Diffraction Data (ICDD) file 00-025-0205. One might also imagine that an amorphous phase is present which would not give rise to sharp reflections in the X-ray diffraction pattern. However, one would expect a broad peak for this amorphous phase. As the base line is flat (fig. 1.3), this possibility seems less probable. Additionally, the high temperatures used during the synthesis or the thermal treatment are not compatible with significant amounts of non-crystallized matter in the sample.

The last possibility constitutes therefore a non-stoichiometric compound concerning the oxygen content. This question has been addressed by Rietveld refinement of the X-ray diffraction data. We refined first the diffraction patterns of  $GdVO_4$  obtained by both synthesis pathways with fixed stoichiometry according to the sum formula (fig. 1.5). The refined parameters are summarized in the two columns on the left of tab. 1.3. We find that unit cell parameters as well as the position of the oxygen atom are virtually the same for both synthesis pathways. Instrumental resolution parameters expressed as the values  $U$ ,  $V$  and  $W$  are identical within the error limits indicating that a robust and precise determination of the instrumental resolution function was possible. The profile broadening parameter with Lorentzian character  $Y$  is slightly different. This behavior is not immediately clear as the comparison of the peak profiles resulted in comparable widths for the materials from both synthesis pathways. A reason for this difference can be found when comparing also the Lorentzian isotropic strain parameter  $X$  which varies in the contrary direction and shows a rather high standard deviation. As strain is not expected in the material after a relaxing treatment at high temperature and as the peak broadening apart from the instrumental resolution function is less significant according to the sharp peaks observed, there might be some mutual compensation in the small and poorly defined values of  $X$  and  $Y$ . The respective thermal agitation factors for vanadium and oxygen correspond within the error limits but a slightly higher difference is observed for gadolinium which cannot be explained. The agreement factors indicate in both cases a refinement of reasonable but not exceptional quality. Any attempts to add further physically founded refinable parameters did not result in a significant lowering of these parameters. Jiménez-Melero *et al.* (2006) has refined neutron

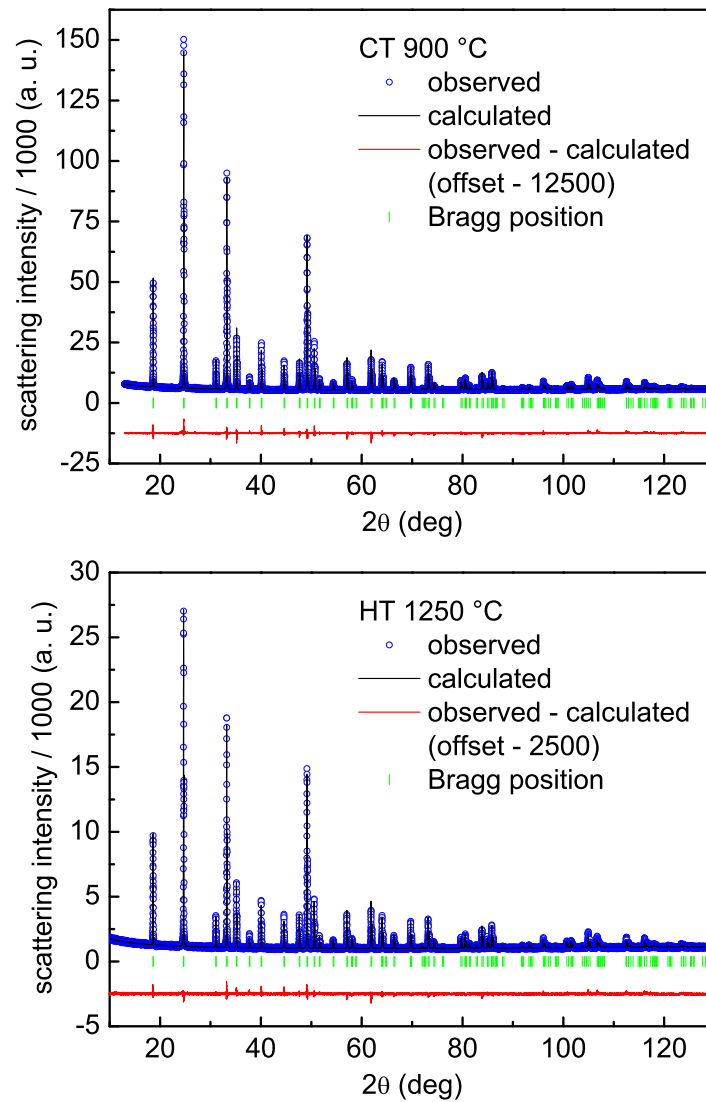


**Figure 1.5: Rietveld refinement of the X-ray diffraction data for  $\text{GdVO}_4$  samples obtained by both synthesis pathways.** Refinement was performed using the FullProf suite with the parameters given in section A.1.12 and fixed occupation factors according to the ideal stoichiometry of  $\text{GdVO}_4$ . HT designates the sample produced by the high temperature ceramic method and CT that obtained by coprecipitation with thermal treatment.

diffraction data for the isostructural compound  $\text{GdCrO}_4$  at 300 K using the same algorithm and obtained values of  $R_F = 4.8\%$  and  $R_{wp} = 20.0\%$  being on the same order of magnitude as ours. This comparison shows that the refinement parameter set is acceptably well defined.

To come back to the main issue, *i. e.* the stoichiometry of the sample obtained by the ceramic method, it is not straightforward to answer this question as the simplest way to additionally vary the occupation factors results in an artifact. Thermal agitation factors reduce the peak intensity particularly at high diffraction angles while occupation factors vary the peak intensities conditioned by the contribution of

**Table 1.3: Parameters obtained from Rietveld refinement.** Values in the left two columns correspond to the refinements depicted in fig. 1.5. The values reported in the right column were obtained by refining the data of the HT 1250 °C sample using the thermal agitation factors of the CT 900 °C sample and allowing for variation of the occupation factors on the vanadium and oxygen sites. Oxygen  $y$ - and  $z$ -positions are expressed in units of the unit cell dimensions. Values in brackets indicate parameters which were set and not refined. Sample designations are the same as in fig. 1.5.

parameter	CT 900 °C	HT 1250 °C	HT 1250 °C non-stoichiometric
$a = b$ (Å)	$7.21469 \pm 0.00001$	$7.21468 \pm 0.00001$	$7.21468 \pm 0.00001$
$c$ (Å)	$6.35044 \pm 0.00001$	$6.34986 \pm 0.00001$	$6.34986 \pm 0.00001$
$U$	$0.0024 \pm 0.0002$	$0.0025 \pm 0.0002$	$0.0025 \pm 0.0002$
$V$	$-0.0024 \pm 0.0002$	$-0.0024 \pm 0.0002$	$-0.0018 \pm 0.0002$
$W$	$0.00137 \pm 0.00004$	$0.00145 \pm 0.00005$	$0.00128 \pm 0.00005$
$X$	$0.071 \pm 0.001$	$0.045 \pm 0.001$	$0.036 \pm 0.001$
$Y$	$0.0111 \pm 0.0004$	$0.0131 \pm 0.0005$	$0.0159 \pm 0.0005$
$y$ -position O	$0.4331 \pm 0.0002$	$0.4347 \pm 0.0003$	$0.4337 \pm 0.0003$
$z$ -position O	$0.2013 \pm 0.0003$	$0.1997 \pm 0.0004$	$0.2015 \pm 0.0004$
$B$ (Gd)	$1.34 \pm 0.01$	$1.17 \pm 0.02$	(1.34)
$B$ (V)	$1.64 \pm 0.03$	$1.56 \pm 0.04$	(1.64)
$B$ (O)	$1.62 \pm 0.06$	$1.76 \pm 0.08$	(1.62)
occupancy Gd	(1)	(1)	(1)
occupancy V	(1)	(1)	$0.970 \pm 0.002$
occupancy O	(4)	(4)	$3.96 \pm 0.02$
$R_p$ (%)	18.8	31.1	31.2
$R_{wp}$ (%)	11.9	16.0	16.0
$R_B$ (%)	6.7	6.3	6.0
$R_F$ (%)	6.4	9.0	8.8
$\chi^2$	6.3	1.9	1.9

the different atoms to a particular peak so that in the present case strong correlation between these parameters leads to unreasonable agitation factors or occupation factors which are not compatible with the compound. To avoid this problem, we had to fix the values of  $B$  so that the occupation factors could be varied. As oxygen loss is an issue during the ceramic method but not when using the coprecipitation and thermal treatment pathway where a formula stoichiometry of the compound can be assumed, it is better to use the thermal agitation factors obtained from this sample. However, refinement of  $B$  for the sample obtained by the ceramic method assuming a formula stoichiometry did not result in big differences. The right column in tab. 1.3 shows that the occupation factors obtained with this procedure attain almost the theoretical values of 1 for vanadium and 4 for oxygen. This result is especially for oxygen remarkable as the occupation factors of light elements have generally only a weak influence on the calculated diffraction pattern and better agreement

between measured and calculated patterns is often achieved by unreasonably large changes in the occupation factors. As the difference from the expected occupation is very small, we can finally confirm that the produced compound is made up from pure and stoichiometric  $\text{GdVO}_4$ . This finding implies that within the error limits of the analysis there is no net reduction of the compound by a change of  $\text{V}^{5+}$  to the  $\text{V}^{4+}$  state. The different colors of the  $\text{GdVO}_4$  powders seen in fig. 1.1 may therefore be explained by a not perfectly ionic V–O bond resulting in vanadium ions in the +4 oxidation state as reported by Gaur *et al.* (1983) and Gaur and Lal (1983). It seems that this process is temperature dependent. We note that such a charge delocalization does not affect the overall oxidation state of the material.

## 1.3 Characterization of the magnetic properties

This section is devoted to the study of the magnetic properties of bulk  $\text{GdVO}_4$  and has to be seen in the continuity of our attempt to study thoroughly the bulk material before continuing with the nanoparticles. Magnetic properties of nanoparticles of the same composition as well as of derivatives will be discussed in section 2.8.3 and serve finally to validate their application as contrast agent in magnetic resonance imaging (chapter 4). In general, we have to distinguish magnetic properties arising from the orientation of individual atomic magnetic moments in a field which are found in the paramagnetic temperature region from those due to cooperative effects and occurring in the low temperature range. The theory of paramagnetism is discussed in appendix section A.2 and only the central expressions necessary for the data analysis are summarized in this section.

### 1.3.1 Paramagnetism

The underlying principles of paramagnetism are discussed in detail in appendix section A.2.2. In brief, the magnetic moment  $\mu$  of an atom or ion in units of the Bohr magneton  $\mu_B$  is given by

$$\frac{\mu}{\mu_B} = g_J J B_J(y), \quad (1.2)$$

where  $g_J$  is the Landé factor,  $J$  the quantum number of the total angular momentum and  $B_J$  the Brillouin function with the argument

$$y = \frac{g_J \mu_B J B}{k_B T}. \quad (1.3)$$

Herein,  $B$  is the magnetic field,  $k_B$  the Boltzmann constant and  $T$  the temperature. In the case of a weak magnetic field and a high temperature, eq. 1.2 simplifies to the classical Curie law

$$\frac{\mu}{\mu_B} = \frac{\mu_B g_J^2 J(J+1)}{3k_B} \cdot \frac{B}{T}. \quad (1.4)$$

The molar Curie constant in  $SI$  units can be calculated to

$$C_{mol}^{SI} = \frac{\mu_0 \mu_B^2 N_A g_J^2 J(J+1)}{3k_B}. \quad (1.5)$$

### 1.3.2 Long range antiferromagnetic order

Interactions between the magnetic moments arising from the electrons can potentially produce a long range order of these moments in a solid. Two principal types of interaction are possible. The first is the direct interaction between magnetic dipoles, an effect which can be understood classically. However, an estimation of the involved energy shows that this effect can only be responsible for magnetic order in materials with very low transition temperatures below 1 K. A much more important contribution arises from the exchange interaction. This effect is based on the quantum mechanical principle that the overall electronic wave function must be antisymmetric relative to the exchange of two electrons. Respecting this condition, direct exchange of unpaired electrons between neighboring atoms or indirect exchange *via* a mediating atom is possible resulting electron delocalization over a larger area and in a reduction of its kinetic energy.

A review of the experimental data concerning the magnetism of rare earth compounds of the composition  $\text{REXO}_4$  with RE being a rare earth and  $X = \text{P, As, Cr or V}$  shows that the predominant magnetic order is the antiferromagnetic arrangement except in  $\text{RECrO}_4$  where the additional magnetic moment of  $\text{Cr}^{5+}$  causes ferromagnetism (tab. B.2). As  $\text{GdVO}_4$  belongs to the group of antiferromagnets, we will limit our theoretical considerations to the case of antiferromagnetism.

Antiferromagnetic order occurs when the exchange integral is negative meaning that the energetically most favorable order for nearest neighbors is the antiparallel coupling of their magnetic moments. The solid can in this case be considered as made up of two interpenetrating sublattices with a magnetization direction  $M_+$  for one of them and  $M_-$  for the other. The net magnetization  $M_+ + M_-$  is vanishing in the ordered state. The temperature of the phase transition to the ordered state is called the Néel temperature  $T_N$ . Above this temperature, the material behaves as a paramagnet. Using the Weiss temperature  $\theta$ , the Curie law can be extended to the Curie-Weiss law which is written for the susceptibility as

$$\chi = \frac{C}{T - \theta}. \quad (1.6)$$

This equation is valid for mass, volume and molar susceptibilities under the condition that the corresponding Curie constant  $C$  is used. Antiferromagnetic order is characterized by a negative Weiss temperature. Although a first order calculation yields  $\theta = T_N$ , experimental data shows often a large discrepancy between these two temperatures indicating the importance of higher order effects.

The behavior of the susceptibility is more complicated below  $T_N$ . As we have discussed, the net magnetization is vanishing in the absence of a magnetic field. However, when a magnetic field is applied, the effect depends on the direction of the field with respect to the moments as an energetic favorable alignment of moments in one sublattice goes along with an expense in energy for the moments on the other sublattice. In the case where the field is oriented perpendicular to the easy axis, an increasing field induces the magnetization of both sublattices to tilt in the field direction. For a constant field, we expect the magnetization and therefore the susceptibility to be the same for all temperatures between  $T = 0$  and  $T = T_N$

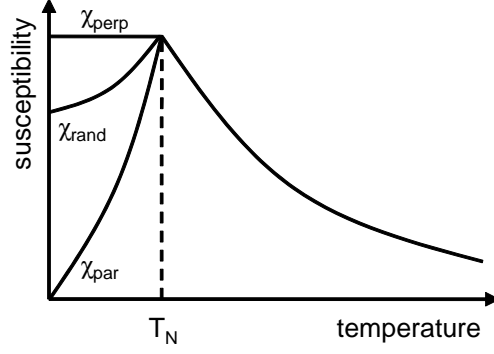


**Figure 1.6: Susceptibility of an antiferromagnet.**  $\chi_{perp}$  and  $\chi_{par}$  are the susceptibilities of a single crystal perpendicular and parallel to the field direction, respectively. Random orientation of the crystallites in a powder sample results in a susceptibility according to  $\chi_{rand}$ .

(fig. 1.6). For an orientation of the field parallel to the easy axis, we expect that a small field has no influence on the antiferromagnetic order at  $T = 0$  resulting in  $\chi_{par}$  being zero. When the temperature increases but remains below  $T_N$ , thermal fluctuations increase the divergence of the spins which may be aligned more easily in the direction of the external field. This results in a temperature dependent magnetization below  $T_N$  and in a susceptibility increasing up to the value of the paramagnetic susceptibility at  $T_N$ . In a powder sample, the orientations of the easy axis are randomly distributed. As only one parallel but two orthogonal perpendicular directions are possible, the susceptibility of a powder sample is given by

$$\chi_{rand} = \frac{2}{3}\chi_{perp} + \frac{1}{3}\chi_{par}. \quad (1.7)$$

The measurement of the susceptibility of an antiferromagnet shows therefore a maximum at  $T_N$ .

### 1.3.3 Cooperative magnetic effects in GdVO<sub>4</sub>

The magnetism of bulk GdVO<sub>4</sub> has been studied for the first time by Cashion *et al.* (1969). Susceptibility measurements have shown that the material undergoes a paramagnetic-antiferromagnetic phase transition at the Néel temperature  $T_N = 2.495$  K. The ordering was reported to occur along the crystallographic  $c$ -axis. The structure was described to be of the simplest two-sublattice type where each Gd<sup>3+</sup> ion interacts with its four nearest neighbors which are in antiparallel orientation. Colwell *et al.* (1971) analyzed the isostructural compound GsAsO<sub>4</sub> and deduced that also in GdVO<sub>4</sub> interactions with the nearest but also with the next neighbors have to be taken into consideration. Gorodetsky *et al.* (1973) performed magnetoelectric measurements with the objective to confirm the magnetic structure. Their results were compatible with the magnetic space group assignment  $I4'_1/a'm'd$ . Susceptibility measurements in the paramagnetic region and above ambient temperature were performed by Gaur *et al.* (1983); Gaur and Lal (1983). The authors found an unusual magnetic behavior as the observed susceptibility was

higher than that calculated for the  $\text{Gd}^{3+}$  ions and explained this effect with the not perfectly ionic V–O bond (section 1.2.3.3) leading to ferromagnetic coupling between  $\text{Gd}^{3+}$  mediated by  $\text{V}^{4+}$ .

### 1.3.4 Experimental protocol

The sample for susceptibility measurements is prepared in polycarbonate capsules. 17.3 mg of finely ground  $\text{GdVO}_4$  obtained by the ceramic method (sample MS8) are filled in the capsule and blocked mechanically by paraffin wax. Magnetic susceptibility is measured using a S600X SQUID magnetometer (Cryogenic) equipped with a liquid helium cryostat. Measurements as a function of the temperature are performed at a magnetic field strength of 100 Oe and from 5 K to 290 K in 5 K steps after sample cooling in zero magnetic field. Measurements as a function of the magnetic field are conducted as a complete cycle between 50000 Oe and  $-50000$  Oe at 4.8 K after zero field cooling. All measured data are corrected for the diamagnetic contribution of the polycarbonate capsule and the paraffin wax.

### 1.3.5 Results and discussion

The result of the temperature dependent susceptibility measurement on bulk  $\text{GdVO}_4$  is depicted in fig. 1.7 as the molar susceptibility in SI units. The fit according to a Curie-Weiss law shows perfect agreement with the measured data confirming the

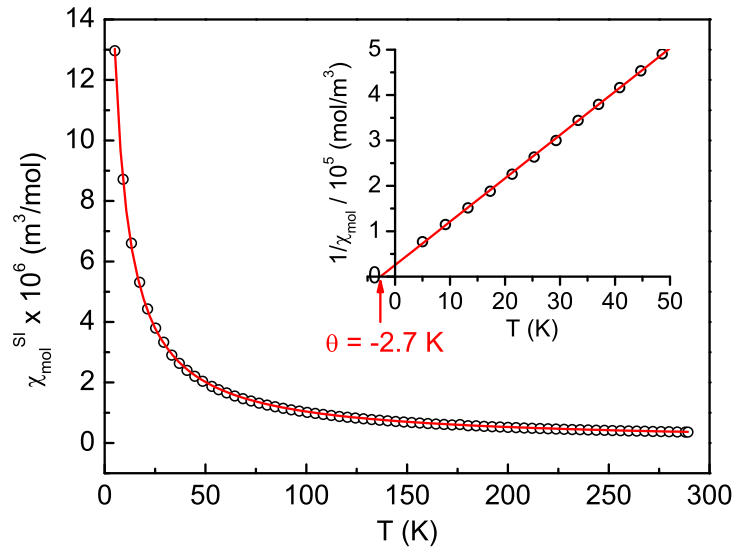


**Figure 1.7: Molar susceptibility of bulk  $\text{GdVO}_4$  as a function of the temperature.** Magnetization data were recorded for the  $\text{GdVO}_4$  sample obtained by the ceramic method and under a magnetic field of 100 Oe. The molar susceptibility was fitted to the equation  $\chi_{mol}^{SI} = \frac{C_{mol}^{SI}}{T-\theta}$  and the values of  $C_{mol}^{SI} = (1.072 \pm 0.003) \cdot 10^{-4} \text{ K m}^3 \text{ mol}^{-1}$  and  $\theta = (-3.23 \pm 0.03) \text{ K}$  were obtained. The inset shows the inverse molar susceptibility plotted as a function of the temperature for the same sample. The linear fit yielded a Curie constant  $C_{mol}^{SI} = (1.047 \pm 0.001) \cdot 10^{-4} \text{ K m}^3 \text{ mol}^{-1}$  and a Weiss temperature of  $\theta = (-2.7 \pm 0.2) \text{ K}$ .

paramagnetic character of the material in the studied temperature range from 290 K down to 5 K. A value of  $\theta = -3.23$  K was determined for the Weiss temperature indicating a phase transition to an antiferromagnetic order. As no susceptibility maximum is observable, the phase transition must occur at a Néel temperature outside the measurement range. A direct visible confirmation of the character of the phase transition can be obtained by plotting the inverse susceptibility (inset in fig. 1.7).  $1/\chi$  is linear as a function of the temperature and a linear fit of the measured values intersects with the temperature axis at the value of the Weiss temperature. By this method, we obtain  $\theta = -2.70$  K which is slightly different from the Weiss temperature extracted by direct fitting of the susceptibility. This can be explained by a different weighting of the measured points depending on the use of the direct or inverse values for the fit and is reflected in the quite different error bars of the Weiss temperature. Cashion *et al.* (1969) reported a Weiss temperature obtained from susceptibility measurements of  $\theta = -2.96$  K. Although they state that the susceptibility was measured with 2% accuracy, they do not give an error of the deduced Weiss temperature. Nevertheless, our values is close to the reported value. As the temperature range of the magnetometer has a lower limit of 5 K, we were not able to follow the susceptibility evolution at the phase transition.

In a next step, we deduced the Landé factor from the Curie constant. The term symbol of the ground state of the  $\text{Gd}^{3+}$  is  $^8\text{S}_{7/2}$  (Wybourne, 1965) meaning that the total angular momentum is  $J = 7/2$ , the angular momentum is vanishing ( $L = 0$ ) and the total spin is  $S = 7/2$ . Using eq. A.62 with the constant from eq. A.63, we get the following expression for the calculation of  $g_J$  from the experimentally measured values of  $C_{mol}^{SI}$ :

$$g_J = \sqrt{\frac{C_{mol}^{SI}}{\frac{7}{2} \cdot \frac{9}{2} \cdot 1.571 \cdot 10^{-6} \frac{\text{K m}^3}{\text{mol}}}} \quad (1.8)$$

We obtain from fitting  $\chi_{mol}^{SI}$  a value of  $g_J = 2.08$  and for the linear fit of  $1/\chi_{mol}^{SI}$  the result  $g_J = 2.06$ . Although eq. A.37 returns a theoretical value of  $g_J = 2$ , experimental Landé factors for  $\text{Gd}^{3+}$  salts being slightly higher than 2 have been reported in the literature (Sucksmith, 1932).

Numerical values of the molar susceptibility are in close agreement to literature data. Our measurement at 290 K resulted in a value of  $\chi_{mol}^{SI} = 3.58 \cdot 10^{-7} \text{ m}^3/\text{mol}$  while the plots of Gaur and Lal (1983) and Gaur *et al.* (1983) yield a value of  $\chi_{mol}^{SI} \approx 3.5 \cdot 10^{-7} \text{ m}^3/\text{mol}$ . In the low temperature range, Cashion *et al.* (1969) give the expression  $\chi_{mol}^{cgs} = \frac{8.04}{T+2.96} \frac{\text{cm}^3}{\text{mol}}$  corresponding to a value of  $\chi_{mol}^{cgs} = 1.01 \text{ cm}^3/\text{mol}$  or  $\chi_{mol}^{SI} = 1.27 \cdot 10^{-5} \text{ m}^3/\text{mol}$  at 5 K. This result is in good agreement with our measurement of  $\chi_{mol}^{SI} = 1.30 \cdot 10^{-5} \text{ m}^3/\text{mol}$ .

We then measured the magnetization as a function of the magnetic field. The result is expressed as a number of Bohr magnetons per  $\text{Gd}^{3+}$  ion in fig. 1.8. Several conclusions can be drawn from the data. First, an applied field of 5 T is not sufficient to reach saturation. However, a saturation value on the order of  $\mu/\mu_B = 7$  is expected. Second, the comparison with the Brillouin function drawn for the theoretical values of  $g_J$  and  $J$  shows a significant deviation from the measured data. Unfortunately due to too less structure in the measured curve

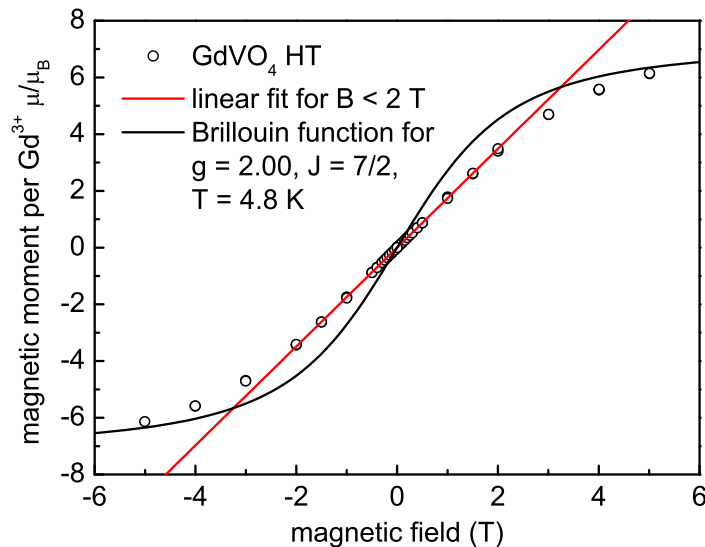


**Figure 1.8: Magnetic moment of  $\text{Gd}^{3+}$  in bulk  $\text{GdVO}_4$  as a function of the magnetic field.** Data were measured for the  $\text{GdVO}_4$  sample from the ceramic method and at a temperature of 4.8 K. The magnetic field was varied  $0 \text{ T} \rightarrow 5 \text{ T} \rightarrow -5 \text{ T} \rightarrow 5 \text{ T}$ . The magnetic moment is given in units of the Bohr magneton per  $\text{Gd}^{3+}$  ion. Data were fitted in the range  $0 - 2 \text{ T}$  to a Curie law  $\frac{\mu}{\mu_B} = C \frac{B}{T}$  and a Curie constant  $C = 1.743 \pm 0.001$  was obtained. A Brillouin function for the theoretical values of  $g = 2.00$  and  $J = 7/2$  at a temperature of 4.8 K is also displayed.

and in particular due to the absence of the saturation plateau, a fit of our data with the relatively complex Brillouin function (eq. A.43) was not possible. We applied instead the linearized low field/high temperature approximation (eq. A.47) to the linear part of the measured values which extends up to about 2 T. The Curie constant obtained from this fit allowed together with eq. 1.8 the calculation of the  $g_J$  factor. As a third and surprising result, we found a low value of  $g_J = 1.54$  which is neither compatible with theory nor with the  $g_J$  factors obtained from the temperature dependent measurement. A possible explanation might be that the observation temperature of 4.8 K is close to the Néel temperature so that the reduced temperature  $T/T_N = 1.9$  is small and critical effects associated with the phase transition are already present. We did not conduct further measurements in this temperature range, as the measurements on bulk  $\text{GdVO}_4$  were intended to serve as a reference for the data relative to the nanoparticles whose application range is mainly limited to ambient temperature.

## 1.4 Conclusion

In this chapter, we presented and discussed the results obtained on  $\text{GdVO}_4$  bulk material. The data are necessary for the further analysis of nanoparticles made up from the same compound. Synthesis of the bulk compound is feasible by two different pathways. The simplest method with the highest yield uses a high temperature synthesis starting from the oxides of gadolinium and vanadium. While

coprecipitation and subsequent thermal treatment to increase the mean crystallite size in the material is much more time consuming and results in a lower yield, this pathway avoids potential problems due to high reaction temperatures. As the literature is controversial about the effect of the low melting temperature of  $V_2O_5$  during a high temperature synthesis and about the question if a pure and stoichiometric compound can be obtained from firing of the precursor oxides, we performed multiple characterizations to elucidate this point. The combination of X-ray diffraction data and elemental analysis revealed that our synthesis conditions were able to produce high purity and stoichiometric  $GdVO_4$ . Rietveld refinement of the diffraction pattern allowed the extraction of important parameters for further analysis of  $GdVO_4$  nanoparticles.

$Gd^{3+}$  ions have an electronic configuration with 7 unpaired electrons resulting in a high total spin and conferring interesting magnetic properties to the  $GdVO_4$  material. We performed magnetic measurements which confirmed the paramagnetism of the compound down to low temperatures. Quantitative data for the molar susceptibility are in close agreement with values reported in the literature. These data will have to be compared to those obtained for the nanoparticles to study the effect of the finite size on the magnetic properties.

# Chapter 2

## Synthesis and characterization of rare earth vanadate nanoparticles

After having studied bulk  $\text{GdVO}_4$ , we will now investigate the effects of finite size resulting from the preparation of  $\text{GdVO}_4$  as nanoparticles. We will first present the synthesis of the nanoparticles and then the steps for surface modification and functionalization. An important part of the chapter will be devoted to the different characterization procedures related to the determination of the vanadate concentration in a given nanoparticle dispersion, the stability and the properties linked to the surface. The crucial parameter for nanoparticles however remains their size. We will therefore use dynamic light scattering, scanning electron microscopy and X-ray microstructural analysis to obtain independent measurements of the particle dimensions. For the latter technique, we will rely on what has already been discussed in the previous chapter and extend the theory to nanoobjects.

### 2.1 Synthesis of nanoparticles

#### 2.1.1 Nanoparticle formation by coprecipitation

Nanoparticles can be synthesized by the colloidal chemistry pathway. We first define what is meant with the term colloid. Hiemenz and Rajagopalan (1997) states that any particle dispersed in a solvent with a linear dimension between  $10^{-9}$  m and  $10^{-6}$  m is considered as a colloid. Another definition says that a colloid is a stable dispersion of small particles in a solvent (Overbeek, 1982). We are in particular interested in colloids made up from an insoluble solid in aqueous phase. The principal preparation method in liquid phase consists of a homogeneous precipitation reaction where, upon mixing of two soluble precursors an insoluble reaction product is formed. During this reaction, two processes can be distinguished. Hierarchically, the first step is the formation of a germ which grows to form particles in a second step. Unfortunately, depending on the actual reaction conditions, these steps occur more or less simultaneously.

Different models have been proposed to explain the mechanism of these steps. In the classical model of LaMer and Dinegar (1950), during the first timespan, the concentration of the dissolved substance, the solute increases. Applied to our homogeneous precipitation reaction, this means that the two solutions are brought into contact by mixing. When saturation reaches almost critical supersaturation,

the formation of stable germs begins. Quickly after the onset of nucleation, the concentration of the solute no longer increases due to the supply of the precursors but decreases as nucleation is very rapid. When the concentration falls below the minimal concentration for nucleation, the latter stops and germs are no longer formed. The existing germs continue to grow until there is no more material to incorporate and the end point of the reaction is defined by the solubility product of the reaction partners.

The size distribution of the particles depends mainly on the duration of the nucleation step. In the ideal case, nucleation occurs almost instantly and growth is slow enough so that the two steps are well separated. In this case, the production of quasi-monodisperse particles is possible. If nucleation is slow, growth of the first formed germs begins while other germs are still produced. As the particle size depends on the duration of growth, early formed germs will become larger than later formed ones.

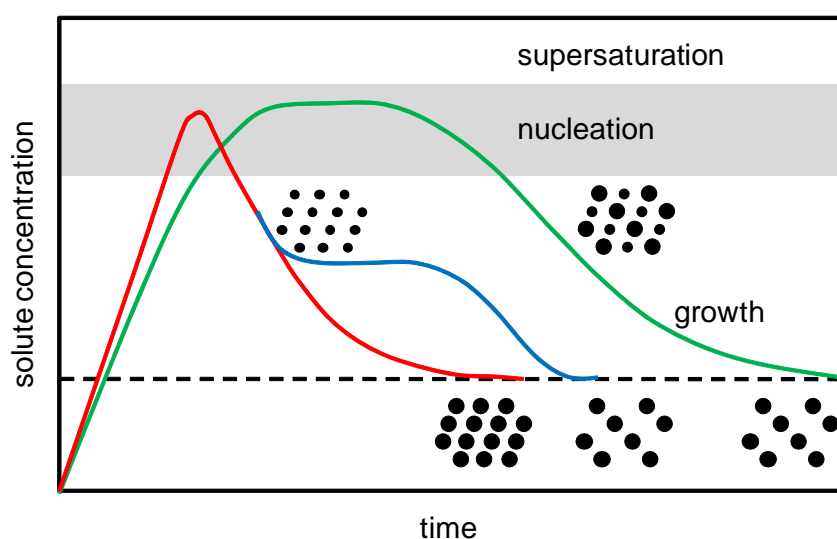


**Figure 2.1: Nucleation-growth models for the synthesis of uniform nanoparticles.** The grey region indicates the zone where nucleation can take place. The dashed line marks the final remaining solute concentration as given by the solubility product. In the classical model of LaMer (red line), diffusion controlled growth occurs after rapid nucleation. Particles of the final size can also be obtained by aggregation of smaller particles shortly after their nucleation (blue line). Ostwald ripening is a process which forms uniform particles from an initial particle dispersion with a larger size distribution (green line). Scheme adapted from Mialon (2009).

Apart from this classical model, two other pathways are possible. In the case of a slower increase of the solute concentration and a temporally extended nucleation process, one obtains first an inhomogeneous dispersion of particles of different size. The process of Ostwald ripening is a self-sharpening mechanism which reduces the system's energy by dissolving small particles and adding this matter to larger particles (Sugimoto, 1987). The mean size of the particles is growing over the time until all particles have uniform size so that no more energy gains is possible and the concentration of the solute has reached the value defined by the solubility product.

It is also possible to obtain uniform particles by aggregation of smaller ones rather than by continuous growth (Ocaña *et al.*, 1995). This process follows at first the same temporal pattern as the classical process but after nucleation took place, it is more favorable for the system to reduce its energy by coalescence of smaller particles than by diffusion controlled growth.

### 2.1.2 Nanoparticle formation control by complexation

Nanoparticle synthesis by coprecipitation of yttrium and orthovanadate yields particles with a diameter on the order of 30 to 40 nm (Huignard, 2001). If one wants to obtain smaller particles, the size increase during the growth phase has to be limited. This can be achieved using a complexing agent for one of the reaction partners (Gacoin *et al.*, 1997). In the case of the present synthesis, it is most appropriate to complex the lanthanide ions (Huignard, 2001). The complexing agent has to be chosen based on its affinity towards the lanthanide ions and the ability to stabilize the nanoparticles during the growth phase and in the final dispersion. Carboxylates are highly suited as complexing agents for colloidal chemistry synthesis routes involving  $Y^{3+}$  for several reasons. First, carboxylates are highly water soluble and the synthesis may therefore be carried out in water. Second, in alkaline conditions, the carboxylic acid functions are deprotonated which allows favorable interaction with  $Y^{3+}$  and prevents the formation and irreversible precipitation of  $Y(OH)_3$  at high pH. Third, the complex formation constants  $pK_f$  are tunable with the number of carboxylate functions. For lanthane for example,  $pK_f$  varies from 2 to 18 if the number of carboxylate functions increases from 1 to 4 (Bjerrum *et al.*, 1957). The possibility of tuning the complexation strength is very important as too strong complexation impedes the particle formation whereas too weak binding limits the size controlling effect.

Huignard *et al.* (2002) has shown that the most suitable complexing agent for the synthesis of yttrium vanadate nanoparticles is sodium citrate (fig. 2.2). The

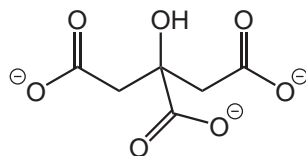


**Figure 2.2: Structure formula of the citrate molecule.**

complex formation constant of citrate is on the order of 8 at 25 °C and is independent of the lanthanide ion (Itoh *et al.*, 1985). This property enables on the one hand the synthesis of Eu-doped nanoparticles as dopant ions are incorporated at the intended stoichiometric ratio and, on the other hand, the substitution of yttrium by gadolinium under otherwise unchanged reaction conditions.

By  $^{51}V$  and  $^1H$  NMR measurements, Huignard *et al.* (2002) explained that the mechanism of nanoparticle formation in the presence of citrate complexation consists of two steps. In the first fast step, a polymeric precipitate containing yttrium,

vanadate and citrate is formed while some vanadate remains in solution. In a second slower step, the free vanadate ions in solution react with yttrium from the polymeric entity forming  $YVO_4$ . The citrate ions are used partly to stabilize the newly formed particles whereas others remain in solution. Stabilization of the particles is achieved by complexation of surface  $Y^{3+}$  ions.

### 2.1.3 Stabilization of colloids

The stability of a colloidal dispersion was explained by Derjaguin and Landau (1941) and Verwey and Overbeek (1948) as the interplay between attractive van der Waals and repulsive electrostatic forces as well as steric repulsion. This explanation is nowadays known under the name DVLO theory. An overview is given in Overbeek (1982).

#### 2.1.3.1 Van der Waals attraction

Attractive van der Waals forces have a long range and can also act across condensed matter, although their strength is weakened by the medium. We consider two spherical particles of radius  $a$  at a distance  $d$  between their centers resulting in a distance  $H = d - 2a$  between the surfaces. Hamaker (1937) derived for the energy due to attraction between two equal spherical particles the expression

$$V_{vdW} = -\frac{A}{6} \left( \frac{2a^2}{d^2 - 4a^2} + \frac{2a^2}{d^2} + \ln \frac{d^2 - 4a^2}{d^2} \right) \quad (2.1)$$

where  $A$  is the Hamaker constant depending strongly on the particles and the medium and which can adopt values between 0.25 and  $25 k_B T$  at ambient temperature. When dealing with the stabilization of colloids, we are interested in the force balance at small interparticle distances. For this range, eq. 2.1 can be approximated by

$$V_{vdW} = -\frac{Aa}{12H}. \quad (2.2)$$

The energy of attraction is on the order of  $k_B T$  for a surface distance  $H \approx 0.1 a$ . We note that the eq. 2.1 and 2.2 are valid for short and very short distances, respectively, and that the van der Waals attraction for large distances scales with  $H^{-6}$ .

#### 2.1.3.2 Electrostatic repulsion

Electrostatic repulsion arises from the charge of the particles due to surface dissociation or preferential adsorption of one type of ions. As the total dispersion of the nanoparticles must be electrically neutral, it is clear that this force cannot originate from a simple Coulomb repulsion but that the surface charge is surrounded by a more or less diffuse layer of counter ions. This layer forms together with the surface charge an electric double layer (fig. 2.3). Two regions within this layer may be distinguished. In the Stern layer, the counter ions strongly interact with the surface charge of the particle. The outer diameter dimension of the particle with its

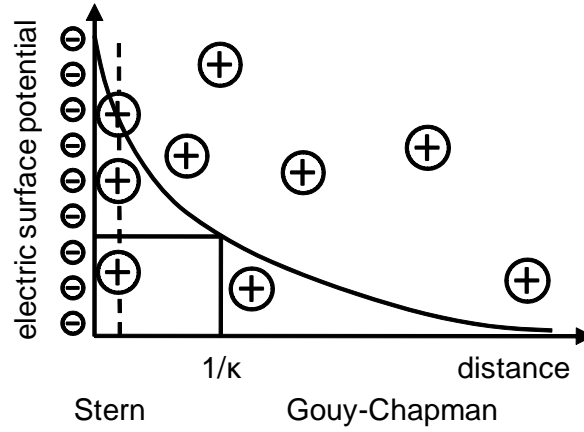


**Figure 2.3: Electric double layer on the surface of a nanoparticle.** We have assumed a preferentially negative surface charge of the nanoparticle. Counter ions are strongly attached to the surface in the Stern layer whereas they only have a weak interaction with the particle in the diffuse Gouy-Chapman layer.

Stern layer corresponds approximately to the hydrodynamic diameter obtained from dynamic light scattering. The electric potential on the surface of the Stern layer is close to the measured  $\zeta$  potential. In the Gouy-Chapman or diffuse outer layer, the counter ions are subject to attraction from the surface and undergo thermal movement. This layer is only loosely bound to the particle. In some distance from the surface, the potential decreases exponentially with the distance with a characteristic distance  $1/\kappa$  and more steeply in the vicinity of the surface. The energy of repulsion between two particles with double layers can be expressed as

$$V_{rep} = +2\pi\epsilon_r\epsilon_0a \left[ \frac{4dT}{zF} \tanh\left(\frac{zF\phi_S}{4dT}\right) \right]^2 \exp(-\kappa H). \quad (2.3)$$

Herein  $\epsilon_r$  is the relative permittivity of the dispersion,  $\epsilon_0$  the vacuum permittivity,  $z$  the charge of the counterions in units of the elementary charge,  $F$  the Faraday constant,  $\phi_S$  the surface potential on the Stern layer and  $\kappa$  the inverse Debye-Hückel length (Debye and Hückel, 1923).

### 2.1.3.3 Kinetic stabilization

Attractive forces decay for very short distances as  $H^{-1}$  and for large distances as  $H^{-6}$ , whereas repulsive forces decay exponentially as  $\exp(-\kappa H)$ . Attraction is therefore predominant at very short and large distances but at intermediate distances on the order of  $H \approx \kappa^{-1}$  repulsion may be more important. An energy barrier which prevents aggregation and stabilizes the dispersion is therefore formed between the two attraction regions (fig. 2.4). The stability of the dispersion depends on the height of the energy barrier compared to the thermal energy  $k_B T$ . The stabilization is therefore of kinetic nature.

The height of the energy barrier depends mainly on two factors. A high charge of the particles increases  $\phi_S$  and concomitantly the height of the energy barrier. A high

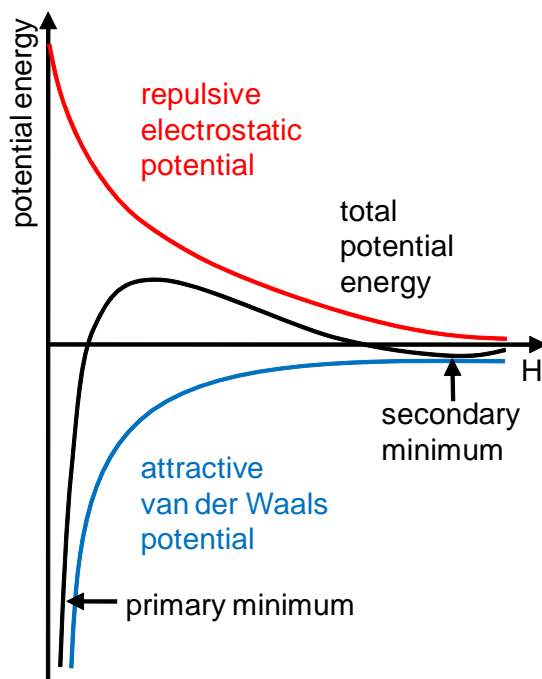


**Figure 2.4: Interplay between electrostatic repulsion and van der Waals attraction.** The potentials are shown as a function of the surface distance  $H$ . The electrostatic repulsion (red line) scales with  $\exp(-\kappa H)$  whereas the van der Waals attraction has a  $H^{-1}$  dependency for small  $H$  and  $H^{-6}$  for large  $H$ . Apart from the primary minimum corresponding to aggregated particles, a second minimum may exist for a stable dispersion.

concentration and/or a large charge number of the counter ions in the surrounding medium compresses the double layer, decreases the region of repulsion and may decrease  $\phi_S$  which in consequence may eliminate the energy barrier. It is necessary to carefully choose counter ions during a synthesis, as already the effect of changing a monovalent ion by a divalent ion can have a tremendous influence on the stability of the colloidal dispersion (Freundlich, 1903).

#### 2.1.3.4 Steric repulsion

Stabilization of a dispersion of particles by steric repulsion is achieved when the surface of the particle is covered with bulky molecules. These molecules which may be adsorbed or bound to the surface are generally composed of long chains. If the chains are soluble in the surrounding medium, they repel one another and generate a strong repulsive force between adjacent particles. The range of the repulsion is on the order of the size of the grafted molecule in a random coil conformation. Steric repulsion is the sum of two effects. First there is an osmotic effect caused by a high concentration of chains in an overlap region. The second contribution comes from a volume restriction effect which originates in the loss of possible conformations of the chains because of the confinement of one chains between the neighboring chains (fig. 2.5). The magnitude of the effect can be tuned by the length and chemical properties of the grafted moieties as well as by the properties of the solvent. We note

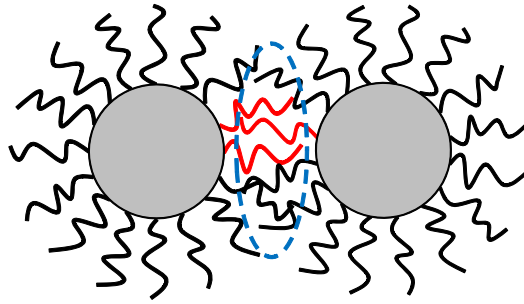


**Figure 2.5: Schematic view of steric repulsion between particles.** The particles are covered with long chains. Steric repulsion is due to an osmotic effect originating from high chain concentration in the overlap zone (blue ellipse) and a volume restriction effect from loss of possible conformations (indicated by the relatively stretched conformations of the red chains.)

that if the surface chains are not soluble in the surrounding medium, they collapse and the steric repulsion is not effective.

The corresponding steric repulsion potential increases very steeply when the particles come in close vicinity to each other so that the surface chains intercalate (fig. 2.6). In contrast, the repulsive effect is negligible if there is no contact between

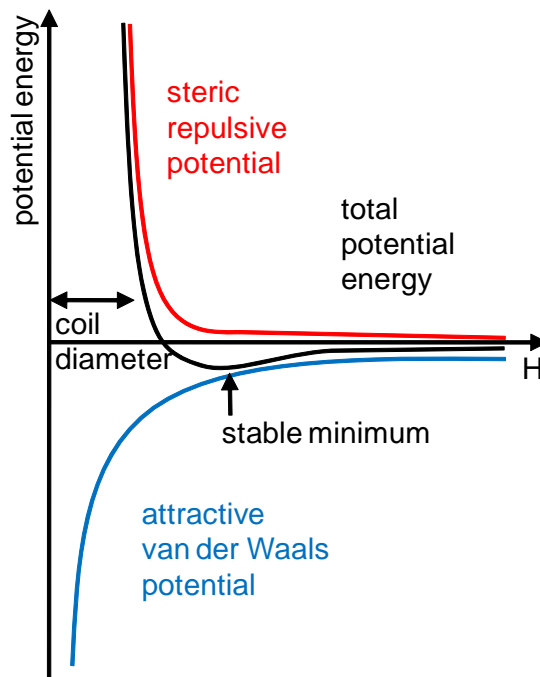


**Figure 2.6: Interplay between steric repulsion and van der Waals attraction.** The potentials are shown as a function of the surface distance  $H$ . The steric repulsion potential increases very steeply when the surface distance reaches the random coil diameter of the particle with its surface chains overcompensating the van der Waals attraction. The primary minimum no longer exists.

the chains. This behavior can almost be described by a hard sphere potential which acts at an approach distance equal to the core diameter of the particle plus its

surface moieties. This steep increase overcompensates the power dependency of the van der Waals attraction. If the surface groups are properly chosen, a primary energy minimum no longer exists. There is only one minimum at a distance  $H$  slightly larger than the dimension of the nanoparticle. Aggregation of the dispersion will therefore not take place.

## 2.1.4 Experimental protocol

$Y_{0.6}Eu_{0.4}VO_4$ ,  $GdVO_4$  and  $Gd_{0.6}Eu_{0.4}VO_4$  nanoparticles were synthesized according to the protocol given by Huignard *et al.* (2000) and discussed in section 1.1.2. We note that in contrast to the synthesis of the bulk material, the addition rate of the reactants is of crucial importance for the formation of nanoparticles of the intended size. We additionally synthesized  $Y_{0.6}Eu_{0.4}VO_4/GdVO_4$  core-shell nanoparticles which should combine the advantages of a  $Y_{0.6}Eu_{0.4}VO_4$  phase concerning the luminescence and of an outer  $GdVO_4$  phase concerning the proton relaxation enhancement.

### 2.1.4.1 Reactant preparation

Sodium orthovanadate  $Na_3VO_4$  (purity 99.9%,  $M_W = 183.91$  g/mol, Alfa Aesar) is dissolved in ultrapure water with a specific resistance of at least  $18.2 M\Omega \cdot cm$  to a final concentration of 0.1 M. The pH of the solution is verified using a pH meter and is adjusted if necessary to the range 12.5–13.0 by adding 1 M sodium hydroxide (Merck). The solution is then filtered through a  $0.22 \mu m$  vacuum filter system (Corning) to remove nonsoluble impurities. The filtered solution can be stocked for several weeks at ambient temperature without alteration of its properties.

Rare earth nitrates are dissolved in ultrapure water to a final concentration of 0.1 M. Solutions were prepared from  $Y(NO_3)_3 \cdot 6H_2O$  (purity 99.8%,  $M_W = 383.01$  g/mol, Sigma Aldrich),  $Gd(NO_3)_3 \cdot 6H_2O$  (purity 99.9%,  $M_W = 451.36$  g/mol, Alfa Aesar) and  $Eu(NO_3)_3 \cdot 6H_2O$  (purity 99.9%,  $M_W = 446.06$  g/mol, Alfa Aesar) and were used as prepared. These solutions can be stocked without alteration for several months provided that they were not contaminated with microorganisms during preparation. We note that rare earth chlorides can equally be employed under otherwise unchanged conditions. If Eu doped nanoparticles were synthesized, rare earth nitrate solutions were mixed by volume to the intended Eu concentration yielding a solution at a total rare earth concentration of 0.1 M.

Sodium citrate dihydrate  $C_6H_5O_7Na_3 \cdot 2H_2O$  (purity > 99%,  $M_W = 294.1$  g/mol, Sigma Aldrich) is dissolved in ultrapure water to a concentration of 0.1 M and used as prepared. If long term storage is intended, the solution must be sterile filtered and solution withdrawal has to be done under sterile conditions to avoid growth of microorganisms.

### 2.1.4.2 Synthesis by normal route

The synthesis is performed according to the protocol given by Huignard (2001). In summary, a volume of 0.1 M sodium vanadate solution at pH 12.5 is placed in a

recipient and stirred vigorously at ambient temperature. The same volume of 0.1 M rare earth nitrate solution is added with a peristaltic pump at a flow rate of about 1 mL/min. Depending on the intended composition of the material, the lanthanide solution was a mixture of either 60 volume %  $\text{Y}(\text{NO}_3)_3$  or  $\text{Gd}(\text{NO}_3)_3$  solution with 40 volume %  $\text{Eu}(\text{NO}_3)_3$  solution or a pure  $\text{Gd}(\text{NO}_3)_3$  solution. We note that it is important that the droplets of the rare earth nitrate solution fall directly in the sodium vanadate solution and do not touch the walls of the recipient as in the latter case the reduced mixing results in the formation of rare earth vanadate aggregates on the walls which act as nucleation germs and impede nanoparticle formation. Proper reaction conditions can readily be monitored by eye as nanoparticles in the intended size region yield a homogeneous white precipitate without any observable aggregates. During the addition, the pH is verified in regular intervals and 1 M NaOH solution is added if the pH approaches 9.5 and until it reaches 10.5. After completion of the addition, the stirring is maintained for further 30 min and the dispersion is then subjected to the purification procedure as described in section 2.1.4.5. The present protocol can be employed under the same conditions for syntheses from 10 mL to 21 final volume.

#### 2.1.4.3 Citrate synthesis route

1 volume equivalent of 0.1 M lanthanide nitrate solution is placed in an Erlenmeyer flask and stirred vigorously at 60 °C. Depending on the intended composition of the material, the lanthanide solution was a mixture of 60 volume %  $\text{Gd}(\text{NO}_3)_3$  solution and 40 volume %  $\text{Eu}(\text{NO}_3)_3$  solution or a pure  $\text{Gd}(\text{NO}_3)_3$  solution. 0.75 volume equivalents of 0.1 M sodium citrate solution are poured slowly into the flask. For lanthanide solution volumes larger than 50 mL, it is preferable to add the citrate solution drop by drop using a peristaltic pump at a flow rate of several mL per minute. This procedure is necessary to maintain the temperature change from the set point small. Addition of citrate to the lanthanide solution results in the formation of a clearly visible slightly yellow precipitate. After reequilibration of the temperature at 60 °C, 0.75 equivalents of 0.1 M sodium vanadate solution at pH 12.5 are added either by hand or using the peristaltic pump depending on the volume as described above. After addition of about 2/3 of the sodium vanadate solution, the precipitate is completely dissolved and a limpid dispersion is obtained. The reaction medium is stirred for another 30 min at 60 °C and then allowed to cool down. The purification procedure is performed by dialysis as described in section 2.1.4.5. We note that purification by centrifugation is very time consuming in this case as the small particle size necessitates long spin times. Yields are also generally lower because of the difficulty to observe by eye the end point of centrifugation as the dispersion is already limpid before spinning.

#### 2.1.4.4 Synthesis of core-shell nanoparticles

We have synthesized core-shell nanoparticles containing an  $\text{Y}_{0.6}\text{Eu}_{0.4}\text{VO}_4$  core and a  $\text{GdVO}_4$  shell. The protocol presented below is a modified version of the normal synthesis route. Using the latter, one obtains generally nanoparticles with a diameter

of about 40 nm. Based on this knowledge, we first calculated the volume ratio between the core volume  $V_c$  and shell volume  $V_s$  using a value of 5 nm for the desired shell thickness. The shell volume is given by  $V_s = V_{NP} - V_c = \frac{4}{3}\pi(r_{NP}^3 - r_c^3)$  where  $V_{NP}$  is the volume of the nanoparticle,  $r_{NP} = 20$  nm the nanoparticle radius and  $r_c = 15$  nm its core radius. In this case, we obtain

$$\frac{V_s}{V_c} = \frac{r_{NP}^3 - r_c^3}{r_c^3} = \left(\frac{r_{NP}}{r_c}\right)^3 - 1 = \left(\frac{20}{15}\right)^3 - 1 = 1.37. \quad (2.4)$$

In a typical assay with a total volume of 75 mL of 0.1 M lanthanide solution, this corresponds to 31.5 mL lanthanide solution for the core and 43.5 mL for the shell. According to the stoichiometry of the material, the lanthanide solution for the core is itself a mixture of 60 volume %  $\text{Y}(\text{NO}_3)_3$  solution and 40 volume %  $\text{Eu}(\text{NO}_3)_3$  solution. For the shell, we use a pure  $\text{Gd}(\text{NO}_3)_3$  solution.

75 mL of 0.1 M sodium vanadate solution at pH 12.5 are placed in a 250 mL Erlenmeyer flask and stirred vigorously at ambient temperature. The mixture containing yttrium and europium nitrate is added at a flow rate of 1 mL/min using a peristaltic pump. After completion of the addition of the core forming solution, the shell forming gadolinium nitrate solution was added immediately at the same flow rate. After completion of all additions, the dispersion is stirred for another 30 min and then subjected to the purification procedure as described in section 2.1.4.5. We note that it is important that the two additions succeed one another directly and without interruption. Trials with a time laps between the additions of 15 min, during which the dispersion was only stirred, have shown that the controlled particle growth was perturbed and that only large aggregates with sizes  $> 1 \mu\text{m}$  were obtained.

#### 2.1.4.5 Purification

The obtained raw nanoparticle dispersion is purified by either dialysis or centrifugation in order to eliminate the counter ions in solution. Dialysis is generally employed for citrate route syntheses and for small synthesis volumes up to about 100 mL. The nanoparticle dispersion was poured into Spectra Por regenerated cellulose dialysis membranes (MWCO 12–14 kDa, Spectrum Labs) and dialyzed against 2 to 5 l of ultrapure water for several days while changing the water repeatedly. Dialysis was stopped after reaching a conductivity of the nanoparticle dispersion below  $100 \mu\text{S}/\text{cm}$ . A volume increase generally takes place during dialysis due to the osmotic pressure across the membrane. If more concentrated dispersions are required, the purified particles can be reconcentrated either by partial water evaporation at  $40^\circ\text{C}$  under reduced pressure or by precipitation and redispersion in a smaller water volume under sonication. In the latter case, centrifugation is typically carried out at 26,323 g for 20 min for particles prepared by the normal route or 2 h for those made by the citrate route, respectively. The precipitate is redispersed in a small quantity of water under sonication at 50 to 100 W output power for several minutes (Branson S-450A sonifier). Concentration by precipitation and redispersion is generally preferable compared to evaporation as excessive heat treatment and water removal during evaporation may induce irreversible aggregation of the particles.

For large volumes obtained using normal routes and core-shell syntheses, purification by centrifugation is performed. The dispersion is spun at 26,323 g for 20 min. The supernatant is then discarded and the precipitate recovered in a glass Erlenmeyer flask. The combined precipitates, if several centrifugation cycles are necessary, are redispersed in about 80 mL Millipore water under stirring for several hours. Plastic recipients should not be used as prolonged stirring may contaminate the nanoparticle dispersion with plastic particles difficult to remove. The initial suspension after synthesis can be concentrated in this step by a factor of 10 to 20 facilitating and speeding up all further purification steps. The centrifugation-redispersion steps are repeated 3 to 5 times depending on the concentration factor and until a conductivity of the redispersed nanoparticles below 100  $\mu\text{S}/\text{cm}$  is reached. In all cases, the nanoparticle dispersion after purification is storable for at least several months without significant alteration.

#### 2.1.4.6 Size selection

Size selection is performed to withdraw large particles and aggregates from the dispersion. For nanoparticles produced by the normal synthesis route, it is generally carried out by two centrifugation steps. The dispersion is placed in a 50 mL plastic conical tube and spun at 500 g for 2 min in a swing bucket rotor. Generally only a small volume of precipitate is found. The supernatant is removed using a pipette and poured in a new conical tube. This tube is spun at 1,000 g for 2 min. The supernatant contains a nanoparticle dispersion with a good compromise between a small size distribution and a high yield. If higher monodispersity is required, the process can be continued by increasing the spinning speed and/or the time for each successive step. A filtration procedure may follow after centrifugation. The nanoparticle dispersion is filtered through syringe filters of decreasing pore size starting with a 0.8  $\mu\text{m}$  Millex hydrophile mixed cellulose ester membrane filter (Millipore) followed by a 0.45  $\mu\text{m}$  Minisart cellulose acetate membrane filter (Sartorius Stedim Biotech) and finally a 0.22  $\mu\text{m}$  filter of the same type. Filtration has additionally the advantage to remove non precipitable dust which interferes with light scattering measurements.

Size selection for nanoparticles produced by the citrate route involves usually the three steps filtration procedure described above. If nanoparticles with smaller polydispersity are required, an additional ultracentrifugation can be carried out. Ultracentrifugation devices state the molecular weight cut off (MWCO) usually as a protein mass  $M_W$  in kDa. This value can be converted approximately to a pore diameter  $p$  using the average protein density 1.22  $\text{g}/\text{cm}^3$  for a globular protein (Andersson and Hovmöller, 1998) by the formula

$$p = \left( \frac{6}{\pi} \frac{M_W[\text{Da}]}{6.022 \cdot 10^{23} \frac{\text{Da}}{\text{g}} \cdot 1.22 \frac{\text{g}}{\text{cm}^3}} \right)^{\frac{1}{3}}. \quad (2.5)$$

Up to 20 mL of the nanoparticle dispersion are placed in a Vivaspin 20 ultracentrifugation device with a polyethersulfone membrane (Satorius Stedim Biotech) with a MWCO of 1,000 kDa corresponding to  $p = 14$  nm. The tube is spun for about 30 min at 3,000 g in a swing bucket rotor centrifuge. The filtrate contains the nanoparticles.

In the case that higher nanoparticle concentrations are required, the filtrate can be poured into an ultracentrifugation tube of the same type and with a MWCO of 300 kDa ( $p = 9$  nm) and spun under the same conditions. The concentrated nanoparticle dispersion remains in the filter and can be redispersed by sonication. In all cases, monitoring of the particle size distribution by DLS is necessary after each step in order to avoid unnecessary loss of nanoparticles.

Results of the characterization of the synthesized nanoparticles will be presented and discussed in the corresponding sections later in this work. Chemical and structural properties will be covered in this chapter, while luminescence properties will be treated in section 3.1 and an application of the magnetic properties will be introduced in chapter 4.

## 2.2 Surface modification of nanoparticles

One crucial point when using nanoparticles for analytic applications, imaging or therapeutics is the targeting of the particle in a living organism. Targeting can be accomplished by special signaling entities linked to the particles. If this signal entity is well chosen, the organism will transport the particle to the region of interest. The prerequisite for such an application is that the signal entity which may be an organic molecule, an inorganic compound, a peptide or a nucleotide sequence can be attached to the nanoparticle by a physical interaction or chemical bond. Giaume *et al.* (2008) have developed a two step method for the functionalization of  $Y_{0.6}Eu_{0.4}VO_4$  nanoparticles. The first step consists in the adsorption of a silica layer to the surface of the particle which serves as a base for the further functionalization. In the second step, a bifunctional molecule is added. One of its functionalities allows for binding to the silica layer whereas the second functionality is an active group. One finally ends up with a nanoparticle covered with a silicate layer exposing an anchor to which the signal entity can be bound. The modification process may also be stopped after the deposition of the first silica layer if one wants to benefit only from its property of dispersion stabilization in water.

### 2.2.1 Silica coating

Giaume (2006) has shown that the first silica layer can be prepared from the condensation of a tetraalkoxysilane  $Si(OR)_4$  precursor. Mialon (2009) has further developed this procedure because it was not directly applicable to monocrystalline nanoparticles obtained from a high temperature annealing reaction (Mialon *et al.*, 2008). However, the latter procedure can also be used in the case of nanoparticles obtained from coprecipitation without thermal treatment. We have chosen the second protocol as it is easier because a step involving solvent exchange can be avoided. This reaction uses sodium metasilicate as the silica source. Performing the silica coating reaction in water under alkaline conditions, the Si–O–Si bonds of the precursor are hydrolyzed to hydroxyl groups which can recondensate to form Si–O–Si bonds (fig. 2.7). The challenge of this reaction resides in the control of the sites where recondensation takes place. In principal, recondensation can occur



**Figure 2.7: Hydrolysis and condensation of sodium metasilicate.** Aqueous solutions of sodium metasilicate contain chains of linked silicate units. The dotted bonds indicate the rest of this chain.

on the surface of the nanoparticles and hence forms the desired silica layer or in solution forming parasitic pure silica nanoparticles.

The mechanism of the recondensation reaction can be explained using the nucleation-growth model from LaMer already discussed in section 2.1.1. We consider a concentration of reactive hydrolyzed silicate molecules higher than the saturation concentration (dotted line in fig. 2.1). Two cases are possible:

- The reactive species are consumed by the condensation reaction on the surface of the rare earth vanadate nanoparticles more rapidly than new hydrolyzed molecules are produced. In this case, the concentration of reactive species does not reach the critical concentration range for nucleation (grey zone in fig. 2.1) and therefore no new particles can be formed. We are in the conditions of growth onto preformed particles.
- Reactive species are produced by hydrolysis faster than they are consumed by condensation. The concentration of reactive species increases during the reaction and can reach the critical value of nucleation. New particles composed of pure silica are formed which contaminate the dispersion of rare earth vanadate nanoparticles.

Surface silica coating instead of formation of new particles can be favored by carefully choosing the reaction conditions. The main parameters which can be adjusted are the concentration of the silica source, the pH of the solution and the reaction temperature.

Another important point besides the condensation of the silica layer itself is how the first silicate molecules interact with the surface of the rare earth vanadate nanoparticles. If there is a strong interaction, hydrolyzed silicate molecules will preferentially interact with the preformed nanoparticles and do not form new particles. The preferential adsorption onto the nanoparticle surface may be explained by the negative charge of the silicate molecules and their interaction with positively charged rare earth ions in the nanoparticle. This interaction should be favored compared to a stabilization by the sodium counter ions as  $\text{Na}^+$  carries only a single positive charge whereas  $\text{RE}^{3+}$  ions carry three resulting in a strong interaction that holds in place the first layer of silicates. Fig. 2.8 shows the formation steps of the silica layer.

### 2.2.2 Functionalization

The silica coated particles can be functionalized in a second step. The works of Giaume (2006) and Mialon (2009) have shown that the best compromise between

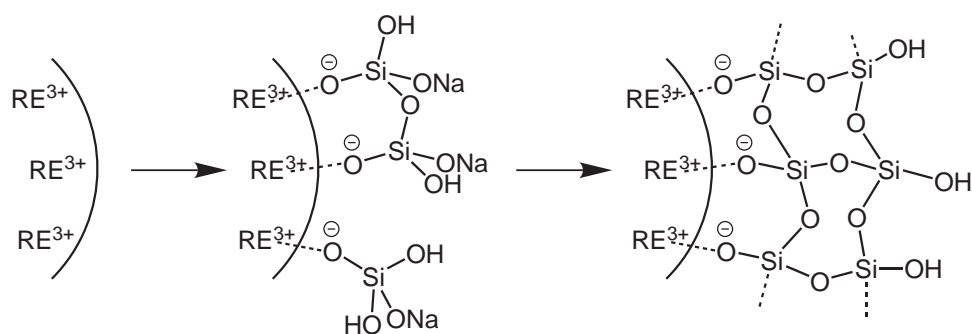


**Figure 2.8: Silication of rare earth vanadate nanoparticles.** Rare earth (RE) vanadate nanoparticles contain  $\text{RE}^{3+}$  ions on the surface (left structure). Hydrolyzed species from sodium metasilicate can adsorb to the surface by interaction between the negatively charged oxygen and the  $\text{RE}^{3+}$  ions (middle structure). The adsorbed silicates act as a basis for the condensation of further units forming a silica shell (right structure). The dotted bonds indicate the rest of this chain.

surface reactivity and stability is obtained when using an amino group as active binding site. As the nanoparticle exhibits already silicate groups on its surface, the molecule forming the active layer should also contain functionalities which can react with silicates. The authors concluded that (3-aminopropyl)triethoxysilane (APTES, fig. 2.9) as precursor in a alkaline water/alcohol reaction medium meets these conditions.

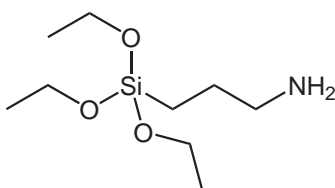


**Figure 2.9: Structure formula of the APTES molecule.**

This choice was motivated by several findings:

- Adsorption and condensation of pure silicates on the surface is achieved without covalent bonds. If the silica coated particles are used in an environment with extreme conditions for *e. g.* pH, hydrolysis and desorption of the silica layer may occur. It is therefore necessary to add a more stable surface modification layer. This can be achieved by using trialkoxysilanes instead of silicates.
- Alkoxysilanes are soluble in alcohol and water/alcohol mixtures. As the nanoparticles cannot be dispersed in alcohol, the use of a water/alcohol mixture is required.
- Hydrolysis of alkoxysilanes can be performed in basic or acidic medium but only a basic medium favors the formation of nanoparticles whereas an acidic medium yields a sol. The reaction conditions of the present functionalization

reaction correspond therefore to the classical silica nanoparticle synthesis from tetraalkoxysilanes first described by Stöber *et al.* (1968).

- In contrast to a synthesis using tetraalkoxysilanes, the reactivity of the precursor is lowered when employing trialkoxysilanes. However, the reactivity can be increased by using alkoxygroups with short alkyl chains which have a small positive inductive effect, resulting in a strong polarization of the Si–O bond and a facile hydrolysis.
- Using a water/alcohol mixture implies a high water concentration and concomitantly a high hydrolysis rate which in turn increases the reactivity.

We note that increasing the hydrolysis vulnerability of the layer forming compound increases also the risk of formation of particles from alcoxysilanes as the critical concentration for nucleation may be exceeded. It is therefore crucial that condensation of the hydrolyzed product is fast. The rapid onward reaction of the hydroxy compound is guaranteed by bringing it into contact with silica coated particles which are an optimum substrate for the condensation reaction. This is the reason why the functionalization reaction is not performed directly with the pure rare earth vanadate nanoparticles but involves the preliminary step of silica coating. The principle of functionalization is summarized in fig. 2.10.

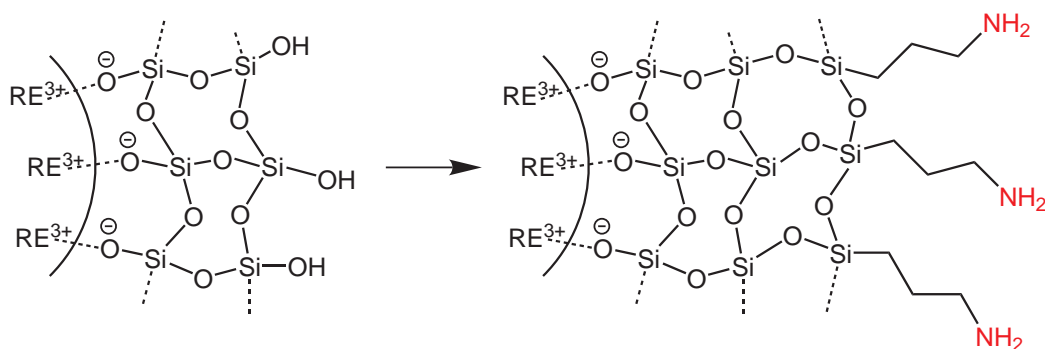


**Figure 2.10: Functionalization of silica coated rare earth vanadate nanoparticles.** APTES is hydrolyzed and its hydroxyl groups condensate with the hydroxyl functions of the silicate layer. An amino functionality (shown in red) is hence added to the nanoparticles.

## 2.2.3 Experimental protocol

### 2.2.3.1 Silica coating of the nanoparticles

Size selected nanoparticles prepared through the normal or the citrate synthesis routes are diluted in ultrapure water to a vanadate concentration in the range of 20 to 50 mM. The solution is placed in a beaker and sonicated at 50 to 100 W output power for several minutes using a Branson S-450A sonifier. The nanoparticle dispersion is then vigorously stirred and the same volume of a 3 mass % sodium silicate solution is immediately added. This reactant is obtained from a commercial sodium silicate

solution ( $\text{Na}_2\text{SiO}_3$ , Riedel-de Haën) containing 27 mass %  $\text{SiO}_2$  and 11 mass %  $\text{Na}_2\text{O}$  by diluting 1 volume part in 8 volume parts ultrapure water. The mixture is stirred overnight at ambient temperature and then dialyzed in Spectra Por regenerated cellulose dialysis membranes (MWCO 12–14kDa) against 2 to 5 l ultrapure water for several days while changing the water repeatedly. Dialysis is necessary in order to eliminate excess silicate not bound to the nanoparticles and is stopped after reaching a conductivity of the nanoparticle dispersion below  $100 \mu\text{S}/\text{cm}$ . Care was taken that the conductivity does not fall below  $50 \mu\text{S}/\text{cm}$  in order to avoid desorption and hydrolysis of the adsorbed silica layer (Mialon, 2009). Note that we have also performed successful silica coating using sodium silicate solutions containing 1 mass % or 10 mass % sodium silicate, respectively. Silicated nanoparticles are size selected by centrifugation and filtration (for nanoparticles obtained by the normal route synthesis) or by filtration and if necessary ultrafiltration (for nanoparticles obtained by the citrate route) as described in section 2.1.4.6.

### 2.2.3.2 Functionalization

Silicated nanoparticles are diluted in ultrapure water to a final vanadate concentration of 3 mM and the pH is adjusted to 9 by adding KOH. 225 mL of absolute ethanol (Carlo Erba) are placed in a 500 mL three-neck round-bottom flask and heated under stirring and reflux to  $90^\circ\text{C}$ . 1.125 mmol APTES ( $M_W = 221.37 \text{ g/mol}$ , Sigma Aldrich) that is 249 mg or 263  $\mu\text{l}$  ( $\rho = 0.946 \text{ g/mL}$ ) are added. This quantity corresponds to 5 times the vanadate quantity that will be subsequently added. 75 mL of the diluted nanoparticle dispersion are added using a peristaltic pump at a flow rate of about 1 mL/min to the boiling ethanolic APTES solution. After completion of the addition, stirring is maintained at  $90^\circ\text{C}$  for 24 h. The next day, about half of the solvent is evaporated under reduced pressure at  $50^\circ\text{C}$  and the remaining dispersion is subjected to purification by centrifugation, conducting three precipitation-redispersion cycles as described in section 2.1.4.5. Redispersion is performed in each cycle in a mixture of water and ethanol in the volume ratio 1:3.

### 2.2.3.3 Analysis of the surface modifications

The silica coating as well as the APTES functionalization were validated by IR spectroscopy and by determination of the isoelectric point. For IR spectroscopy, a drop of the nanoparticle dispersion is placed on a piece of a n-doped silicon wafer and dried in an oven at  $100^\circ\text{C}$ . Spectra are recorded for this sample as well as for a piece of the same n-doped silicon wafer but without nanoparticles as reference on a Bruker Equinox 55 IR spectrometer (Bruker Optik) in a nitrogen atmosphere and in the wavelength range from  $500 \text{ cm}^{-1}$  to  $4000 \text{ cm}^{-1}$ . Transmission data for the sample is divided by the reference transmission.

The isoelectric point was determined from measurements of the  $\zeta$ -potential as a function of pH using a Zetasizer Nano ZS apparatus (Malvern) and the corresponding implemented routine. 200  $\mu\text{l}$  nanoparticle dispersion are mixed with 7 mL of 0.1 M potassium chloride (KCl, Sigma Aldrich) and sonicated for 20 s. The pH is then brought to 12 by adding 1 M KOH solution. The  $\zeta$ -potential is determined on an

aliquot of 700  $\mu\text{l}$  in a clear disposable capillary cell (DTS1061, Malvern). The pH of the remaining dispersion is then lowered by one unit by adding HCl and the  $\zeta$ -potential is remeasured. This cycle is repeated until a final pH of 2 is obtained. The isoelectric point corresponds to the point of vanishing  $\zeta$ -potential and can be determined from a plot of the measured data.

Particle sizes were determined by dynamic light scattering after purification for each step of the modification reaction. Measurements were done as described in section 2.5.1.

## 2.2.4 Results and discussion

Nanoparticle silica coating and functionalization by APTES were characterized by infrared spectroscopy. A comparison of the spectra after the different synthesis steps is shown in fig. 2.11. Three characteristic bands allow to monitor the evolution of the

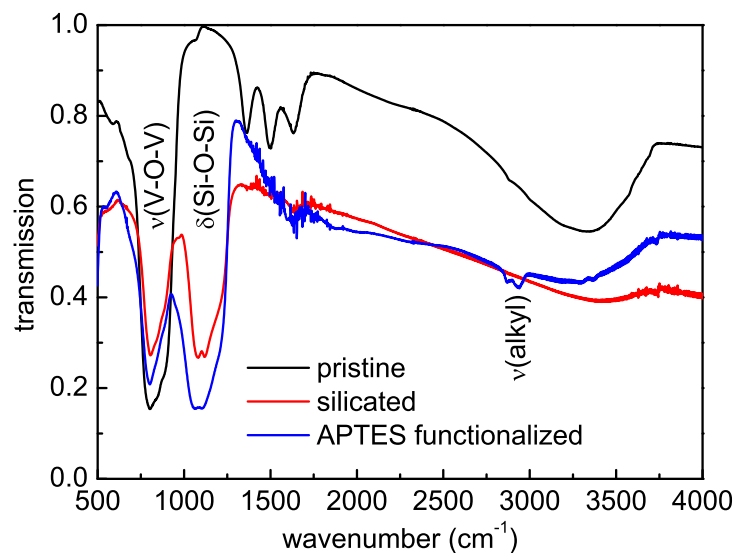


**Figure 2.11: Infrared spectra of pristine, silica coated and APTES functionalized  $\text{Y}_{0.6}\text{Eu}_{0.4}\text{VO}_4$  nanoparticles.**

surface. For pristine nanoparticles obtained by coprecipitation and without further modifications, we find a broad and intense peak at  $802\text{ cm}^{-1}$  which can be attributed to the asymmetric valence vibration of V–O–V (Touboul and Popot, 1985; Yu *et al.*, 2005). The very broad peak around  $3300\text{ cm}^{-1}$  is due to water molecules adsorbed to the surface (Giaume, 2006). Upon silica coating of the surface, a new broad and intense peak appears at  $1100\text{ cm}^{-1}$  arising from the asymmetric vibration of the Si–O–Si bond in silica (Lien-Vien *et al.*, 1991; Alonso and Sanchez, 2000). As the peak of the vanadate vibration is also visible, the modification reaction has not damaged the initial nanoparticles. Differences in the overall transmission are due to changing nanoparticle layer thicknesses on the Si wafer from one sample to another. After the functionalization step with APTES, the peaks due to vanadate and silicate remain as expected and two weak and sharp peaks at  $2870\text{ cm}^{-1}$  and  $2939\text{ cm}^{-1}$  appear. These

new peaks are due to the vibrations of the methylene groups of the alkyl chain in the aminopropyl group (Yim *et al.*, 2005). Furthermore, the broad peak originating from adsorbed water has strongly decreased. The addition of another surface layer is also indicated by the change in the relative intensity between the vanadate and silicate peaks. While the transmission for these two peaks is approximately equal after silica coating, functionalization with APTES changes the intensities in favor of the silicate band. This result is immediately clear as APTES is a functionalized alcoxysilane and its condensation on top of the silicate layer increases the thickness of the latter.

The surface  $\zeta$ -potential is another indicator for the nature of the modification layer and the isoelectric point (IEP) can be determined from its measurement (fig. 2.12). As data points are not very dense due to the time consuming measurement process,

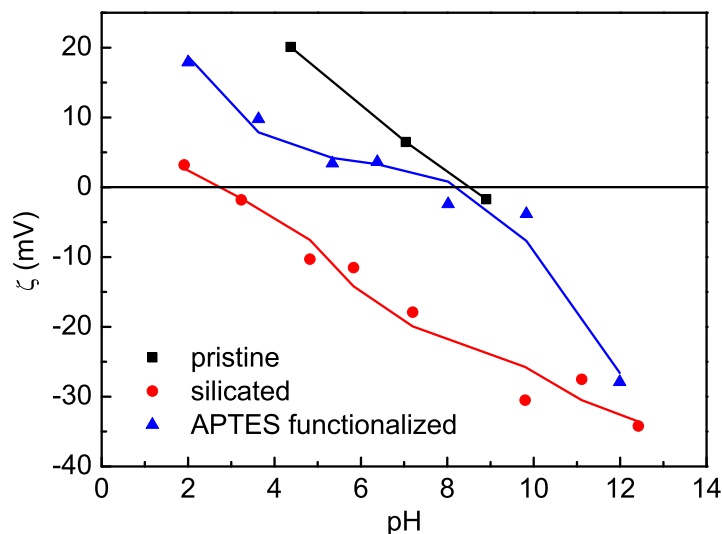


**Figure 2.12: Zeta potential of pristine, silica coated and APTES functionalized  $Y_{0.6}Eu_{0.4}VO_4$  nanoparticles.** Smoothed lines are a guide to the eye.

accuracy of the IEP is moderate. Nevertheless, the result shows that the IEP changes with the different steps of surface modification. Pristine nanoparticles have an IEP of about 8.5. Upon silica coating the IEP decreases to 3 and functionalization with APTES reincreases it to 8. Giaume *et al.* (2008) have observed values of 7, 4 and 9 for pristine, silica coated and APTES functionalized nanoparticles, respectively. Although these values are slightly different from ours, we find the same evolution.

The hydrodynamic diameter of the nanoparticles was measured by dynamic light scattering. The measurement procedure will be explained in section 2.5.1 and we will here only discuss the size evolution upon surface modification. The number average size distributions are depicted in fig. 2.13. It is clearly visible that the average size increases upon silica coating and further upon functionalization with APTES. In all cases, we find only one single peak. This finding shows that the silica layer was grown on the surface of the existing rare earth vanadate particles and that no new pure silica particles were formed.

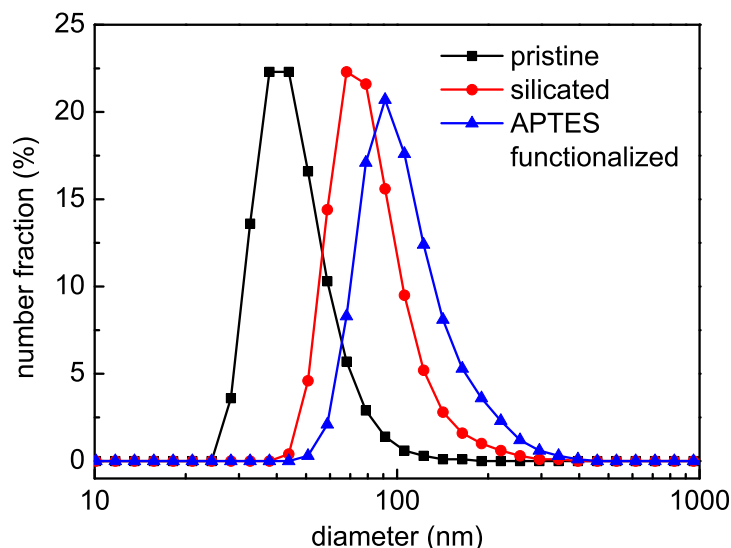


**Figure 2.13: Number average size distribution of pristine, silica coated and APTES functionalized  $Y_{0.6}Eu_{0.4}VO_4$  nanoparticles.**

Combination of IR spectroscopy, measurement of the surface  $\zeta$ -potential and size determination allows us to prove unambiguously that all modification reactions took place on the surface of the initial rare earth vanadate nanoparticles.

## 2.3 Vanadate concentration

It is of crucial importance to possess an accurate measure of the rare earth vanadate quantity in a dispersion as for the intended application as contrast agent, one needs to know which signal enhancement can be obtained for which quantity of contrast agent. However, the concentration of nanoparticles is difficult to assess and is dependent on the size and on the size distribution. A better measurement is the determination of the concentration of one of the components of the nanoparticles. The concentration of the other component is then immediately obtained from the simple total lanthanide to vanadate 1:1 stoichiometry. In principal, one could determine the concentration of either lanthanides or vanadates. Furthermore, measurements are possible in either nanoparticle dispersions or in a solution of dissolved nanoparticles. At last, the protocol should be simple and use only commonly accessible laboratory equipment. Concerning lanthanides, one might think of the fluorescence of europium as indicator but this protocol would not be applicable in the case of  $GdVO_4$  nanoparticles. Another possibility is the complexometric determination of lanthanides from dissolved particles but these reactions require usually a stabilized and not too acidic pH which is not compatible with the use of strong acidic conditions in order to dissolve the nanoparticles (Mialon, 2009). We have therefore focused on concentration measurements based on a quantification of the vanadate ions in either nanoparticles or in free form after dissolution of the nanoparticles.

### 2.3.1 Quantification by UV absorption

Mialon (2009) has shown that the concentration of vanadate in a solid rare earth vanadate structure can be determined from UV absorption measurements at 280 nm. The corresponding absorption band disappears when the vanadate ions are liberated from the crystal structure into solution. However, when measuring the intensity decrease of a UV beam at 280 nm, one has not only to account for intensity loss by absorption but also by scattering as we are dealing with objects with a size being on the same order of magnitude as the wavelength of the incident radiation. In order to correct for the scattering contribution, we use a Matlab<sup>®</sup>. Absorption has to be measured in the range 200 – 800 nm. Intensity  $I_{sc}$  measured by the detector due to scattering is approximated by fitting the region 400 – 800 nm where no absorption peak is present with the function

$$I_{sc} = a_1 + \frac{a_2}{\lambda} + \frac{a_3}{\lambda^4}. \quad (2.6)$$

Herein,  $a_1$ ,  $a_2$  and  $a_3$  are constants and  $\lambda$  is the wavelength. The modeled scattering contribution is then subtracted from the recorded spectrum in the whole range 200 – 800 nm in order to obtain the pure absorption from vanadate without scattering (fig. 2.14) The vanadate concentration can then be evaluated employing

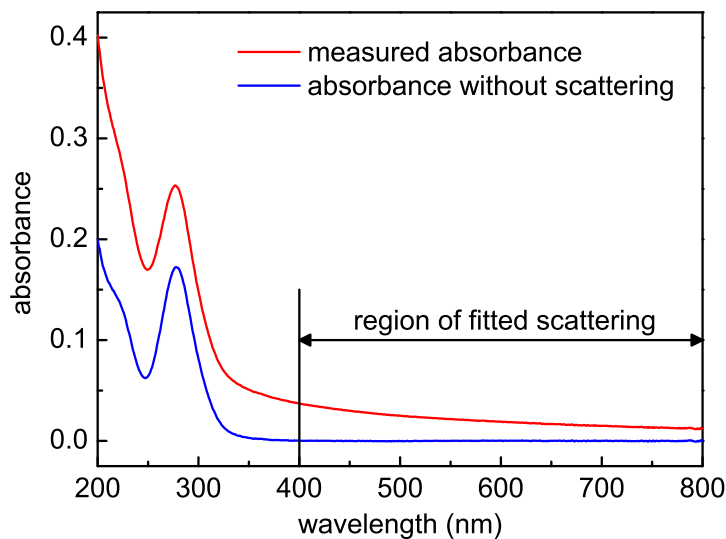


**Figure 2.14: UV-VIS spectrum of silica coated  $Y_{0.6}Eu_{0.4}VO_4$  nanoparticles.** The measured data was fitted with eq. 2.6 in the range 400 – 800 nm and the scattering contribution obtained from these parameters was subtracted from the whole spectrum.

the absorption coefficient and the thickness of the used cuvette. Although this measurement procedure is fast and simple and is well suited to follow the relative evolution of the vanadate concentration during a reaction, it cannot provide reliable absolute concentrations. Our trials with nanoparticle dispersions of known vanadate concentrations have shown that the measured concentration depends strongly on the concentration, size and size distribution. This finding can be explained by

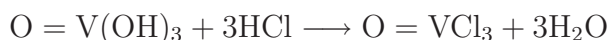
a change in the optical pathway due to scattering. While in diluted dispersions of small particles most of the radiation travels straight through the cuvette, big particles in high concentrations cause multiple scattering of the incident radiation resulting in a prolonged pathway in the cuvette. In the latter case, the measured intensity is no longer the sum of absorption and scattering. The described method has therefore been found not to be applicable in the case where precise concentration measurements are needed, for example for the calculation of the relaxivity of a contrast agent (section 4.2.2.1).

### 2.3.2 Colorimetric quantification

Accurate measurements of the vanadate concentration can be performed using a colorimetric detection method (Charlot, 1966; Wright and Mellon, 1937) based on the reaction initially described by Barreswil (1847). Under strongly acidic conditions (Greenwood and Earnshaw, 1986), the orthovanadate crystal structure is dissolved by forming orthovanadic acid



which in turn is transformed to the chloride form by dehydration by the action of hydrochloric acid:



The present hydrogen peroxide transforms the vanadium(V) oxychloride in an orange-brown trichloromonoperoxovanadium(V) complex:



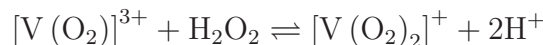
The former steps can be combined to the sum equation



We note that no change in the oxidation state of the vanadium ion takes place. The oxidation number is +5 for orthovanadate as well as in the trichloromonoperoxovanadium(V) complex.

The  $[\text{V}(\text{O}_2)\text{Cl}_3]$  complex is only stable in low pH and structural characterization is therefore difficult. Rumpf (1937) described this complex as pentacoordinated with an  $\eta^2 - \text{O}_2^{2-}$  ligand and three chloride ions occupying the remaining coordination sites. The actual geometry was not determined to our knowledge but the abundant data on  $[\text{VO}(\text{O}_2)]^+$  oxoperoxocomplexes (Bagno *et al.*, 1997; Tatiarsky *et al.*, 2009) suggests that the  $[\text{V}(\text{O}_2)\text{Cl}_3]$  complex has a trigonal-bipyramidal structure (fig. 2.15). The trichloromonoperoxovanadium(V) complex can be quantified by its absorption at 460 nm.

Hydrogen peroxide in excess attenuates the coloration of the solution which may show a pure yellow color at high hydrogen peroxide concentrations. Hartkamp (1959) explained this finding by the equilibrium between the monoperoxo- and the diperoxovanadium complexes:



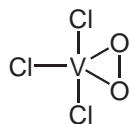


**Figure 2.15: Hypothetical trigonal-bipyramidal structure of the monoperoxovanadium(V) complex.** The peroxide ion is in a  $\eta^2$  side-on configuration. The other coordination sites are occupied by chloride ions.

We note that the author did not report about the occupation of the remaining coordination sites. The equilibrium of this reaction may be shifted to the left by increasing the acid concentration, but a better option is to operate at the isosbestic point of the two peroxo complexes at 405 nm where the measured absorption is independent of the acid and hydrogen peroxide concentration in a wide range. This method has however the disadvantage of an approximately 25 % reduced sensitivity due to the lower extinction coefficient.

According to the protocole given in Charlot (1966), the quantification reaction can be performed with 1 – 5 mg vanadium in 100 mL. This corresponds to a molar concentration of orthovanadate between roughly 0.2 mM and 1 mM. The reaction is therefore of relatively low sensitivity compared to other colorimetric procedures. Wright and Mellon (1937) state that some other ions perturb the detection because they form also colored complexes with hydrogen peroxide but the influence of lanthanide ions was not studied. Peroxolanthanide(III) complexes with various ligands are reported in the literature (Djordjevic and Vuletic, 1980). Their formation captures hydrogen peroxide which is no longer available for the reaction with vanadate and may also form colored species. In order to correct for this effect, we have added rare earth ions in the same concentration as orthovanadate to the samples for the calibration measurement.

### 2.3.3 Experimental protocol

We have discussed in the previous section 2.3.2 that a too high hydrogen peroxide concentration perturbs the reaction. Charlot (1966) recommends the use of 0.6 – 3 mL  $\text{H}_2\text{O}_2$  at a concentration of 3 % (w/w) per 100 mL reaction volume. We have therefore used 1.5 mL per 100 mL of the specified hydrogen peroxide solution for all further experiments.

#### 2.3.3.1 Reactant preparation

For the calibration samples, solutions are prepared from rare earth chlorides. We note that nitrates must not be used as the nitrate ion has a strong UV absorption at 302 nm (measured from sodium nitrate, data not shown) which interferes with the precise extraction of the absorptions at 405 nm and 460 nm.  $\text{YCl}_3$  (purity 99.99 %,  $M_W = 195.26$  g/mol, Sigma Aldrich) and  $\text{EuCl}_3$  (purity 99.99 %,  $M_W = 366.41$  g/mol, Sigma Aldrich) were dissolved in Millipore water to a final concentration of 20 mM whereas  $\text{GdCl}_3$  (pure,  $M_W = 263.61$  g/mol, Prolabo) was

dissolved to 15 mM. These solutions were used as prepared. Mixtures to a total rare earth concentration of 20 mM were made using 60 volume % of the  $Y^{3+}$  solution and 40 volume % of the  $Eu^{3+}$  solution. Sodium orthovanadate  $Na_3VO_4$  (purity 99.9%,  $M_W = 183.91$  g/mol, Alfa Aesar) was dried in an oven at 100 °C for several hours prior to weighing to eliminate concentration errors due to humidity. The powder was dissolved in ultrapure water to a final concentration of 20 mM and 15 mM, respectively. In contrast to the solution preparation for the nanoparticle synthesis, no sodium hydroxide was added.

### 2.3.3.2 Calibration graph

Calibration samples are prepared as follows. For the first sample, 450  $\mu$ l of rare earth solution are placed in the recipient and 450  $\mu$ l of sodium vanadate solution of the same concentration (15 mM or 20 mM) are added. The next sample contains 50  $\mu$ l less of rare earth and vanadate ions as the preceding one and the total volume is filled up to 900  $\mu$ l with ultrapure water. This procedure is repeated until only 50  $\mu$ l of each solution are employed. The necessary acidity is ensured by 100  $\mu$ l of 37 mass % hydrochloric acid (Prolabo). The mixture is vortexed and 6 mL of 1.15 M hydrochloric acid are added. After vortexing again, the colored complex is formed by addition of 105  $\mu$ l of 3 mass % hydrogen peroxide. The mixture is vortexed a last time. 3 mL of each sample are transferred in a 10 mm QS 100 quartz cuvette (Helma) and the absorption is measured between 200 nm and 800 nm using a Carry 50 UV-VIS spectrophotometer (Agilent Technologies). 1.15 M HCl is used as reference. Two series of samples were prepared. The first series contained only gadolinium ions in a concentration of 20 mM whereas the mixture of yttrium and europium ions at a concentration of 15 mM was used in the second series.

### 2.3.3.3 Sample quantification

To determine the concentration of the nanoparticle dispersions, the sample is first diluted by a factor  $d_p$  to about 5 mM vanadate concentration in 1 mL volume. The factor  $d_p$  for any freshly synthesized sample can be estimated based on the used sodium orthovanadate quantity and the final volume. 900  $\mu$ l of this dilution are placed in a 10 mL glass vial and 100  $\mu$ l of 37 mass % HCl are added. Pristine nanoparticles are readily dissolved by vortexing while silica coated ones need an additional heating step of about 1 min at 100 °C for complete dissolution. The vial is tightly closed during the thermal treatment to avoid water evaporation and an error in the concentration determination. The mixture is then diluted with 6 mL of 1.15 M HCl and vortexed. The red-brown color is formed upon addition of 105  $\mu$ l of 3 mass % hydrogen peroxide and a final vortexing. Absorption measurements were carried out as described for the calibration samples. If the relative absorption at 460 nm is outside the limits 0.03 and 0.3, the dilution has to be adjusted accordingly and the procedure has to be repeated. Based on the ratio of the total volume in the vial to the volume of the rare earth solution, one has to account for a dilution factor of  $d_1 = 7.89$  additional to the predilution factor  $d_p$ .

### 2.3.3.4 Synthesis yield determination

Reaction yields for nanoparticle syntheses according to the normal or citrate route were calculated based on the initially used quantity of orthovanadate in the sodium orthovanadate solution and the quantity of orthovanadate in the nanoparticle dispersion recovered after all purification and size selection steps. The latter was calculated from a concentration determination of the nanoparticle dispersion as described in section 2.3.3.3 and the recovered total volume. Yields for the silica coating step were calculated based on the known quantity of the non-modified nanoparticle dispersion and that calculated from the concentration measurement of the silica coated sample and the recovered volume after all purification and size selection steps. The yield for the silica coating reaction concerns therefore only this step and does not include the yield of the preparation of the pristine rare earth vanadate nanoparticles.

## 2.3.4 Results and discussion

### 2.3.4.1 Molar extinction coefficient

We have recorded the UV-VIS spectra for the colorimetric determination of orthovanadate for the calibration samples containing either  $\text{Gd}^{3+}$  ions or a mixture of  $\text{Y}^{3+}$  and  $\text{Eu}^{3+}$  ions. The result for the first case is depicted in fig. 2.16. The

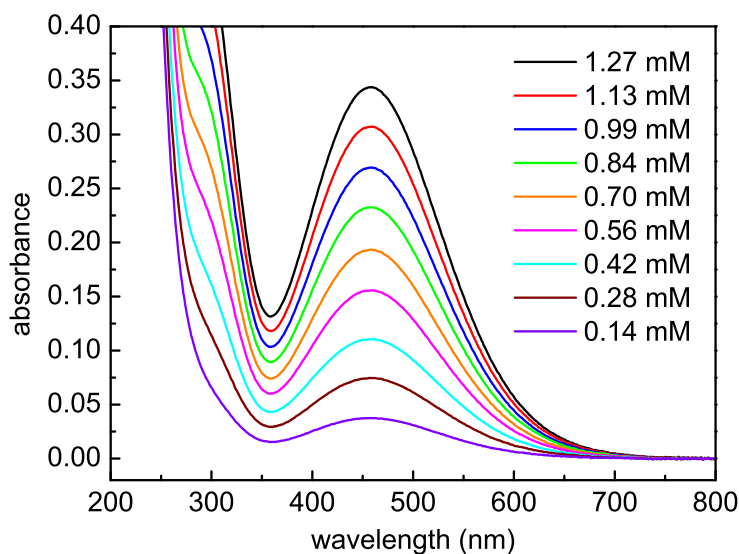


**Figure 2.16: Absorbance of calibration samples for the colorimetric determination of orthovanadate.** The indicated concentration is the final orthovanadate concentration in the cuvette. In order to obtain the orthovanadate concentration of the used rare earth solution, the value has to be multiplied by  $d_1$ . The measurements were performed in the presence of a stoichiometric amount of  $\text{Gd}^{3+}$ .

absorption was read off at the peak maximum situated at 460 nm as well as at the isosbestic point at 405 nm were the mono- and diperoxovanadium complexes have

the same molar extinction coefficient  $\epsilon$ . The graph representing  $\epsilon$  as a function of the orthovanadate concentration (fig. 2.17) shows a very good linearity in the studied concentration range and confirms that the vanadium concentration can be measured by the colorimetric method in a range between 0.1 mM and 1.2 mM which is slightly extended compared to the range initially given by Charlot (1966). An equally good

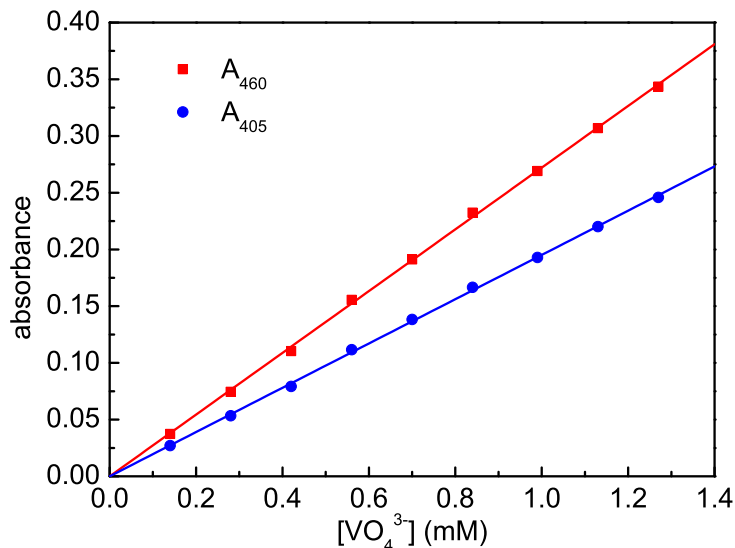


**Figure 2.17: Calibration curve for the colorimetric determination of orthovanadate.** The points correspond to the absorbance at 460 nm and 405 nm, respectively, taken from the spectra in fig. 2.16. Data was fitted with the equation  $A = \epsilon_{\lambda}lc$  using a path length of 1 cm.

linearity was obtained for the second measurement series using a mixture of yttrium and europium ions instead of gadolinium (graph not shown). The calculated molar extinction coefficients together with their errors are listed in table 2.1.

**Table 2.1: Molar extinction coefficients for aqueous solutions of trichloromonoperoxovanadium(V) in the presence of rare earth ions.**

rare earth	$\epsilon_{460}$ (mM <sup>-1</sup> cm <sup>-1</sup> )	$\epsilon_{405}$ (mM <sup>-1</sup> cm <sup>-1</sup> )
Gd	$0.272 \pm 0.001$	$0.195 \pm 0.001$
60 mol % Y + 40 mol % Eu	$0.275 \pm 0.002$	$0.199 \pm 0.002$

#### 2.3.4.2 Error in vanadate quantification

The error bar of the slope of the linear fit to the data in fig. 2.17 gives us a first indication about the error encountered when titrating vanadate concentrations. The values listed in tab. 2.1 show that this error is on the order of 1%. This quantity includes all errors resulting in a deviation of the measurement points from a linear

behavior. Contributions to this error come from inaccuracies in pipetting while preparing the individual samples, from the absorption measurement itself and from the determination of the absorption values at 460 nm and 405 nm. However, this value does not include the concentration error from the preparation of the initial orthovanadate solution as such an error would generate a linear relationship but with another slope. This independent error is due to inaccuracies from weighing the powder and measuring the solvent quantity. Care was taken in order to maintain these errors small as solutions were always prepared from orthovanadate quantities in the several hundred milligram range with a corresponding pipetted water quantity in the several tens of milliliter range. Pipetting errors must be smaller than 1 % otherwise a standard deviation of 1 % or less would not be possible for the fit. Weighing is exact to 0.1 mg resulting in a relative error of the order of 0.1 % when using masses in the hundreds of milligram range. Remaining humidity in the sodium orthovanadate powder is difficult to quantify but an estimate of less than 1 % seems reasonable as the powder is not described as hygroscopic. We may therefore estimate the relative error in the concentration of the sodium orthovanadate solution to a maximum of 1 %. As the preparations of this solution and of the standard samples of different dilutions are independent, we have to add the relative errors and finally get a total error of the vanadate concentration determination of less than 2 %.

#### 2.3.4.3 Influence of the rare earth

An important finding concerns the influence of the type of lanthanide ion present in the solution. Assuming a total quantification error on the order of 2 % as previously explained, the molar extinction coefficients for the samples containing only  $\text{Gd}^{3+}$  ions or a mixture of  $\text{Y}^{3+}$  and  $\text{Eu}^{3+}$  ions agree within these error limits. This means that the actual type of the rare earth contained in the nanoparticle to quantify is not important and that the obtained values of  $\epsilon$  may also be used for other particle compositions. Nevertheless, we will use the values obtained from measurements with gadolinium for all Gd-containing nanoparticles and that from the mixture of yttrium and europium for all those containing Y. We note that this finding does not imply that there is no influence on the colorimetric reaction from the rare earths at all. Charlot (1966) report values of  $\epsilon_{460} = 0.275 \text{ mM}^{-1} \text{ cm}^{-1}$  and  $\epsilon_{405} = 0.207 \text{ mM}^{-1} \text{ cm}^{-1}$  for the reaction without rare earth ions but the exact protocol is not given. It seems that rare earths do not influence the absorption at 460 nm but the difference at 405 nm is at the limit of the measurement error.

#### 2.3.4.4 Synthesis yield

Once we have determined the concentration of the final colloidal dispersion of known volume, it is simple to calculate the synthesis yield. The different syntheses carried out in the course of this work are listed together with their respective yields in tab. 2.2. For easier discussion, we have divided the syntheses in three classes according to the chemical reaction which was carried out. At a first glance, we notice that the reaction yields are very different for a same reaction type. This finding may be explained by the fact that all values have been determined after purification and size

**Table 2.2: Yield of nanoparticle syntheses by the normal and citrate route.** Samples from the citrate route are designated by the superscript cit. Modification layers on a core compound are indicated by a slash. Silicated samples present generally the same sample number as their non silica coated precursor material followed by the designation Si except samples MS18 where the non-modified form is not listed and MS19 which is the silica coated form of MS6R.

reaction type	composition	sample	yield (%)
normal route synthesis	$Y_{0.6}Eu_{0.4}VO_4$	MS1	83
	$Y_{0.6}Eu_{0.4}VO_4$	E110316	71
	$GdVO_4$	MS2	85
	$GdVO_4$	MS4	54
	$GdVO_4$	MS6R	72
	$Y_{0.6}Eu_{0.4}VO_4/GdVO_4$	MS26	55
citrate route synthesis	$GdVO_4^{cit}$	MS3	31
	$GdVO_4^{cit}$	MS23	20
	$Gd_{0.6}Eu_{0.4}VO_4^{cit}$	MS24	12
silica coating	$Y_{0.6}Eu_{0.4}VO_4/SiO_2$	MS1Si	91
	$Y_{0.6}Eu_{0.4}VO_4/SiO_2$	E110316Si	74
	$Y_{0.6}Eu_{0.4}VO_4/SiO_2$	MS18	18
	$Y_{0.8}Eu_{0.2}VO_4/SiO_2$	GM080215Si	47
	$GdVO_4/SiO_2$	MS2Si	18
	$GdVO_4/SiO_2$	MS19	21

selection. The latter always includes centrifugation steps. Depending on whether purification was carried out by dialysis or centrifugation, additional centrifugation steps may be added. As small differences in the particle size and size distribution affect the sedimentation properties, multiple centrifugation and redispersion steps can strongly influence the quantity of recovered nanoparticles. The number of necessary centrifugation steps increases generally with the concentration of the nanoparticle dispersion. Therefore higher loss is possible for highly concentrated dispersions. Nevertheless, some general tendencies can be deduced from the data. Normal route syntheses can produce nanoparticle dispersions with yields on the order of 70 %. The yields of nanoparticles synthesized using the citrate route are, with about 20 %, lower. This difference in the yields between the two reactions can however be explained easily. First, the citrate molecules are used to complex the rare earth ions during synthesis and to reduce the growth of the nanoparticles. But also after completion of the precipitation reaction, a certain amount of rare earth ions remain in solution as citrate complexes and cannot participate in the formation of rare earth vanadate. These complexes are eliminated during dialysis or centrifugation. Second, due to the small size of these nanoparticles, precipitation during centrifugation is even for long centrifugation times incomplete and some nanoparticles are eliminated with the supernatant. Differences in the yield are still larger for the silica coating reaction. This behavior is possibly linked to the formation

of aggregates in the non-modified nanoparticle dispersion. The dispersions have been sonicated prior to silica coating in order to disassemble the aggregates but depending on the degree of disassembling, it is possible that some aggregates were stabilized by coating them with a silicate layer. As these aggregates were subsequently removed during the size selection procedure, a lower yield can result.

## 2.4 Stability

A central aspect in diagnostic and therapeutic applications of nanoparticles is their biological tolerance in the body. The biological effect of the nanoobject is obviously determined by the circulation time and clearance rate but also by its stability. While a nanoparticulate probe is designed to provide a maximum intended effect and minimize the side effects when in its administered form, reaction or decomposition products may have very different behavior. In this section, we will discuss the biological effects of rare earth and orthovanadate ions, the two possible decomposition products of our nanoparticles. To evaluate the effect of the decomposition products, one needs to know their concentration. As the stoichiometry of the compound  $GdVO_4$  is known, it is sufficient to quantify either Gd or vanadate ions. Due to the required high sensitivity, quantification was performed by dosing free rare earth ions instead of vanadate.

### 2.4.1 Toxicology of nanoparticle decomposition products

#### 2.4.1.1 Rare earth ions

Rare earth metals have no physiological role in the body and show a certain toxicity (Thunus and Lejeune, 1999). The median lethal dose,  $LD_{50}$ , that is the dose required to kill half of the members of a tested population, has been determined for  $EuCl_3$  administered by intraperitoneal injection in mice to 550 mg/kg body weight (Haley *et al.*, 1965). Gadolinium shows a higher toxicity in its free form reflected in a  $LD_{50}$  in the range of 100-200 mg/kg body weight for  $GdCl_3$  in mice (Caille *et al.*, 1983). Rare earths are generally soluble in their nitrate, chloride, and sulfate form. In the body, they are rapidly transformed to insoluble carbonates, phosphates and hydroxides (Hirano and Suzuki, 1996). Retention and tissue distribution of intravenously injected rare earths depend therefore mainly on their stability in the blood (Hirano and Suzuki, 1996). The insoluble colloids are taken up by the reticuloendothelial system and deposited in the liver, spleen and bones (Oksendal and Hals, 1993; Hirano and Suzuki, 1996; Penfield and Reilly, 2007). Clearance from these accumulation sites is slow at a rate less than 1 % per day (Tweedle, 1992).

Gadolinium in its free form is toxic already at low concentrations in the micro- and nanomolar range as a result of its action as inorganic blocker of different types of voltage-gated calcium channels (Bellin and van der Molen, 2008). It inhibits physiological processes depending on  $Ca^{2+}$  influx as well as the activity of some metabolic enzymes. Rare earths can bind to  $Ca^{2+}$  or  $Mg^{2+}$  binding sites of Calmodulin or ATPases (Hirano and Suzuki, 1996). Another problem

is nephrogenic systemic fibrosis (NSF) caused by free gadolinium in patients with decreased renal function (Penfield and Reilly, 2007). NSF is a severe, potentially fatal, adverse reaction caused by a rare idiopathic skin condition which is accompanied by pain and loss of mobility and involves systemically also other organs (Hasebroock and Serkova, 2009).

However, acute and long term toxicity of rare earth ions can be significantly reduced by their incorporation in a structure from which release is hindered for example by complexation (Thunus and Lejeune, 1999). Although complexation is the best studied way to achieve this goal, other strong binding systems like nanoparticles have the same effect. Tolerance of rare earth ions by organisms is increased by a factor of more than 100 if the rare earth ion is presented in a bound form like a metal complex (Thunus and Lejeune, 1999). A Gd-containing formulation must be sufficiently stable in order to avoid transmetallation between  $\text{Gd}^{3+}$  and other metal ions present in the body such as  $\text{Zn}^{2+}$ ,  $\text{Cu}^{2+}$  and  $\text{Ca}^{2+}$  as this reaction leads to accumulation of free  $\text{Gd}^{3+}$  in bones and skin (Hermann *et al.*, 2008). Transmetallation is favored if the compound stays in the body for a long time as a consequence of decreased renal excretion (Hasebroock and Serkova, 2009).

#### 2.4.1.2 Vanadate

Although neither the physiological role of vanadium is clear nor if vanadium is an essential element (Domingo, 1996), studies have shown that the human body contains about 100  $\mu\text{g}$  vanadium (Sigel and Sigel, 1995). 90% of the vanadium in the blood circulation is in a form bound to proteins and less than 10% is in free form (Nechay, 1984). The portion of intracellular vanadium which is unbound is still lower and reaches only values of 1% (Chasteen *et al.*, 1986). On the one hand, it was reported that vanadates can mimic most of the actions of insulin and lower the blood glucose level (Domingo, 1996, 2002; Pepato *et al.*, 2008). On the other hand, high concentrations of vanadium are toxic but this toxicity is much more difficult to evaluate than that of gadolinium as the biological effect depends on many factors (Domingo, 2002):

- Oxidation state. The toxicity of vanadium compounds increases with increasing oxidation number of the vanadium ion (Llobet and Domingo, 1984).
- Chemical form. The effect of orthovanadate is different from that of metavanadate although the oxidation number is the same.
- Mode of administration. The toxicity depends on whether the subject is exposed to vanadium orally or parenterally.
- Time of exposure. The effect differs during pregnancy where maternal and fetal toxicity are distinct.

Many studies have addressed specific questions of the toxicity of vanadates. Cortizo *et al.* (1997) reported that highly concentrated vanadium is cytotoxic and mitogenic. Ciranni *et al.* (1995) showed that intragastrically administered sodium orthovanadate has genotoxic effects in mice and causes chromosome aberrations.

Sanchez *et al.* (1991) demonstrated the toxicity of sodium orthovanadate administered by gavage in mice at doses above  $15 \text{ mg kg}^{-1} \text{ d}^{-1}$ . A significant number of deaths at doses higher than  $30 \text{ mg kg}^{-1} \text{ d}^{-1}$  was found. Fetal development toxicity was also observed at doses above  $30 \text{ mg kg}^{-1} \text{ d}^{-1}$ . The cellular toxicity was tested on a bovine kidney cell culture. Bracken and Sharma (1985) observed 15 % cytotoxicity after incubation of the cells with  $20 \mu\text{M}$  sodium orthovanadate. The cytotoxicity increased to 60 % for  $500 \mu\text{M}$  sodium orthovanadate. It reached even values of 75 % after 24 h for doses of  $1000 \mu\text{M}$  (Bracken *et al.*, 1985). Cortizo *et al.* (2000) reported that cell survival decreased to 80 % when incubating murine osteoblast-like cells with 0.1 – 10 mM sodium orthovanadate during 4 h. Vanadium compounds can cause cell toxicity by oxidative stress through the formation of reactive oxygen species (Stohs and Bagchi, 1995). An about four-fold higher ROS production in osteoblast-like cells after incubation with 2.5 mM orthovanadate for 4 h was observed by Cortizo *et al.* (2000). From the aforementioned data and using a worst-case assumption of intracellularly released orthovanadate, we may define a limit of about  $20 \mu\text{M}$  free orthovanadate that should not be exceeded.

One of the rare cases where the toxicity of orthovanadate is well understood on the molecular level is the inhibition of ATPases. Cantley *et al.* (1977) reported for the (Na, K)ATPase in the presence of  $28 \text{ mM MgCl}_2$  an inhibition constant of  $K_i = 50 \text{ nM}$ , that is the quantity of orthovanadate necessary for a decrease of the ATPase activity to 50 %, and a total inhibition at concentrations in the millimolar range. The  $K_i$  value increases to  $100 \text{ nM}$  in the presence of physiological  $\text{Mg}^{2+}$  concentrations (Cantley *et al.*, 1978). The molecular mechanism of action was revealed by X-ray structure analysis of the myosin ATPase domain (fig. 2.18) by Smith and Rayment (1996). The orthovanadate–ADP complex mimics the trigonal-

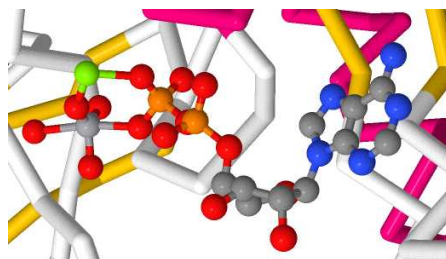


**Figure 2.18: X-ray structure of the  $\text{Mg}^{2+}$ –ADP–orthovanadate complex in the myosin ATPase domain.** The myosin motor domain was isolated from *Dictyostelium discoideum*. The structure is refined to  $1.9 \text{ \AA}$  resolution (Smith and Rayment, 1996) and is drawn according to the entry number 1VOM from the Research Collaboratory for Structural Bioinformatics protein data bank (data freely available online at <http://www.rcsb.org/pdb>). Atom color code: carbon (dark grey), nitrogen (blue), oxygen (red), phosphorus (orange), vanadium (light grey) and magnesium (green).

bipyramidal transition state during ATP hydrolysis (fig. 2.19). In contrast to the hydrolysis of ATP, the  $\text{VO}_4^{3-}$ –ADP complex is not hydrolyzable and inhibits therefore the ATPase activity.

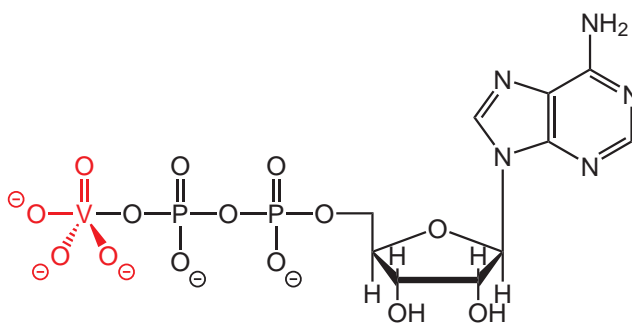


**Figure 2.19: Structure formula of the ADP–orthovanadate complex.** The ADP part is drawn in black and the orthovanadate ion in red. The trigonal-bipyramidal configuration of the oxide ions around the vanadium ion mimics the ATP hydrolysis transition state.

### 2.4.2 Colorimetric rare earth quantification

Considering the negative effects of both free gadolinium and vanadate ions, we have to quantify the leaching rate of these ions from the nanoparticles. For convenience reasons, is it better to measure the rare earth concentration than that of vanadate. The quantity of free rare earth ions can be assessed by a complexometric titration using an indicator which shows a different color depending on whether it is free or bound to the metal ions. The most commonly used indicator for trivalent rare earth ions is xylenol orange (Havel *et al.*, 1994). Its structure is shown in fig. 2.20. The color of an aqueous solution of xylenol orange depends on the

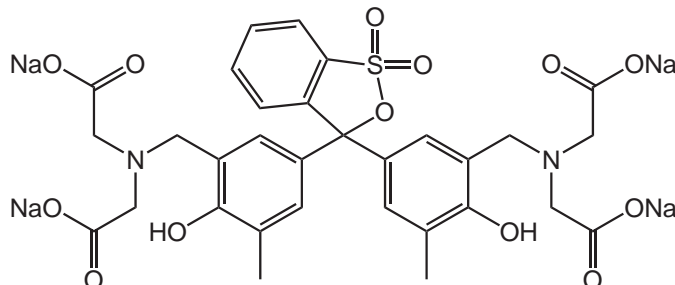


**Figure 2.20: Structure formula of the xylenol orange molecule.**

pH (Barge *et al.*, 2006). The solution is yellow in acidic and neutral conditions, whereas a change to violet is observed when the pH is becoming alkaline. This color change is due to the deprotonation of the phenolic hydroxyl group resulting in the formation of a semiquinone structure. In this configuration, the conjugation of the  $\pi$ -electrons is possible over the whole system of phenyl rings. The extended electronic delocalization shifts the absorption to higher wavelengths. Coordination of the metal ion is achieved by the N and O atoms of the iminodiacetate groups and a deprotonated phenolic oxygen atom. The binding of the metal ion has therefore the same effect on the  $\pi$ -system as an increasing pH: the color turns into violet. The pH has to be maintained accurately in a slightly acidic range during the

colorimetric detection otherwise the color change is not only a function of the metal ion concentration but results from a complex interplay with the protonation state.

The complex formation constant with respect to  $\text{Gd}^{3+}$  ions has a value of  $pK_{\text{GdL}} = 5.8$  (Yatsimirsky *et al.*, 1966) which is significantly lower than those of the commercial contrast agents based on gadolinium chelates (table 4.3). The compound does therefore not remove complexed gadolinium but binds only free Gd ions in solution. The same conditions should also apply in the case where the gadolinium ions are incorporated in a solid structure like our nanoparticles.

## 2.4.3 Experimental protocol

### 2.4.3.1 Preparation of xylenol orange solution

In a 500 mL bottle are placed 1.44 mL of glacial acetic acid (100 %, Merck) and about 400 mL ultrapure water are added. The pH is adjusted to 5.80 by adding 1 M sodium hydroxide solution (Merck) under stirring. The solution is transferred to a 500 mL flask and the volume is filled up to 500 mL with ultrapure water. The acetate buffer has a final concentration of 50 mM.

36 mg solid xylenol orange tetrasodium salt (3,3'-bis[*N,N*-bis(carboxymethyl)-aminomethyl]-*o*-cresolsulfonephthalein tetrasodium salt, Molekula) are placed in a 100 mL flask and dissolved in about 50 mL of the prepared acetate buffer. The volume is adjusted to 100 mL with acetate buffer. The obtained orange solution is aliquoted in 1 mL volumes in 1.5 mL Eppendorf™ tubes and immediately frozen at  $-20^\circ$ . The frozen xylenol orange solution can be stored for several months. Once thawed, the dye solution must be used within 45 min and must not be refrozen.

### 2.4.3.2 Preparation of rare earth solutions

902.7 mg  $\text{Gd}(\text{NO}_3)_3 \cdot 6\text{H}_2\text{O}$  (purity 99.9 % trace metal basis,  $M_W = 451.36$  g/mol, Acros Organics) are dissolved in 20 mL ultrapure water in order to obtain a 100 mM solution. This stock solution is diluted further with ultrapure water to prepare a solution at a concentration of 600  $\mu\text{M}$   $\text{Gd}^{3+}$ . The same protocol applies to europium, where 892.1 mg  $\text{Eu}(\text{NO}_3)_3 \cdot 6\text{H}_2\text{O}$  (purity 99.9 %,  $M_W = 446.06$  g/mol, Alfa Aesar) are dissolved in 20 mL ultrapure water yielding a 100 mM stock solution from which a 600  $\mu\text{M}$  solution is obtained. From the latter solutions, a mixture containing 60 volume %  $\text{Gd}^{3+}$  solution and 40 volume %  $\text{Eu}^{3+}$  solution is prepared.

### 2.4.3.3 Determination of the calibration equation

Calibration samples were prepared in 10 mL glass vials. For the first sample, 2.8 mL of acetate buffer (pH 5.80, 50 mM), 100  $\mu\text{L}$  of xylenol orange solution (36 mg/100 mL) and 100  $\mu\text{L}$  of ultrapure water are placed in the recipient and vortexed. The next sample contains the same quantities of acetate buffer and xylenol orange solution but 5  $\mu\text{L}$  less ultrapure water, which is replaced by 5  $\mu\text{L}$  of rare earth solution at 600  $\mu\text{M}$ . This procedure is repeated until 40  $\mu\text{L}$  ultrapure water and 60  $\mu\text{L}$  rare earth solution are employed. All samples contain finally xylenol orange in a concentration of 1.2 mg/100 mL and 48.3 mM acetate buffer. Two series of samples were prepared.

The first series contains only gadolinium ions in a concentration range of 1 – 13  $\mu\text{M}$  whereas a mixture of gadolinium and europium ions in the same concentration range is used in the second series.

The samples are completely transferred in a 10 mm QS 100 quartz cuvette and the absorption is measured between 200 nm and 800 nm. Acetate buffer at pH 5.80 and a concentration of 50 mM is used as reference.

Absorbances at 573 nm  $A_{573}$  and at 433 nm  $A_{433}$  are read off the spectra and the ratio  $A_{573}/A_{433}$  is plotted as a function of the final total rare earth concentration. Data is fitted linearly with a non-zero  $y$ -intercept as the  $A_{573}/A_{433}$  ratio is not zero for the pure xylenol orange dye.

#### 2.4.3.4 Quantification of free rare earths in nanoparticle dispersions

As discussed in section 2.3.1, diffuse scattering from nanoparticles is non-negligible and affects the measured absorbances. The protocol initially proposed for gadolinium chelates was therefore adapted in order to eliminate this contribution.

Several tubes containing 1 mL of colloidal dispersion from the normal synthesis route with the composition  $\text{Gd}_{0.6}\text{Eu}_{0.4}\text{VO}_4$  and at a vanadate concentration equal to a total rare earth concentration of 120 mM are spun in a centrifugation tube at 64,397 g for 10 min. We note that already 5 min spinning at the indicated speed are sufficient to obtain a clear supernatant and a clearly separated precipitate. The supernatant is discarded and the precipitate is redispersed in 1 mL ultrapure water by vortexing. The time of redispersion serves as point zero for the leaching kinetics. At the time  $t$ , an aliquot of 250  $\mu\text{l}$  is withdrawn and spun at 64,397 g for 5 min. The supernatant is removed and placed in a Millipore Ultrafree-4 centrifugal filter device containing a Biomax membrane with a MWCO of 30 kDa (Millipore). The filter device is spun at 5,525 g for 2 min. This step serves to remove traces of nanoparticles remaining in the supernatant after the first centrifugation. The colorimetric reaction is performed using 2.8 mL acetate buffer at pH 5.80 and a concentration of 50 mM, 100  $\mu\text{l}$  xylenol orange solution (36 mg/100 mL) and 100  $\mu\text{l}$  of the obtained filtrate. Absorption measurements are carried out as described for the calibration samples. Based on the ratio of the total volume in the vial to the volume of the filtrate, one has to account for a dilution factor of  $d_2 = 30$  when calculating the free gadolinium concentration in the tested sample.

## 2.4.4 Results and discussion

### 2.4.4.1 Calibration equation

The UV-VIS spectra of the calibration samples containing a mixture of  $\text{Gd}^{3+}$  and  $\text{Eu}^{3+}$  ions in the presence of the complexometric indicator xylenol orange are depicted in fig. 2.21. The change from the absorption maximum of the free xylenol orange at 433 nm to the absorption maximum of the metal bound form at 573 nm is clearly visible. The isosbestic point between the two forms of the indicator lays at about 470 nm. The largest absolute change in the absorbances at the two maxima is obtained in the concentration range between 0 and 5  $\mu\text{M}$

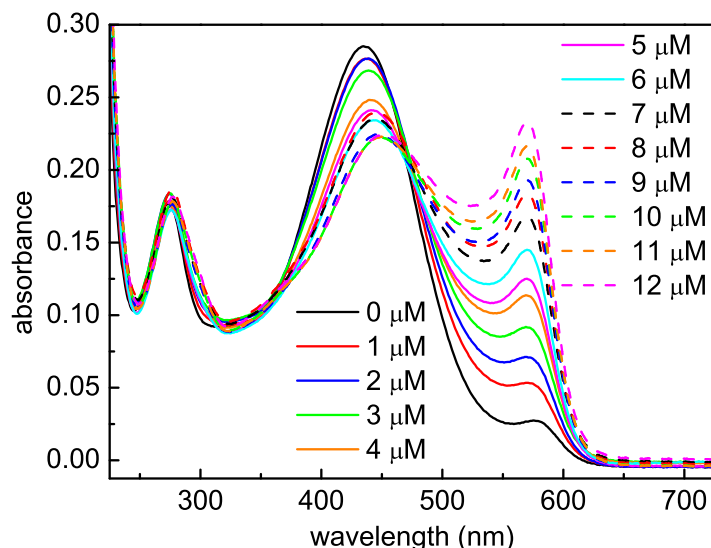


**Figure 2.21: Absorbance of the xylenol orange – rare earth complex.** The indicated concentration is the final total rare earth concentration in the cuvette and is obtained from a mixture of 60 mol %  $\text{Gd}^{3+}$  and 40 mol %  $\text{Eu}^{3+}$ .

for the rare earth. Quantification should therefore be the most accurate in this range. The calculated absorbance ratio  $A_{573}/A_{433}$  as a function of the total rare earth concentration is shown in fig. 2.22. We generally find a linear behavior over the whole studied concentration range. However, as the change in the spectrum is more pronounced below  $5 \mu\text{M}$ , quantifications should preferentially be conducted at low rare earth concentrations. This concentration range is consistent with the range proposed by Barge *et al.* (2006), where the authors found a linear behavior between 0 and  $4.5 \mu\text{M}$  final gadolinium concentration. Our result confirms further that xylenol orange can be used for the titration of gadolinium as well as europium. This result is in agreement with the literature where one can find numerous reports of the use of xylenol orange for the quantification of various metal ions including bismuth (Onishi and Ishiwatari, 1960), zirconium and hafnium (Cheng, 1963) as well as rare earths (Tonosaki and Otomo, 1962). Nevertheless, the affinity of the ligand to the different metal ions is not the same and a calibration curve must be recorded for each metal or mixture of metals. We have therefore repeated the same procedure in order to calculate the calibration curve for pure gadolinium solutions (graph not shown). A comparably good linearity with the same effect of higher deviations from the linear behavior for concentrations above about  $5 \mu\text{M}$  was found. In both cases, we have fitted linearly the  $A_{573}/A_{433}$  ratio as a function of the rare earth concentration  $c$  using the equation

$$A_{573}/A_{433} = ac + A_0 \quad (2.7)$$

where  $a$  is the proportionality constant and  $A_0$  the absorbance ratio for the free unchelated xylenol orange. The obtained values together with their errors are listed in table 2.3. The comparison confirms that the fitted parameters are significantly

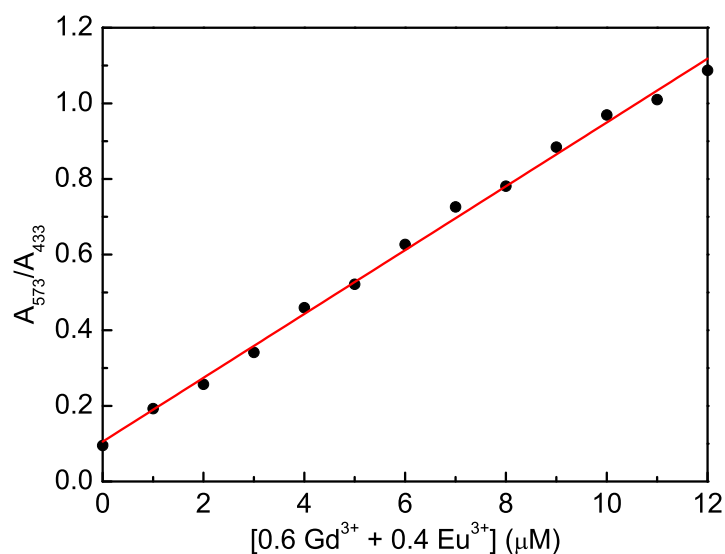


**Figure 2.22: Calibration curve for the colorimetric determination of free rare earths.** The points correspond to the absorbance ratio  $A_{573}/A_{433}$  taken from the spectra in fig. 2.21. Data were fitted to the equation  $A_{573}/A_{433} = ac + A_0$  where  $a$  is the proportionality constant and  $A_0$  the absorbance ratio for the free unchelated xylenol orange.

**Table 2.3: Fit parameters for the quantification of free rare earth ions.**

rare earth	$a$ ( $\mu\text{M}^{-1}$ )	$A_0$
Gd	$0.084 \pm 0.002$	$0.11 \pm 0.01$
60 % Gd + 40 % Eu	$0.090 \pm 0.002$	$0.07 \pm 0.01$

different, outside the error bars, for pure gadolinium and the gadolinium/europium mixture.

As we observe from tab. 2.3, the standard deviation of the slope of the fit is about 2% but it reaches values on the order of 10% for the  $y$ -intercept. The total error of the quantification can be estimated using the law of the propagation of uncertainties. With the values  $a$  and  $A_0$  from tab. 2.3, we obtain a concentration error on the order of  $0.2 \mu\text{M}$  maximum for a measured concentration in the range up to  $5 \mu\text{M}$ . In principle, we should add the error from the preparation of the standard solutions which was estimated to be about 1% in section 2.3.4.2. As the error resulting from the concentration measurement is much larger, we can estimate the total error of the rare earth concentration in the cuvette to  $0.2 \mu\text{M}$ . We remind that the dilution factor in the cuvette is 30, so that the error of the total rare earth concentration in the original sample is about  $6 \mu\text{M}$ .

#### 2.4.4.2 Rare earth leaching from nanoparticles

We measured the kinetics of rare earth leaching from a dispersion of  $\text{Gd}_{0.6}\text{Eu}_{0.4}\text{VO}_4$  (MS6R) nanoparticles. The recorded UV-VIS spectra are depicted in fig. 2.23 for different times after nanoparticle redispersion in water free of rare earth ions. A

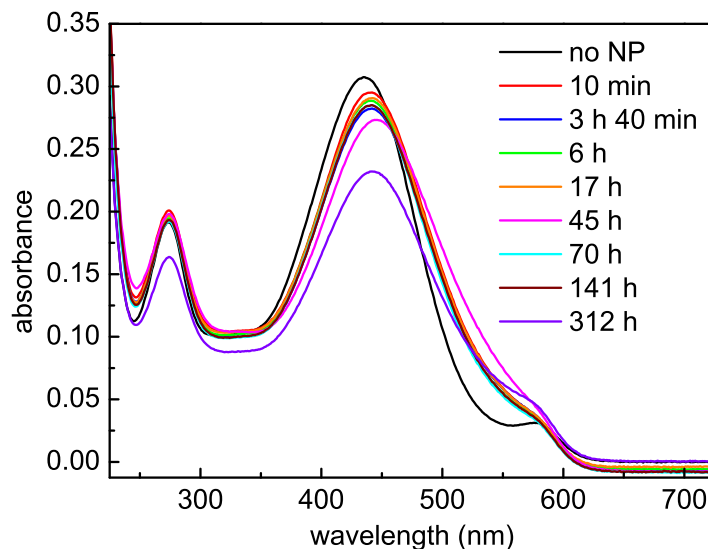


**Figure 2.23: Temporal evolution of the absorption spectrum of xylenol orange due to rare earth leaching.** "No NP" signifies the spectrum of pure xylenol orange without any rare earth ions.

qualitative comparison of the spectra acquired in the possible presence of leached rare earth ions with that of pure xylenol orange shows that the shape is in all cases the same. We find only the very pronounced maximum of the free form of xylenol orange at 433 nm. We can deduce that the rare earth concentration must be very low as most of the indicator remains in its unchelated form. We observe further that there is no clear temporal evolution of the measured free rare earth concentration over almost 2 weeks. This finding can be explained by either that the leached rare earth quantity remains almost constant over the whole timespan or that the total free rare earth quantity is below the detection limit of this method. The last measurement at 312 h has an overall lower absorbance as seen especially in the range below 350 nm. This behavior is probably due to some inaccuracies in the acquisition of the spectrum of a new reference sample.

We used the calibration equation (eq. 2.7) to calculate quantitatively the free rare earth concentration. The obtained values are shown in fig. 2.24 as a function of time. Concentrations were corrected for the dilution factor and represent the free rare earth concentration in the extract from the nanoparticle dispersion. Most values lie in the range between  $10\ \mu\text{M}$  and  $15\ \mu\text{M}$ . We note that these concentrations for the nanoparticle dispersion correspond to a rare earth concentration in the cuvette of about  $0.5\ \mu\text{M}$  that is between the first two points of the calibration graph (fig. 2.23) and that the measurement accuracy is therefore limited as the detection limit is approached. The high apparent concentration obtained from the measurement

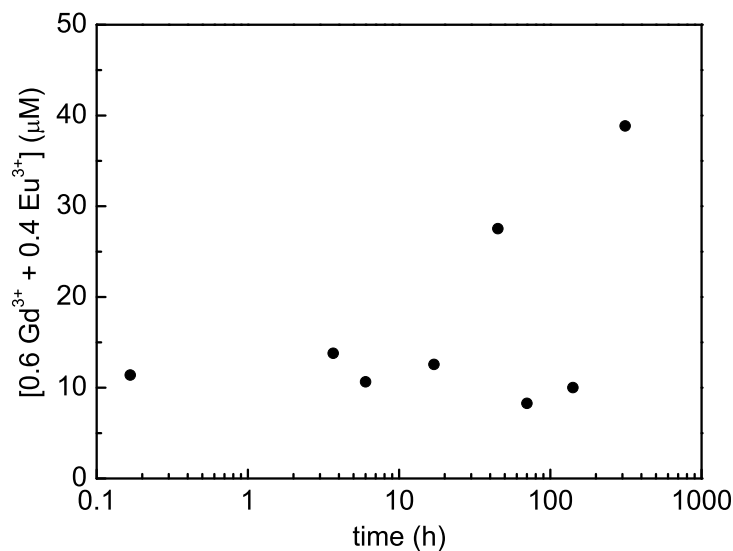


**Figure 2.24: Temporal evolution of the free rare earth concentration.** The concentration calculated with the calibration equation (eq. 2.7) was multiplied by the dilution factor  $d_2$ .

at 312 h may be explained by the incorrect spectrum of the reference. The value of 27  $\mu\text{M}$  at 45 h is compatible with the other concentrations if we assume a free rare earth concentration of 20  $\mu\text{M}$  and a standard deviation of 6  $\mu\text{M}$  as estimated in the previous section. As we have already seen from the qualitative analysis, the measured rare earth concentration does not seem to be time dependent. Additionally to the effects arising from a free rare earth concentration being in the order of magnitude of the detection limit, it is possible that the rare earth quantity caused by leaching is much lower than the measured concentration and that the latter is mainly generated by residual rare earth ions from the synthesis that were not removed during the precipitation and redispersion steps. The determined concentration of about 20  $\mu\text{M}$  free rare earth ions after almost two weeks has thus to be understood as an upper limit of the rare earth leaching.

Assuming that the temporally constant rare earth concentration indicates that a stable solubility equilibrium has been reached, we may compare our concentration to literature data. Hifumi *et al.* (2006) reported for dextran-coated  $\text{GdPO}_4$  nanoparticles with an initial concentration of 2.2 mM rare earths a leached concentration of 6.5  $\mu\text{M}$  after two weeks at 4 °C. Huang *et al.* (2008) found 33  $\mu\text{M}$  and 43  $\mu\text{M}$  of free gadolinium after 8 days at 37 °C for hollow and porous  $\text{Gd}_2\text{O}_3$  nanoparticles, respectively. Considering the aforementioned sources of determination uncertainty, the comparison shows that our nanoparticles are at least as stable as the other proposed Gd-containing nanoparticle systems and release only negligible quantities of gadolinium.

## 2.5 Particle size

The determination of the particle size and their morphology constitutes an important aspect of the characterization. The size of the particles can be obtained by dynamic light scattering and scanning electron microscopy. Each technique has its advantages and inherent drawbacks. While dynamic light scattering enables an easy ensemble measurement, simplifying assumptions concerning the particle shape have to be made in order to relate the measured data to a particle size. On the other hand, electron microscopy does not need any preliminary assumptions but sample preparation and data analysis can be time consuming. In the attempt of conciseness, we will review the theory of both methods in appendix sections A.3 and A.4 and discuss in the following only the results.

### 2.5.1 Experimental protocol

Dynamic light scattering (DLS) is performed using a Zetasizer Nano ZS apparatus (Malvern Instruments). The nanoparticle dispersions are prediluted until transparency is almost reached. 1 mL of the diluted dispersion is placed in a 3 mL clear polystyrene cuvette and the cuvette is thermostated in the Zetasizer for 1 min at 25 °C. The Zetasizer contains an attenuator system which allows to adjust automatically the incident light intensity in the range of 100 % to 0.0003 % of the laser output power depending of the scattering intensity of the sample. A further dilution is therefore only necessary if the adequate scattering intensity could not be reached by the attenuator system. The parameters in the Zetasizer software are set for a measurement in water at 25 °C with a viscosity of  $\eta = 0.8872 \text{ mPa} \cdot \text{s}$  (Sengers and Watson, 1986) and a refractive index of 1.33 (Schiebener *et al.*, 1990) for a He-Ne laser operating at 633 nm. For all rare earth vanadate materials, the refractive index is assumed to be the same as that of  $\text{YVO}_4$  reported to be 1.99 (Bass *et al.*, 2010) at 25 °C and 633 nm. For each sample, three independent runs are conducted and the results are averaged. The Zetasizer software performs an automated data analysis and returns (i) the  $z$ -average particle diameter and the polydispersity index from the cumulant analysis as well as (ii) the position, the width and the percentage of the most intense peak using the CONTIN algorithm for intensity, volume and number weighting.

### 2.5.2 Results and discussion

The results of the DLS measurements are displayed together for all synthesized nanoparticles in tab. 2.4. The particle size data allow us to draw several conclusions. First, the experimental data confirm the theoretical consideration wthat the apparent particle size should decrease from intensity to volume to number weighting.

Second, the  $z$ -average size obtained from a data analysis according to the method of cumulants represents a good measure of the particle size only if the polydispersity is low and approaches a value on the order of 0.1. This result is obvious considering that the  $z$ -average particle size is obtained from the fit of the

**Table 2.4: Nanoparticle sizes obtained from dynamic light scattering.** The CONTIN algorithm was used to characterize the nanoparticle dispersions by the particle diameter  $d$ , the width of the size distribution  $\Delta d$  and the fraction being in the specified size class  $f$ . The indices  $I$ ,  $V$  and  $n$  indicate intensity, volume and number weighting, respectively.  $d_z$  is the  $z$ -average particle size from the analysis using the method of cumulants and  $p$  the corresponding polydispersity index. Sample designations are the same as in tab. 2.2. The designation N in the sample name indicates that the sample carries an APTES surface modification.

composition	sample	$d_{\langle I \rangle}$ (nm)	$\Delta d_{\langle I \rangle}$ (nm)	$f_I$ (%)	$d_{\langle V \rangle}$ (nm)	$\Delta d_{\langle V \rangle}$ (nm)	$f_V$ (%)	$d_{\langle n \rangle}$ (nm)	$\Delta d_{\langle n \rangle}$ (nm)	$f_n$ (%)	$d_z$ (nm)	$p$
$Y_{0.6}Eu_{0.4}VO_4$	MS1	116	60	100	72	43	99	47	15	100	94	0.20
$Y_{0.6}Eu_{0.4}VO_4/SiO_2$	MS1Si	182	98	95	133	75	67	85	31	100	171	0.37
$Y_{0.6}Eu_{0.4}VO_4/SiO_2/NH_2$	MS1N	204	88	97	203	90	70	112	44	100	187	0.24
$Y_{0.6}Eu_{0.4}VO_4$	E110316	205	141	97	124	107	93	62	23	100	150	0.29
$Y_{0.6}Eu_{0.4}VO_4/SiO_2$	E110316Si	189	69	100	178	74	100	120	43	100	167	0.11
$Y_{0.6}Eu_{0.4}VO_4/SiO_2$	MS18	217	91	99	205	97	91	121	49	100	190	0.18
$Y_{0.8}Eu_{0.2}VO_4/SiO_2$	GM080215Si	160	77	100	116	74	100	62	24	100	129	0.18
$GdVO_4$	MS2	140	53	100	117	53	100	82	26	100	124	0.12
$GdVO_4/SiO_2$	MS2Si	119	42	100	96	39	100	72	21	100	106	0.10
$GdVO_4$	MS4	113	54	100	66	39	100	41	14	100	91	0.18
$Gd_{0.6}Eu_{0.4}VO_4$	MS6R	85	34	100	57	25	100	42	13	100	72	0.14
$Gd_{0.6}Eu_{0.4}VO_4/SiO_2$	MS19	122	52	100	86	45	100	57	19	100	100	0.17
$GdVO_4^{cit}$	MS3	11	4	92	7	2	100	6	1	100	41	0.33
$GdVO_4^{cit}/SiO_2$	MS3Si	35	15	89	24	9	100	20	5	100	33	0.20
$GdVO_4^{cit}$	MS23	68	46	79	15	10	100	11	3	100	34	0.38
$Gd_{0.6}Eu_{0.4}VO_4^{cit}$	MS24	44	25	100	20	11	100	14	5	100	34	0.23
$Y_{0.6}Eu_{0.4}VO_4/GdVO_4$	MS26	97	36	100	72	29	100	55	16	100	86	0.11

intensity autocorrelation function to a single exponential function. In the case of a polydisperse sample, the scattering intensity from big particles is strongly dominating, so that small particles are almost not detectable and the fit returns an apparent size representative of the big particles.

Third, we find that in number weighting we always have only a single particle population indicated by a value of  $f_n = 100\%$  whereas in intensity weighting  $f_I$  approaches  $100\%$  but does not always reach this value. We can explain this behavior by an example. Let us consider two populations of particles with a diameter of  $d_s = 50$  nm and  $d_b = 100$  nm and let us further assume that the 50 nm particles make up  $90\%$  of the signal in intensity weighting and the 100 nm particles account for the other  $10\%$ . We have explained in section A.3.3 that the scattering intensity scales with  $d^6$  which means that the peak surface ratio changes by a factor  $(d_b/d_s)^6 = 2^6 = 64$  when transforming the intensity weighted size distribution to a number weighted one. In our concrete example, this means that a  $10\%$  intensity fraction for the 100 nm particles corresponds only to a number fraction of  $10\%/64 = 0.16\%$  which is negligible.

Fourth, we would expect that the measured particle size is always larger after silica coating; this, however, is not always the case for our measured values. The explanation for this finding lies in the complex interplay between the chemical properties of the silica coating reaction and the theory of the scattering experiment. During silica coating, a layer of silicate is added to the particles. This layer electrostatically stabilizes the particles and prevents aggregation, as we have explained in section 2.2. It is therefore possible that an initially polydisperse sample due to the simultaneous presence of individual nanoparticles and aggregates becomes almost monodisperse after silica coating as the aggregates are destroyed and the individual particles stabilized. In this case, the measured particle size by DLS before silica coating would be mainly influenced by the aggregates and would thus overestimate the real particles size. After silica coating, although the size of the individual particles has increased, the measured value may be smaller as there is no longer an influence from the aggregates. As light scattering initially measures an intensity-weighted particle size from which the other size averages are deduced and as the intensity-weighted value depends on the 6th power of the particle size, it is possible that the size increase upon silica coating cannot compensate the loss in apparent size due to the removal of aggregates.

Last, the comparison of the data allows us to specify an approximate size for nanoparticles produced by the normal and citrate synthesis route. We will give this size estimation in terms of the number-weighted mean value, as this quantity seems to be closest to the real size, determined from the comparison with size estimations from other techniques. In doing so, we find a diameter of generally about 50 nm for nanoparticles produced by the normal route and 10 nm for those from the citrate route.

### 2.5.3 Comparison to electron microscopy data

We performed electron microscopy to possess an additional measure of the particle size and for comparison to the data obtained from DLS. The experimental protocol

is given in appendix section A.4. In brief, scanning electron microscopy necessitates the deposition of the nanoparticles on a support. A comparison between the micrographs obtained from samples deposited on wafers with and without polymer coating showed that the presence of the polymer layer generally results in well distributed nanoparticles with only a small amount of aggregates. However, due to the additional isolating layer, the sample became quickly charged and the image faded. Although this configuration would allow for better statistics on the nanoparticle size distribution as most particles can be imaged individually, we had to resume observation of nanoparticles on wafers without polymer coating for practical reasons. Non-silica coated nanoparticles deposited on surfaces without polymer resulted in strong aggregate formation which impeded analysis of single particles. For silica coated nanoparticles on the same surface, more aggregates were observed than in the case with polymer but imaging of individual particles was still possible (fig. 2.25). However, one has to keep in mind that the nanoparticles shown in the

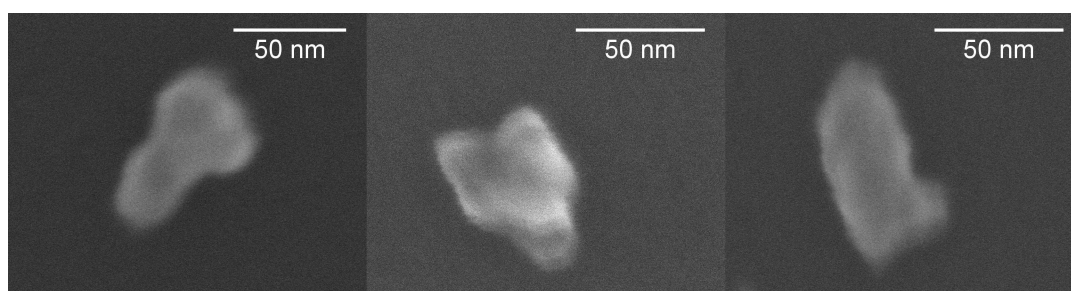


**Figure 2.25: SEM micrographs of silica coated  $\text{GdVO}_4$  nanoparticles.** The sample MS2Si was used. The micrographs were acquired at a magnification of 700,000 (left) and 800,000 (middle and right), respectively.

micrographs might not be representative for the total population contained in the sample. Nevertheless, a close observation of the micrographs suggests that some substructure exists in the nanoparticles. We will address this issue more in detail in section 2.6.

The size analysis yielded the dimensions listed in tab. 2.5. We find a mean dimension of about  $70 \text{ nm} \times 40 \text{ nm}$  and an aspect ratio on the order of 1.5–2. Giaume (2006) analyzed the transmission electron micrographs of 1180 nanoparticles of the

**Table 2.5: Nanoparticle size analysis.** The dimensions concern the nanoparticles shown in the micrographs in fig. 2.25. Considering that the projection of the particle shape is an ovoid,  $a$  designates the major and  $b$  the minor axis as well as  $\zeta = b/a$  the aspect ratio.

nanoparticle	$a$ (nm)	$b$ (nm)	$\zeta$
left	74	42	1.8
middle	64	45	1.4
right	77	39	2.0

composition  $Y_{0.6}Eu_{0.4}VO_4$  synthesized using the same protocol as ours and found dimensions of about 35 nm and 20 nm for the major and minor axis, respectively. The average thickness of the silica layer was reported to be about 2 nm yielding the dimensions 40 nm  $\times$  25 nm for the silica coated nanoparticles. When comparing these values to those obtained in the present study, we have to take into account two main differences. First, our images were acquired by scanning and not by transmission electron microscopy. Due to the effect of preferential secondary electron emission at the outer boundaries of the nanoparticle, SEM tends to overestimate the particle size. Second, the analysis of a reduced number of particles and the choice of the individual particles during image acquisition was likely biased by the operator. Our data has therefore not the same statistical weight as the data from Giaume (2006) and has to be understood rather as an size estimation than determination. Nevertheless, it seems that our nanoparticles are slightly larger than those synthesized by Giaume.

Dynamic light scattering on the sample analyzed by SEM yielded a number average diameter of 72 nm and a width of the size distribution of 21 nm (tab. 2.4). We remind that light scattering can only measure particle sizes based on a spherical particle model and that larger dimensions, that means here the major axis, dominate the obtained result. It is therefore not surprising that the estimated size corresponds approximately to the maximum particle dimension. These findings indicate that the number average size from dynamic light scattering for a quasi-monodisperse nanoparticle dispersion as in the present case and with a polydispersity index of  $p = 0.10$  can give a good estimate for the major axis of the particles. Nevertheless, in the case of a broader size distribution, one would expect the value  $d_{\langle n \rangle}$  to be larger than the dimensions measured from SEM due to the domination of big particles.

## 2.6 Microstructural analysis of X-ray data

In addition to dynamic light scattering and scanning electron microscopy, X-ray diffraction can also yield information about the structure of the nanoobjects. However, the information obtained on size and shape is different from that obtained with the former two techniques. Microstructural analysis of X-ray data is an ensemble method which provides data on the *crystallites* that are the smallest entities with a three-dimensional long range structural order in the material. A careful analysis of the data obtained from electron microscopy and X-ray diffraction allows to elucidate the relationship between nanoparticles and crystallites as, in general, a nanoparticle must not necessarily be made up of only one single crystallite.

### 2.6.1 Theoretical considerations

When a bulk material is reduced to nanoparticles, the Bragg peaks in the X-ray diffraction pattern become broader. This broadening is due to two effects (Guinier, 1963; Pannetier, 1993). The first is linked to the limited size of the crystallites so that the assumption of an infinite crystal lattice is no longer valid. The second arises from deformations in the crystal lattice and from crystal defects. The aforementioned

effects can be treated in three degrees of approximation that we will present in the following.

### 2.6.1.1 Coherence length

In a first approximation, we may assume that the peak broadening is exclusively due to the finite crystallite size. For its analysis, we have to extract the sample contribution to the integral peak breadth. The observed peak breadth is actually the convolution of the instrument resolution function with the sample contribution. Depending on the used peak shape function, we obtain the integral breadth due to finite size effects as

$$\beta_{L,s} = \beta_L - \beta_{L,i} \quad (2.8)$$

for a pure Lorentzian (index  $L$ ) peak shape and as

$$\beta_{G,s}^2 = \beta_G^2 - \beta_{G,i}^2 \quad (2.9)$$

for a pure Gaussian (index  $G$ ) peak shape (Pannetier, 1993). The index  $s$  designates the pure sample effect and  $i$  stands for the contribution of the instrument resolution. In the case of a peak shape described by a pseudo-Voigt function, the extraction of the sample contribution is more complicated and necessitates first the deconvolution of the pseudo-Voigt function into its Lorentzian and Gaussian components (section A.1.5). However, as the present approximation is only valid in the case of a predominant size effect where the peak shape can generally be well described using only a Lorentzian function, we may neglect the Gaussian contribution. The instrument resolution and therefore the value of  $\beta_i$  can be obtained from the measurement of a powdered and well crystallized sample where the crystallite size effect is negligible. Scherrer (1918) devised an equation which links the integral breadth of the peak  $\beta_s$  due to the crystallite size to the coherence length:

$$L_c = \frac{K\lambda}{\beta_s \cos \theta} \quad (2.10)$$

Herein,  $\beta_s$  must be given in radians and  $K$  is the Scherrer constant. The value of  $K$  depends on how the peak width is determined, on the shape of the crystallite, on the crystal symmetry, on the crystallographic direction, and on the size distribution.  $K$  may vary between about 0.5 and 2 (Langford, 1978). When using the integral breadth,  $K$  has for example the value of 1.0747 for spherical crystallites or 1.0000 for the (100) reflection for cubic crystallites of cubic symmetry. In the present approximation, we used a value of  $K = 1$ . In the most general case, the obtained coherence lengths will vary depending on the analyzed Bragg peak. In order to decide whether this distribution is only due to the anisotropy of the crystallite shape or if there are additional effects such as *e. g.* strain, a more sophisticated analysis has to be performed.

### 2.6.1.2 Williamson-Hall analysis

The Williamson-Hall analysis is based on the determination of the coherence length but allows additionally to assess the effect of crystal defects and strain. Assuming

a Lorentzian diffraction peak shape, Williamson and Hall (1953) proposed the expression

$$\frac{\beta_s \cos \theta}{\lambda} = 2\xi \frac{\sin \theta}{\lambda} + \frac{1}{t}, \quad (2.11)$$

where  $\xi$  is the strain parameter and  $t$  the apparent crystallite size. Setting the strain parameter  $\xi = 0$ , equation 2.11 reduces to Scherrer's expression for the coherence length (eq. 2.10) with  $K = 1$ . In order to extract the size and strain parameters, one has to plot  $\frac{\beta_s \cos \theta}{\lambda}$  as a function of  $\frac{\sin \theta}{\lambda}$ . The  $y$ -intercept of the linear fit returns the inverse crystallite size and the slope gives the strain. When the data points cannot be fitted all together with one straight line, this indicates an anisotropy in the crystallite shape or in the strain state. In this case, only peaks whose indices designate the same crystallographic direction must be fitted together. In practice, and especially in the case of structures with high symmetry, this is often not possible because of too few data points per family of Miller indices and a still more general analysis has to be performed.

### 2.6.1.3 Anisotropic broadening

Anisotropy in size-broadening can be implemented in the Rietveld refinement code using a model based on particle shape modeling by spherical harmonics as proposed by Popa (1998). This model accounts for direction-dependent crystallite sizes as well as anisotropic strain. We denote  $\mathbf{h}$  the unit vector of the reciprocal lattice vector  $\mathbf{H}$ ,  $\xi_{hh} = -\Delta H/H$  the relative change of the corresponding interplanar distance  $H$  as a result of the strain and  $R_h$  the crystallite radius along the direction  $\mathbf{h}$ . From the Bragg law, it follows that  $H = d_{hkl}^{-1} = 2 \sin \theta_H / \lambda$ . We indicate by  $\langle \dots \rangle$  the averaging over the orientations of the crystallites, their size distribution and the mean value for equivalent  $\mathbf{H}$ . With the scattering vector  $q$ , the normalized size-strain peak profile can be written as a Voigt function:

$$V_H(q) = \int_{-\infty}^{+\infty} L(q + 2\pi\Delta H) \cdot G(\Delta H) d(\Delta H) \quad (2.12)$$

This Voigt function is the convolution of the Lorentzian contribution

$$L_H(q) = \frac{\frac{3}{4\pi} \langle R_h \rangle}{1 + \frac{9}{16} \langle R_h \rangle^2 (q - 2\pi H)^2} \quad (2.13)$$

accounting for the size effect and of the Gaussian contribution

$$G_H(\Delta H) = \frac{1}{H \sqrt{2\pi \langle \xi_{hh}^2 \rangle}} \exp \left[ -\frac{(\Delta H)^2}{2H^2 \langle \xi_{hh}^2 \rangle} \right] \quad (2.14)$$

representing the strain broadening. Herein,  $\langle R_h \rangle$  is the radius of an average crystallite. With the Bragg law and the definition of the scattering vector, the integral breadths can be calculated:

$$\beta_{LH} = \frac{2\lambda}{3 \langle R_h \rangle \cos \theta_H} \quad (2.15)$$

$$\beta_{GH} = 2 \tan \theta_H \sqrt{2\pi \langle \xi_{hh}^2 \rangle} \quad (2.16)$$

As observable in the electron micrographs (fig. 2.25), the nanoparticles show a significant deviation from the spherical shape. We expect therefore that the shape has a pronounced effect on the anisotropic peak broadening. Strain effects should be of minor importance so that we may neglect all terms concerning strain and focus our theoretical considerations on finite size induced phenomena. A justification for this assumption will be given in section 2.6.3.2.

An analytical expression for  $\langle R_h \rangle$  can only be found if one assumes an explicit crystallite model. As a large variety of shape models exist, the result of such an operation would be strongly dependent on the chosen model and is in practice not very useful. Although there is no general analytical model, it is always possible to develop  $\langle R_h \rangle$  in a convergent series of symmetrized spherical harmonics of the type  $P_{2l}^m(\cos \Phi) \cos m\varphi$  and  $P_{2l}^m(\cos \Phi) \sin m\varphi$ .  $\Phi$  and  $\varphi$  are the polar and azimuthal angles in an orthogonal coordinate system  $(\mathbf{x}_1, \mathbf{x}_2, \mathbf{x}_3)$  with the  $\mathbf{x}_3$  axis oriented along the highest symmetry axis of the crystal structure and the  $\mathbf{x}_1$  axis along a twofold axis. In the case of the tetragonal space group  $I4_1/amd$  this means that  $\mathbf{x}_3$  lies along the crystallographic  $c$ -axis and  $\mathbf{x}_1$  in the  $ab$ -plane.  $P_l^m(x)$  is given by the normalized Legendre polynomials

$$P_l^m(x) = \frac{(-1)^{l-m}}{2^l l!} \sqrt{\frac{(l+m)! (l+\frac{1}{2})}{(l-m)!}} (1-x^2)^{-\frac{m}{2}} \frac{d^{l-m}(1-x^2)^l}{dx^{l-m}} \quad (2.17)$$

and the polar and azimuthal angles for a tetragonal Bravais lattice by

$$\cos \Phi = \frac{lc^*}{H} \quad (2.18)$$

$$\tan \varphi = \frac{k}{h} \quad (2.19)$$

where  $h$ ,  $k$  and  $l$  are Miller indices and \* indicates a lattice constant in the reciprocal lattice. For the space group  $I4_1/amd$  belonging to the Laue class  $4/mmm$  one obtains finally (Popa, 1992)

$$\begin{aligned} \langle R_h \rangle = & R_0 + R_1 P_2^0(\cos \Phi) + R_2 P_4^0(\cos \Phi) + R_3 P_4^4(\cos \Phi) \cos(4\varphi) + \\ & + R_4 P_6^0(\cos \Phi) + R_5 P_6^4(\cos \Phi) \cos(4\varphi) + \dots \end{aligned} \quad (2.20)$$

Herein,  $R_0$  is the particle radius for the isotropic case and  $R_i$  with  $i > 1$  indicate higher order anisotropic contributions. Generally, one has to add terms starting from the isotropic case until the coefficient becomes negligible. In FullProf, the implementation of this method does not vary directly the coefficients  $R_i$  but the parameters  $C_{2l}^m$  according to the expression

$$\begin{aligned} \langle R_h \rangle = & \mathcal{R} (C_0^0 + C_2^0 P_2^0(\cos \Phi) + C_4^0 P_4^0(\cos \Phi) + C_4^4 P_4^4(\cos \Phi) \cos(4\varphi) + \\ & + C_6^0 P_6^0(\cos \Phi) + C_6^4 P_6^4(\cos \Phi) \cos(4\varphi) + \dots) \end{aligned} \quad (2.21)$$

As the coefficient  $C_0^0$  is, in contrast to the description of the method given by Järvinen (1993), not normalized to unity,  $\mathcal{R}$  is a characteristic dimension of the system but not the diameter of the spherical particle from the first-order approximation. In the case of tetragonal symmetry, the sum is calculated up to the 6th order that is until the coefficient  $C_6^4$ .

## 2.6.2 Experimental protocol

### 2.6.2.1 Data acquisition

Powder GdVO<sub>4</sub> nanoparticles (sample MS4) are prepared by drying the corresponding dispersion overnight at 100 °C. The dried powder is then ground using an agate mortar. Due to the generally lower sample quantity for nanoparticles compared to bulk samples, a glass plate is first placed in the sample holder for volume reduction and the remaining volume is filled with the sample so that the whole irradiated area is homogeneously covered with powder. A step width of 0.01° with an integration time of 100 s is sufficient due to the large broadening of the Bragg peaks. All other experimental and instrumental parameters are the same as for the acquisition of the X-ray diffraction pattern of the bulk samples and described in appendix section A.1.

### 2.6.2.2 Manual Williamson-Hall analysis

For the analysis according to the method of Williamson and Hall (1953), we fitted the Bragg peaks individually using the corresponding subroutine of the FullProf suite. Only non-overlapping and non-degenerated reflections are used. Each peak is fitted to a doublet corresponding to the  $K_{\alpha 1}$  and  $K_{\alpha 2}$  contributions in order to obtain the peak position as well as the integral breadth  $\beta$  and its deconvolution in the Lorentzian and Gaussian component  $\beta_L$  and  $\beta_G$ , respectively. The effect of the instrument resolution is either neglected by assuming that  $\beta_s \approx \beta$  or accounted for by calculation of the pure sample contributions with eq. 2.8 and 2.9 where the instrument contribution is obtained from the bulk material (sample MS8). In the second case, the pure contribution  $\beta_{L,s}$  serves for the determination of the coherence length according to eq. 2.10.

### 2.6.2.3 Automated microstructural analysis

Microstructural analysis is performed using the FullProf implementation of the procedure of Popa (1998) working as a two step process. First, the instrument resolution function has to be determined, and is then used to assess the crystallite dimensions from the analysis of the line broadening. We have discussed in section A.1.7 that the best model substance for the determination of the instrument resolution is the bulk GdVO<sub>4</sub> sample (MS8). Instrument broadening is accounted for by the parameters  $U$ ,  $V$ ,  $W$ ,  $X$ , and  $Y$  obtained for the bulk sample synthesized by the ceramic method as displayed in the middle column of tab. 1.3.

In a second step, the diffraction pattern acquired for GdVO<sub>4</sub> nanoparticles (sample MS4) is refined. We have performed the analysis using the model of spherical crystallites according to the Scherrer procedure and without any preliminary assumption concerning the shape of the crystallites using the spherical harmonics procedure. The following settings are used in FullProf in both cases:

- General parameters as listed in section A.1.12.
- Use of the  $y$ - and  $z$ -coordinates of the oxide ions, the individual thermal agitation factors and the unit cell parameters obtained from refinement of

the bulk  $\text{GdVO}_4$  sample from the ceramic method (middle column in tab. 1.3). Use of fixed occupation factors according to the  $\text{GdVO}_4$  stoichiometry.

- Use of the instrument resolution parameters  $U$ ,  $V$ ,  $W$ ,  $X$ , and  $Y$  obtained in the first step.

For the Scherrer method, we also refined the Lorentzian size and strain parameters,  $X$  and  $Y$ , respectively. These values are additional to those already contained in the instrument resolution file. For the spherical harmonics method, we refined the coefficients of the spherical harmonics with even parity  $P_0^0(x)$ ,  $P_2^0(x)$ ,  $P_4^0(x)$ ,  $P_4^4(x)$ ,  $P_6^0(x)$  and  $P_6^4(x)$  according to the size model 21 for tetragonal crystal symmetry. The coefficients for  $P_4^4(x)$  and  $P_6^4(x)$  with odd parity are fixed to zero. The two analysis procedures are finally compared using the agreement factors defined in section A.1.11.

## 2.6.3 Results and discussion

### 2.6.3.1 Crystal structure

Fig. 2.26 depicts the normalized diffraction profiles of  $\text{GdVO}_4$  as bulk sample and in the form of nanoparticles. For the latter, a hydrodynamic diameter  $d_{\langle n \rangle} = (40 \pm 10)$  nm has been determined (tab. 2.4). The comparison of the data shows clearly the

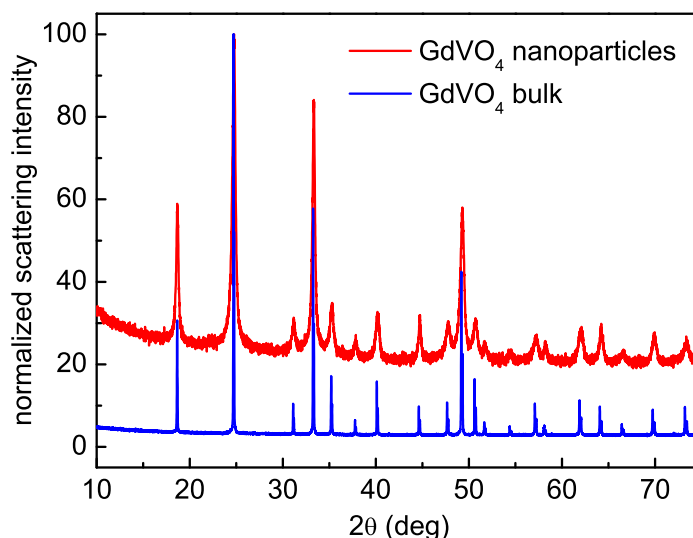


**Figure 2.26: X-ray diffraction patterns of bulk and nanoparticulate  $\text{GdVO}_4$ .** The diffracted intensities have been normalized to that of the (200) peak, the most intense peak in the diffraction pattern. Count rates for this peak before normalization were 40,961 cps (bulk, sample MS8) and 6,720 cps (nanoparticles, sample MS4).

agreement between the diffraction patterns. No additional peaks are visible in the diffraction pattern of the nanoparticles confirming that a pure phase was obtained. Compared to the bulk material, the Bragg reflections of the nanoparticulate sample

are considerably broadened resulting in a lower signal to noise ratio. However, this peak broadening contains valuable information about the size and shape of the crystallites in the particles that we can exploit and compare to the particle size determined by scanning electron microscopy.

### 2.6.3.2 Spherical crystallite model

The first approach to extract the morphology of the crystallites for the  $\text{GdVO}_4$  nanoparticles consisted in a manual analysis of the Bragg reflections. We determined the integral breadths of unambiguously identifiable peaks and calculated the quantities  $\beta \cos \theta / \lambda$  and  $\sin \theta / \lambda$ . These values were plotted according to the Williamson-Hall representation (eq. 2.11) in fig. 2.27 and fitted linearly. Although

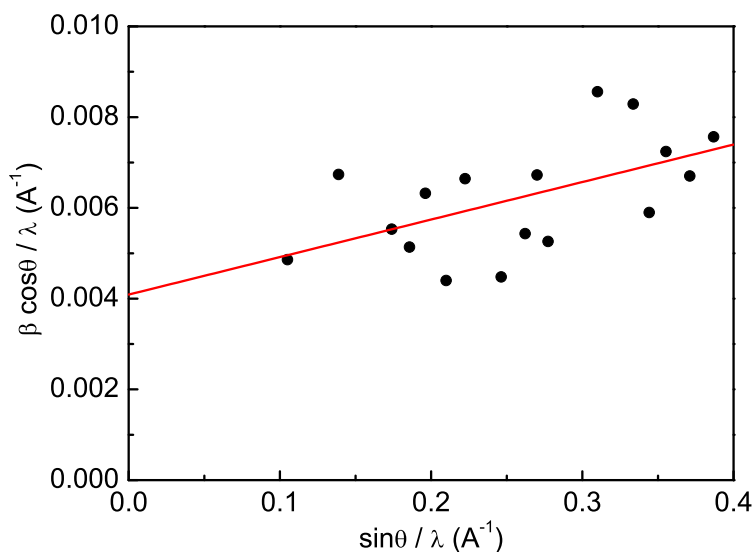


**Figure 2.27: Williamson-Hall plot for  $\text{GdVO}_4$  nanoparticles.** The integral breadth of the diffraction peaks is plotted without correction. A linear fit of the data was performed according to the equation  $\frac{\beta_s \cos \theta}{\lambda} = 2\xi \frac{\sin \theta}{\lambda} + \frac{1}{t}$ . An apparent crystallite size  $t = (240 \pm 50) \text{ \AA}$  and a strain  $\xi = 0.004 \pm 0.002$  were found.

this type of representation predicts a linear dependence of the two calculated quantities, our data shows a large scatter around the linear fit. This behavior may have several reasons. First, the strain parameter extracted from the slope of the fit is quite small and its error reaches about one half of the value itself indicating that the strain is, as expected, less important. Second, the apparent crystallite size of  $240 \text{ \AA}$  has a standard deviation of about 20% which may arise from a direction dependency of the crystallite dimensions. Nevertheless, the obtained value gives a first estimation of the crystallite size.

To obtain further evidence for a non-spherical shape of the crystallites, it is convenient to correct the measured integral breadths for the instrument resolution and to consider only the Lorentzian contribution which is responsible for the crystallite size broadening (Thompson *et al.*, 1987). The corrected data can then

be fitted linearly with Scherrer's formula (eq. 2.10) applied to  $\beta_{L,s}$ . The graphical representation of the coherence length in fig. 2.28 shows that a large scattering of the data is also observable. Although the mean value of 220 Å is in close vicinity to that

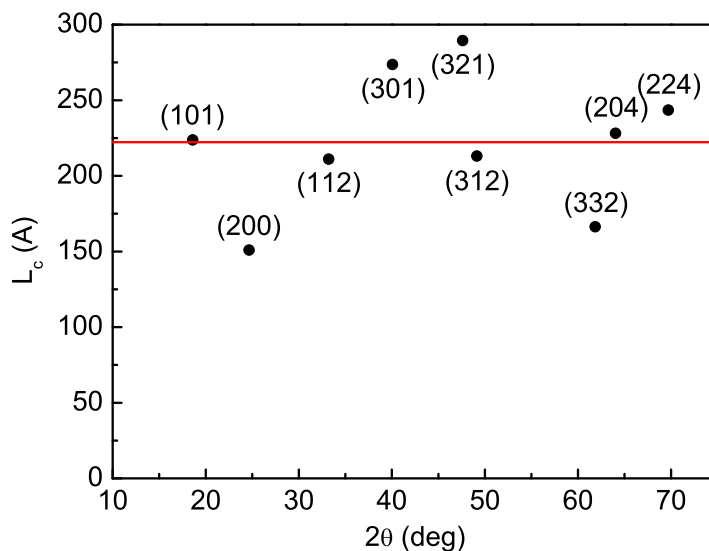


**Figure 2.28: Coherence length for GdVO<sub>4</sub> nanoparticles.** The Lorentzian component of the integral breadth of the diffraction peaks was corrected for the instrument resolution and the obtained quantity  $\beta_{L,s}$  fitted to the Scherrer equation  $L_c = \frac{K\lambda}{\beta_s \cos \theta}$  using  $K = 1$ . The linear fit of the data yielded a coherence length  $L_c = (220 \pm 10)$  Å. Each peak is labeled with its Miller indices.

obtained by the analysis without correction, the extreme values range from 150 Å to about 300 Å. As this deviation should only be due to size effects, we can assume that the crystallites have a shape that significantly differs from a sphere. Due to the high symmetry of the unit cell of the compound, we observe only a small number of non-overlapping peaks impeding an analysis of the coherence lengths according to certain families of Miller indices. Another analysis method employing the global information contained in the diffraction pattern is therefore necessary in order to further elucidate the crystallite shape.

### 2.6.3.3 Non-spherical crystallite model

The Rietveld method allows for extraction of crystallographic information by fitting the entire diffraction profile and also provides information on the crystallite shape. This microstructural analysis requires first data on the instrument resolution as the crystallite size will be extracted from the difference in the width of observed Bragg reflections compared to that resulting only from the instrument setup. As we have discussed in section A.1.7, the best suited material for the determination of the instrument resolution is the bulk GdVO<sub>4</sub> compound. We refined the diffraction pattern assuming spherical crystallites (upper graph in fig. 2.29) in order to validate our approach by comparison of the extracted size with that obtained by the methods described in section 2.6.3.2. For this, we used the instrument resolution function

but we allowed for refinement of the Lorentzian size and strain parameters  $X$  and  $Y$ . Although the width of the observed Bragg peaks can be modeled satisfactorily,

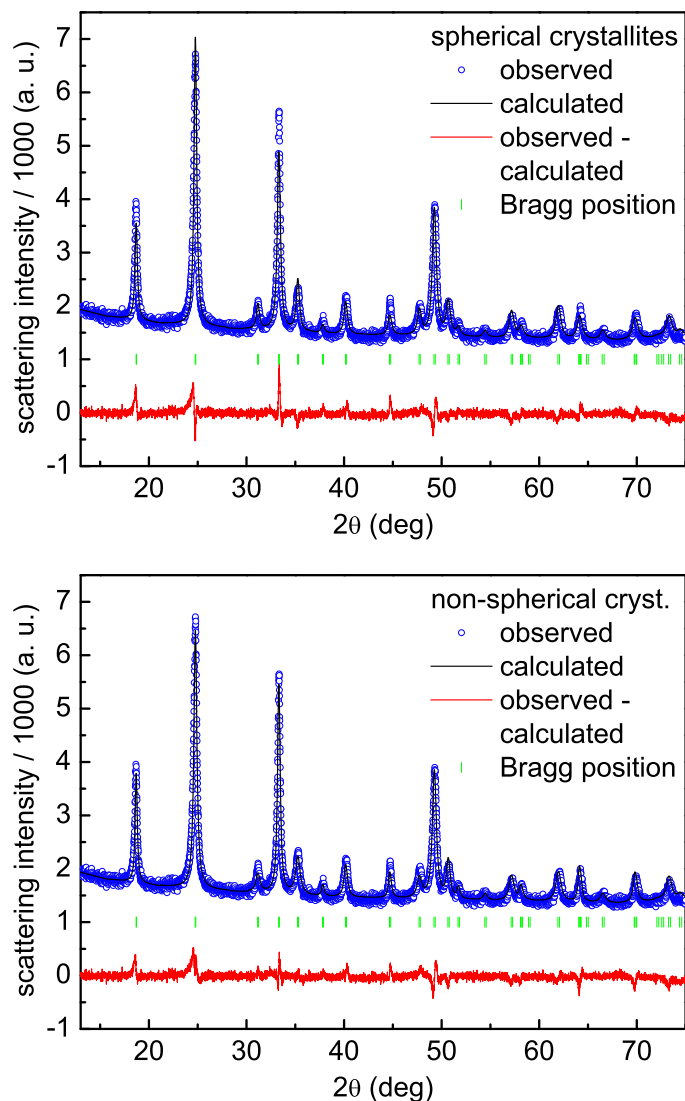


**Figure 2.29: Microstructural analysis of the X-ray data for  $\text{GdVO}_4$  nanoparticles.** Refinement was performed using FullProf with the parameters given in section 2.6.2.3. The upper graph shows the data refinement for spherical crystallites and the lower graph the refinement without shape constraints and by modeling the crystallites by a sum of spherical harmonics.

the measured Bragg peak intensities differ significantly from the calculated profile as shown by the difference plot. Nevertheless, a crystallite size of  $290 \text{ \AA}$  which is on the same order of magnitude as the values obtained previously confirms that this procedure is able to provide a good approximation.

In a next step, we applied the method used for modeling anisotropic crystallite shape by a sum of spherical harmonics which does not need any assumption on the actual shape. The refined diffraction pattern obtained by this method is shown in the lower graph of fig. 2.29. It can immediately be seen that the peak intensities are

better reproduced and the observation of the difference plot demonstrates the better agreement between the measured and calculated profiles. A numerical confirmation of this is obtained by comparing the agreement factors for the two methods listed in tab. 2.6. We notice that all agreement factors are smaller in the case of non-spherical crystallites confirming that this model describes better the real crystallite shape.

**Table 2.6: Parameters obtained from the microstructural analysis.** Data is for GdVO<sub>4</sub> nanoparticles (sample MS4). Values in the left column correspond to nanoparticles for which a spherical shape was assumed and those in the right column were obtained without shape constraints and by modeling the nanoparticle shape with a sum of spherical harmonics. Values in brackets indicate parameters originating from the bulk GdVO<sub>4</sub> sample (HT 1250 °C in tab. 1.3) which were set and not refined. Data for  $X$  and  $Y$  in the case of spherical crystallites corresponds to the additional size and strain contributions from the crystallites.  $d$  designates the average particle size and  $\Delta d$  its standard deviation calculated after the refinement process. Coefficients  $C_{2l}^m$  of the spherical harmonics are given in the units used by FullProf.

parameter	spherical crystallites	non-spherical crystallites
$a = b$ (Å)	(7.21468)	(7.21468)
$c$ (Å)	(6.34986)	(6.34986)
$y$ -position O	(0.4347)	(0.4347)
$z$ -position O	(0.1997)	(0.1997)
$B$ (Gd)	(1.17)	(1.17)
$B$ (V)	(1.56)	(1.56)
$B$ (O)	(1.76)	(1.76)
occupancy Gd	(1)	(1)
occupancy V	(1)	(1)
occupancy O	(4)	(4)
$X$	$0.42 \pm 0.02$	0
$Y$	$0.196 \pm 0.005$	0
$C_0^0$	–	$5.69 \pm 0.05$
$C_2^0$	–	$-2.25 \pm 0.08$
$C_4^0$	–	$0.53 \pm 0.12$
$C_4^4$	–	$-0.78 \pm 0.04$
$C_6^0$	–	$1.61 \pm 0.14$
$C_6^4$	–	$-0.07 \pm 0.02$
$d$ (Å)	290	170
$\Delta d$ (Å)	0	45
$R_p$ (%)	30.5	29.0
$R_{wp}$ (%)	21.3	20.0
$R_B$ (%)	15.0	14.4
$R_F$ (%)	16.6	15.4
$\chi^2$	3.4	2.9

The last step consisted in the visualization of the calculated crystallite shape. The software GFourier allows drawing a contour plot in a two-dimensional projection of the crystallite (fig. 2.30 and 2.31). The calculated form may be described

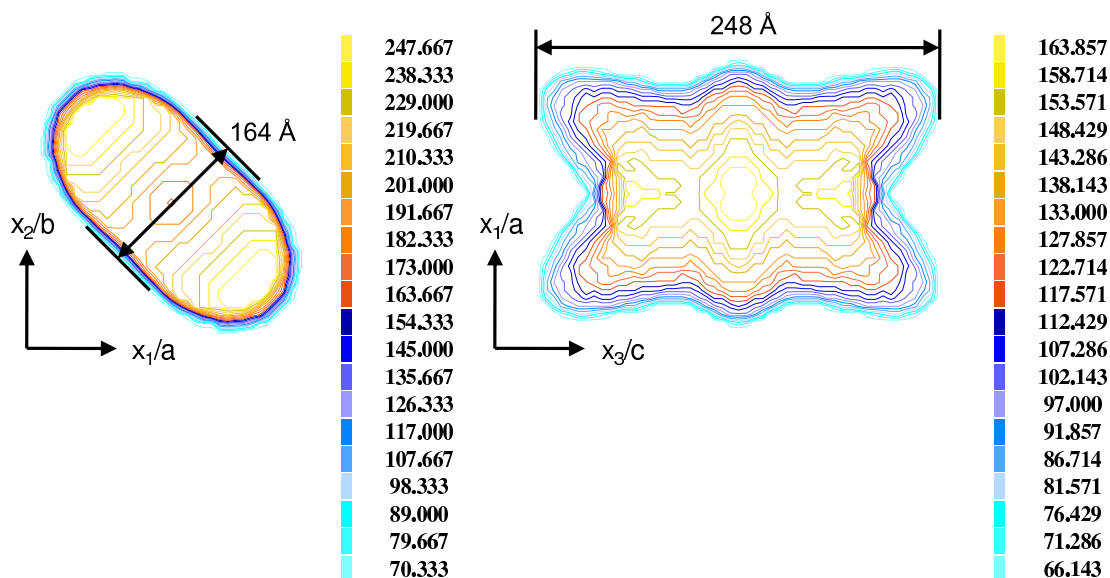


**Figure 2.30: Reconstruction of the crystallite shape.** The reconstructed crystallite is projected in a plane defined by two of the axes of the coordinate system of the spherical harmonics. The third projection in the  $x_2x_3$ -plane is not shown as the shape is the same as for the  $x_1x_3$ -plane. Axes are scaled with the unit cell dimensions, however the given dimensions of height and length are real measures and not scaled. The color maps indicate the height of the crystallite in the third direction orthogonal to the drawing plane in Å. The left legend corresponds to the left figure and the right one to the right figure. The six humps seem to be an artifact arising from the summation of a limited number of spherical harmonics.

approximately as a compressed prolate spheroid. This form can in principle be understood by examining the values of  $C_{2l}^m$ . The coefficient  $C_0^0$  is the largest with a small error indicating a spherical base structure. However,  $C_2^0$  is also large and negative resulting in a subtraction of volume along the  $c$ -direction and finally a flattening of the initial spherical shape. The effect of higher order coefficients is less intuitive because of the complex form of the spherical harmonics but results in a modification of the contour of the structure far away from the center of gravity of the crystallite. However, the six humps seem to be an artifact arising from the summation of a limited number of spherical harmonics rather than a real physical effect. The average crystallite size of  $170 \text{ \AA}$  with a standard deviation of  $45 \text{ \AA}$  obtained from the modeling using spherical harmonics can be better understood on the basis of the reconstruction. The maximal thickness of the crystallite was determined to be  $160 \text{ \AA}$  which corresponds approximately to the average size  $d$  but a smaller thickness is found in the region of the humps. The maximum length including the humps is  $250 \text{ \AA}$ , *i. e.* larger than  $d + \Delta d = (170 + 45) \text{ \AA}$  indicating the weak influence of the outermost parts of the humps on the average, supporting further that the real shape is smoother.

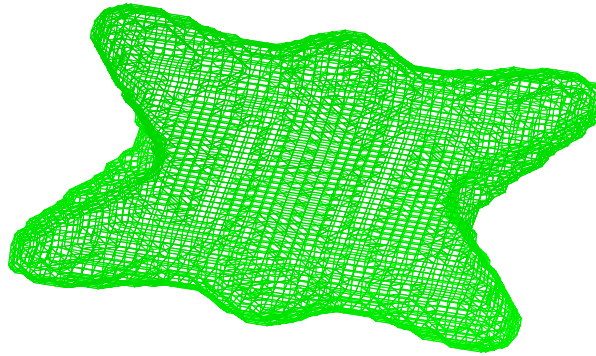


**Figure 2.31: 3D view of the crystallite shape.** The surface of the crystallite is represented by a mesh plot. The six humps seem to be an artifact arising from the summation of a limited number of spherical harmonics.

We will now compare the results from the present size and shape analysis to those from electron microscopy and to the data obtained in previous work. Giaume (2006) and Mialon (2009) acquired X-ray diffraction and electron microscopy data on  $Y_xEu_{1-x}VO_4$  nanoparticles. The analysis of the X-ray reflection broadening using the Scherrer formula or Williamson-Hall analysis yielded for both studies coherence lengths between about 10 nm and 25 nm with a mean value on the order of 15 nm. The observation by transmission electron microscopy of a large number of particles showed that the two-dimensional projection of their form is an ovoid with the two major axes having lengths on the order of 20 nm and 35 nm, respectively. From our microscopic observations of several silica coated  $GdVO_4$  nanoparticles (section 2.5.3) showing also an ovoid shaped projection, we deduced a size of the non-silica coated nanoparticles described by two major axes of about 35 nm and 65 nm. Although our  $GdVO_4$  nanoparticles seem to have bigger dimensions than the  $Y_xEu_{1-x}VO_4$  ones, the present data indicate in both cases that the nanoparticles are larger than the crystallites meaning that the nanoparticles are polycrystalline. However, as the calculated thickness of 16 nm and the length of 25 nm representative of the crystallites are on the same order of magnitude as the nanoparticles, the expression oligocrystalline would be more appropriate. This designation indicates that the nanoparticle is only made up from a few but not many crystallites. When comparing the size of the crystallites to that of the nanoparticles, we have to be aware of what is observed. During electron microscopy, we acquire micrographs of particles on a substrate. As the particles have the form of prolate spheroids, they are most likely lying flat on the surface so that we cannot observe their height but only the width and length. In contrast, X-ray data analysis yields both the height and length. Under consideration of this situation, we propose an alignment of several crystallites as a possible model of the substructure of a nanoparticle (fig. 2.32). The ratio between the nanoparticle and crystallite sizes suggests that an individual nanoparticle is formed by two to three overlapping crystallites in length and two crystallites in width and height. Although this model is compatible with the experimental data, we have yet no experimental proof of such a substructure alignment.

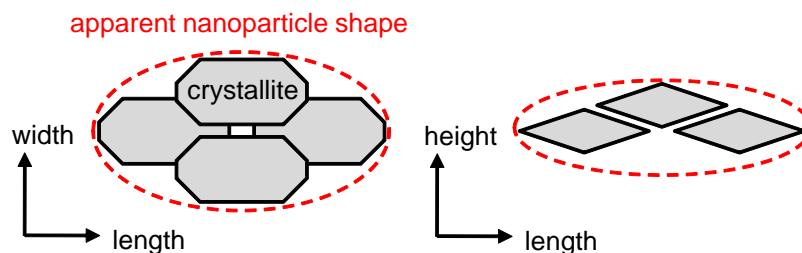


**Figure 2.32: Formation of nanoparticles from crystallites.** A possible model is that a single nanoparticle is made up from several crystallites resulting in an overall shape depicted in fig. 2.31.

## 2.7 Specific surface

With regard to the intended biological applications of the nanoparticles and in particular for their use as a magnetic resonance imaging contrast agent, a high specific contact surface is of great interest. However, these biological applications often also require a functionalization of the surface only achievable after silica coating. It is therefore worth studying if the nanoparticles which possess after their synthesis a high specific surface due to porosity (Mialon, 2009; Mialon *et al.*, 2009) maintain at least partly this high specific surface or if the silica coating step smooths out all surface structure. We therefore performed gas adsorption measurements on silica coated nanoparticles to determine the specific surface. Starting from a degassed sample, a continuous increase of the gas pressure over the sample leads to the adsorption of the gas molecules on the sample surface. Information about the properties of the sample can be obtained qualitatively from the shape of the adsorption isotherms and quantitatively from a detailed analysis using an adsorption model. Further details on the method are given in appendix section A.5.

### 2.7.1 Experimental protocol

The nitrogen adsorption measurement was performed on silica coated  $\text{GdVO}_4$  nanoparticles (sample MS2Si) using a Micromeritics ASAP 2001 physisorption analyzer. The sample is placed in the bulb of a glass sample tube and connected to the apparatus. A second identical empty sample tube serves to measure the saturation pressure which varies with nitrogen evaporation and a subsequent change in the filling level of the Dewar as well as with dilution of nitrogen by oxygen. The nanoparticle powder is out-gassed overnight at  $150^\circ\text{C}$  and the tube is backfilled with helium in order to remove adsorbed gas molecules and humidity. A volume calibration of the sample chamber using helium is performed at ambient temperature and with the sample tube immersed in liquid nitrogen at  $77.3\text{ K}$ , respectively. This step allows for the calculation of the accessible volume in the sample chamber, that is the volume of the sample chamber minus the volume of the powder. Helium is used as a probe because of its negligible adsorption. The two temperatures are necessary to correct for the fact that helium is not an ideal but a real gas. After the calibration step, the sample and reference tubes remain immersed in liquid nitrogen

and the adsorption-desorption measurement using nitrogen is started. In total, about 50 points are recorded for a complete adsorption and desorption cycle. The sample tube is weighed after completion of the adsorption-desorption measurement and the obtained mass of 63.3 mg is used for further analysis. The specific surface is calculated using the Brunauer-Emmett-Teller (BET) method as described in section A.5.2. The data is fitted linearly in the relative pressure range  $p/p_0 = 0.05 - 0.25$  and we verified that the correlation coefficient reaches at least a value of 0.999.

## 2.7.2 Results and discussion

We recorded the adsorption and desorption isotherm for silica coated  $\text{GdVO}_4$  nanoparticles synthesized by the normal route using nitrogen as adsorbate at 77.3 K. The obtained data is displayed in fig. 2.33. The comparison of the shape of the

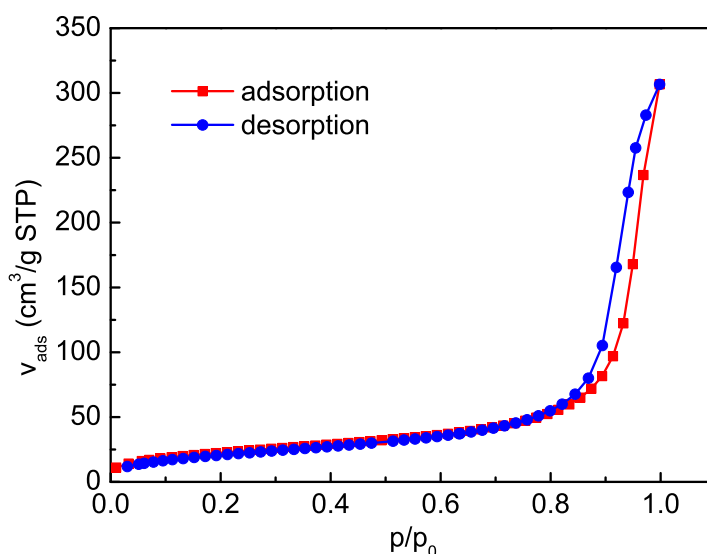


**Figure 2.33: Nitrogen adsorption isotherm for silica coated  $\text{GdVO}_4$  nanoparticles.** The sample MS2Si was used. Data is shown as the volume of adsorbed gaseous nitrogen at standard temperature and pressure (STP,  $T = 273.15$  K and  $p = 10^5$  Pa).

measured isotherm with the isotherms in fig. A.10 shows that our material behaves according to type II. In contrast to the model isotherm, the present material shows a small hysteresis loop. The point B indicating the completion of the first monolayer lies at very low relative pressure, presumably below 0.05. The exact position cannot be deduced due to the limited resolution in the low relative pressure region. Such a value signifies a facile adsorption of the nitrogen molecules on the sample surface, suggesting an easy access of the gas molecules to the adsorption sites. These findings indicate that the analyzed nanoparticles after silica coating are non-microporous. However, this qualitative analysis does not exclude a porosity on a larger scale.

Further information can be gained when comparing the BET surface area to the geometric surface area. The BET analysis (fig. 2.34) yields a surface area of  $(83.2 \pm 0.3) \text{ m}^2/\text{g}$ . The geometrical surface area can be estimated from the size of

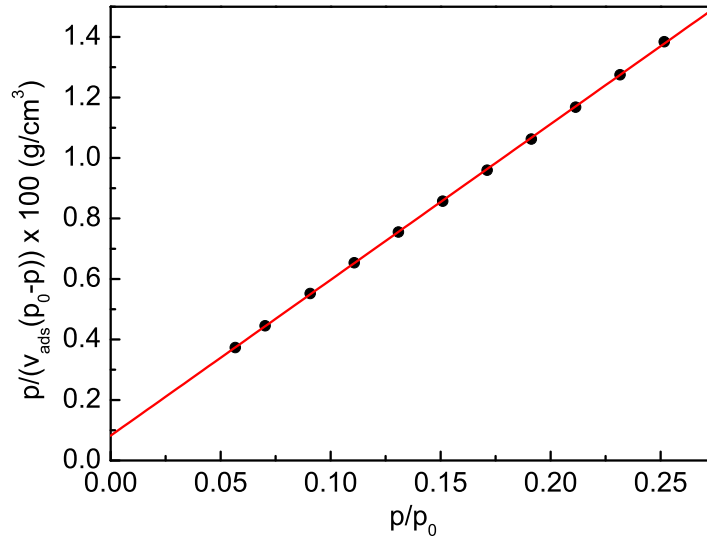


**Figure 2.34: BET analysis of the nitrogen adsorption data for silica coated GdVO<sub>4</sub> nanoparticles.** The measured data for the sample MS2Si has been fitted linearly in the relative pressure range  $p/p_0 = 0.05 - 0.25$ .

the particles. DLS measurement yielded a number average diameter of 72 nm based on an assumed spherical shape (tab. 2.4). Electron microscopy studies revealed however that the two-dimensional projection of the particle shape corresponds more likely to an ellipse. As all observed projections resemble to ellipses, we may assume that the three-dimensional particle shape is a prolate spheroid with the half-main axis dimensions  $a = b = 20$  nm and  $c = 35$  nm (section 2.5.3). We have discussed in the aforementioned section that the nanoparticles are composed of a GdVO<sub>4</sub> core and a silica shell of 2 nm thickness. Using the densities of  $\rho_c = 5.47$  g/cm<sup>3</sup> for GdVO<sub>4</sub> (Swanson *et al.*, 1967) and  $\rho_s = 2.2$  g/cm<sup>3</sup> for silica (Dabadie *et al.*, 1996), the mass of the core can be determined to

$$m_c = \rho_c V_c = \rho_c \frac{4}{3} \pi a_c^2 c_c = 2.4 \cdot 10^{-16} \text{ g}, \quad (2.22)$$

where the index  $c$  stands for quantities concerning only the core. The mass of the silica shell (index  $s$ ) can be calculated by

$$m_s = \rho_s V_s = \rho_s (V - V_c) = \rho_s \frac{4}{3} \pi (a^2 c - a_c^2 c_c) = 3.1 \cdot 10^{-17} \text{ g}. \quad (2.23)$$

Quantities without index concern the entire nanoparticle. 1 g powder contains therefore  $N = \frac{1 \text{ g}}{m_c + m_s} = 3.7 \cdot 10^{15}$  nanoparticles. The surface of one prolate spheroid is given by

$$S = 2\pi \left\{ a^2 + c^2 \frac{\arccos(a/c)}{\tan[\arccos(a/c)]} \right\} = 7.7 \cdot 10^3 \text{ nm}^2 \quad (2.24)$$

and 1 g of nanoparticle powder has therefore a total surface of

$$S_{total} = NS = 28 \text{ m}^2. \quad (2.25)$$

The ratio of the measured to the geometrical surface area is on the order of 3 suggesting the presence of some porosity. Based on the data obtained from the microstructural analysis, we propose that this apparent porosity is due to the space between the individual crystallites forming the nanoparticle. We note that Mialon (2009) reported for pristine  $Y_{0.9}Eu_{0.1}VO_4$  nanoparticles produced by the normal route a specific surface of  $206 \text{ m}^2/\text{g}$  while the geometrical surface was evaluated to  $56 \text{ m}^2/\text{g}$  corresponding to a measured to geometrical specific surface ratio of 3.7. Our lower ratio might be explained by sealing of small pores initially present in the pristine nanoparticles during silica coating.

## 2.8 Magnetic properties of Gd-containing nanoparticles

### 2.8.1 Finite size effects in nanomaterials

The principal characteristic of nanomaterials is that their microscopic structure influences largely their macroscopic properties and gives rise to new phenomena which are not observed in the corresponding bulk material. These features are due to the interplay between the intrinsic material properties, the size distribution and shape of the nanoparticles, finite size effects and interparticle interaction (Batlle and Labarta, 2002). The intrinsic magnetic material properties of  $GdVO_4$  have been discussed in section 1.3.3. Interparticle interactions are of interest in particular for ferro- or ferrimagnetic materials but are less important for antiferromagnets and paramagnets. The term finite size effect encompasses the pure phenomenon due to the limited volume but also the fact that the surface to volume ratio is important for nanoparticles.

The critical temperature of a magnetic phase transition is strongly dependent on the particle size and decreases with decreasing particle volume. This behavior is a consequence of the interplay between pure limited volume and surface effects and can be described quantitatively by the scaling law (Barber, 1983)

$$\frac{T_c(d) - T_c(\infty)}{T_c(\infty)} = \pm \left( \frac{d}{d_0} \right)^{-\frac{1}{\alpha}}, \quad (2.26)$$

where  $T_c(d)$  is the critical temperature for the nanoparticles,  $T_c(\infty)$  the corresponding temperature of the bulk phase,  $d_0$  a characteristic length in the system and  $\alpha$  the correlation length exponent. The sign may be either positive or negative depending on the type of magnetic order. The parameters  $d_0$  and  $\alpha$  are defined by the actual system and values of the order of the lattice parameters are found for  $d_0$  while  $\alpha$  is of the order of unity. We note that the transition temperature is not only a function of the size of the nanoparticle but also of its shape (Alloyeau *et al.*, 2009) described by the aspect ratio. Considerably different dimensions of a nanoparticle result in a transition temperature corresponding to a spherical object with a diameter between the extreme values of the dimension.

## 2.8.2 Experimental protocol

Magnetization measurements are performed as described in section 1.3.4. In particular, powders are produced from dispersed  $\text{GdVO}_4^{\text{cit}}$  (sample MS23) and  $\text{Gd}_{0.6}\text{Eu}_{0.4}\text{VO}_4^{\text{cit}}$  (MS24) nanoparticles, both obtained by the citrate route synthesis, by drying the corresponding dispersions overnight at  $100^\circ\text{C}$ . The dry powder is then finely ground using an agate mortar. Capsule filling quantities were 13.9 mg for sample MS23 and 14.6 mg for sample MS24. Temperature- and field-dependent measurements were performed. All measured data were corrected for the diamagnetic contribution of the polycarbonate capsule and the paraffin wax.

## 2.8.3 Results and discussion

We measured the temperature dependent molar susceptibility of  $\text{Gd}_{0.6}\text{Eu}_{0.4}\text{VO}_4^{\text{cit}}$  nanoparticles produced by the citrate route. The result is depicted in fig. 2.35.

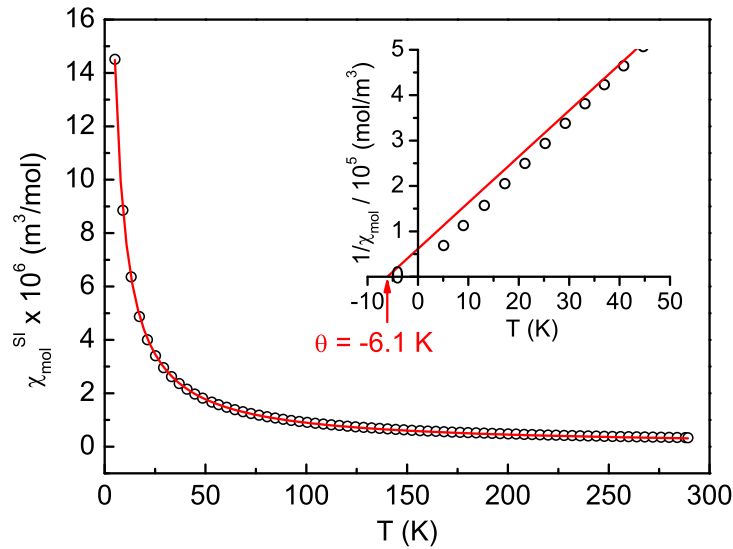


**Figure 2.35: Molar susceptibility of  $\text{Gd}_{0.6}\text{Eu}_{0.4}\text{VO}_4^{\text{cit}}$  nanoparticles as a function of the temperature.** Data were measured for the sample MS24 synthesized by the citrate route and at a magnetic field of 100 Oe. The molar susceptibility was fitted to the equation  $\chi_{mol}^{SI} = \frac{C_{mol}^{SI}}{T - \theta}$  and the values of  $C_{mol}^{SI} = (9.07 \pm 0.02) \cdot 10^{-5} \text{ K m}^3 \text{ mol}^{-1}$  and  $\theta = (-1.17 \pm 0.01) \text{ K}$  were obtained. The inset shows the inverse molar susceptibility plotted as a function of the temperature for the same sample. The linear fit yielded a Curie constant  $C_{mol}^{SI} = (9.85 \pm 0.02) \cdot 10^{-5} \text{ K m}^3 \text{ mol}^{-1}$  and a Weiss temperature of  $\theta = (-6.1 \pm 0.4) \text{ K}$ .

The graph confirms a paramagnetic behavior and the absence of a paramagnetic-antiferromagnetic phase transition within the measurement range down to 5 K. However, the existence of such a phase transition is indicated in the graphic representation of the inverse susceptibility whose fit intersects the temperature axis at a negative value.

A big difference between the two fitting procedures is found for the Weiss temperature. While the fit of the direct susceptibility yields a Weiss temperature of

about  $-1.2$  K, a value of  $-6.1$  K is obtained from the fit of the inverse susceptibility. Based on the standard deviations, we may assume that the real Weiss temperature lies more likely around  $-1$  K. We may compare the result to the data for bulk  $\text{GdVO}_4$  (section 1.3.5) under the assumption that the magnetic properties of the nanoparticles are only dependent on the  $\text{Gd}^{3+}$  and not on the  $\text{Eu}^{3+}$  ions. Using the first order approximation that the Weiss temperature is linked to the transition temperature, the decrease in the Weiss temperature corresponds to the theory which predicts a lower transition temperature according to the scaling law (eq. 2.26). Recent investigations on the antiferromagnetic compounds  $\text{DyPO}_4$  with a bulk transition temperature of  $T_N = 3.4$  K and  $\text{GdPO}_4$  ( $T_N = 0.77$  K) confirmed a temperature decrease of the point of discontinuity in the susceptibility value for nanoparticles of  $d \approx 2.6$  nm (Evangelisti *et al.*, 2011). However, these transitions have no longer the character of a paramagnetic-antiferromagnetic transition. Due to missing magnetic neighbors and surface disorder, net magnetic moments occur in the particles which induce an interparticle interaction and become finally frozen in a glassy spin state. As the phase transition takes place outside the accessible temperature range of the measurement, we have unfortunately no further indication about the nature of the transition occurring in our nanomaterials.

The magnetic moment per  $\text{Gd}^{3+}$  ion as a function of the magnetic field is shown in fig. 2.36. The comparison between the data for the pure and Eu-doped

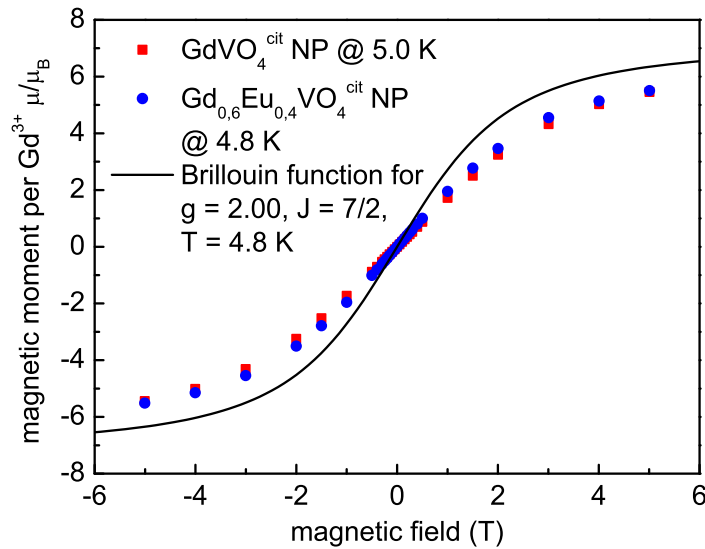


**Figure 2.36: Magnetic moment of  $\text{Gd}^{3+}$  in  $\text{GdVO}_4^{\text{cit}}$  and in  $\text{Gd}_{0.6}\text{Eu}_{0.4}\text{VO}_4^{\text{cit}}$  nanoparticles as a function of the magnetic field.** Data was measured for  $\text{GdVO}_4^{\text{cit}}$  (sample MS23) at a temperature of 5.0 K and for  $\text{Gd}_{0.6}\text{Eu}_{0.4}\text{VO}_4^{\text{cit}}$  (MS24) at a temperature of 4.8 K. Both samples were obtained by the citrate synthesis route. One magnetic field sweep from  $-5$  T to  $5$  T is shown. The magnetic moment is given in units of Bohr's magneton per  $\text{Gd}^{3+}$  ion. A Brillouin function for the theoretical values of  $g = 2.00$  and  $J = 7/2$  at a temperature of 4.8 K is also displayed for comparison.

sample shows that the two magnetization curves, which are normalized to the  $\text{Gd}^{3+}$  content, superimpose almost perfectly. The slight deviation may arise from the 0.2 K temperature difference between the measurements. The steeper increase of

the magnetization for the sample measured at 4.8 K supports this explanation. The result validates, at least for the low temperature region, that doping with  $\text{Eu}^{3+}$  ions does not alter the magnetic properties of the host material. In contrast to the measurement on the  $\text{GdVO}_4$  bulk material (fig. 1.8), we approach at 5 T the saturation magnetization whose value seems to lie around 5.5 – 6 and considerably lower than the theoretical bulk value of 7. The comparison with the Brillouin function drawn for the theoretical values of  $g_J$  and  $J$  confirms the observation made for the bulk sample of a reduced initial slope. Unfortunately, as the saturation plateau is not clearly marked, the impossibility to fit the data with free parameters impedes a further interpretation of the data.

## 2.9 Conclusion

In this chapter, we presented and discussed the synthesis and characterization of nanoparticles composed of rare earth vanadates, in particular of yttrium and gadolinium vanadate with or without europium doping. Whereas Eu-doped yttrium vanadate nanoparticles have already been synthesized in previous works,  $\text{GdVO}_4$  and  $\text{Gd}_{0.6}\text{Eu}_{0.4}\text{VO}_4$  nanoparticles constitute a new material. The synthesis can conveniently be performed using the colloidal chemistry pathway allowing for the formation of nanoparticles by coprecipitation of soluble precursor ions in water. Two principal reaction routes yield formation of either nanoparticles having a hydrodynamic diameter of about 50 nm or smaller particles with a hydrodynamic diameter of about 10 nm. Due to the use of a growth controlling complexing agent for the production of the small particles and caused by the less efficient precipitation during centrifugation, the overall synthesis yield is only about 20 % and much lower than that for the particles of normal size where values in the order of 70 % can be reached. Raw particles can be dispersed easily in water; however, their long term stability is greatly increased by adding a silica layer onto the surface of the particles changing the surface potential of the latter. This silica layer can simultaneously serve as a base material for the functionalization of the nanoparticle. Condensation of an amino-group carrying silica precursor with the silica surface adds reactive amino groups to the particle and enables coupling with a variety of molecules. Such a surface functionalization is of special importance when considering the potential applications for luminescence (chapter 3) and magnetic resonance imaging (MRI) contrast enhancement (chapter 4) where a targeting of the particles is desirable.

Characterization of the particles was first done in terms of concentration and stability. The concentration of the rare earth compound can simply be determined when measuring the content in vanadate. Vanadate ions absorb in the UV range of the spectrum; however, their quantitative analysis using absorption measurements is hindered by the large scattering contribution of the nanoparticles. A much better and more precise method uses a colorimetric detection of a vanadate complex which can be formed by acidic dissolution of the nanoparticles and complex formation with hydrogen peroxide. Our studies showed that a high precision quantification with an error below 2 % is possible with this method. The exact knowledge of the vanadate and concomitantly the rare earth concentration is of crucial importance for the

application of such particles as MRI contrast agents. Another significant point in this relation is the stability of the particles. As vanadate as well as rare earth ions and especially gadolinium ions are highly toxic in their free form, a stable incorporation of these ions in the nanoparticles is needed. We applied a colorimetric protocol for dosing the leached quantity of rare earth ions which allows a determination with a resolution of 6  $\mu\text{M}$ . The result indicated that the free rare earth concentration does not exceed 20  $\mu\text{M}$  after about two weeks and the comparison with literature data confirmed the good stability of our nanoparticles.

An important issue in the characterization of nanoparticles is their size and shape. Several techniques exist but the obtained information depends on the method. While dynamic light scattering yields the average hydrodynamic diameter of a solution of assumed spherical nanoobjects, scanning electron microscopy allows for direct observation of the nanoparticles but lacks a simple possibility to obtain an ensemble average. From DLS, we obtained number-averaged diameter of 50 nm for particles from the normal route and of 10 nm from the citrate synthesis route. The electron micrographs of silica-coated nanoparticles from the normal synthesis route yielded in agreement with the literature an about elliptic form of the projection in the observation plane and showed main axes of approximately 70 nm and 40 nm, respectively. Due to the enormous weight of large objects in the total observed scattered intensity in dynamic light scattering, we observed consequently a hydrodynamic diameter corresponding to the major axis.

Microstructural analysis of X-ray data, a third method for structural characterization, enabled a simple and convenient analysis of an ensemble of nanoparticles. The method allows to reconstruct the size and shape of the crystallites in the material but as one nanoparticle is not necessarily composed of a single crystallite, a conclusion on the nanoparticle size and shape requires additional data *e. g.* from electron microscopy. We were able to show that the crystallites in the material are better described by compressed prolate spheroids or platelets than by spheres. Quantitative analysis has shown that one crystallite has approximately a length of 25 nm and a height of 15 nm. The comparison with the nanoparticle dimensions from electron microscopy allows to deduce that one particle contains several but not many crystallites. We propose therefore to call the nanoparticles oligocrystalline rather than polycrystalline.

A measurement of the specific surface of silica coated nanoparticles and its comparison to the theoretical surface calculated with the dimensions from the electron micrographs revealed that the measured surface is about 3 fold higher than calculated. This result together with the shape of the adsorption isotherm indicates a porous but not microporous surface after silica coating. With recourse to the microstructural analysis and the electron micrographs, where a particle substructure seems to be visible, we propose that this porosity arises from the space between the crystallites making up a nanoparticle.

Magnetic characterization of Gd-containing rare earth vanadate nanoparticles confirmed the conservation of the paramagnetic behavior of  $\text{GdVO}_4$  in the studied temperature range down to 5 K. Doping of the material with europium ions does not seem not to alter the magnetic properties arising from the  $\text{Gd}^{3+}$  ions. The

magnetic characterization provides valuable information for the further studies in relation with the application of these nanoparticles as a contrast agent in MRI.

# Chapter 3

## Rare earth vanadate nanoparticles as optical hydrogen peroxide sensor

The following chapter contains two parts. In the first, we will discuss the theoretical fundamentals of the luminescence of rare earth materials in general and the optical properties of  $Y_{1-x}Eu_xVO_4$  materials in particular. A second and major part will be devoted to the biological effect of hydrogen peroxide and its detection. We will review the pathways of endogenous  $H_2O_2$  production as well as the transduction and regulation of hydrogen peroxide mediated signals. Currently available detection methods for hydrogen peroxide will be discussed together with their specific advantages and drawbacks. We will present the knowledge about the  $H_2O_2$  detection capabilities of  $Y_{0.6}Eu_{0.4}VO_4$  nanoparticles and compare characteristic parameters for nanoparticles from different syntheses. We note that the theoretical principles are discussed in a comprehensive manner as they serve also as a basis for the explanation of the experimental results obtained with the new type of multifunctional nanoparticles containing gadolinium and europium which will be discussed in chapter 4.

### 3.1 Luminescence of rare earth vanadates

Luminescence effects in rare earths as well as their quantum mechanical origin are treated comprehensively in the book of Wybourne (1965) and more recently in that of Liu and Jacquier (2005). We will give a short overview over the topics crucial for understanding the luminescence properties of the nanoparticles used in this study.

#### 3.1.1 Electronic structure of lanthanides

The group of the lanthanides within that of the rare earths comprises the elements from lanthanum with the atomic number 57 to lutetium having an atomic number of 71 (Holleman *et al.*, 1995). The theoretical electronic configuration of the neutral state can be written as  $[Xe] 6s^2 5d^1 4f^n$  where  $[Xe]$  designates the electronic configuration of the xenon atom with  $1s^2 2s^2 2p^6 3s^2 3p^6 3d^{10} 4s^2 4p^6 4d^{10} 5s^2 5p^6$ .  $n$  indicates the number of electrons in the  $4f$  shell, increasing from  $n = 0$  for lanthanum to  $n = 14$  for lutetium. We note that in most elements within this group, the electron of the  $5s$  state is in the ground state located in the  $4f$  shell resulting in a  $4f^{n+1}$  configuration. This is the case for Eu but not for Gd. The spatial extension of the  $4f$

eigenfunction decreases steeply with increasing atomic number of the lanthanides. In La (atomic number  $Z = 57$ ), the  $4f$  shell is still mainly located outside the xenon structure but already in Nd ( $Z = 60$ ), the  $4f$  shell has contracted so that its maximum lies inside the  $5s^25p^6$  shell. This phenomenon is known under the name lanthanide contraction. In consequence, all further electrons are inner electrons and do not participate in the formation of chemical bonds which are mediated by the outer valence electrons resulting in very similar chemical properties of the rare earths. Upon ionization, the outermost electrons in the  $6s$  and  $5d$  shells are removed so that the obtained ion has the oxidation state +3 with an electronic configuration  $[\text{Xe}]6s^05d^04f^n$ . The actual electronic configurations of rare earth atoms and ions used in this study are listed in tab. 3.1. A lanthanide ion presents only fully occupied outer  $5s^25p^6$  orbitals which shield the  $4f$  electrons against the surroundings and prevent usually any strong interaction with the latter. Crystal field effects on rare earth ions in solid matter are therefore small and can be treated using perturbation theory.

**Table 3.1: Electronic configurations of rare earth ions used in this study.** The term symbols are given for the ground state of the atom and ion, respectively. Rare earth is abbreviated as RE.

rare earth	RE <sup>0</sup>		RE <sup>3+</sup>	
	configuration	term	configuration	term
europium	$4f^76s^2$	$^8S_{7/2}$	$4f^6$	$^7F_0$
gadolinium	$4f^75d6s^2$	$^9D_2$	$4f^7$	$^8S_{7/2}$

### 3.1.2 Electronic excitations and energy levels

Electrons in trivalent rare earth ions RE<sup>3+</sup> can be excited in several manners. The majority of the applications uses  $4f^n - 4f^n$  intra-configuration transitions because of the weak coupling of the  $4f$  electrons with the surroundings and due to corresponding wavelengths located in the visible spectral range or in its close vicinity. These transitions are possible due to the breakdown of the degeneracy of the  $4f$  states as a result of interaction effects. However, transitions with higher energy which involve  $5d$ ,  $6s$  and  $6p$  states lying more than  $30,000\text{ cm}^{-1}$  above the ground state are also possible. The transitions with the lowest energy in this group are  $4f^n - 4f^{n-1}5d$  inter-configuration transitions which are parity allowed in RE<sup>3+</sup> ions and can have intensities up to 10,000 times stronger than the most intense  $4f^n - 4f^n$  transitions. As the visible red luminescence of europium-doped rare earth vanadate nanoparticles used in this study is due to the intra-configuration mechanism, we will limit our considerations to the energy levels within the  $4f$  shell.

Electronic energy levels for solid rare earth compounds can be calculated using quantum theory for atomic spectroscopy where all solid state effects are treated commonly as the so-called crystal field interaction by perturbation theory.

This approach is justified when considering the energies involved in the different interaction mechanisms. Tab. 3.2 shows that the crystal field influence is considerably smaller than that of other contributions.

**Table 3.2: Energy scales of different interactions encountered in solid rare earth compounds.**

The central-field approximation serves as zero for the energy scale.  $L$ ,  $S$  and  $J$  are the quantum numbers of the spin, the angular momentum and the total angular momentum, respectively. The value in the last column designates the remaining degeneracy of the state after taking into account the interaction mechanism cited in the first column.

interaction mechanism	energy ( $\text{cm}^{-1}$ )	degeneracy
central field	–	$\frac{14!}{(14-n)!n!}$
electron-electron	$10^4$	$(2L + 1)(2S + 1)$
spin-orbit	$10^3$	$2J + 1$
crystal field	$10^2$	$\geq 1$ if $n$ even, $\geq 2$ if $n$ odd

During the calculation procedure, several interactions have to be considered. The central field approximation which takes only into account the interaction between the nucleus and the electrons yields only one totally degenerated  $4f$  energy level. Addition of the electrostatic Coulomb interaction between the electrons in the  $4f$  state splits this energy level further. According to the commutation relations, the matrix element of the electronic Coulomb interaction is diagonal in the quantum numbers  $L$  and  $S$  (appendix section A.2.1). In total,  $2L + 1$  different values of the angular momentum and  $2S + 1$  different values for the spin are possible, resulting in a remaining degeneracy of  $(2L + 1)(2S + 1)$  states. Besides the electrostatic interaction of the electrons, we also have to consider the magnetic interaction from spin-spin and spin-orbit coupling, where the spin-orbit interaction is predominant. We recall that the two coupling schemes  $L$ - $S$  and  $j$ - $j$  coupling exist for the two extreme cases (section A.2.1) but that in rare earth ions the best suited scheme is the intermediate coupling.

The surrounding of a free ion has spherical symmetry and each energy level is  $2J + 1$  fold degenerate. Upon placing of the ion in a solid structure, the spherical symmetry is destroyed to a somehow lower symmetry defined by the symmetry of the crystal. The electrical field of the surrounding of the ion induces a splitting of the energy level while the degree of splitting is dependent on the point symmetry at the position of the rare earth ion. For an even electron number, the degeneracy may be completely removed under the condition of an appropriate symmetry, but in the case of an odd electron number, an at least two-fold degeneracy remains which can only be removed in a magnetic field.

A calculation of the energy levels considering the three discussed interactions yields an energy diagram as shown in fig. 3.1. Due to the fact that  $4f$  electrons are located in an inner electron shell, the actual energy of a particular ion varies only negligibly when changing the surrounding matrix material and an energy

diagram calculated for one specific matrix material is therefore generally valid in other matrices, too.

### 3.1.3 Radiative transitions

The nature of radiative transitions depends on whether we deal with free ions or ions in a crystal. The two cases have therefore to be analyzed separately.

#### 3.1.3.1 Free rare earth ions

The Hamiltonian  $H_F$  for a free atom or ion with  $n$  electrons is composed of the elements

$$H_F = H_0 + H_C + H_{SO}, \quad (3.1)$$

where  $H_0$  is the contribution from the kinetic energy of the electrons and their potential energy in the electric field of the nucleus,  $H_C$  is the potential for the Coulomb repulsion between the electrons and  $H_{SO}$  is the energy due to spin-orbit coupling. As the Coulomb potential contained in  $H_0$  and  $H_C$  is a scalar potential, and the spin-orbit coupling constant in  $H_{SO}$  depends only on the distance of the coupling partners, the parity operator  $P$  commutes with  $H_F$ . According to the Laporte rule (Laporte and Meggers, 1925), electric dipole transitions between states of the same parity, which is the case for  $4f^n - 4f^n$  intra-configurational transitions, are strictly forbidden. Nevertheless, magnetic  $4f^n - 4f^n$  transitions are allowed. If  $L$ - $S$  coupling is predominant, the selection rules  $\Delta S = 0$ ,  $\Delta L = 0, \pm 1$ , and  $\Delta J = 0, \pm 1$  except  $0 \leftrightarrow 0$  hold. A change in the coupling scheme to intermediate or  $j$ - $j$  coupling leads to a weakening or breakdown of the selection rules in  $S$  and  $L$ . Only the selection rule in  $J$  subsists as it is independent of the coupling scheme.

#### 3.1.3.2 Rare earth ions in a crystal

Upon placing of a rare earth ion in a crystal, the corresponding Hamiltonian can be written as

$$H = H_F + V, \quad (3.2)$$

where  $H_F$  is the Hamiltonian of the free ion discussed in section 3.1.3.1 and  $V$  is the crystal field potential at the position of the ion of interest generated by its neighbors. The symmetry of  $V$  is defined by the surrounding of the ion and is basically the same as the crystallographic site symmetry which is generally lower than spherical. This additional term provokes that the Hamiltonian does no longer commute with the parity operator  $P$  and electric dipole transitions become weakly allowed. Theoretical selection rules are  $\Delta l = \pm 1$ ,  $\Delta S = 0$ ,  $\Delta L \leq 2l$  and  $\Delta J \leq 2l$  but spin-orbit interaction usually leads to a breakdown of the selection rules in  $S$  and  $L$ . The selection rule  $\Delta J \leq 6$  for  $4f$  electrons ( $l = 3$ ) remains valid as long as  $J$  is a good quantum number. In the absence of crystal field mixing of states with different  $S$  and  $L$ , electric dipole transitions are limited to  $0 \leftrightarrow 2$ ,  $0 \leftrightarrow 4$  and  $0 \leftrightarrow 6$  transitions in  $J$ . Crystal field mixing in turn may violate these rules so that  $0 \leftrightarrow 1$  and  $0 \leftrightarrow 3$  transitions become visible. The selection rules are summarized in tab. 3.3.

Figure withdrawn due  
to copyright restrictions

**Figure 3.1: Dieke energy level structure for trivalent rare earth ions in LaF<sub>3</sub>.** The energy levels are based on computed crystal-field energies and are labeled with  $^{2S+1}L$  and/or  $J$ , where the dominant character of the levels can clearly be assigned. The red arrows indicate the most intense transitions observed in the luminescence spectrum of Y<sub>0.6</sub>Eu<sub>0.4</sub>VO<sub>4</sub> nanoparticles. Energy diagram without arrows reprinted with permission from W. Carnall *et al.*, J. Chem. Phys. 90 (7), 3443-3457. Copyright 1989. American Institute of Physics.

**Table 3.3: Selection rules for transitions in lanthanide ions in a crystal.** The listed selection rules are valid for a lanthanide ion in a non-spherical crystal field and in the absence of crystal field mixing of states with different  $S$  and  $L$ .

transition	selection rule
electric dipole	$\Delta J = \pm 2, \pm 4, \pm 6$
magnetic dipole	$\Delta J = \pm 1$ , but not $0 \leftrightarrow 0$

The intensities of  $4f^n - 4f^n$  intraconfigurational transitions have been explained by Ofelt (1962) and Judd (1962). The latter author reported that certain transitions in the lanthanide spectrum and especially those with  $\Delta J = \pm 2$  are hypersensitive to small changes in the symmetry of the crystallographic site of the lanthanide ion that increase tremendously the intensity of the corresponding transition. This intensity gain may be of such magnitude that the normally forbidden electric dipole transitions predominate over allowed magnetic dipole transitions.

### 3.1.4 Non-radiative transitions

Non-radiative transitions provoke a deexcitation without emission of radiation. Two pathways of energy transfer are possible. The first is especially important for nanoparticles in aqueous solution. Here, energy can be transferred from inside the nanoparticle to a surface defect from where it is dissipated to the surrounding water molecules (Kropp and Windsor, 1965; Haas and Stein, 1972). The second pathway involves energy trapping within the nanoparticle structure by different mechanisms which we will detail in the following. Fig. 3.2 summarizes schematically the two pathways.

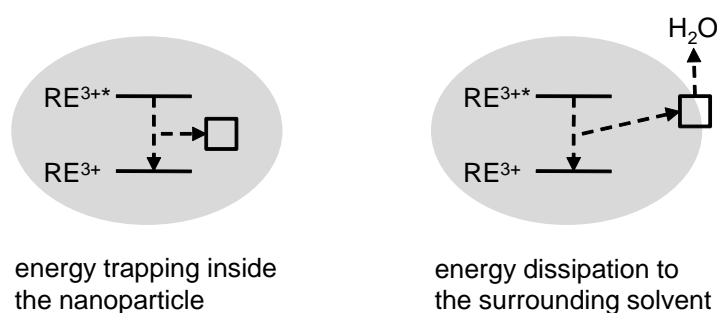


**Figure 3.2: Pathways of non-radiative RE<sup>3+</sup> deexcitation.** Energy may be trapped inside the crystal (left figure) or dissipated via the surface by interaction with solvent molecules, here water (right figure). The star indicates the excited state and non-radiative energy transfers are displayed by broken arrows.

### 3.1.4.1 Multiphonon relaxation

A  $\text{RE}^{3+}$  ion can be deexcited by transferring its energy to the crystal lattice under creation of several phonons (fig. 3.3). This process is called multiphonon relaxation (Ermenoux *et al.*, 2000; Reed and Moos, 1973). The rate constant of deexcitation  $k_{mp}(T)$  is given by the expression

$$k_{mp}(T) = k_{mp}(0\text{K}) \left[ \frac{1}{\exp\left(\frac{h\nu}{k_B T}\right) - 1} + 1 \right]^p, \quad (3.3)$$

where  $k_B$  is the Boltzmann constant,  $h\nu$  the energy of one phonon and  $p = \frac{E_{JJ'}}{h\nu}$  the number of phonons generated during the deexcitation  $J \rightarrow J'$  with the energy  $E_{JJ'}$  (Riseberg and Moos, 1968). We observe that  $k_{mp}(T)$  is strongly dependent on the temperature and increases with the number of phonons which can be generated using the energy of the rare earth ion deexcitation process. As  $p$  depends also on the energy of the phonon, which in turn is a function of the matrix material, this relaxation process can be influenced by changing the surrounding matrix.

### 3.1.4.2 Energy transfer

Energy may also be transferred within the crystal structure from a donor to an acceptor if their distance is appropriate. Depending on the excitation mechanism (section 3.1.5), the donor can be a vanadate group or a  $\text{RE}^{3+}$  ion. The acceptor is in both cases the  $\text{RE}^{3+}$  ion. The energy transfer can be performed in a resonant manner, where all excitation energy is transferred, or non-resonant, where only a part of the excitation energy is transferred to the acceptor and the rest to other mechanisms (fig. 3.3). Such a non-resonant transfer is for example found in the cross relaxation between the states



of two  $\text{Eu}^{3+}$  ions (Blasse and Grabmaier, 1994).

In the case of a resonant process, the energy transfer is operated either by multipole interactions if the distance between the donor and the acceptor is large (Poluektov and Gava, 1971) or by exchange interactions for neighboring donors and acceptors (Van Uitert and Johnson, 1966). For exchange interaction, an overlap of the orbitals of donor and acceptor is necessary. The transfer rate constant  $k_{ex}$  is dependent on the distance  $R$  between donor and acceptor according to the expression (Shionoya and Yen, 1998)

$$k_{ex} \propto \exp\left(-\frac{2R}{R_B}\right), \quad (3.4)$$

where  $R_B$  is the effective Bohr radius. For lanthanide doped  $\text{YVO}_4$  materials, Mialon (2009) has calculated that the minimal distance  $R$  between two rare earth ions does not fall below  $4\text{ \AA}$  while  $R_B = 1.15\text{ \AA}$ . The author has deduced that the exchange interaction between rare earth ions is negligible in this material. However, this

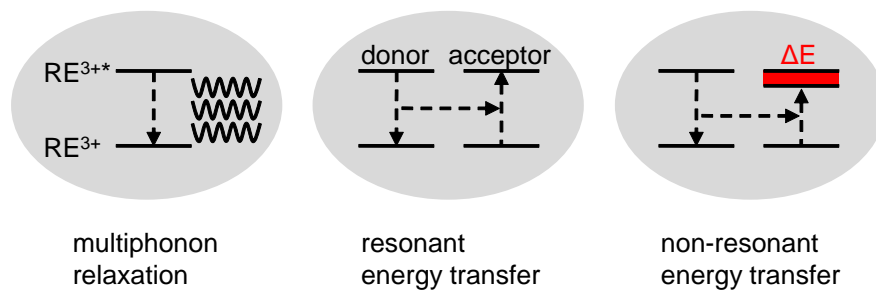


**Figure 3.3: Non-radiative transitions with energy trapping inside the crystal.** Multiphonon relaxation transfers energy from  $\text{RE}^{3+}$  deexcitation to lattice oscillations (left figure). Energy transfer can occur in a resonant manner with complete transfer of the excitation energy (middle figure) or in a non-resonant manner, where the excitation energy is only partially transferred (right figure). The star and the broken arrows have the same meaning as in fig. 3.2.

mechanism is quite efficient for the energy transfer between vanadate groups and a vanadate group and a  $\text{RE}^{3+}$  ion (Blasse, 1966; Van Uitert and Johnson, 1966).

Energy transfer between rare earth ions, especially when these are present at high concentration, is mainly performed by multipole interactions. The rate constant of energy transfer by multipole interactions (Förster, 1948; Dexter, 1953; Inokuti and Hirayama, 1965) is given by

$$k_{tr}(R) = \frac{1}{\tau_0} \left( \frac{R_0}{R} \right)^m, \quad (3.5)$$

where  $R_0$  is the critical donor-acceptor distance at which the rate of energy transfer is equal to the deexcitation rate of the donor,  $\tau_0$  is the lifetime of the excited state of the donor in absence of an acceptor and  $m$  the multiplicity of the multipole interaction.  $m = 6$  for a dipole-dipole interaction,  $m = 8$  for the interaction between one dipole and one quadrupole and  $m = 8$  if two quadrupoles interact. The high order power law in  $R$  shows us that this interaction is strongly dependent on the donor-acceptor distance which is given by the dopant concentration.

### 3.1.5 Optical properties of $\text{Y}_{1-x}\text{Eu}_x\text{VO}_4$ materials

Huignard (2001) and Mialon (2009) have studied in detail the photophysical properties of  $\text{Eu}^{3+}$  doped  $\text{YVO}_4$  materials which we will to summarize in this section. Like we have already seen in chapter 1 concerning the structural properties of the nanoparticles, the comprehension of their luminescent properties requires also a recourse to the bulk material. Finite size effects and the relatively high surface to volume ratio of the nanoparticles give rise to additional parameters which are difficult to treat without the knowledge of the properties of the bulk material. Although several rare earth ions have energy levels suitable for luminescence emission (fig. 3.1), europium is the element of choice for multiple reasons:

- $\text{Eu}^{3+}$  is one of the most efficient activators of yttrium vanadate.

- The relevant energy level structure of  $\text{Eu}^{3+}$  is relatively simple as emission almost exclusively originates from the  $^5\text{D}_0$  level.
- $\text{Eu}^{3+}$  is less sensitive than several other rare earth ions to luminescence quenching due to energy dissipation to water molecules because the transition energies in  $\text{Eu}^{3+}$  do not lay close to the harmonics of the O–H oscillation.
- $\text{Eu}^{3+}$  shows a high quantum yield and a long luminescence lifetime (Stein and Würzberg, 1975).

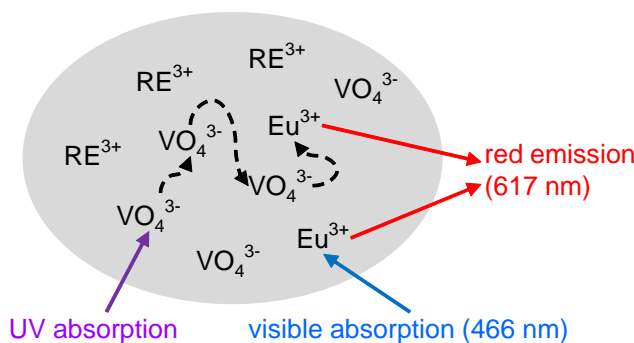
The luminescence excitation and emission spectra for a bulk  $\text{Y}_{0.95}\text{Eu}_{0.05}\text{VO}_4$  sample are shown in fig. 3.4. The excitation spectrum contains two contributions.

Figure withdrawn due  
to copyright restrictions

**Figure 3.4: Excitation and emission spectra for bulk  $\text{Y}_{0.95}\text{Eu}_{0.05}\text{VO}_4$ .** Left graph: Excitation spectrum. Luminescence was recorded at 620 nm. Note that the absorption band at 280 nm is saturated. Right graph: Emission spectrum. Luminescence was excited at 280 nm. Figure from Mialon (2009).

The broad absorption band in the UV range up to a wavelength of about 350 nm is due to a charge transfer between oxygen and vanadium atoms in the orthovanadate groups. The narrow absorption lines at higher wavelengths correspond to  $4f^n - 4f^n$  intra-configurational transitions in the  $\text{Eu}^{3+}$  ion. As these transitions are only weakly allowed, their absorption is low. The excitation spectrum evidences the presence of two different mechanisms for excitation of the  $\text{Eu}^{3+}$  luminescence.  $\text{Eu}^{3+}$  ions can either be excited directly but with low efficiency in the visible range or by highly efficient energy transfer from the vanadate matrix upon excitation of the latter at higher energy in the UV range. The two excitation pathways are depicted in fig. 3.5.

The emission spectrum obtained from excitation of the vanadate band contains several narrow peaks which arise from  $4f^n - 4f^n$  transitions in the  $\text{Eu}^{3+}$  ions. The peak designations according to Brecher *et al.* (1967) show that intense transitions originate from the  $^5\text{D}_0$  energy level. The levels  $^5\text{D}_1$  and  $^5\text{D}_2$  are mainly deexcited by non-radiative conversion to  $^5\text{D}_0$  and the corresponding emission peaks are therefore



**Figure 3.5: Mechanism of  $\text{Eu}^{3+}$  luminescence in a rare earth vanadate matrix.**  $\text{Eu}^{3+}$  ions may be excited either directly or by energy transfer from the vanadate groups. Non-radiative transitions are indicated by broken arrows. In both cases, red luminescence emission is observed.

not observed. The  $\text{Eu}^{3+}$  ion occupies a non-centrosymmetric site with symmetry  $D_{2d}$  within the crystal structure and the electric dipole transitions are therefore not strictly forbidden as we have discussed in section 3.1.3.2. According to the selection rules, peaks with reasonable intensity exist for the  ${}^5\text{D}_0 - {}^7\text{F}_4$  ( $\Delta J = 4$ ) and  ${}^5\text{D}_0 - {}^7\text{F}_2$  ( $\Delta J = 2$ ) transitions. The latter is the most intense transition in the spectrum due to its hypersensitivity to small distortions from the centrosymmetry of the  $\text{Eu}^{3+}$  site. We do not want to discuss further the substructure of the peak and we here only note that it has two components at 615 nm and 619 nm. The transitions with  $\Delta J = 1$  and 3, which are only allowed in a higher order approximation, are slightly visible indicating that crystal field mixing of states with different  $S$  and  $L$  takes place. The transition  ${}^5\text{D}_0 - {}^7\text{F}_0$  ( $\Delta J = 0$ ) is forbidden and no peak is therefore observed in the spectrum.

The emission from  $\text{Eu}^{3+}$  following an excitation in the UV range is a well studied multi-step process (Powell and Blasse, 1980) which comprises the following steps:

- Energy absorption by the vanadate groups. Upon illumination of the material in the UV range, charges are transferred from the occupied  $2p^6$  orbital of the  $\text{O}^{2-}$  ion into the empty  $3d^0$  orbital of the  $\text{V}^{5+}$  ion. Due to the strong interaction between  $\text{V}^{5+}$  and  $\text{O}^{2-}$ , the absorption band is very broad. This process results in the formation of a Frenkel exciton localized on a crystallographic site.
- Energy migration in the matrix. The Frenkel exciton can migrate in a thermally activated process on the sublattice of the vanadate groups (Hsu and Powell, 1975; Venikouas and Powell, 1978). The energy is transferred by exchange interactions between the oxide ions. The average diffusion length of the exciton has been determined to be 9 nm (Powell and Blasse, 1980) which corresponds to about 10 unit cells of  $\text{REVO}_4$ .
- Transfer of the absorbed energy to  $\text{Eu}^{3+}$  ions. During the migration, the exciton may be trapped by a non-radiative recombination center or by a  $\text{Eu}^{3+}$  ion giving rise to luminescence. Energy transfer to the europium ion

is accomplished by exchange interactions between the orbitals of  $V^{5+}$  and  $Eu^{3+}$  mediated by those of the  $O^{2-}$  ions (Blasse, 1966; Mooney and Toma, 1967). Here, the good geometrical overlap of the orbitals and the low energy difference between the emission of vanadate and the  $^5D$  states of europium act favorably for a high transfer rate.

- Luminescence emission. The  $Eu^{3+}$  ions are excited to a  $^5D_J$  state with  $J > 0$ . Non-radiative deexcitation takes place until the state  $^5D_0$  is reached from which the return to a  $^7F$  state is accompanied by luminescence emission. Most intensity is found in the hypersensitive  $^5D_0 - ^7F_2$  transition, for which  $\Delta J = 2$  holds.

Fig. 3.6 depicts an energy level diagram of the above mentioned transitions involved in  $Eu^{3+}$  luminescence.

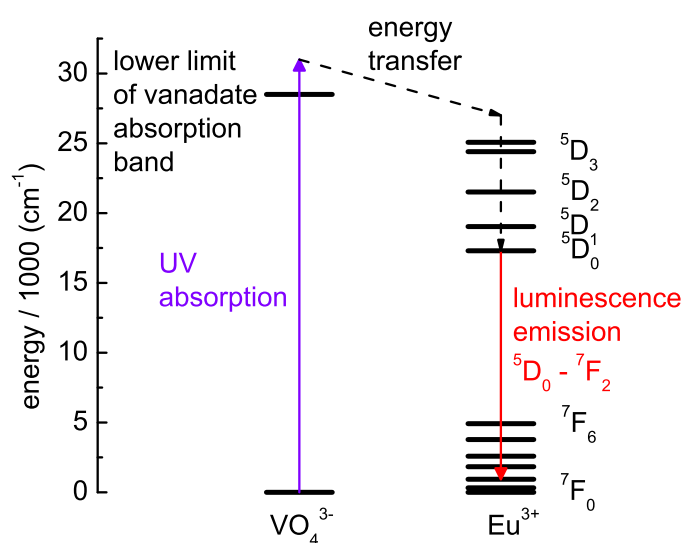


**Figure 3.6: Energy diagram of  $Eu^{3+}$  luminescence in a rare earth vanadate matrix.** The scheme depicts the case of indirect  $Eu^{3+}$  excitation by energy transfer from the vanadate matrix. The lower limit of the vanadate absorption band was estimated to be situated at 350 nm. All  $Eu^{3+}$  energy levels are to scale according to the calculated data from Carnall *et al.* (1989). Radiative transitions are illustrated by solid arrows, non-radiative transitions by broken arrows.

This multi-step excitation-emission process has the advantage to use the strong absorption of the vanadate groups in the UV range to excite the  $Eu^{3+}$  ions. The emission of the latter is stronger than if they were excited directly. However, due to the harmful effect of UV radiation on living organisms, *in vivo* experiments require usually an excitation at 466 nm at the expense of a lower luminescence intensity.

### 3.1.6 Luminescence spectra and quantum yield

We have recorded luminescence excitation and emission spectra for europium-containing nanoparticle dispersions in order to calculate the luminescence quantum

yield. For reasons of conciseness, we here only present and discuss the results. Further theoretical and experimental details can be found in appendix section A.6.2.

### 3.1.6.1 Excitation- and emission spectra

In the present chapter, we will mainly recapitulate the luminescence properties of the well studied material  $\text{Y}_{0.6}\text{Eu}_{0.4}\text{VO}_4$  as it serves as a comparison standard for all other compositions. The luminescence properties of  $\text{Gd}_{0.6}\text{Eu}_{0.4}\text{VO}_4$  samples will be further discussed in section 4.4.3. Fig. 3.7 depicts the excitation and emission spectra for  $\text{Y}_{0.6}\text{Eu}_{0.4}\text{VO}_4$  nanoparticles. The assignment of the peaks shows that

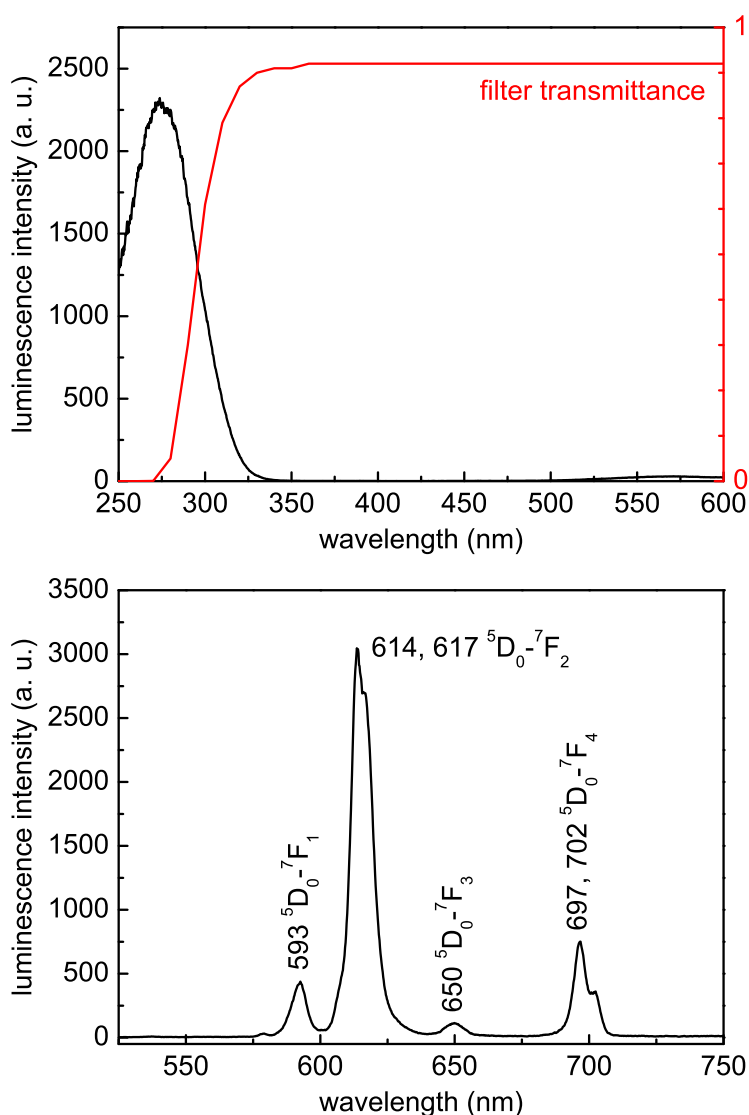


**Figure 3.7: Luminescence excitation and emission spectrum for  $\text{Y}_{0.6}\text{Eu}_{0.4}\text{VO}_4$  nanoparticles.** Data is for sample MS1. Upper graph: Excitation spectrum. Luminescence was recorded at 617 nm. Lower graph: Emission spectrum. Luminescence was excited at 280 nm. The peak positions as well as the corresponding transitions are indicated.

we observe in the nanoparticle dispersion basically the same peaks as for the bulk same (fig. 3.4) with a negligible shift on the order of 1 – 2 nm. As expected, the hypersensitive transition  ${}^5D_0 - {}^7F_2$  gives rise to the most intense peak followed by the second allowed transition  ${}^5D_0 - {}^7F_4$ . The transitions with  $\Delta J = 1$  and 3, forbidden in first order, are more visible than for the bulk material. Peaks are generally broader for the nanoparticles compared to the bulk. The double peak structure for the  ${}^5D_0 - {}^7F_2$  and  ${}^5D_0 - {}^7F_4$  transitions can only be guessed but is not well resolved.

### 3.1.6.2 Luminescence quantum yield

We determined the luminescence quantum yields for nanoparticle syntheses containing europium ions. The results are listed in tab. 3.4. The comparison allows us to

**Table 3.4: Luminescence quantum yields for nanoparticle dispersions.** Sample designations are the same as in tab. 2.2. The designation N indicates that the respective sample carries an APTES surface modification.

composition	sample	$Q$ (%)
$Y_{0.6}Eu_{0.4}VO_4$	MS1	12.4
$Y_{0.6}Eu_{0.4}VO_4/SiO_2$	MS1Si	11.5
$Y_{0.6}Eu_{0.4}VO_4/SiO_2/NH_2$	MS1N	11.4
$Y_{0.6}Eu_{0.4}VO_4$	E110316	18.7
$Y_{0.6}Eu_{0.4}VO_4/SiO_2$	E110316Si	15.5
$Gd_{0.6}Eu_{0.4}VO_4$	MS6R	3.8
$Gd_{0.6}Eu_{0.4}VO_4/SiO_2$	MS19	0.7
$Gd_{0.6}Eu_{0.4}VO_4^{cit}$	MS24	10.1
$Y_{0.6}Eu_{0.4}VO_4/GdVO_4$	MS26	10.3

draw several conclusions. First, the quantum yield of  $Y_{0.6}Eu_{0.4}VO_4$  nanoparticles synthesized by the normal route synthesis reaches values on the order of 10 – 20 %. The range is compatible with the determination uncertainty of 5 %. Second, silica coating of the particles results generally in a slightly reduced quantum yield. A third result concerns the quantum yields of nanoparticles containing europium ions in a gadolinium vanadate matrix where the values of  $Q$  are lower than for europium ions in a yttrium vanadate matrix. A possible explanation is that the  $GdVO_4$  matrix is less efficient than  $YVO_4$  for the energy transfer from the vanadate ions to the europium ions. The quantum yield is further reduced when adding a  $SiO_2$  layer in agreement with what we have found in the case of the composition  $Y_{0.6}Eu_{0.4}VO_4$ . Lastly, we obtain for the core-shell nanoparticles  $Y_{0.6}Eu_{0.4}VO_4/GdVO_4$  (sample MS26) containing a  $Y_{0.6}Eu_{0.4}VO_4$  core, within the error bar, the same quantum yield as for particles made up purely from this material. This value further confirms that the quantum yield is mainly determined by the direct environment of the europium ions and that the actual composition of an outer shell, may be it  $SiO_2$  or  $GdVO_4$ , has only a small influence.

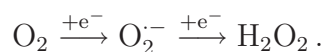
## 3.2 Hydrogen peroxide detection

### 3.2.1 Hydrogen peroxide in living organisms

Reactive oxygen species (ROS) and in particular hydrogen peroxide have for a long time only been seen as non-specific agents of destruction (Gough and Cotter, 2011). However, in the 1970s, it was found that exogenously added hydrogen peroxide is able to mimic the signaling activity of insulin (Czech *et al.*, 1974) and growth factors (Czech, 1976). A bit later, endogenous production of hydrogen peroxide was reported (Mukherjee *et al.*, 1978; Mukherjee and Mukherjee, 1982). Although it became evident that low concentrations of H<sub>2</sub>O<sub>2</sub> provoke cell proliferation (Burdon *et al.*, 1989), early studies usually assumed that ROS were produced accidentally because of the large amount of known ROS-eliminating enzymes (Lambeth, 2004). It was not until the existence of NADPH oxidases (NOX), enzymes whose only biochemical function is producing reactive oxygen species (ROS) and in particular hydrogen peroxide, was discovered in non-phagocytic cells (Suh *et al.*, 1999; Lassègue *et al.*, 2001; Cheng *et al.*, 2001) that the signaling activity of ROS was recognized and the subject was boosted.

#### 3.2.1.1 Hydrogen peroxide as a cellular second messenger

The stepwise reduction of molecular oxygen generates several types of reactive oxygen species (D'Autréaux and Toledano, 2007). Considering the most stable form under physiological conditions, the beginning of the reduction pathway can be written as



Hydrogen peroxide can be further reduced in a Fenton type reaction with metal ions such as Fe<sup>2+</sup> or Cu<sup>+</sup> to yield hydroxyl radicals



where Me<sup>n+</sup> is one of the above cited metals.

Not all of these ROS can act as second messengers. For a molecule to be considered as a second messenger, it needs to have specificity in the interaction with its effectors (Forman *et al.*, 2010). The superoxide radical O<sub>2</sub><sup>·-</sup> is produced by NADPH oxidases (section 3.2.1.2). Dismutases catalyse its dismutation to H<sub>2</sub>O<sub>2</sub> with a rate constant much higher than that for the superoxide-dependent oxidation of biological targets, for example thiols. O<sub>2</sub><sup>·-</sup> is therefore supposed to rather have the role of a precursor of H<sub>2</sub>O<sub>2</sub>. The hydroxyl radical OH<sup>·</sup>, on the other hand, reacts in a diffusion controlled manner with nearly every organic molecule, lacking thus the necessary specificity to be considered as a second messenger. Singlet oxygen can be produced by photochemically activated non-enzymatic reactions. As the site and time specific generation is not ensured, singlet oxygen cannot act as second messenger. In contrast, hydrogen peroxide H<sub>2</sub>O<sub>2</sub> is produced and degraded enzymatically providing spatiotemporel specificity, acts almost selectively on the oxidation of thiol groups, and hence constitutes a potent second messenger.

The cellular effects of the various ROS species can be assessed more quantitatively when considering their concentration and characteristic lifetime (Giorgio *et al.*, 2007). The corresponding data is summarized in tab. 3.5. The comparison

**Table 3.5: Characteristic data for cellular ROS species.**  $T_{1/2}$  is the timespan necessary for degradation of one half of the initial concentration of the specified ROS.  $c$  is the average cellular concentration. Data from Giorgio *et al.* (2007).

ROS species	$T_{1/2}$ (s)	$c$ (M)
$O_2^-$	$10^{-6}$	$10^{-10}$
$H_2O_2$	$10^{-5}$	$10^{-7}$
$OH^\cdot$	$10^{-9}$	$10^{-15}$

shows clearly that  $H_2O_2$  has a longer lifetime and a considerably higher cellular concentration than the other ROS species. We note that the cellular effect of  $H_2O_2$  depends on its concentration. While  $10^{-8} - 10^{-7}$  M hydrogen peroxide act proliferative,  $10^{-6} - 10^{-5}$  M provoke a growth arrest and  $10^{-4}$  M lead to apoptosis (Giorgio *et al.*, 2007). The cellular response to hydrogen peroxide is therefore finely dependent on its concentration, allowing for triggering of different events with one and the same second messenger.

The hydrogen peroxide molecule is polar showing a dipole moment of 2.2 D due to the dihedral angle of  $120^\circ$  and an H–O–O angle of  $95^\circ$  (Meyer *et al.*, 1966). The binding energy of the H–O bond reaches 90 kcal/mol while the central O–O bond is weaker and has only a binding energy of 51 kcal/mol (Kerr, 1966). This central bond can therefore be broken more easily during biological reactions, for example in the Fenton reaction. The standard potential for the reduction to water is  $E^0 = 1.776$  V indicating that  $H_2O_2$  acts as a strong oxidant (Forman *et al.*, 2010). Hydrogen peroxide can also be oxidized to oxygen where the reaction has a standard potential of  $E^0 = 0.682$  V.

### 3.2.1.2 Generation of hydrogen peroxide by NADPH oxidases

Endogenous hydrogen peroxide is generated by NADPH oxidase enzymes (NOX) (Lambeth, 2004) as a response to cellular stimulation with various factors including growth factors (Sundaresan *et al.*, 1995; Bae *et al.*, 1997), cytokines (Groeger *et al.*, 2009) and vasoconstricting peptides such as endothelin 1 (ET-1) (Clempus and Griendling, 2006; Paravicini and Touyz, 2006; Chen *et al.*, 2006). Several isoforms of NOX exist which differ in their domain structure and regulatory properties (fig. 3.8). The best studied form is gp91phox also known as NOX2. NOX1, 3 and 4 have a nearly identical size and structure compared to gp91phox. All enzymes of this class contain six transmembrane  $\alpha$ -helical domains forming a channel which allows for the transport of electrons. The latter are delivered by nicotinamide adenine dinucleotide phosphate (NADPH) and are transferred via flavin adenine dinucleotide (FAD) and two heme groups to molecular oxygen (Lambeth, 2004).

## Figure withdrawn due to copyright restrictions

**Figure 3.8: H<sub>2</sub>O<sub>2</sub> generation by NOX-type transmembrane enzymes.** The enzymes gp91phox/NOX2 as well as NOX1, NOX3 and NOX4 have a similar structure composed of six  $\alpha$ -helical transmembrane domains which enclose 2 heme groups. The latter form a channel allowing electrons to pass the membrane. Molecular oxygen is reduced in a one electron transfer process to a superoxide anion which can react with another superoxide ion and two protons to form hydrogen peroxide on the extracellular side of the membrane. Generated H<sub>2</sub>O<sub>2</sub> can serve as an oxidant for the oxidation of a substrate R in a separate peroxidase (MPO: myeloperoxidase). The C-terminal cytosolic domain contains binding sites for the co-enzymes FAD and NADPH. NOX5 differs from the first mentioned group by presence of an additional N-terminal cytosolic Ca<sup>2+</sup> binding domain. Dual oxidase enzymes (DUOX) contain an integral peroxidase domain. Reprinted by permission from Macmillan Publishers Ltd: D. Lambeth, *Nature Rev. Immunol.*, 4 (3), 181-189. Copyright 2004.

In NOX1, 2, 3 and 5, the generation of hydrogen peroxide relies on a two step mechanism (Gough and Cotter, 2011). First, NADPH is oxidized by the enzyme on the cytosolic side of the membrane and molecular oxygen is reduced across the membrane to form superoxide anions



on the extracellular side of the membrane. Superoxide dismutases (SOD) catalyze the reaction further to hydrogen peroxide



NOX5 has the same core structure as gp91phox but contains additionally an amino-terminal calmodulin-like domain conferring to the enzyme the ability to be regulated by Ca<sup>2+</sup> (Bánfi *et al.*, 2001). In dual oxidase (DUOX) enzymes, an amino-terminal integral peroxidase domain is linked to the calcium-binding domain by an additional transmembrane  $\alpha$ -helix. This domain uses H<sub>2</sub>O<sub>2</sub> to oxidize substrates on the extracellular side of the plasma membrane (Lambeth, 2004). It was found recently that NOX4 does not produce superoxide but directly hydrogen peroxide due to an integral dismutase domain (Takac *et al.*, 2011). New studies have also suggested

that hydrogen peroxide does not diffuse freely through the membrane but that its transmembrane movement is accomplished by aquaporin-3 (Miller *et al.*, 2010). NOX enzymes have also been discovered in a multitude of subcellular compartments like endoplasmic reticulum, nucleus and mitochondria (Gough and Cotter, 2011).

### 3.2.1.3 Regulation of NADPH oxidases

In consideration of the deleterious effect of excessive concentrations of hydrogen peroxide, its production must be carefully controlled. The best studied enzyme concerning the production regulation is gp91phox (Lambeth, 2004). Its short-term regulation is achieved by its subunit structure made up from the membrane-associated catalytic core gp91phox and p22phox, the cytosolic p47phox, p67phox and p40phox subunits as well as the small GTPase RAC. p22phox forms a stabilizing complex with gp91phox and serves as a binding site for p47phox. In the inactive form, p47phox is complexed in the cytosol with p40phox and p67phox and autoinhibited so that the binding site to p22phox is not accessible. RAC-GDP in turn is bound to its inhibitor protein RhoGDP-dissociation inhibitor (RhoGDI). Activation is achieved by multiple triggers resulting in the phosphorylation of the autoinhibitory domain of p47phox allowing its binding to p22phox. A guanine nucleotide exchange factor (GEF) acts on RAC-GDP catalyzing the transition to the form RAC-GTP which can bind to p67phox and the membrane lipids. The architecture of the active complex gp91phox is shown in fig. 3.9. The formation of

Figure withdrawn due  
to copyright restrictions

**Figure 3.9: Architecture of the active gp91phox/NOX2 complex.** For further explanation see text. Reprinted in respect of the Creative Commons License from D. Gough and T. Cotter, *Cell Death Dis.*, 2, e213, 2011.

a complex from several subunits has also been reported for NOX1 but is not clear for NOX3 (Lambeth, 2004). NOX4 is constitutively active and ROS production by this enzyme might be regulated on the expression level. NOX5 and DOUX enzymes in contrast are regulated by  $\text{Ca}^{2+}$ .

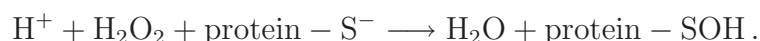
## 3.2.2 Hydrogen-peroxide mediated signaling pathways

Hydrogen peroxide operates as an intracellular signaling molecule but its mode of action is significantly different from that involved in many other signal transduction pathways (D'Autréaux and Toledano, 2007). Classical signal transduction is mainly achieved by non-covalent binding of a ligand to its corresponding receptor where the receptor-ligand interaction is governed by complementarity of the macromolecular shape. Hydrogen peroxide does not possess this ability resulting in the apparent paradox that a reactive molecule which chemically modifies its target is involved in signaling processes requiring specificity. It is nowadays generally admitted that it is less the presence of hydrogen peroxide itself but rather the fluctuations in the cellular redox level which reversibly modulate cellular survival signaling pathways or provoke injury processes and induce cell death (Barford, 2004; Tanner *et al.*, 2011). Fig. 3.10 summarizes the different cellular sites of hydrogen peroxide production and shows the most important targets as well as the enzymes involved in the regulation of the cellular ROS level.

### 3.2.2.1 Switching on the signaling cascade

Signaling pathways originating from low hydrogen peroxide concentrations use three main mechanisms for transduction of survival signals (Gough and Cotter, 2011): inhibition of phosphatases, activation of tyrosine kinases, and activation of transcription factors. Protein tyrosine kinases induce activation of several pathways while phosphatases inactivate them. The inactivation mechanism is well studied for protein tyrosine phosphatases. A cysteine residue in the active center which serves as an acceptor for the phosphate group is oxidized by  $\text{H}_2\text{O}_2$  to sulfenic acid so that it can no longer receive the phosphate group resulting in an inhibition of the activity of the phosphatase (Meng *et al.*, 2002) and an increase of the duration of pro-proliferative signaling. On the other hand, the non-receptor tyrosine kinase Src is oxidized by hydrogen peroxide at two cysteine residues resulting in an activation of its kinase functionality (Giannoni *et al.*, 2008). The mammalian transcription factor NF- $\kappa$ B contains cysteine residues which allow activity modulation through oxidation (Groeger *et al.*, 2009).

The preceding examples show us that the physiological function of the second messenger hydrogen peroxide is defined by the covalent modification of cysteine residues (Cys) by oxidation of the thiol group to sulfenic acid (Forman *et al.*, 2010; Finkel, 2011). This reaction is achieved according to the mechanism of a nucleophilic substitution. The active center of the enzyme first deprotonates the thiol group to a thiolate anion in order to increase its nucleophilicity (Barton *et al.*, 1973). After the nucleophilic attack of the thiolate on the hydrogen peroxide molecule and the transfer of a OH moiety, the poor leaving group  $\text{OH}^-$  is protonated by the enzyme so that finally water as a good leaving group is formed and the reaction becomes favorable in biological conditions:



This reaction constitutes simultaneously the key for the controlled action of  $\text{H}_2\text{O}_2$  within the signaling cascade. Depending on the actual surrounding of the Cys

## Figure withdrawn due to copyright restrictions

**Figure 3.10: The H<sub>2</sub>O<sub>2</sub> cycle inside the cell.** Hydrogen peroxide generating enzymes (shown in purple) are situated in multiple cellular compartments: NADP/H oxidase (NOX) and phagocytic oxidase (PHOX) in the plasma membrane, superoxide dismutase (SOD2), mitochondrial p66<sup>S<sup>hc</sup></sup> (p66) and amine oxidase (AO) in mitochondria, peroxisomal oxidase (POX) in peroxisomes, sulphhydryl oxidase (SOX) in the endoplasmatic reticulum, amion-acid oxidase (AAO), cyclooxygenase (COX), lipid oxygenase (LOX), xanthine oxidase (XO) and superoxide dismutase (SOD1) in the cytosol. Regulating enzymes (shown in green) like catalases (CAT) and glutathione peroxidases (GPX) control the hydrogen peroxide level. Targets of hydrogen peroxide including the mitochondrial permeability transition pore (PTP) and transcription factors like the nuclear factor  $\kappa$ B (NF $\kappa$ B) and the hypoxia inducible factor 1 $\alpha$  (HIF $\alpha$ ) are shown in blue. Broken arrows indicate the possible diffusion of cytoplasmic hydrogen peroxide in the nucleus. Reprinted by permission from Macmillan Publishers Ltd: M. Giorgio *et al.*, *Nature Rev. Mol. Cell Biol.*, 8 (9), 722-728. Copyright 2007.

residue defined by the oxidizing enzyme and the substrate itself, the Cys reactivity can change by a factor of 10<sup>6</sup> (D'Autréaux and Toledano, 2007). This enormous range provides the signal selectivity and specificity in response to a given hydrogen peroxide concentration. Additionally, the possibility to alter reversibly the redox states of Cys makes it an exquisite target of hydrogen peroxide signaling.

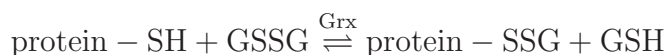
### 3.2.2.2 Switching off the signaling cascade

Cysteine oxidation is in principle not limited to the first two-electron process yielding sulfenic acid; higher oxidation products such as sulfinic and sulfonic acid are

theoretically possible (Forman *et al.*, 2010). However, after reaching the oxidation state of sulfenic acid, several processes compete with further oxidation. In the cell, these processes have the task to avoid non-reversible higher oxidation states, to limit the hydrogen peroxide induced signaling and to return the signaling components to their non-activated ground state. One major switch off mechanism consists in the formation of disulfide linkages between proteins oxidized to the sulfenic acid state and other Cys-carrying proteins. Disulfide formation can be achieved by glutathionylation that is the reaction with glutathion (GSH) according to the scheme



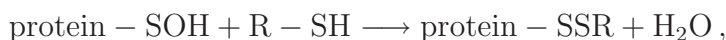
The same arguments given for the Cys oxidation reaction (section 3.2.2.1) hold for the nucleophilicity increase of the cysteine group of GSH by deprotonation to thiolate. We note that glutathionylation is also possible by reaction of the reduced cysteine group in the protein with disulfide-linked GSSG under catalysis by glutaredoxin (Grx):



GSSG in turn is produced in a hydrogen peroxide dependent mechanism catalyzed by glutathion peroxidase (Gpx) according to



Disulfide linkage must not necessarily occur between the protein and another low molecular weight substance but can also be performed in the protein carrying the sulfenic acid group itself. An exemple is the bacterial transcriptional regulator OxyR which stimulates the transcription of genes conferring resistance to oxidative stress by interaction with RNA polymerase (Zheng *et al.*, 2001). The cysteine sulfenic acid formed initially in the protein reacts with another distant cysteine in the same protein



resulting in the formation of a disulfide linkage and a major conformational change (fig. 3.11) which enables site-specific binding to a DNA promotor region (Choi *et al.*, 2001; Kim *et al.*, 2002). In the above equation, we have written protein and R as the second thiol may in the general case be provided by any other Cys-carrying molecule yielding an intermolecular disulfide. The return of a disulfide-linked protein to its

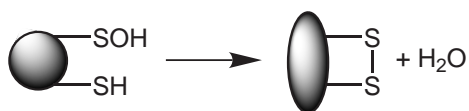
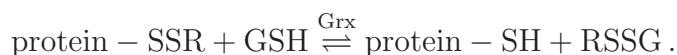


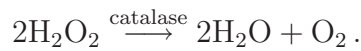
**Figure 3.11: Conformational change induced by intramolecular disulfide linkage.**

ground state is performed by a Grx-catalyzed thiol-disulfide exchange.

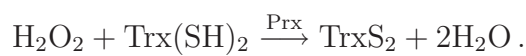


In the special case of OxyR, R corresponds to protein and complete reduction requires a second reaction with GSH.

Regulation of the cellular response to hydrogen peroxide is also possible by acting directly on its concentration. There exists a complex interplay of several antioxidant systems which protect the cell against damage by irreversible oxidation of cellular macromolecules caused by excessive hydrogen peroxide (Gough and Cotter, 2011). Besides the action of glutathion peroxidase, the enzyme catalase catalyzes the disproportionation of hydrogen peroxide to water and oxygen



Peroxiredoxins constitute another cellular system which catalyzes the oxidation of thioredoxin (Trx), a reaction consuming hydrogen peroxide



### 3.2.2.3 Hydrogen peroxide regulation of growth, proliferation and apoptosis

In this section, we will discuss the interplay between different hydrogen peroxide dependent signal transducers for the regulation of growth and proliferation as well as apoptosis for the well studied example of endothelial cells (fig. 3.12). The complex

Figure withdrawn due  
to copyright restrictions

**Figure 3.12: H<sub>2</sub>O<sub>2</sub> mediated signaling pathways in endothelial cells.** For further explanation see text. Reprinted by permission of Oxford University Press. H. Cai, *Cardiovasc. Res.*, 68 (1), 26-36. Copyright 2005.

regulatory system in this cell line was reviewed by Cai (2005). Endothelial cells contain NOX4 in a more abundantly expressed amount than other NOX isoforms.

Interestingly, NOX4 acts in a growth suppressive manner while NOX1 mediates growth signaling. The observation of a different effect of ROS produced by different NOX isoforms was also made in smooth muscle cells and explained by a distinct subcellular localization of the different NOX isoforms. NOX1 activation is achieved by binding of vascular endothelial growth factor (VEGF) to its corresponding receptor named fetal liver kinase 1/kinase insert domain receptor (Flk1/KDR) also known as VEGF receptor 2 (VEGFR-2), a receptor tyrosine kinase. The active receptor activates NOX by a mechanism not yet fully elucidated. We note that cyclic strain may also activate NOX enzymes. In both cases, superoxide and subsequently hydrogen peroxide is generated that can diffuse inside the cell. There,  $\text{H}_2\text{O}_2$  activates protein kinases such as p38 mitogen-activated protein kinase (p38 MAPK), extracellular signal-regulated kinase 1 and 2 (ERK1/2), protein kinase C (PKC) as well as the nuclear factor  $\text{NF}\kappa\text{B}$  and the eukaryotic translation initiation factor 4E (eIF4E). Downstream effectors activated by ERK1/2 include the transcription factor early growth response protein 1 (Egr-1) and the p90 ribosomal S6 kinase (p90RSK) which mediate cell proliferation and growth.  $\text{H}_2\text{O}_2$  also upregulates the expression of VEGF in a feed-forward mechanism by activation of PKC and  $\text{NF}\kappa\text{B}$ . High concentrations of  $\text{H}_2\text{O}_2$  above 200  $\mu\text{M}$  induce cell apoptosis by activation of c-Jun N-terminal kinase (JNK) together with the proto-oncogene tyrosine-protein kinase Src-dependent activation of the epidermal growth factor receptor (EGFR) and by upregulation of Fas. Hydrogen peroxide concentrations in this range increase also transferrin receptor (TfR)-dependent intracellular iron uptake and induce DNA damage in mitochondria, both triggering apoptosis. Hydrogen peroxide-induced apoptosis is inhibited by unidirectional shear stress which decreases the activity of JNK and increases reduction of oxidized proteins by enhancing the activity of glutathione reductase.

### 3.2.3 Techniques for the measurement of hydrogen peroxide

The measurement of hydrogen peroxide is feasible by a multitude of techniques. Nonreversible molecular probes, reversible systems based on various design principles and our  $\text{Y}_{0.6}\text{Eu}_{0.4}\text{VO}_4$  nanoparticles can be used for this task which is essential for elucidation of signal transduction pathways. The domain was recently comprehensively reviewed by Schäferling *et al.* (2011) and Chen *et al.* (2011). We will discuss some exemplary systems together with their characteristic advantages and drawbacks in the following.

#### 3.2.3.1 Nonreversible molecular probes

The best studied probes for hydrogen peroxide detection are modified fluorescent dyes which are in a non-fluorescent state when added to the system in which the measurement will be carried out. By reaction with  $\text{H}_2\text{O}_2$ , the molecule is transformed into the fluorescent state allowing for its detection. Numerous dyes with different activation mechanisms are currently available. All these systems are characterized by the property that a return to the initial state of the probe is not possible.

Amplex Red (*N*-acetyl-3,7-dihydroxy-phenoxazin) is a non-fluorescent molecule which is converted enzymatically by peroxidases to the red fluorescent dye resorufin (fig. 3.13, Zhou *et al.* (1997)). The system has a low detection limit of 50 nM H<sub>2</sub>O<sub>2</sub>

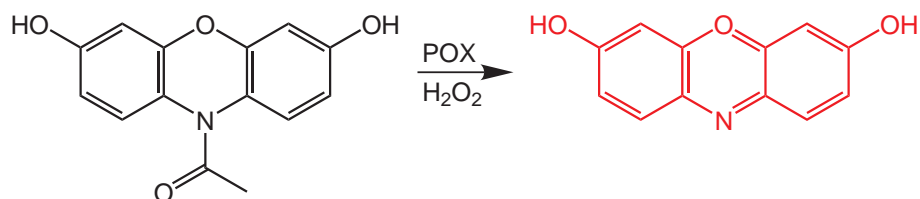


**Figure 3.13: Hydrogen peroxide detection using Amplex Red.** Amplex Red is oxidized to the red fluorescent dye resorufin in the presence of hydrogen peroxide and peroxidases (POX).

but demands the presence of peroxidase enzymes whose activity can be strongly influenced by the biological environment. A similar mechanism (Ohashi *et al.*, 2002) is found for the oxidation of dihydro-rhodamin 123 by hydrogen peroxide under POX catalysis (reaction not shown).

Acetylated 2',7'-dichloro-dihydrofluorescein is lipophilic and can pass the cell membrane. Upon arrival in the cell, endogenous esterases cleave the ester group and the resulting molecule can be oxidized by hydrogen peroxide to the intensely green fluorescent dye 2',7'-dichlorofluorescein (fig. 3.14, Brandt and Keston (1965); LeBel *et al.* (1992)). We note that the oxidation of the dihydrofluorescein derivative

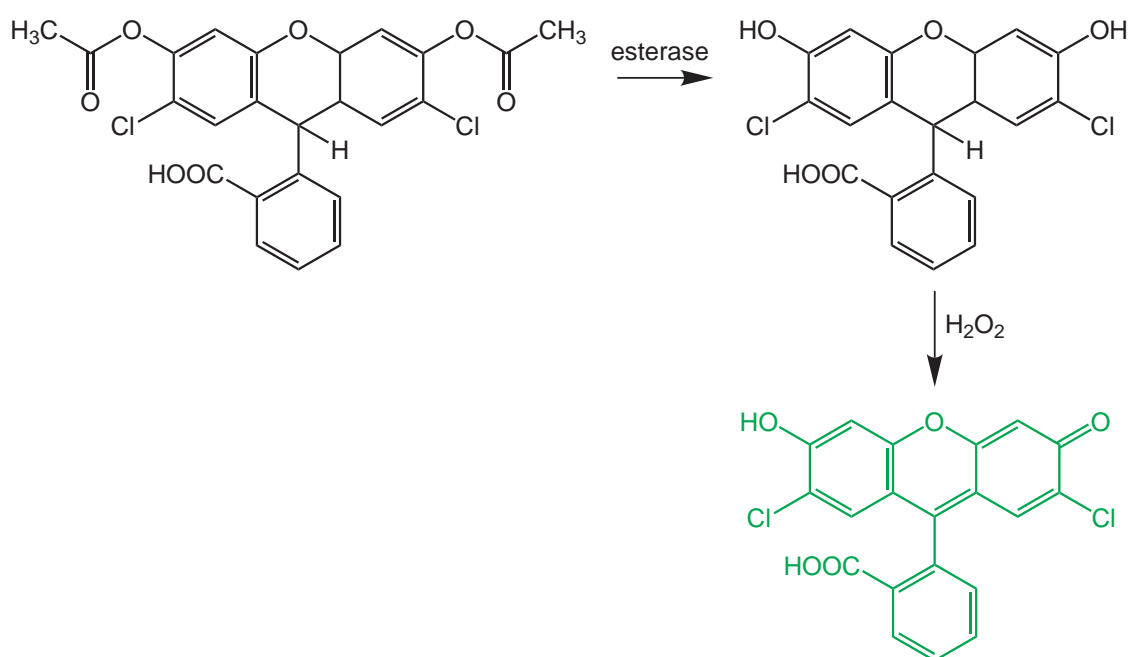


**Figure 3.14: Hydrogen peroxide detection using dichloro-dihydrofluorescein.** Esterases cleave the acetyl groups of the precursor after its passage across the cell membrane to yield 2',7'-dichloro-dihydrofluorescein which is oxidized by hydrogen peroxide to the fluorescent dye 2',7'-dichlorofluorescein.

does not require peroxidases but their presence significantly increases the response to hydrogen peroxide. The oxidation can also be performed by hydroxyl radicals, nitric oxide and peroxyxynitrite. A disadvantage resides in the autooxidation of the dihydrofluorescein derivative due to the excitation light.

Problems with enzyme-linked assays can be circumvented by using cleavable fluorescence quenching groups. Cyclic boronate groups in 3' and 6' position of fluorescein induce the formation of an efficiently quenched lactone structure (fig. 3.15, Miller and Chang (2007); Zhao (2009)). The boronate groups can be hydrolytically

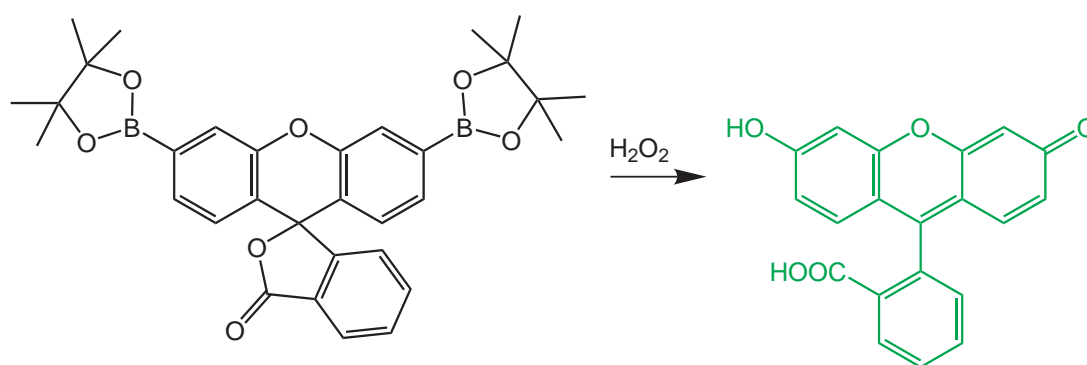


**Figure 3.15: Hydrogen peroxide detection by deprotection of a fluorescein boronate derivative.**  
 $\text{H}_2\text{O}_2$  induced deprotection of 3',6'-bis(pinacolatoboron)fluoran yields the fluorescent dye fluorescein.

removed in the presence of hydrogen peroxide but without the implication of peroxidases resulting in ring opening of the lactone and a 1000-fold increase in the fluorescence intensity. The selectivity of this probe for  $\text{H}_2\text{O}_2$  is more than 500 times higher than for other ROS, NO and hypochlorite.

The selective hydrolysis of boronates is also exploited in the non-fluorescent protected coumarin derivative shown in fig. 3.16 (Lo and Chu, 2003). Boronate

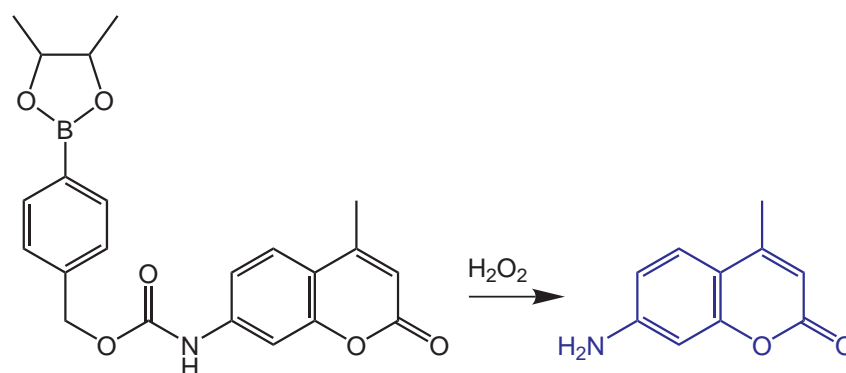


**Figure 3.16: Hydrogen peroxide detection by deprotection of a coumarin boronate derivative.**  
 The protective group *p*-dihydroxyborylcarboxybenzyl is cleaved by hydrogen peroxide to yield the fluorescent dye aminocoumarin.

perhydrolysis results in a spontaneous deprotection of the aminocoumarin which

becomes hereby fluorescent. A linear correlation was found between the fluorescence and the hydrogen peroxide concentration in the range 0.1 – 5.0  $\mu\text{M}$ .

A similar mechanism applies to the fluorescein sulfonic ester derivative shown in fig. 3.17 (Maeda *et al.*, 2004). The perfluorobenzenesulfonate protection group

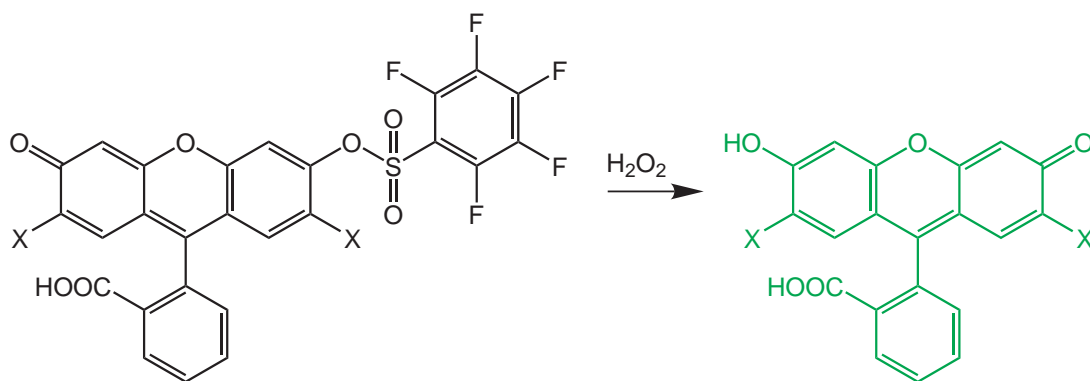


**Figure 3.17: Hydrogen peroxide detection by deprotection of a fluorescein sulfonate derivative.**  
Hydrogen peroxide induces the perhydrolysis of 2',7'-dichlorofluorescein pentafluoro-benzenesulfonate to a fluorescent fluorescein derivative.

is cleaved in a non-oxidative and non-enzymatic perhydrolysis reaction depending on the concentration of hydrogen peroxide. The compounds have detection limits between 5 pM and 230 pM H<sub>2</sub>O<sub>2</sub> depending on the temperature and the type of the substituent X. Although the perhydrolysis is strongly pH-dependent, this reaction proceeds generally slowly.

Another design principle for hydrogen detecting probes relies on photoinduced electron transfer (PIET). This mechanism occurs generally between a PIET donor and an excited fluorophore as acceptor, quenching the fluorescence of the latter. Diphenylphosphine groups (fig. 3.18) are effective electron donors which can quench the fluorescence of a coumarin moiety (Soh *et al.*, 2005). Hydrogen peroxide dependent oxidation of the diphenylphosphine group yields the only poorly electron donating diphenylphosphine oxide group resulting in an about 100-fold increase of the coumarin fluorescence. The system has a dynamic range of 0 – 20  $\mu\text{M}$  H<sub>2</sub>O<sub>2</sub> but superoxide anions and nitric oxide have a similar effect.

A ratiometric hydrogen peroxide sensor can be constructed by the combination of a coumarin moiety and a boronate protected and in the lacton structure existing non-fluorescent fluorescein moiety (fig. 3.19, Albers *et al.* (2006)). In the absence of H<sub>2</sub>O<sub>2</sub>, only blue emission from coumarin is observed. Upon perhydrolysis of the boronate groups and lacton ring opening, fluorescence resonance energy transfer (FRET) becomes possible between coumarin as donor and fluorescein as acceptor resulting in a change of the emission to green. Measurement of the blue to green emission ratio allows for detection of hydrogen peroxide with high selectivity over other ROS.

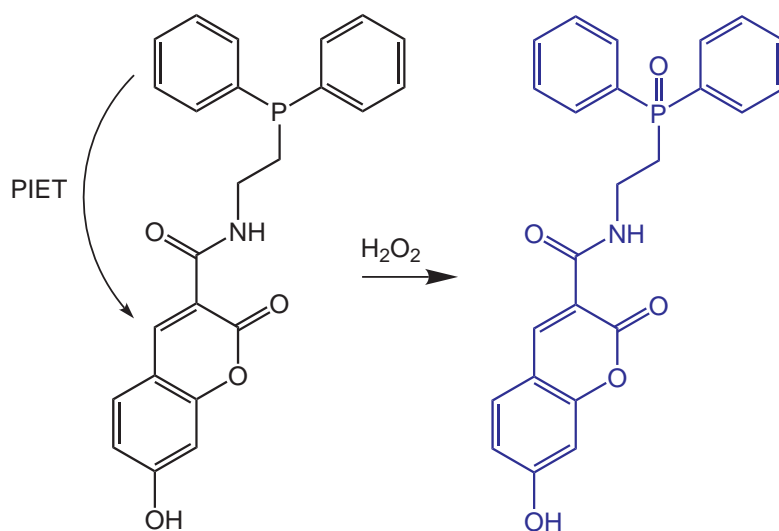


**Figure 3.18: Hydrogen peroxide detection by photoinduced electron transfer.** A change in the ability to perform photoinduced electron transfer (PIET) after oxidation of a coumarin derivative increases its fluorescence.

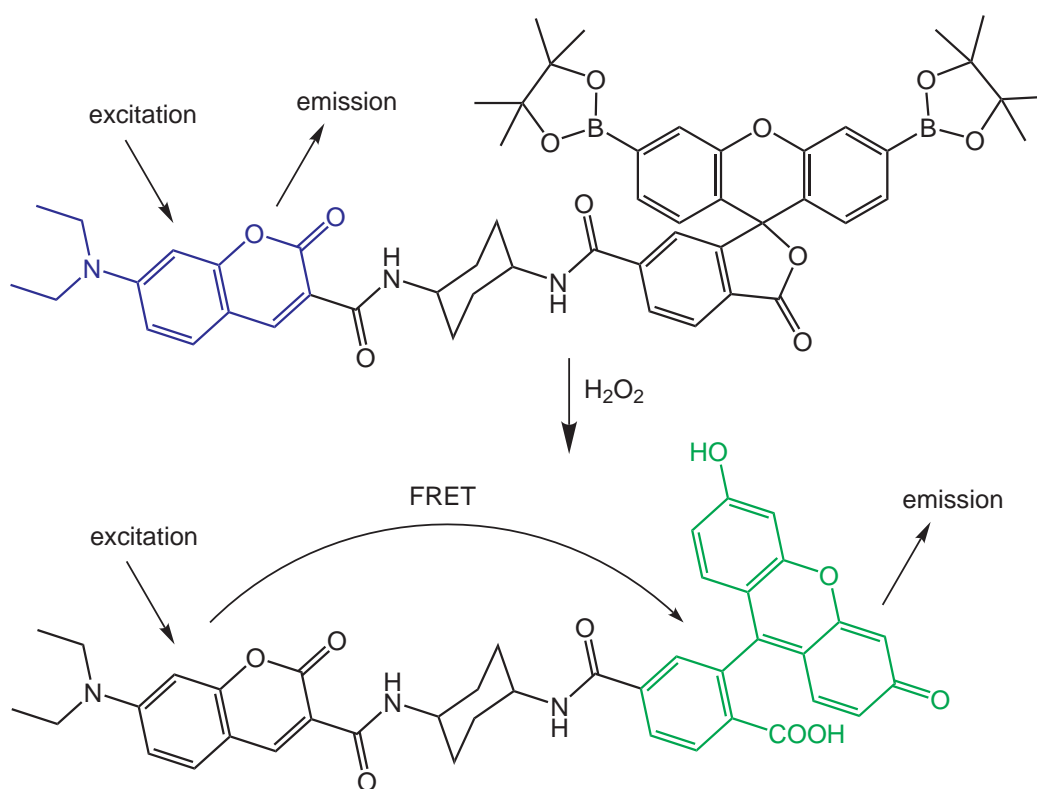


**Figure 3.19: Hydrogen peroxide detection by emission wavelength shift.** Hydrogen peroxide induced cleavage in the fluorescein derivative enables FRET and shifts the emission from that of coumarin to fluorescein.

### 3.2.3.2 Reversible probes

All the presented probes in section 3.2.3.1 allow only for detection of the maximal cumulated hydrogen peroxide concentration as irreversible reactions take place in the fluorophore. A cellular signaling event involving a decrease in the  $\text{H}_2\text{O}_2$  concentration after an initial burst cannot be detected as the induced probe fluorescence will be conserved. Several systems with different design strategies allowing to deal with this problem have been developed.

The fluorescent fluorescein derivative redoxfluor-1 can be transferred into its reduced form by mild reductants accompanied by a decrease in the fluorescence intensity of a factor of more than 50 (fig. 3.20, Miller *et al.* (2007)). Loading of

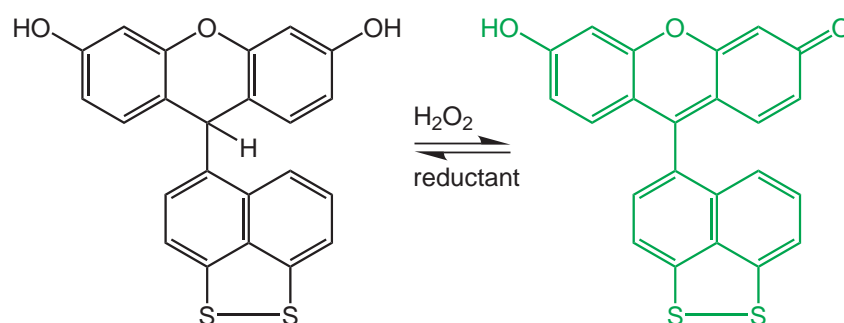


**Figure 3.20: Reversible molecular probe for hydrogen peroxide detection.** Hydrogen peroxide induces oxidation of the fluorescein derivative to redoxfluor-1 accompanied by a strong fluorescence increase.

cells with the acetomethylester derivative of reduced redoxfluor-1 as a membrane-permeable form and incubating the cells with  $\text{H}_2\text{O}_2$  results in an fluorescence increase. The fluorescence vanishes after several minutes due to the reductive cellular environment. Multiple oxidation-reduction cycles have been demonstrated. We note, however, that the authors do not give data on the toxicity of this polycyclic aromatic compound.

Another design principle relies on the luminescence of europium ions. A complex between  $\text{Eu}^{3+}$  and tetracycline increases 15-fold its luminescence after addition of hydrogen peroxide (fig. 3.21, Wolfbeis *et al.* (2002)). Although the crystal structure

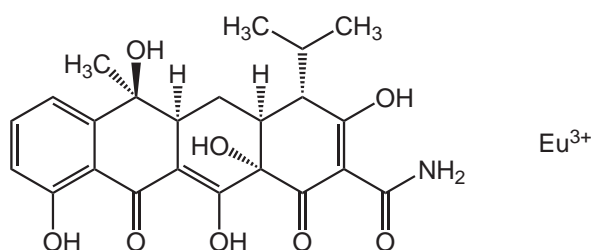


**Figure 3.21: Europium complex for reversible hydrogen peroxide detection.** The binding of hydrogen peroxide to a  $\text{Eu}^{3+}$ -tetracyclin complex increases strongly its luminescence.

has not been determined, the authors suppose that the hydrogen peroxide molecule occupies the ninth coordination site of the  $\text{Eu}^{3+}$  ion. The dynamic range of the sensor was given to be  $2 - 400 \mu\text{M H}_2\text{O}_2$ . However, an *in vivo* application seems not to be feasible as also other physiological molecules may occupy the ninth coordination site and the stability of the compound respective to the transmetallation with endogenous divalent cations is not guaranteed. In fact, studies have shown that tetracyclines are good chelators of ions such as  $\text{Ca}^{2+}$  and  $\text{Mg}^{2+}$  (Ohyama and Cowan, 1995) and their potential binding may release toxic free  $\text{Eu}^{3+}$  ions. Another problem may arise from the action of tetracycline as a broad spectrum antibiotic.

Fluorescent proteins have also been used as reversible hydrogen peroxide sensors. A circularly permuted yellow fluorescent protein (cpYFP) was inserted in the regulatory domain of the procaryotic  $\text{H}_2\text{O}_2$ -sensitive transcriptional regulator OxyR (section 3.2.2.2) to yield the redox-sensitive protein HyPer (fig. 3.22, Belousov *et al.* (2006)). Hydrogen-peroxide induced intra-molecular disulfide linkage induces a

Figure withdrawn due  
to copyright restrictions

**Figure 3.22: Reversible hydrogen peroxide detection using HyPer.** Fluorescence emission is observed after a conformational change in cpYFP due to hydrogen peroxide dependent disulfide-linkage of the adjacent OxyR regulatory domains (RD). N and C stand for amino- and carboxy-terminus, respectively. With kind permission from Springer Science + Business Media: M. Schäferling *et al.*, Luminescent probes for detection and imaging of hydrogen peroxide, *Microchim. Acta* 174 (1), 1-18. Copyright 2011.

conformation change which in turn increases strongly the fluorescence of cpYFP. The signal is switched off by glutaredoxin-mediated reductive cleavage of the disulfide linkage. Although HyPer is highly selective for  $\text{H}_2\text{O}_2$ , already concentrations of  $250 \text{ nM}$  produce a complete oxidation of the protein so that this system is too sensitive for most measurements. An other drawback in routine applications is that this sensor protein must be genetically encoded in the target organism and is not a ready-to-use probe.

Another system for hydrogen peroxide detection on the single molecule level using single-walled carbon nanotubes (SWNT) was recently reported (Jin *et al.*, 2010). The binding of hydrogen peroxide molecules to SWNT results in a quenching of excitons observable as a change in the fluorescence intensity under near infrared illumination. However, hydrogen peroxide detection has up to now only been demonstrated for cells lying on the sensor but not for an intracellular application of the SWNT. A further disadvantage resides in the fact that although the sensor is sensible on the single molecule level, the assessment of the spatio-temporal  $\text{H}_2\text{O}_2$  production in a cell requires the analysis of many SWNT and long observation times.

### 3.2.3.3 Europium-doped inorganic nanoparticles

Although the detection systems presented in section 3.2.3.2 feature reversibility in contrast to the systems based on a simple activation of a fluorophore, several drawbacks still remain. These can at least partially be overcome using europium-doped yttrium vanadate nanoparticles which measure hydrogen peroxide inside cells with spatio-temporal resolution (Casanova *et al.*, 2009). The system allows a quantitative detection of  $\text{H}_2\text{O}_2$  in the concentration range 1 – 50  $\mu\text{M}$  which is precisely the range of interest for signaling (tab. 3.5). This application relies on the facile and reversible reduction of  $\text{Eu}^{3+}$  ions contained in the nanoparticles to the  $\text{Eu}^{2+}$  state. While  $\text{Eu}^{3+}$  ions show narrow absorption and emission peaks due to the crystal field induced and only weakly allowed electric dipole  $4f^6 - 4f^6$  intra-configuration transitions (section 3.1.3.2 and fig. 3.4),  $\text{Eu}^{2+}$  ions exhibit broad absorption and emission bands corresponding to the electric dipole allowed  $4f^65d^1 - 4f^7$  inter-configuration transitions (Dorenbos, 2003). It has been shown previously in our laboratory, that prolonged illumination of the  $\text{Eu}^{3+}$ -containing nanoparticles with high intensity laser radiation results in a luminescence decrease at 617 nm. Fig. 3.23 shows the excitation and emission spectra of densely spincoated nanoparticles on a coverslip before and after photoreduction. The broad absorption and emission bands which are visible after photoreduction correspond to the spectra of  $\text{Eu}^{2+}$ . In contrast, no absorption or emission is detected in this wavelength range before photoreduction in agreement with the spectra of  $\text{Eu}^{3+}$  ions.

$\text{Eu}^{2+}$  ions can be reoxidized to the initial  $\text{Eu}^{3+}$  state by various oxidants. Intracellularly available oxidants which have been shown to perform this oxidation process include hydrogen peroxide, hypochlorite  $\text{ClO}^-$ ,  $\text{O}_2^-$  and NO (Casanova *et al.*, 2009). However, due to the low concentrations and stabilities of the latter three compounds, their effect is negligible compared to the action of hydrogen peroxide. Reoxidation experiments on spincoated nanoparticles were therefore executed using hydrogen peroxide as oxidant (fig. 3.24). Several conclusions have been drawn from the results (Casanova, 2008; Nguyễn, 2009):

- The photoreduction kinetics is multiexponential and can be fitted best with a Becquerel function. The reasons for this non-monoexponential behavior lie presumably in the involvement of crystal defects in the photoreduction reaction.
- Photobleaching necessitates resonant excitation of the europium ions.

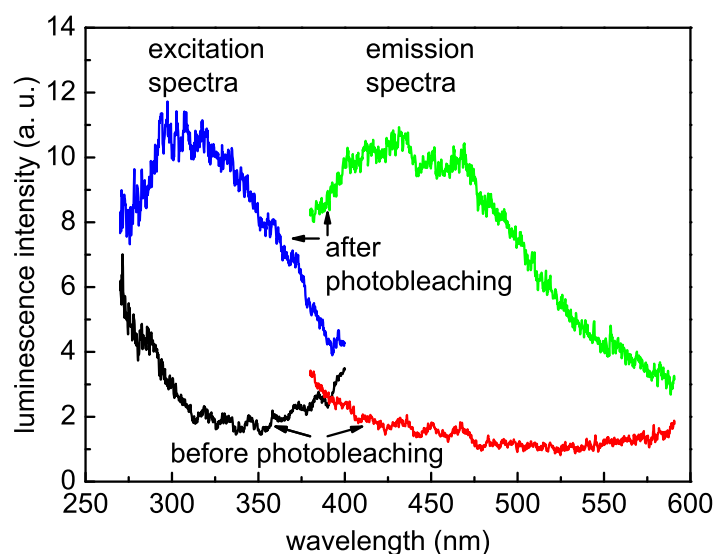


**Figure 3.23: Excitation and emission spectra of  $Y_{0.6}Eu_{0.4}VO_4$  nanoparticles before and after photoreduction.** The black and red lines are for the nanoparticles before photoreduction and the blue and green lines are for the same nanoparticles after photoreduction at  $3 - 5 \text{ kW/cm}^2$  for 30 s. The black and blue lines constitute the excitation spectra (emission recorded at 425 nm) whereas the red and green lines the emission spectra (excitation at 310 nm). Data obtained previously in our laboratory and published in Casanova *et al.* (2009).

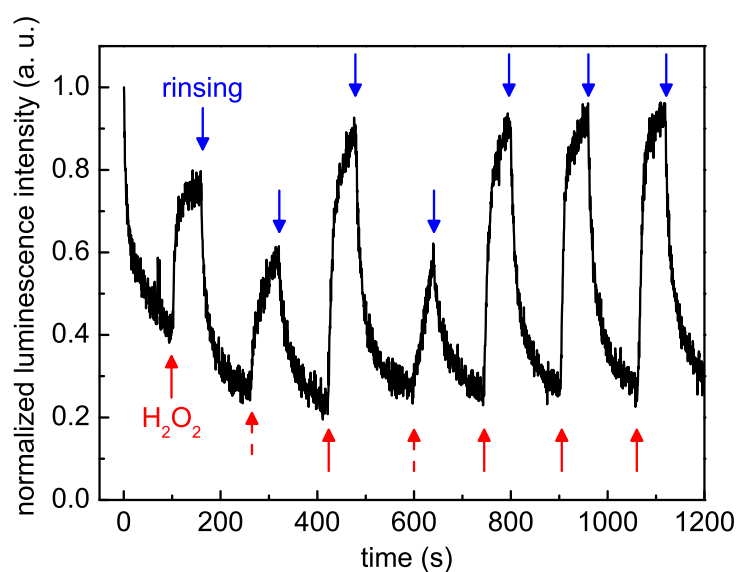


**Figure 3.24: Cyclic photoreduction and reoxidation of a single  $Y_{0.6}Eu_{0.4}VO_4$  nanoparticle.** Red arrows indicate addition of hydrogen peroxide (solid arrows 10 mM, broken arrows 5 mM) while blue arrows stand for rinsing. Acquisition was interrupted at the end of each cycle for rinsing the coverslip several times with phosphate buffer at pH 7.4. Excitation at 466 nm with an intensity of  $5 \text{ kW/cm}^2$ . Acquisition at  $617 \pm 4 \text{ nm}$  with an integration time per data point of 0.5 s. Data obtained previously in our laboratory and published in Casanova *et al.* (2009).

- Reoxidation and luminescence recovery do not take place spontaneously, at least on a time scale of 20 min.
- The amount of luminescence recovery is a function of the added hydrogen peroxide concentration.
- Luminescence recovery is accelerated by illumination of the nanoparticles. In contrast to the photoreduction, a resonant excitation is not necessary.
- Multiple cycles of photoreduction and reoxidation are possible without alteration of the dynamic parameters of the sensor.
- The measured value of luminescence recovery results from an equilibrium between photoreduction by the illumination used for the measurement and the oxidizing action of hydrogen peroxide.

The finding that multiple cycles of photoreduction and chemical reoxidation by  $\text{H}_2\text{O}_2$  can be performed, confirms that  $\text{Y}_{0.6}\text{Eu}_{0.4}\text{VO}_4$  nanoparticles can be used as a hydrogen peroxide sensor. Calibration measurements with various hydrogen peroxide concentrations (fig. 3.25) have shown that this sensor allows for quantitative detection of the oxidant. Moreover, the response represented by the normalized luminescence recovery factor in the steady state region for long

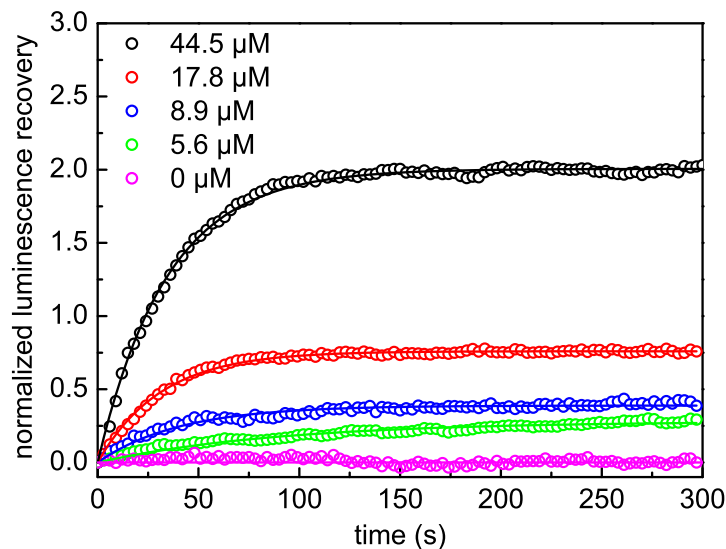


**Figure 3.25: Concentration-dependent luminescence recovery of  $\text{Y}_{0.6}\text{Eu}_{0.4}\text{VO}_4$  nanoparticles.**

Luminescence recovery was measured for several hydrogen peroxide concentrations as a function of time. The displayed data is the average of the analysis of about 20 individual spincoated nanoparticles. Black lines are fits according to the exponential  $\Delta S/S_0 = A(c) \cdot \left[1 - \exp\left(-\frac{t}{\tau(c)}\right)\right]$ , where  $\Delta S/S_0$  is the fluorescence recovery normalized to the initial value,  $A(c)$  and  $\tau(c)$  the  $\text{H}_2\text{O}_2$  concentration dependent maximum luminescence recovery and the characteristic recovery time, respectively. Excitation at 466 nm with an intensity of  $5 \text{ kW/cm}^2$ . Acquisition at  $617 \pm 4 \text{ nm}$  with an integration time per data point 0.5 s. Data obtained previously in our laboratory and published in Casanova *et al.* (2009).

observation times is directly proportional to the hydrogen peroxide concentration in a range 1 – 45  $\mu\text{M}$ . In this concentration range, the response of the sensor is additive meaning that the stepwise addition of a concentration  $c_1$  and then  $c_2$  has the same effect as adding directly the concentration  $c_1 + c_2$ . We note that within the linearity range, it is not necessary to wait until a steady state luminescence level is reached. By acquiring the luminescence intensity and calculating the derivative of this signal, it is possible to obtain unambiguously the actual hydrogen peroxide concentration with a time resolution of about 10 – 30 s (Casanova *et al.*, 2009). The application range of the sensor can be increased by varying the intensity of the incident laser beam. As the measured intensity depends on the ratio of photoreduction to hydrogen peroxide-dependent recovery, a low laser intensity allows the measurement of low  $\text{H}_2\text{O}_2$  concentrations. On the other hand, using high laser intensities extends the detection range in the mM region.

### 3.2.4 Experimental protocol

#### 3.2.4.1 Luminescence microscopy setup

Nanoparticle observation relies on the excitation of the  ${}^7\text{F}_{0,1} - {}^5\text{D}_2$  transition at 466 nm and the detection of the  ${}^5\text{D}_0 - {}^7\text{F}_2$  transition composed of two lines at 614 nm and 617 nm (sections 3.1.5 and 3.1.6.1). The extinction coefficient of the  ${}^7\text{F}_{0,1} - {}^5\text{D}_2$  transition is about  $24,000 \text{ M}^{-1}\text{cm}^{-1}$  for  $\text{Y}_{0.6}\text{Eu}_{0.4}\text{VO}_4$  nanoparticles of 30 nm diameter which allows for individual nanoparticle detection (Casanova *et al.*, 2009).

Nanoparticle imaging is carried out on an Axiovert S100TV inverted microscope (Carl Zeiss MicroImaging) under wide-field illumination by an Innova 300 argon ion laser (Coherent) at 466 nm. A lens with 15 cm focal distance is placed in the excitation path generating a convergent beam at the aperture of the objective and allowing for the illumination of a larger zone of the coverslip. The morphology of VSMC is verified under white light illumination by an Hal 100 lamp (Zeiss) and using either bright field or differential interference contrast detection. Nanoparticle luminescence is collected by an Apochromat 63 $\times$  1.40 numerical aperture oil immersion objective (Zeiss) and selected by a 500DCLP dichroic mirror (Chroma Technology) and a D617/8m bandpass filter (FWHM 8 nm, Chroma). Image acquisition is performed by a QuantEM 512SC CCD camera (Photometrics) with  $512 \times 512$  pixels of  $16 \mu\text{m} \times 16 \mu\text{m}$  individual size and a maximum repetition rate of 31.5 frames per s. Raw data is treated and visualized with the software MetaVue (Molecular Devices). The setup is depicted schematically in fig. 3.26.

#### 3.2.4.2 Sample preparation for nanoparticle observation

Nanoparticles are first selected in size by centrifugation to eliminate too small particles and aggregates, respectively. The obtained dispersion is deposited on cleaned silica coverslips and observations are carried out in phosphate buffer. The latter is prepared from dipotassium hydrogenphosphate ( $\text{K}_2\text{HPO}_4$ ,  $M_W = 174.18 \text{ g/mol}$ , Merck) and potassium dihydrogen phosphate ( $\text{KH}_2\text{PO}_4$ ,  $M_W =$

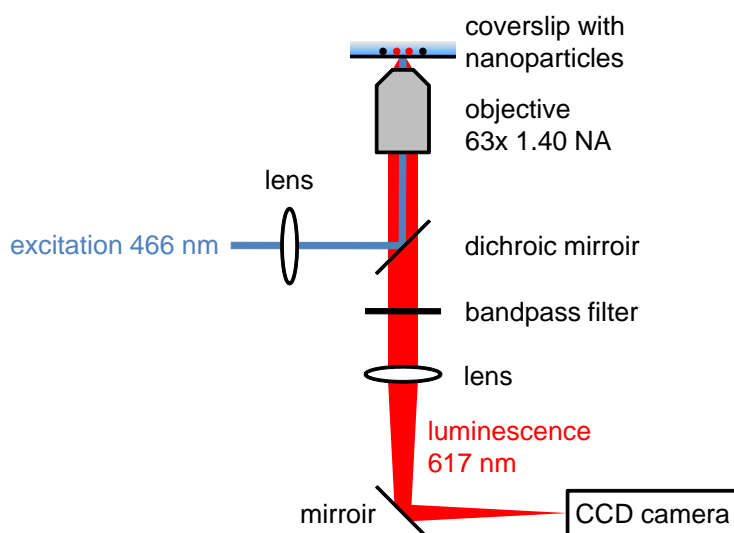


**Figure 3.26: Luminescence microscopy setup.** For further explanation see text.

136.09 g/mol, Merck). From the two salts, stock solutions with 1 M concentration are prepared by dissolving 17.4 g  $\text{K}_2\text{HPO}_4$  and 13.6 g  $\text{KH}_2\text{PO}_4$  in 100 mL ultrapure water, respectively. For a buffer at pH 7.4 with an ionic strength of 50 mM, 40 mL 1 M  $\text{K}_2\text{HPO}_4$  and 10 mL 1 M  $\text{KH}_2\text{PO}_4$  solution are combined and diluted to 1 l. The pH of the buffer solution is measured with a pH meter and adjusted if necessary by adding some drops of either 1 M HCl or 1 M NaOH to reach 7.4.

Prior to each microscopy experiment, nanoparticles are selected in size. For this, 25  $\mu\text{l}$  of the nanoparticle stock solution with a vanadate concentration on the order of 10 mM are placed in a 1.5 mL Eppendorf<sup>®</sup> tube and diluted with 175  $\mu\text{l}$  phosphate buffer (50 mM, pH 7.4). The dilution is sonicated three times for 5 s at 90 W output power using a vibra-cell VCX 130 sonifier (Sonics); the sample is allowed to cool down for 10 s between each sonication cycle. The nanoparticle dispersion is then centrifuged at 2,000 rcf for 5 min. The supernatant containing non-aggregated nanoparticles is removed under observation on a UV plate so that mixture with the precipitate is avoided. The precipitate is discarded and the supernatant placed in a new Eppendorf<sup>®</sup> tube. The latter is sonicated three times with the same parameters as before and centrifuged at 4,000 rcf for 30 min. This time, the supernatant is removed under observation on the UV plate and discarded. The precipitate containing nanoparticles of the intended size is redispersed in 200  $\mu\text{M}$  phosphate buffer (50 mM, pH 7.4) and sonicated three times as before. We note that the initial volume of the nanoparticle stock solution is given for a typical assay and that an adjustment might be necessary depending on the actual size of the nanoparticles which determines mainly the quantity of recovered nanoparticles after the size selection protocol.

Round silica coverslips with 25.4 mm diameter and 0.17 mm thickness (UVFS window, Catech) are cleaned in a piranha mixture freshly prepared from 3 volumes of concentrated sulfuric acid and 1 volume of 30 % hydrogen peroxide for about

30 min. The cleaned coverslips are rinsed several times with ultrapure water and stored under ultrapure water until they are used. For application of a nanoparticle layer to the coverslip, the latter is dried under a nitrogen flow and placed on a spincoater. 40  $\mu\text{l}$  of the size selected nanoparticle dispersion are added in the middle of the coverslip and the latter is spun at 2,500 rpm for 40 s resulting in a nanoparticle layer covering of the whole surface.

### 3.2.4.3 Nanoparticle response to hydrogen peroxide

The response of spincoated nanoparticles to hydrogen peroxide is assessed by luminescence microscopy and data acquisition on a CCD camera. Coverslips with nanoparticles are mounted in a home-made tight sample holder and 1 mL phosphate buffer (50 mM, pH 7.4) is added. One drop of immersion oil (Cargille Laboratories) is placed on the objective aperture and the mounted coverslip is installed in the microscopy stage. Focusing is achieved in luminescence mode using a high laser intensity and a short image integration time on the order of 50 ms. After having obtained a sharp image, the shutter is closed and the microscopy stage is slightly and carefully displaced so that a region of nanoparticles which have not been exposed to the laser beam is in front of the aperture while maintaining the initial focus. The laser intensity is set to 1.6 kW/cm<sup>2</sup> and the image integration time to 0.8 s. The acquisition is started, the shutter is opened simultaneously and images are acquired during 5 min with a frequency of 1 image per s. After this photoreduction period, the nanoparticles should have reached a stable intensity level. The laser intensity is set to 0.3 kW/cm<sup>2</sup> and images are acquired with an integration time of 2.8 s for 5 min at a frequency of 1 image per 3 s. This timespan serves to check that the luminescence is stable and allows also for small focus corrections if necessary. The acquisition is stopped and a quantity hydrogen peroxide (Sigma Aldrich) prediluted in phosphate buffer and corresponding to the intended final H<sub>2</sub>O<sub>2</sub> concentration is prepared. Hydrogen peroxide is added and image acquisition is started simultaneously for 10 – 20 min at 0.3 kW/cm<sup>2</sup> laser beam power and an image integration time of 2.8 s. This protocol is valid for the detection of individual nanoparticles as well as for ensemble measurements.

### 3.2.4.4 Cell culture

Murine vascular smooth muscle cells (VSMC) are isolated from C57BL/6J mice (Charles River) as described elsewhere (Nguyễn, 2009). In brief, the aorta is removed from sacrificed mice and VSMC are extracted by digestion using collagenase. The cells are isolated by multiple centrifugations and placed in 25 cm<sup>2</sup> cell culture flasks (Iwaki Cell Biology).

Cell culture is performed in a Hepa Class 100 Steri Cycle CO<sub>2</sub> incubator (Thermo Fisher Scientific) at 37 °C in a humid atmosphere containing 5 % CO<sub>2</sub>. Cells are cultivated in 75 cm<sup>2</sup> or 25 cm<sup>2</sup> flasks with vented caps (Iwaki) depending on the required quantity. A preparation of RPMI-1640 GlutaMAX<sup>®</sup> cell culture medium (Gibco) containing 20 % (v/v) fetal bovine serum (FBS, Gibco) and 1 % (v/v) 100×

penicillin/streptomycin antibiotics (Gibco) will be referred to as complete medium in the following.

We here describe the protocol for treatment and preparation of 25 cm<sup>2</sup> flasks. The quantities have to be multiplied by three for 75 cm<sup>2</sup> flasks. Cells are splitted at 80 – 90 % confluency but harvesting may occur earlier. The complete medium is removed and replaced by 5 mL RPMI-1640 GlutaMAX<sup>®</sup> medium. The cells are rinsed with the latter in order to eliminate traces of serum. The liquid is removed and 1 mL 0.25 % trypsin-EDTA solution (Gibco) is homogeneously dispersed on the surface of the flask. After incubating the flask for 5-10 min, cells are detached by hitting the flask against the workbench. Following complete detachment, 5 mL complete medium are added in order to inhibit the protease activity. For passage, 2 mL of this cell suspension are diluted in 13 mL complete medium and 5 mL of the dilution are placed in each of three 25 cm<sup>2</sup> flasks. For harvesting, trypsinated cells in suspension are centrifuged at 200 rcf for 5 min. The supernatant is discarded and the precipitate is resuspended in a small volume of complete medium. An aliquot of 25 µl is placed in a Malassez hemocytometer, the number of cells is counted within 25 areas from which the number of cells per mL can be calculated.

Cells arising from the second and third passage are used for microscopy studies. For this purpose, the cell dispersion after centrifugation is diluted to a concentration of 60,000 cells per mL. One 25 mm-diameter round glass coverslip (Menzel Glas) is placed in each well of a 6-well polystyrene cell culture plate (Iwaki). 700 µl of the diluted cell suspension are placed in the middle of each coverslip and the 6-well plate is put in the incubator for 2 days. After this period, the complete medium is exchanged against 2 mL pure RPMI-1640 GlutaMAX<sup>®</sup> medium in order to remove proteins with fluorescent cofactors and to present a maximum of non-occupied receptors on the cell membrane for the following cell stimulation experiment.

#### 3.2.4.5 Loading cells with nanoparticles

Nanoparticles are internalized into VSMC by pinocytosis followed by an osmotic shock for rupture of the pinocytic vesicles. This procedure has the advantage that many cells can be treated simultaneously while microinjection allows only for the treatment of one single cell at a time. The experimental protocol was proposed by Okada and Rechsteiner (1982) and the materials are today commercialized under the name Influx<sup>®</sup> pinocytic cell-loading reagent by Molecular Probes.

In a first step, the hypertonic loading reagent and the hypotonic lysis medium are prepared. For the hypertonic loading reagent, 5 mL RPMI-1640 GlutaMAX<sup>®</sup> medium (Gibco) without serum are prewarmed to 37 °C. The polyethylene glycol (PEG) and sucrose preparation is placed in a water bath at 80 °C until the PEG is molten. 4.7 mL prewarmed cell culture medium are added and the tube is vortexed until complete dissolution of the sucrose crystals. 250 µl FBS and 50 µl 1 M HEPES buffer (4-(2-hydroxyethyl)-1-piperazineethanesulfonic acid, Sigma Aldrich) at pH 7.4 are added and the tube is vortexed again. This mixture can be stored at 4 °C but the solution containing the nanoparticles is only prepared directly before the experiment. The volumes for the preparation of the nanoparticle-containing loading reagent are given for one coverslip. If more coverslips have to be treated, the volumes are

multiplied correspondingly. 150  $\mu\text{l}$  of the aforementioned preparation are pipetted in another tube and 6  $\mu\text{l}$  of the size selected nanoparticle dispersion in phosphate buffer are added. After vortexing, the loading medium is ready for use. This medium has the task to create pinocytic vesicles inside the cells which contain the extracellular medium with the nanoparticles. The hypotonic lysis medium is prepared from 30 mL RPMI-1640 GlutaMAX<sup>®</sup> culture medium and 20 mL autoclaved distilled water. The mixture is prewarmed to 37 °C. The lysis medium provokes the explosion of the pinocytic vesicles and the liberation of the nanoparticles.

The coverslip with the adherent VSMC is lifted with a needle and removed from the well with a forceps. Excess culture medium is removed by touching the coverslip with an edge to absorbent paper. The coverslip is then placed cell-side up in a 100 mm diameter cell culture dish (Corning) on the removed lid of a 1.5 mL Eppendorf<sup>®</sup> tube as a pedestal. The latter allows for facile removal of the coverslip after the procedure and avoids breaking of the glass. 150  $\mu\text{l}$  of the hypertonic loading medium containing the nanoparticles is pipetted onto a corner of the coverslip so that the dense loading medium displaces remaining culture medium without mixture. The culture dish with the lid is then placed for 10 min in the incubator. After incubation, the coverslip is taken with a forceps and the loading medium is removed by touching it with the corner to absorbent paper. The coverslip is placed vertically in a teflon stand and submerged immediately in a beaker containing the hypotonic lysis medium. The coverslip stays for 2 min in this solution. Excess liquid is removed by touching the coverslip to absorbent paper. The coverslip is finally put back into its well containing RPMI-1640 GlutaMAX<sup>®</sup> medium without serum and incubated for 30 min at 37 °C.

After recovery of the cells, the coverslip is mounted in a microscopy adapter and rinsed several times with Hank's buffered salt solution (HBSS, Gibco) containing  $\text{CaCl}_2$ ,  $\text{MgCl}_2$  and 50 mM Hepes. After the last rinsing step, 195  $\mu\text{l}$  of the same HBSS/Hepes buffer are pipetted in the coverslip holder as observation buffer.

#### **3.2.4.6 In vivo hydrogen peroxide monitoring**

The mounted coverslip is installed in the microscopy stage. Cell selection for the experiment is performed based on morphological parameters. A cell is considered as suited if there is one clearly visible nucleus and if the cell has a star-shaped form. After selection of a cell, one image is acquired in white light with an integration time between 20 ms and 100 ms depending on the actual incident intensity. Then, white light illumination is stopped and the shutter is closed. The laser intensity is set to 1.6  $\text{kW}/\text{cm}^2$  and the integration time to 0.8 s. The acquisition is started, the shutter is opened simultaneously and images are acquired during 5 min with a frequency of 1 image per s. At the beginning of the acquisition, bright spots corresponding to the luminescent nanoparticles should be observable. In the absence of such spots, the acquisition is stopped and another cell is chosen. After the photoreduction period, the laser intensity is set to 0.3  $\text{kW}/\text{cm}^2$  and images are acquired with an integration time of 2.8 s for 5 min at a frequency of 1 image per 3 s. This timespan serves to check the luminescence stability and allows also for small focus corrections if necessary. The shutter is closed, 30  $\mu\text{l}$  endothelin-1 (ET-1, Sigma Aldrich) with a concentration

of 2  $\mu\text{M}$  are withdrawn from the stock solution kept under argon, the protein solution is added to the observation buffer and the acquisition is started immediately after addition. The given ET-1 quantity corresponds to a final concentration in the observation buffer of 266 nM. Images are acquired at 0.3 kW/cm<sup>2</sup> laser intensity with an integration time of 2.8 s for about 30 min.

### 3.2.4.7 Data analysis

Data analysis can be performed in two distinct ways. In the case of spincoated nanoparticles which are present in a high concentration so that the surface is either completely covered or shows at least extended regions of complete coverage, analysis is feasible on the whole region, since the fluorescence signal due to the coverslip can be considered negligible. If nanoparticles are spincoated at low density or are internalized into cells, analysis is done on individual particles. In both cases, normalized data is obtained by dividing the time-dependent luminescence by the measured luminescence at the time  $t = 0$  corresponding to the start of the illumination.

Analysis on extended zones is done directly in MetaVue. For photoreduction, the integrated intensity is measured in a circular zone for each image. The numerical data can then be exported to a graphics software. For recovery, a circle of the same size is placed in the same position in order to allow for analysis of the same particles. We note that the selected zone must not contain regions without nanoparticle coverage as, in this case, the background luminescence can not be neglected against that arising from the nanoparticles.

Analysis of individual particles is done with a routine in Matlab<sup>®</sup> written by Cédric Bouzigues at the LOB. In the acquired stack of images, the position of a presumable nanoparticle is marked manually. A two-dimensional Gaussian is used to fit the intensity profile for each marked spot and for all images. The total signal of the emission spot above the background and the FWHM in  $x$ - and  $y$ -direction of the two-dimensional Gaussian are output for each image. After graphical representation of the data, several tests are applied to identify spots resulting from nanoparticles and to eliminate artifacts. The first test concerns the position stability. Only spots which stay within a several pixels range from the initial position pass this test and are retained for the next step. We note that in the case of nanoparticles inside cells, a collective movement of the nanoparticles may be observed due to the vasoconstricting properties of ET-1. Big jumps in the position indicate a non-unambiguous identification of a nanoparticle and such spots are therefore eliminated. Spots which passed the first test are subjected to the second test consisting in the observation of the FWHM of the fit. The  $x$  and  $y$ -values should stay in a small range throughout the whole observation indicating that the particles remain focused throughout the whole experiment. Spots which passed these two tests are analyzed and their integrated luminescence intensity is plotted as a function of the observation time. The individual responses are generally averaged and fitted with one or two exponential functions depending on the run.

## 3.2.5 Results and discussion

### 3.2.5.1 Kinetics of photoreduction and reoxidation

We first used spincoated silicated  $Y_{0.6}Eu_{0.4}VO_4$  nanoparticles and the procedure of analysis of individual spots in order to compare the response of newly synthesized samples to the data published by Casanova *et al.* (2009). Data was therefore acquired under the same conditions as given in the paper. The average of the normalized luminescence intensity of 25 nanoparticles observed during photoreduction was calculated and fitted. As described by Casanova (2008), the best fit of the experimental data is found using a Becquerel function. However, as our goal is not the comprehensive analysis of the photophysical properties but rather to allow for a facile comparison of the data obtained for different syntheses and material compositions, we will use a biexponential function which can be seen as a second order approximation to the Becquerel function. The analysis of the average of the individual nanoparticles (fig. 3.27) yielded a luminescence decrease of 34% with two time constants in the range of several tenths and several hundreds of seconds. The addition of 20  $\mu\text{M}$   $\text{H}_2\text{O}_2$  yielded a luminescence recovery of 56%. While the photoreduction is less important than shown by Casanova *et al.* (2009), the recovery reaches almost the reported value where 75% intensity increase was found after addition of 17.8  $\mu\text{M}$   $\text{H}_2\text{O}_2$ . These findings show that the sensor properties vary slightly between different syntheses but the order of magnitude of the characteristics are generally maintained. Small differences may arise from changes in the surface texture and in the particle size.

In a second experiment, we have tested the effect of the analysis of an extended zone with many nanoparticles instead of an average of individual objects (fig. 3.28). It is striking that a hydrogen peroxide concentration 5 times higher than that used in the first experiment results in a lower luminescence recovery of only 41%. The explanation for this apparent contradiction can be found in the analysis procedure. While analysis of individual particles accounts only for the intensity of the spot without background, detection in an extended zone integrates all luminescence arising from the nanoparticles, from the background and also from the coverslip in the interparticle space. The latter does not change upon addition of hydrogen peroxide. Thus, the change of the integrated signal depends on the ratio between nanoparticle luminescence and that of all other sources. Non-nanoparticle dependent luminescence can be minimized by using zones with homogeneous nanoparticle coverage but it is always present to some extent. More importantly, hydrogen peroxide may have less access to aggregated nanoparticles. This test confirms that detection is also possible using the less time-consuming zone detection procedure but with lower sensitivity.

### 3.2.5.2 Intracellular hydrogen peroxide production

We also verified the response of internalized individual nanoparticles from a new synthesis after stimulation of the VSMC with ET-1. A white light image of the observed cell is shown in fig. 3.29. Intensity data for photoreduction and reoxidation by intracellular hydrogen peroxide production is depicted in fig. 3.30.

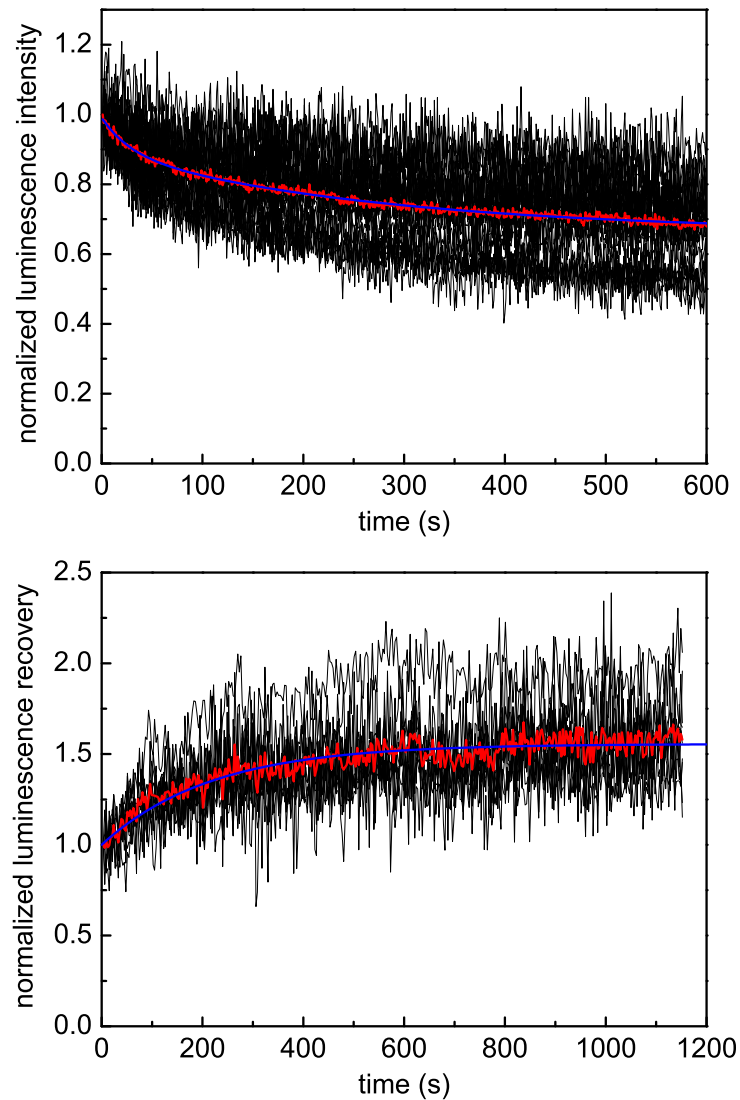


**Figure 3.27: Luminescence of silica coated  $\text{Y}_{0.6}\text{Eu}_{0.4}\text{VO}_4$  nanoparticles detected individually.**

Data are for sample MS1Si. Normalized luminescence intensities are shown for each individual particle (black lines) as well as their average (red line) and its fit (blue line). Illumination was performed at 466 nm. Upper graph: Photoreduction.  $N = 25$  nanoparticles. Laser intensity:  $1.6 \text{ kW/cm}^2$ . Exposition time: 800 ms. 1 image per s. Data was fit with a biexponential decay function:  $I = I_\infty + a_1 \exp\left(-\frac{t}{\tau_1}\right) + a_2 \exp\left(-\frac{t}{\tau_2}\right)$ . The fit yielded the decay constants  $\tau_1 = 28 \text{ s}$  and  $\tau_2 = 275 \text{ s}$  as well as the remaining intensity  $I_\infty = 66 \%$ . Lower graph: Luminescence recovery after adding  $20 \mu\text{M}$  hydrogen peroxide.  $N = 10$  nanoparticles. Laser intensity:  $0.3 \text{ kW/cm}^2$ . Exposition time: 2800 ms. 1 image per 3 s. Data was fit with a monoexponential growth function:  $I = 1 + \Delta I \cdot \left[1 - \exp\left(-\frac{t}{\tau^*}\right)\right]$ . We obtained a normalized luminescence recovery of  $\Delta I = 56 \%$  with a recovery constant  $\tau^* = 217 \text{ s}$ .

Efficient photoreduction to a low residual intensity is clearly visible. Incubation of the coverslip with ET-1 results in an increase of the luminescence intensity due to the production of hydrogen peroxide in the cell. Casanova *et al.* (2009) found under the same experimental conditions as ours a luminescence recovery of about

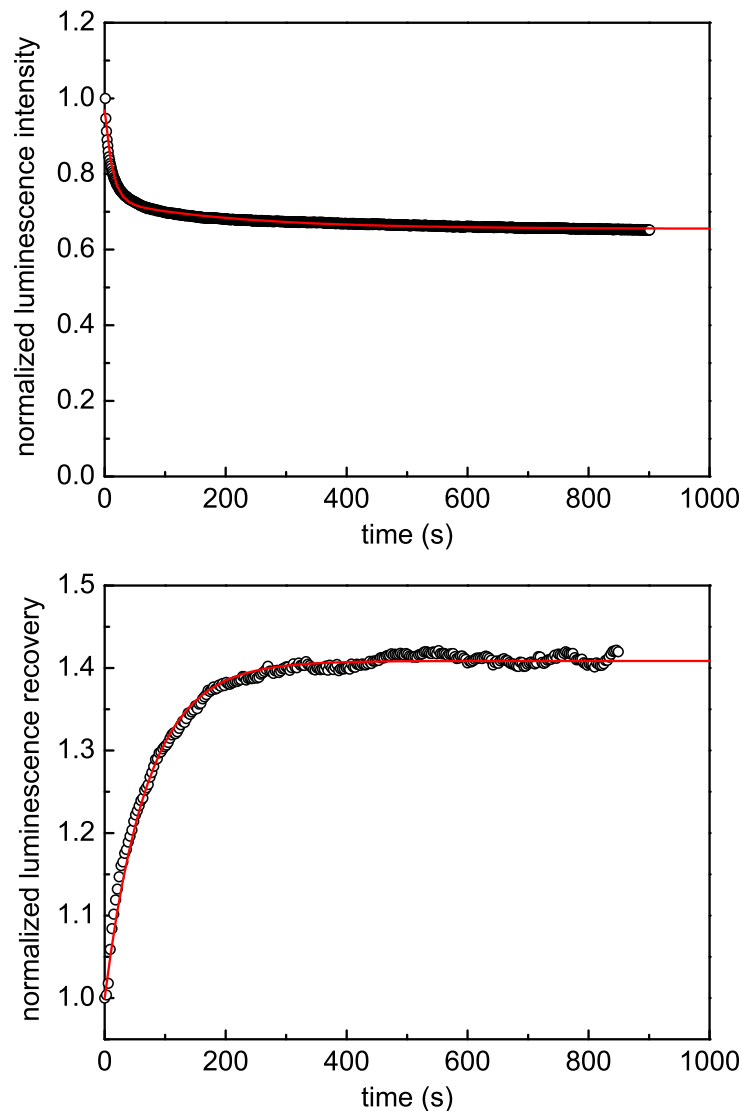


**Figure 3.28: Luminescence of silica coated  $\text{Y}_{0.6}\text{Eu}_{0.4}\text{VO}_4$  nanoparticles in ensemble detection.**

Data are for sample MS18. Nanoparticles were analyzed in an extended zone. Illumination was performed at 466 nm. Upper graph: Photoreduction. Laser intensity:  $1.6 \text{ kW/cm}^2$ . Exposition time: 800 ms. 1 image per s. Data was fit with a biexponential decay function:  $I = I_{\infty} + a_1 \exp\left(-\frac{t}{\tau_1}\right) + a_2 \exp\left(-\frac{t}{\tau_2}\right)$ . The fit yielded the decay constants  $\tau_1 = 12 \text{ s}$  and  $\tau_2 = 213 \text{ s}$  as well as the remaining intensity  $I_{\infty} = 66 \%$ . Lower graph: Luminescence recovery after adding  $100 \mu\text{M}$  hydrogen peroxide. Laser intensity:  $0.3 \text{ kW/cm}^2$ . Exposition time: 2800 ms. 1 image per 3 s. Data was fit with a monoexponential growth function:  $I = 1 + \Delta I \cdot [1 - \exp\left(-\frac{t}{\tau^*}\right)]$ . We obtained a normalized luminescence recovery of  $\Delta I = 41 \%$  with a recovery constant  $\tau^* = 70 \text{ s}$ .

50 – 70 % after 30 min depending on the observed nanoparticle. Our data indicates a luminescence increase of 50 % 30 min after stimulation in good agreement with the previous data and confirming once more that only small differences are found between different syntheses.

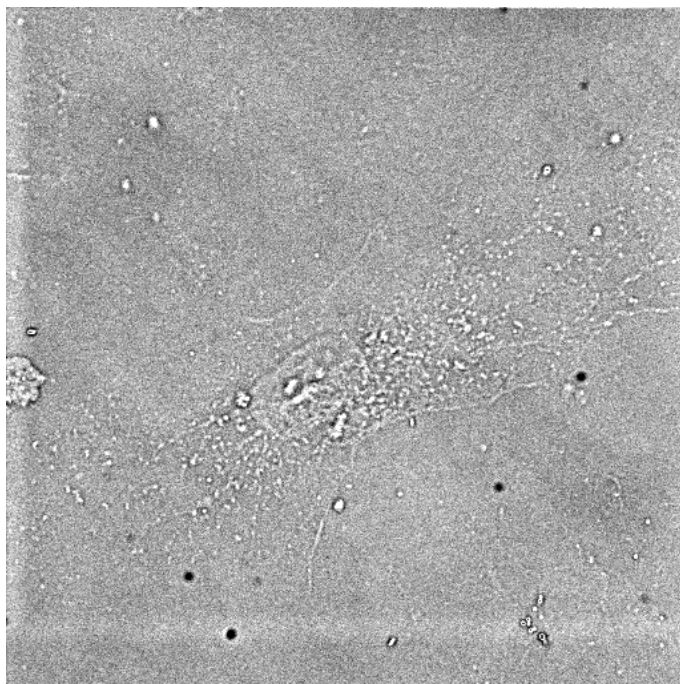
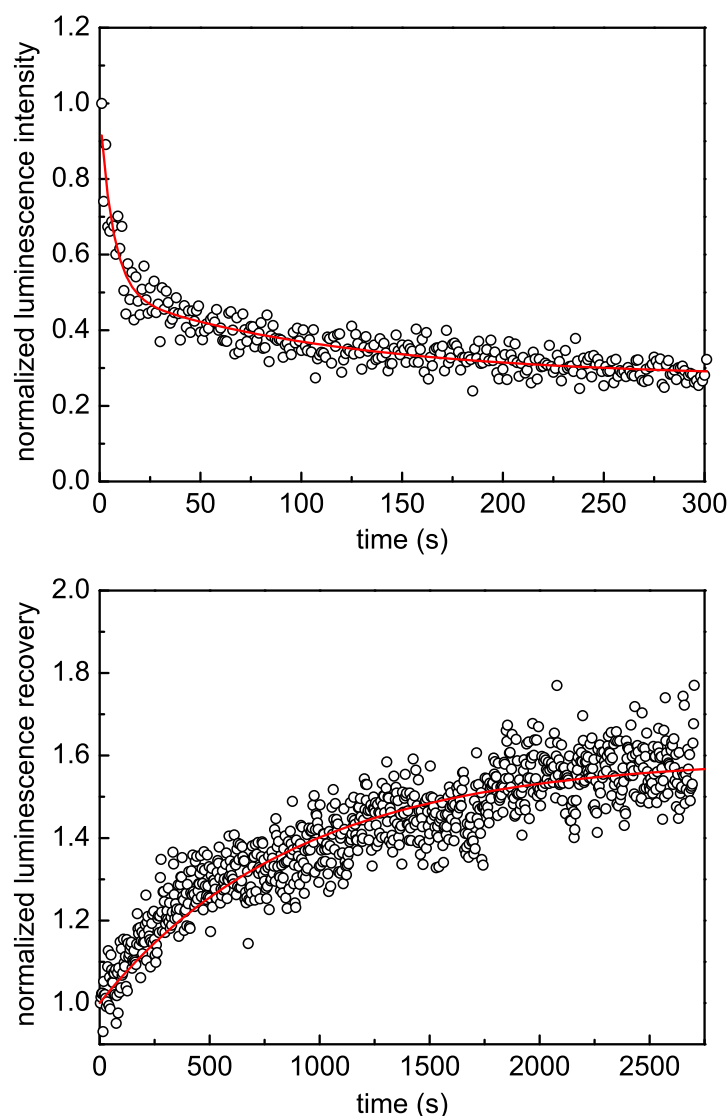


Figure 3.29: White-light transmission image of a vascular smooth muscle cell.

### 3.3 Conclusion

This chapter was devoted to the presentation and discussion of the optical properties of rare earth vanadate nanoparticles as well as their application as hydrogen peroxide sensors. These luminophors show red luminescence after either direct excitation or excitation of the vanadate matrix and energy transfer to the europium ions. In both cases, the emission intensity is largely concentrated in one transition. This transition is forbidden in free ions and becomes only weakly allowed after placing the ion in a crystal. The corresponding spectral line is narrow which makes the nanoparticles particularly interesting for luminescence studies where narrow emission filters can efficiently reject cell fluorescence. Although the quantum yield of  $Y_{0.6}Eu_{0.4}VO_4$  nanoparticles reaches only 10 – 20% which is considerably lower than that of efficient organic fluorophores, they have the distinct advantage that the emission is concentrated in a narrow spectral range, that they do not photobleach irreversibly, and that they show no blinking. Lower quantum yields were found for gadolinium vanadate matrices indicating that yttrium vanadate is more favorable for  $Eu^{3+}$  emission. Core/shell nanoparticles showed approximately the same quantum yield as pure  $Y_{0.6}Eu_{0.4}VO_4$  ones suggesting that the shell material does not disturb the luminescence.

The nanoparticles have the additional feature that their luminescence spectrum is dependent on the oxidation state of the europium ions: +2 or +3. The latter can be reversibly modified by photoreduction and chemical reoxidation making these nanoparticles a potent sensor of oxidants. Hydrogen peroxide constitutes the most abundant cellular oxidant and the knowledge of its concentration with spatio-



**Figure 3.30: Individually detected silica coated  $Y_{0.6}Eu_{0.4}VO_4$  nanoparticle as a cellular hydrogen peroxide sensor.** Data are for sample MS1Si. Nanoparticles were internalized in VSMC and analyzed individually. Data is shown for one single nanoparticle. Illumination was performed at 466 nm. Upper graph: Photoreduction. Laser intensity:  $1.6 \text{ kW/cm}^2$ . Exposition time: 800 ms. 1 image per s. Data was fit with a biexponential decay function:  $I = I_{\infty} + a_1 \exp\left(-\frac{t}{\tau_1}\right) + a_2 \exp\left(-\frac{t}{\tau_2}\right)$ . The fit yielded the decay constants  $\tau_1 = 7 \text{ s}$  and  $\tau_2 = 114 \text{ s}$  as well as the remaining intensity  $I_{\infty} = 27 \%$ . Lower graph: Luminescence recovery after adding ET-1 to a final concentration of 266 nM. Laser intensity:  $0.3 \text{ kW/cm}^2$ . Exposition time: 2800 ms. 1 image per 3 s. Data was fit with a monoexponential growth function:  $I = 1 + \Delta I \cdot [1 - \exp\left(-\frac{t}{\tau^*}\right)]$ . We obtained a normalized luminescence recovery of  $\Delta I = 59 \%$  with a characteristic time constant  $\tau^* = 8.9 \cdot 10^2 \text{ s}$ .

temporal resolution is of great interest for the elucidation of signal transduction pathways. The classical molecular probes suffer generally from the non-reversibility of the signal which means that only cumulated concentrations can be measured. Some recent molecular or protein constructs which are reversible suffer from either

the fact that they can not be used *in vivo* or that the quantitative detection range is not suited to the intracellular concentrations and that genetic engineering is time consuming, respectively.  $Y_{0.6}Eu_{0.4}VO_4$  nanoparticles are not toxic for VSMC (Casanova *et al.*, 2009; Nguyễn, 2009), fulfill the condition of reversibility, allow a quantitative detection in the concentration range of 1 – 50  $\mu$ M hydrogen peroxide, show spatio-temporal resolution and constitute therefore an excellent sensor. The comparison between individual nanoparticles and ensemble detection has shown that both methods allow for  $H_2O_2$  detection but individual detection allows for higher sensibility albeit at the price of a more complex analysis procedure. The differences in the properties of nanoparticles of the same type but produced by different syntheses are generally small; however, a quantitative detection necessitates a calibration of each batch of nanoparticles. The results from this chapter will help us evaluate the performance of the multifunctional probe presented in chapter 4.



# Chapter 4

## Rare earth vanadate nanoparticles as multimodal contrast agent

In this chapter, we will study the multimodal aspect of rare earth vanadate nanoparticles containing gadolinium and europium. We will introduce the mechanisms of nuclear relaxation and how contrast can be obtained from the different relaxation properties. We will then consider the possibilities of contrast enhancement by contrast agents and discuss the state of the art in clinical applications and contrast agent research. Some examples of existing contrast agents which can be used for multimodal imaging will be presented. We will finally discuss our results concerning the luminescence, hydrogen peroxide detection ability and the proton relaxation enhancement of the synthesized multifunctional nanoparticles. A comprehensive discussion of the underlying principles of nuclear magnetic resonance and image formation in magnetic resonance imaging is given in appendix section A.7.

### 4.1 Magnetic resonance imaging

Magnetic resonance imaging (MRI) also called magnetic resonance tomography (MRT) is a non-invasive imaging technique used in radiology which allows to produce detailed two-dimensional views of the internal structure of the body. It is based on the principles of nuclear magnetic resonance (NMR) applied to protons in water molecules. The first measurements of NMR signals were reported independently by Bloch *et al.* (1946); Bloch (1946) and Purcell *et al.* (1946) for which they were awarded the Nobel prize in physics in 1952. The foundations for all modern imaging applications were laid by the pioneering work of Lauterbur (1973) in which he reported that the position of a particular nucleus can be determined by using magnetic field gradients. He also predicted that this technique will find “many useful applications in studies of internal structure”. The first cross-sectional view of a living mouse was published in 1974 by Lauterbur and clinical MRI scans on humans started in 1980 (Bottrill *et al.*, 2006). Lauterbur was awarded jointly with Mansfield the Nobel Prize in Medicine in 2003 for their discoveries concerning MRI.

When a magnetic moment  $\boldsymbol{\mu}$  arising from the nuclear spin is brought in a magnetic field  $\mathbf{B}_0 = (0, 0, B_0)$ , the energy  $E$  of the system depends on its spin state

$$E = -\boldsymbol{\mu} \cdot \mathbf{B}_0 = -\mu_z B_0 = -\gamma m_I \hbar B_0, \quad (4.1)$$

where  $\gamma$  designates the gyromagnetic ratio of the proton and  $m_I$  the magnetic nuclear spin quantum number. Due to the energy difference in the spin states, one observes for a piece of matter containing multiple spins  $\sum_i \mu_{z,i}$  an equilibrium magnetization in  $z$ -direction according to

$$M_z^{eq} = \frac{\sum_i \mu_{z,i}}{V}, \quad (4.2)$$

with  $V$  being the volume of the sample.

### 4.1.1 Magnetic relaxation

Magnetic relaxation is the process which brings the magnetization back to the equilibrium level after application of an electromagnetic pulse (Abragam (1983), Levitt (2008), fig. 4.1). We have to distinguish the spin-lattice and the spin-spin relaxation mechanisms.

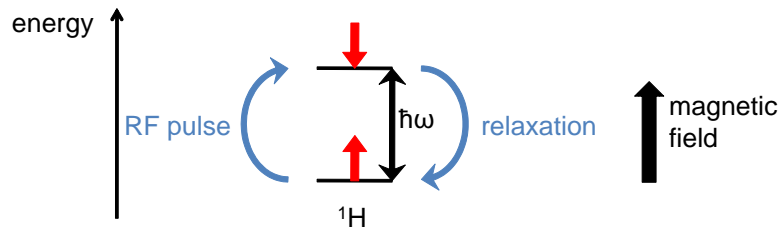


**Figure 4.1: Magnetic resonance and relaxation.** Proton spin excitation is achieved by a radio frequency (RF) pulse with the energy  $\hbar\omega$ . Relaxation brings the spin back to its thermal equilibrium state.

Spin-lattice or longitudinal relaxation is the mechanism which acts on the  $z$ -component of the magnetization vector. The population of the energy states initially altered by the electromagnetic radiation reaches its equilibrium value and energy is hereby dissipated to the surroundings of the nucleus *i. e.* the lattice. This mechanism is characterized by the spin-lattice relaxation time  $T_1$ . The magnetization in  $+z$ -direction evolves according to the equation

$$M_z(t) = M_z^{eq} \cdot \left( 1 - \exp \frac{-t}{T_1} \right) \quad (4.3)$$

where  $M_z^{eq}$  is the equilibrium magnetization in  $z$ -direction.

Spin-spin or transverse relaxation concerns the dephasing of the precessing spins. When a  $\pi/2$ -pulse of electromagnetic radiation rotates the  $z$ -component of the magnetization vector in the  $xy$ -plane, the individual magnetic moments that make up the magnetization vector begin to precess about the  $z$ -axis (appendix section A.7.4). The actual Larmor frequency of each spin depends on its surrounding so that small differences in this frequency result in a dephasing and the total magnetization in the  $xy$ -plane gradually vanishes. This mechanism can be described by the equation

$$M_{xy}(t) = M_{xy}(0) \cdot \exp \frac{-t}{T_2} \quad (4.4)$$

where  $M_{xy}(0)$  is the magnetization in the  $xy$ -plane immediately after the radio frequency pulse.

Additional to this pure molecular  $T_2$  effect, there are other factors which contribute to dephasing and which do not depend on the substance examined. The most important contribution comes from inhomogeneities of the static external field  $B_0$ . The observed transverse relaxation is therefore characterized by a relaxation time  $T_2^*$  for which the expression

$$\frac{1}{T_2^*} = \frac{1}{T_2} + \frac{1}{T_{inhom}} = \frac{1}{T_2} + \gamma |\Delta B_0| \quad (4.5)$$

holds. Herein  $T_{inhom}$  is the relaxation time due to the field inhomogeneities  $|\Delta B_0|$ .  $T_2^*$  is the decay time of the free induction decay, the observed NMR signal. The relationship between  $T_2^*$  and  $T_2$  is illustrated in appendix section A.7.6.

### 4.1.2 Bloembergen-Purcell-Pound relaxation theory

Bloembergen *et al.* devised in 1948 a theory, nowadays known as the BPP theory, explaining the relaxation mechanisms in a spin-1/2 system on a molecular level. In the absence of a contrast agent, the main reason of relaxation is the thermal motion of magnetic dipole nuclei during spin-spin interaction. The local magnetic field at the position of one nucleus produced by its neighboring nuclei can be expressed as a function of powers of  $1/\tau_R$  where  $\tau_R$  is the characteristic correlation time of Brownian motion. Using this expansion, the authors found for the longitudinal and transverse relaxation times the analytical expressions (in SI units)

$$\frac{1}{T_1} = \frac{3}{10} \frac{\mu_0^2}{16\pi^2} \frac{\gamma^4 \hbar^2}{r^6} \left( \frac{\tau_R}{1 + \omega^2 \tau_R^2} + \frac{4\tau_R}{1 + 4\omega^2 \tau_R^2} \right) \quad (4.6)$$

$$\frac{1}{T_2} = \frac{3}{20} \frac{\mu_0^2}{16\pi^2} \frac{\gamma^4 \hbar^2}{r^6} \left( 3\tau_R + \frac{5\tau_R}{1 + \omega^2 \tau_R^2} + \frac{2\tau_R}{1 + 4\omega^2 \tau_R^2} \right) \quad (4.7)$$

with the magnetic constant  $\mu_0 = 4\pi \cdot 10^{-7}$  and the interproton distance  $r$ . The rotational correlation time can be estimated from the Stokes-Einstein equation

$$\tau_R = \frac{4\pi\eta a^3}{3k_B T} \quad (4.8)$$

where  $\eta$  is the viscosity of the liquid and  $a$  the radius of the molecule which is assumed to be spherical. Concerning MRI, the molecules with the largest abundance of hydrogen are water and lipids. A simple evaluation shows the huge difference in the relaxation behavior. For water molecules at 20 °C, a correlation time of about  $\tau_R = 3.5 \cdot 10^{-12}$  s can be calculated (Bloembergen *et al.*, 1948). Lipid molecules are bigger than water molecules and it is immediately clear from eq. 4.8 that  $\tau_R$  must also be larger. A value of  $\tau_R \approx 10^{-8}$  s at 37 °C for the overall motion of a phospholipid can be found in the literature (Dufourc *et al.*, 1992). The interproton distance in water is 1.52 Å (Lide, 2008) and we may assume that it is also valid for protons bound to  $sp^3$  hybridized carbon in lipids. Based on these values, we calculated  $T_1$  and  $T_2$  relaxation times (fig. 4.2).

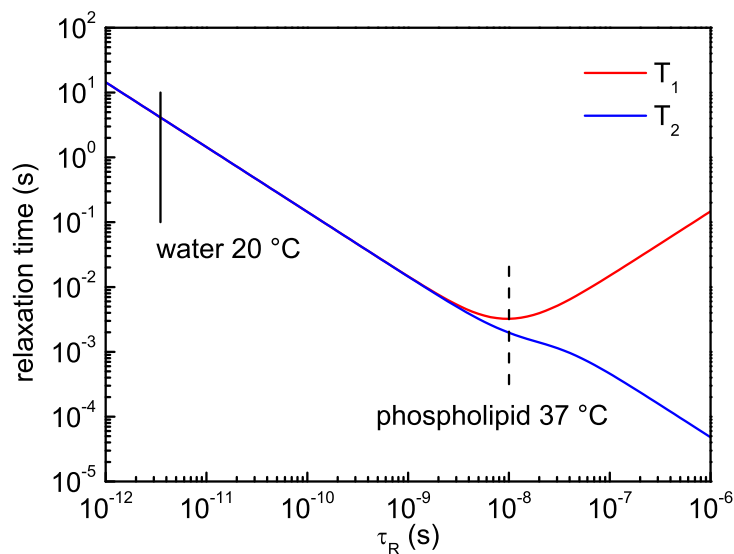


**Figure 4.2: Rotational correlation time dependent relaxation times according to the BPP theory.** The relaxation times were calculated using eq. 4.6 and 4.7 for a magnetic field strength of 1.5 T ( $\omega/2\pi = 63.86$  MHz) and the rotational correlation times of  $\tau_R = 3.5 \cdot 10^{-12}$  s for water at 20 °C (full line) as well as  $\tau_R \approx 10^{-8}$  s at 37 °C for the overall motion of a phospholipid (dashed line).

## 4.2 Contrast and contrast agents

Contrast is a central point when dealing with imaging techniques. Contrast in general is produced from measurable differences in the properties of the imaged object that enable to distinguish structures in the object and to delimit the object of interest from the background. Without contrast one may have signal but an image cannot be constructed. MRI uses as probes the protons in the water molecules inside the body. Contrast can only be obtained if a property of these protons changes in the body. It is possible that intrinsic tissue-dependent property differences are sufficient to construct an image. If this is not the case, an extrinsic material, a so called contrast agent, must be administered to the patient for generating of a bright contrast.

In the following section, we will first present the different intrinsic contrast mechanisms and we will then describe how and by which compounds contrast can be enhanced. A last subsection will be devoted to MRI contrast agents that can simultaneously generate contrast for other clinically used imaging techniques.

### 4.2.1 Contrast generating mechanisms

Contrast in MRI means that the image contains areas with high signal usually shown in white and others with low signal, usually dark. A tissue with high signal has a large transverse component of magnetization as the signal is recorded in the  $xy$ -plane (appendix section A.7.5). Intrinsic image contrast in MRI can be obtained

from chemical shift, through  $T_1$  recovery, and  $T_2$  decay as well as from differences in proton density (Westbrook and Kaut, 1998).

#### 4.2.1.1 Contrast from chemical shift

Water and adipose tissue or simply fat constitute the two extreme cases when considering contrast through a difference in the Larmor frequency. In water molecules, hydrogen is linked to electronegative oxygen which draws off some of the electron density of the hydrogen atom. The proton is according to Lenz' law deshielded and senses almost the total external magnetic field. Lipid molecules are generally big and due to a small difference in electronegativity, the electron density of the hydrogen atom is more concentrated around the nucleus. This results in an effective shielding against the external magnetic field. Therefore the Larmor frequency of hydrogen in water is higher than that of hydrogen in fat.

Chemical shift imaging (CSI) is a method that allows for mapping the spatial distribution of nuclei with a particular resonance frequency (Brateman, 1986) in contrast to conventional MRI where the entire spectrum of resonance frequencies is imaged. CSI is mainly applied for sensing the distribution of water protons and methylene protons from fat. A drawback in CSI is that the necessary pulse sequences for spectral resolution are time-consuming and result in long scan times. CSI is therefore preferentially used for defined small volumes such as the liver where it can be of great diagnostic importance for the detection of fatty liver disease.

CSI may also be used in order to increase the image quality. As the frequency-encoding gradient determines the resonance frequency of a type of nuclei according to their position in the gradient, water and fat protons from one slice are not in resonance simultaneously because of their different chemical shift and one acquires the resonance from water protons in one slice and fat protons in another slice. Morphological information is not the same in both slices and so the overlapping degrades the image quality. Selective water or fat imaging may solve this problem but obviously at the cost of longer scan times. We note that exclusive water or fat imaging can be obtained by either selecting one type of nuclei as in CSI or by saturating and suppressing one type of nuclei using the different relaxation times of water and fat protons together with saturation pulse sequences (sections 4.2.1.2 and 4.2.1.3).

#### 4.2.1.2 $T_1$ contrast

Lipid molecules show a slow tumbling rate resulting in a small  $T_1$ . On the contrary, water has a high  $T_1$  value (fig. 4.2).  $T_1$  contrast can be obtained by variation of the repetition time  $TR$  (appendix section A.7.6). When choosing a short  $TR$ , neither water nor lipids can completely recover. As  $T_1$  is shorter for lipids than for water,  $M_z$  recovers faster for lipids and the following  $90^\circ$  pulse will generate more magnetization in the detection plane emerging from fat than from water. A larger precessing fat magnetization vector means a higher signal according to eq. A.93 and lipids appear therefore brighter. Such images are called  $T_1$  weighted images. The shorter  $T_1$  of fat, the brighter the signal.

### 4.2.1.3 $T_2$ contrast

According to eq. 4.7 also  $T_2$  is smaller in lipids than in water and the magnetization in the  $xy$ -plane decays faster for lipids. In order to obtain a  $T_2$ -weighted image, the echo time  $TE$  (appendix section A.7.6) must be long so that transverse magnetization can decay in lipids and water. Due to the difference in  $T_2$ , more water magnetization remains in the detection plane. As above, a higher  $M_{xy}$  value from water means a larger detected signal and water appears therefore brighter than lipid. These images are called  $T_2$ -weighted images. The longer  $T_2$  of fat compared to water, the stronger the signal.

### 4.2.1.4 Proton density contrast

As MRI observes the relaxation from protons, there is a contrast emerging from differences in the proton density. Tissues with a high proton density (*e. g.* brain tissue) appear therefore bright on the proton density contrast image whereas regions with low proton density (*e. g.* bones) are dark. Proton density contrast is always present in biological tissues and is the main MRI contrast. A long  $TR$  with a short  $TE$  diminishes the effects of  $T_1$  and  $T_2$  weighting and allows to obtain a proton density weighted image.

## 4.2.2 Contrast enhancing agents

### 4.2.2.1 Mode of action

Routine MRI exams are mainly used to image different types of soft matter tissue and not bones. In this case, contrast is determined by the proton relaxation times  $T_1$  and  $T_2$  (sections 4.2.1.2 and 4.2.1.3). The administration of a contrast agent (CA) is indicated when there is too little intrinsic contrast between the regions of interest, in clinical diagnosis usually between healthy and pathological tissue. Contrast agents are compounds that are able to alter tremendously the relaxation times of water protons in the tissue where they are present and can therefore improve medical diagnosis in terms of higher specificity, better tissue characterization, reduction of image artifacts and functional information (Aime *et al.*, 2005). Depending on the principal effect, contrast agents can be divided into two classes:  $T_1$  or positive contrast agents mainly act on the longitudinal relaxation time whereas  $T_2$  or negative contrast agents mainly shorten the transverse relaxation time (Bottrill *et al.*, 2006). Although we will present examples for both positive and negative contrast agents, we will restrict all theoretical considerations to the best understood case of positive paramagnetic contrast agents and discuss negative contrast agents only on a qualitative level. Fig. 4.3 shows schematically the functional principle of a positive contrast agent.

The performance of a contrast agent is characterized by the concentration-normalized relaxivity (Laufer, 1987)

$$r_i = \frac{\left(\frac{1}{T_i}\right)_p}{[\text{CA}]} = \frac{\left(\frac{1}{T_i}\right)_{obs} - \left(\frac{1}{T_i}\right)_{solv}}{[\text{CA}]} \quad (4.9)$$

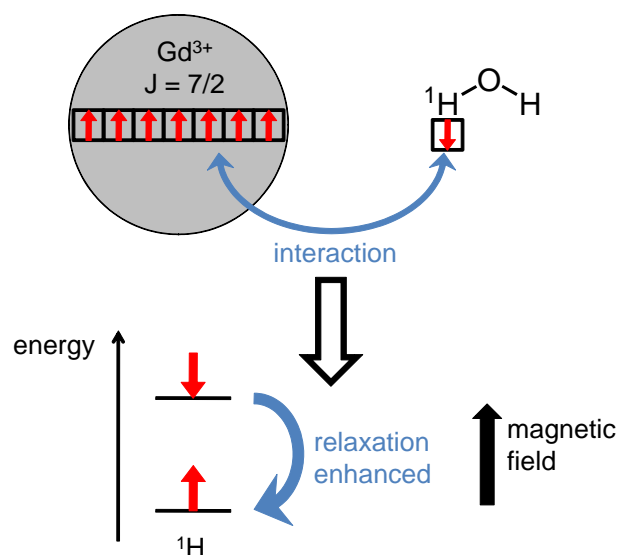


**Figure 4.3: Mode of action of a contrast agent.** The interaction between the nuclear spin of the proton in the water molecule with a high electronic spin element (here shown for Gd) enhances the relaxation from the excited nuclear energy state to the ground state.

where the index  $p$  denotes the pure paramagnetic contribution from the contrast agent which is obtained from the observed inverse relaxation time of the solution of the paramagnetic contrast agent (index *obs*) at the concentration  $[\text{CA}]$  and that of the pure diamagnetic solvent (index *solv*) and  $i$  can be either 1 or 2. Values are usually given in units of  $\text{mM}^{-1} \text{s}^{-1}$  (Aime *et al.*, 1999). The observed MRI signal increases with an increase in  $1/T_1$  and decreases with an increase in  $1/T_2$  but as a contrast agent affects commonly both relaxation times (Caravan *et al.*, 1999), the predominant effect decides finally whether the contrast agent acts as a positive or negative one. Relaxation time shortening depends always on the combination of inner-sphere and outer-sphere relaxation mechanisms (Lowe, 2002) which will be discussed in detail in sections 4.2.3.1 and 4.2.3.2, respectively. A quantity which allows to decide whether the  $T_1$  or  $T_2$  effect is dominant is the relaxivity ratio

$$\kappa = \frac{r_2}{r_1}. \quad (4.10)$$

A low ratio about 1 indicates a positive contrast agent whereas a ratio  $\gg 1$  means that the compound act as a negative contrast agent.

#### 4.2.2.2 Types and design

Positive contrast agents are usually made up from paramagnetic material with a large number of unpaired electrons. Materials of choice are  $\text{Gd}^{3+}$  with 7 unpaired electrons and  $\text{Mn}^{2+}$  with 5 unpaired electrons (Bottrill *et al.*, 2006). Negative contrast can be obtained from iron oxide nanoparticles which can disturb dramatically the magnetic field homogeneity on a long range scale (Aime *et al.*, 2005). About 35% of all MRI scans are performed with a contrast agent and  $\text{Gd}^{3+}$  reagents are the most commonly used (Bottrill *et al.*, 2006).

When designing a contrast agent, one has to consider the toxicity of  $\text{Gd}^{3+}$  already discussed in detail in section 2.4.1.1 which is due to the fact that its ion size is approximately the same as that of  $\text{Ca}^{2+}$ . As the charge of  $\text{Gd}^{3+}$  is higher than that of  $\text{Ca}^{2+}$ ,  $\text{Gd}^{3+}$  can interfere with  $\text{Ca}^{2+}$ -mediated signaling as its complexes are stronger and can accumulate in the body. This *in vivo* transmetallation can be minimized by using a biocompatible form of  $\text{Gd}^{3+}$  obtained by choosing a suitable ligand and using not free but complexed  $\text{Gd}^{3+}$  ions (Caravan *et al.*, 1999). Several aspects have to be considered when making a choice for the ligand: water solubility and stability in aqueous phase, rapid renal excretion, low osmolarity and the possibility of water exchange. The last point is a crucial point for the relaxation behavior of the complex. For efficient interaction, at least one water molecule should be bound to the gadolinium center but this molecule must also exchange rapidly with the other surrounding water molecules in order to affect the relaxation of a large number of water molecules (Bottrill *et al.*, 2006).

### 4.2.3 Paramagnetic relaxation enhancement

Paramagnetic relaxation enhancement of water protons is the result of time fluctuations of the coupling between the magnetic moment of the electrons of the metal ion and the nuclear magnetic moment of the proton (Kowalewski *et al.*, 1985; Banci *et al.*, 1991; Bertini and Luchinat, 1996). At least two contributions, an inner-sphere and an outer-sphere mechanism, can be differentiated (fig. 4.4). Depending on the actual structure of the compound, an additional second-sphere contribution might be present if hydrogen-bond interactions are possible with the water molecules. As the second-sphere contribution is difficult to quantify, it is often treated together with either the inner-sphere or the outer-sphere mechanisms depending on the strength of the hydrogen bond (Caravan *et al.*, 1999; Aime *et al.*, 2005).

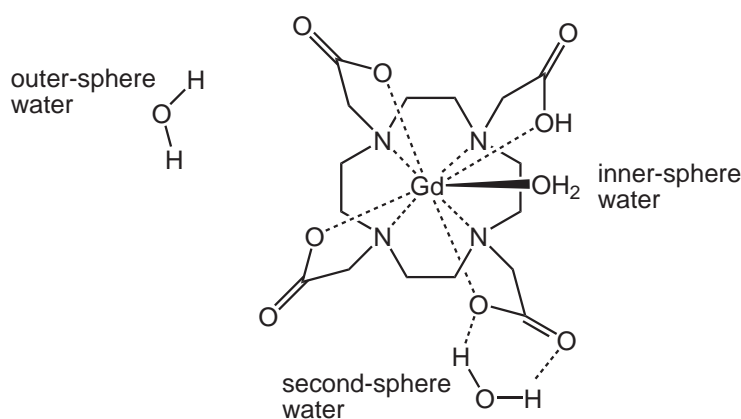


**Figure 4.4: Multiple contributions to the overall relaxivity.** The contributions are shown for the example of a Dotarem<sup>®</sup> complex. Inner-sphere water molecules are directly coordinated to the metal center. Outer-sphere water are molecules which diffuse close to the complex. If hydrogen bonds can be formed between functional groups of the contrast agent and the water molecules, outer-sphere water molecules might get trapped and give rise to an additional second-sphere contribution.

The observed overall inverse relaxation time is a function of the inverse relaxation times for both processes (Caravan *et al.*, 1999):

$$\left(\frac{1}{T_i}\right)_p = \frac{1}{T_i^{IS}} + \frac{1}{T_i^{OS}} \quad (4.11)$$

The superscripts *IS* and *OS* stand for inner-sphere and outer-sphere, respectively.

#### 4.2.3.1 Inner-sphere relaxivity

Although analytical expressions exist for the inner-sphere contribution to the transverse relaxation time, we will limit our considerations to the longitudinal relaxation time for two reasons. First, the expressions for  $T_1$  are easier and imply less parameters but allow nevertheless to discuss the different contributions. Second, we have conducted frequency dependent relaxation time measurements only for the longitudinal relaxation time.

The contribution to the longitudinal relaxation time due to the water molecule(s) directly bound to the  $\text{Gd}^{3+}$  ion can be described by (Caravan *et al.*, 1999; Aime *et al.*, 2005)

$$\frac{1}{T_1^{IS}} = \frac{[\text{CA}]}{55.6 \text{ mol l}^{-1}} \frac{q}{T_{1M} + \tau_M}. \quad (4.12)$$

Herein,  $55.6 \text{ mol l}^{-1}$  stands for the molar concentration of water and the first term describes therefore the mole fraction of the contrast agent. The hydration number  $q$  indicates the number of water molecules bound to the metal center,  $T_{1M}$  the longitudinal relaxation time of the bound water protons and  $\tau_M$  the mean residence time of the bound water molecule. An analytical expression for  $T_{1M}$  can be found in the Solomon-Bloembergen-Morgan (SBM) equations (Solomon, 1955; Bloembergen and Morgan, 1961). For the case of protons,  $T_{1M}$  is governed by two relaxation mechanisms. The first gives rise to a dipole-dipole term (superscript *DD*) resulting from the interaction between the total spin of the electrons of the contrast agent and the nuclear spin of the proton. The second describes a scalar or contact mechanism (*SC*) independent of the spin orientations. Both mechanisms are characterized by their respective relaxation times:

$$\frac{1}{T_{1M}} = \frac{1}{T_1^{DD}} + \frac{1}{T_1^{SC}} \quad (4.13)$$

For the dipolar component, the authors derived the expression

$$\frac{1}{T_1^{DD}} = \frac{2}{15} \frac{\gamma_H^2 g^2 S(S+1) \mu_B^2}{r_M^6} \left( \frac{3\tau_{c1}}{1 + \omega_H^2 \tau_{c1}^2} + \frac{7\tau_{c2}}{1 + \omega_S^2 \tau_{c2}^2} \right) \quad (4.14)$$

with  $\gamma_H$  being the gyromagnetic ratio for the proton,  $g$  the electronic Landé factor,  $S$  the quantum number of the electronic spin and  $\mu_B$  the Bohr magneton.  $r_M$  designates the distance between the metal ion and the coordinated water protons,  $\omega_H$  and  $\omega_S$  the proton and electron Larmor frequencies, respectively, and  $\tau_{ci}$  the dipole-dipole interaction correlation time. We note that eq. 4.14 is obtained by

averaging over all possible dipole orientations. The scalar mechanism is described by

$$\frac{1}{T_1^{SC}} = \frac{2}{3}S(S+1) \left(\frac{A}{\hbar}\right)^2 \left(\frac{\tau_{e2}}{1 + \omega_S^2 \tau_{e2}^2}\right) \quad (4.15)$$

with  $A/\hbar$  being the electron-nuclear hyperfine coupling constant and  $\tau_{e2}$  the scalar correlation time. We observe that the scalar contribution does not depend on the distance between the metal ion and the coordinated water proton.

The correlation times for dipole-dipole and scalar interaction depend on  $\tau_M$  and the longitudinal and transverse electron spin relaxation times  $T_{e1}$  and  $T_{e2}$ .  $\tau_{ci}$  is additionally a function of the rotational correlation time  $\tau_R$ :

$$\frac{1}{\tau_{ci}} = \frac{1}{\tau_M} + \frac{1}{T_{ei}(\omega_S)} + \frac{1}{\tau_R} \quad (i = 1, 2) \quad (4.16)$$

$$\frac{1}{\tau_{ei}} = \frac{1}{\tau_M} + \frac{1}{T_{ei}(\omega_S)} \quad (i = 1, 2) \quad (4.17)$$

As  $\tau_{ei}$  does not depend on the rotational correlation time of the Gd-containing compound and  $T_1^{SC}$  is only a function of  $\tau_{ei}$  and not of  $\tau_{ci}$ , the scalar component is less sensitive to changes in the structure of the contrast agent and we will, in an attempt of simplification, restrain our discussion to the dipolar contribution. We note that the electron spin relaxation times are a function of  $\omega_S$  and the correlation time of the modulation of the zero-field splitting, aspects which are discussed in detail in Kowalewski *et al.* (2005) and Bertini *et al.* (2005). The typical longitudinal inner-sphere relaxivity obtained with the upper equations applied to a commercial contrast agent based on a DTPA or DOTA ligand (fig. 4.5 and 4.6) and a monohydrated complex ( $q = 1$ ) at 0.5 T and 25 °C is  $r_1^{IS} \approx 2.5 - 3.5 \text{ mM}^{-1} \text{ s}^{-1}$  (Tóth *et al.*, 2001).

As it can be seen from the former equations, parameters which allow tuning of the relaxivity include  $q$ ,  $\tau_R$  and  $\tau_M$ . A very important parameter is the hydration number as  $q$  acts as a scaling factor in eq. 4.12. However, due to the necessity of a very stable complexation of Gd under physiological conditions,  $q$  is 1 in all commercial Gd(III)-based contrast agents as a decrease in the denticity of the ligand would be accompanied by a decrease in the thermodynamical stability of the complex (Aime *et al.*, 2005). A significant increase in relaxivity can be obtained by slowing down the tumbling motion of the complex that is increasing  $\tau_R$  (Lauffer, 1987). This is possible by increasing the size of the paramagnetic compound as it can be seen from eq. 4.8. For low molecular weight complexes up to several kDa, in the case that the condition  $\omega_S \tau_{e2} \gg 1$  holds and at a common field strength of 1.5 T, relaxivity and molecular weight are linearly correlated. Although this relation is not longer valid for high molecular weight compounds, a high-relaxivity contrast agent requires a slow tumbling rate, longer than the nanosecond (Aime *et al.*, 2005). Further increase in relaxivity can be gained from a fine tuning of the residence lifetime  $\tau_M$ . The effect of  $\tau_M$  becomes only important for the inner-sphere relaxation when  $\tau_R > 500 \text{ ps}$  at 20 MHz (Aime *et al.*, 2005). Water exchange in a nona-coordinate lanthanide occurs through an octa-coordinate transition complex (Tóth *et al.*, 2001; Parker *et al.*, 2002) and the energy difference between these states, itself determined by the strength of the lanthanide-oxygen bond, is important. Another factor

affecting the residence lifetime is the steric accessibility of the binding site.  $\tau_M$  can therefore be optimized by optimizing the direct environment of the water binding site.

#### 4.2.3.2 Outer-sphere relaxivity

A contrast agent can show relaxivity even if no water molecule is directly bound to the metal center because of an outer-sphere contribution (Aime *et al.*, 1994; Caravan *et al.*, 1999). This component can be expressed using an equation proposed by Freed (1978) which takes into account the effects of the translational diffusion of hard sphere water molecules in the vicinity of a hard sphere  $\text{Gd}^{3+}$  complex as well as the electron spin relaxation. Restraining ourselves as before to the longitudinal relaxation, the corresponding analytical expression reads

$$\frac{1}{T_1^{OS}} = C^{OS} \frac{[\text{CA}]}{aD} [3J_1(\omega_H) + 7J_1(\omega_S)] , \quad (4.18)$$

Herein,  $C^{OS}$  is a constant,  $a$  is the closest approach of the water molecules depending on the molecular dimension and charge distribution of the complex and  $D$  is the relative diffusion coefficient of solute and solvent.  $C^{OS}$  is calculated by

$$C^{OS} = \frac{32\pi}{405} \gamma_H^2 \gamma_S^2 \hbar^2 S(S+1) \frac{N_A}{1000} , \quad (4.19)$$

where  $\gamma_S$  is the gyromagnetic ratio of the electron and  $N_A$  the Avogadro constant.  $J_1(\omega_X)$  are non-Lorentzian spectral density functions, for which the following expression holds

$$J_1(\omega_X) = \Re \left[ \frac{1 + \frac{1}{4} \left( i\omega_X \tau_d + \frac{\tau_d}{T_{e1}} \right)^{1/2}}{1 + \left( i\omega_X \tau_d + \frac{\tau_d}{T_{e1}} \right)^{1/2} + \frac{4}{9} \left( i\omega_X \tau_d + \frac{\tau_d}{T_{e1}} \right) + \frac{1}{9} \left( i\omega_X \tau_d + \frac{\tau_d}{T_{e1}} \right)^{3/2}} \right] . \quad (4.20)$$

$X$  stands either for the proton ( $X = H$ ) or the electron ( $X = S$ ) and the respective Larmor frequencies have to be used.  $\tau_d = a^2/D$  is the time of contact determined by diffusion.

For all small Gd chelates and for  $\omega_H > 10$  MHz one obtains very similar values of  $r_1^{OS} \approx 2.1 - 2.5 \text{ mM}^{-1} \text{ s}^{-1}$  (Aime *et al.*, 2005). We remind that eq. 4.18 only considers analytically the contribution from diffusion of water molecules near the complex but not their interaction by hydrogen bonds to the surface of the contrast agent. If such interactions are possible, the additional second-sphere contribution must be taken into account and eq. 4.18 gives only an estimation of the outer-sphere contribution (Aime *et al.*, 2005). In general, if one wants to separate inner- and outer-sphere contributions to the total measured relaxivity, it is necessary to carry out frequency- or temperature dependent measurements.

#### 4.2.4 Clinically approved contrast agents

We will now give an overview of existing contrast agents. It seems appropriate to present first the contrast agents used in clinical practice as common structure

principles exist. In contrast, for newer developments reported in the literature such a structure classification is much more complicated.

#### 4.2.4.1 Gd-containing positive contrast agents

By June 2011, 8 Gd-containing contrast agents were approved by the US Food and Drug Administration for clinical use in the USA <sup>1</sup>. The latest compound has been approved in March 2011. These products are listed in tab. 4.1. Things are

**Table 4.1: FDA approved Gd-containing contrast agents in the USA.**

brand name	date of approval	manufacturer	active component
Magnevist <sup>®</sup>	June 2, 1988	Bayer Healthcare	Gadopentetate dimeglumine
Prohance <sup>®</sup>	November 16, 1992	Bracco	Gadoteridol
Omniscan <sup>®</sup>	January 8, 1993	GE Healthcare	Gadodiamide
OptiMARK <sup>®</sup>	December 8, 1999	Mallinckrodt	Gadoversetamide
Multihance <sup>®</sup>	November 23, 2004	Bracco	Gadobenate dimeglumine
Eovist <sup>®</sup>	July 3, 2008	Bayer Healthcare	Gadoxetate disodium
Ablavar <sup>®</sup>	December 22, 2008	Lantheus Medical	Gadofosveset trisodium
Gadavist <sup>®</sup>	March 14, 2011	Bayer Healthcare	Gadobutrol

more complicated within the European Union as drugs are generally approved by an individual member state. Furthermore one and the same active compound can be commercialized under different trade names. At the time of research, the only contrast agents with a European-wide approval were OptiMARK<sup>®</sup> and Ablavar<sup>®</sup><sup>2</sup>. The other contrast agents listed in tab. 4.2 have approvals for one or several European countries. The listing might not be exhaustive<sup>3</sup>.

When deciphering the trivial names of the ligands, it becomes obvious that all these ligands are derivatives from two basic structures: the cyclic tetraazacyclododecanetetraacetic acid (DOTA, fig. 4.5) and the linear diethylenetriaminepentaacetic acid (DTPA, fig. 4.6). Both structures are octa-dentate ligands with high affinities to Gd reflected in their stability constants  $pK_{GdL} > 20$  (Caravan *et al.*, 1999) and show longitudinal relaxivities in the order of 4 to 6 mM<sup>-1</sup> s<sup>-1</sup> (tab. 4.3). The DTPA ligand is commercially available but DOTA requires a time consuming preparation of the cyclic system (Weisman and Reed, 1996). The stereochemistry of the two ligands is very different. DTPA bound to Gd forms a distorted tricapped trigonal prism

<sup>1</sup>Orange Book: Approved Drug Products with Therapeutic Equivalence Evaluations, US Food and Drug Administration, Silver Spring, MD, USA (2011)

<sup>2</sup>Online data bank of the European Medicines Agency at <http://www.ema.europa.eu>

<sup>3</sup>Online data bank of the Heads of Medicines Agencies at <http://www.hma.eu>

**Table 4.2: Approved Gd-containing contrast agents in the EU.**

brand name	date of approval	manufacturer	active component
Multihance <sup>®</sup>	March 11, 1993	Bracco	Gadobenate dimeglumine
Gadovist <sup>®</sup>	June 15, 2000	Schering	Gadobutrol
Gadograf <sup>®</sup>	August 27, 2001	Schering	Gadobutrol
Dotarem <sup>®</sup>	May 28, 2003	Guerbet	Gadoterate meglumine
Artirem <sup>®</sup>	March 6, 2004	Guerbet	Gadoteric acid
Primovist <sup>®</sup>	September 28, 2004	Schering	Gadoxetic acid disodium
Omniscan <sup>®</sup>	June 13, 2006	GE Healthcare	Gadodiamide
Gadopentetat <sup>®</sup>	June 6, 2007	Curagita	Gadopentetic acid
Magnegita <sup>®</sup>	September 6, 2007	Curagita	Gadopentetic acid
Handvist <sup>®</sup>	January 21, 2010	Jacobsen Pharma	Gadopentetic acid
Magnetolux <sup>®</sup>	February 18, 2010	Sanochemia Pharmazeutika	Gadopentetic acid

**Table 4.3: Physical constants of main contrast agents.** Data except for EOB-DTPA have been taken from Caravan *et al.* (1999) and references therein for a proton resonance frequency of 20 MHz and the closest available temperature to 37 °C. EOB-DTPA data for 20 MHz and 37 °C is from Vander Elst *et al.* (1997).  $r_2$  values have in the most cases not been reported.

ligand	$pK_{GdL}$	$r_1$ (mM <sup>-1</sup> s <sup>-1</sup> )	$r_2$ (mM <sup>-1</sup> s <sup>-1</sup> )
DOTA	25.3	3.56	4.75
HP-DO3A	23.8	3.7	
DO3A-butrol	21.1	4.8	
DTPA	22.5	3.8	
DTPA-BMA	16.9	3.96	
BOPTA	22.6	4.39	5.56
DTPA-BMEA	16.8	4.7	
MS-325		6.6	
EOB-DTPA		5.4	

with the three nitrogens, the five oxygens from the carboxyl group and one water molecule (Stezowski and Hoard, 1984). In DOTA-chelated Gd complexes, the Gd<sup>3+</sup> ion is situated in the center of a capped square antiprism, with the water molecule in an axial position (Chang *et al.*, 1993). When comparing the two neutral complexes Gd(DTPA-BMA) and Gd(HP-DO3A) with similar thermodynamic stability, the HP-DO3A ligand confers higher kinetic stability to the complex because the cyclic

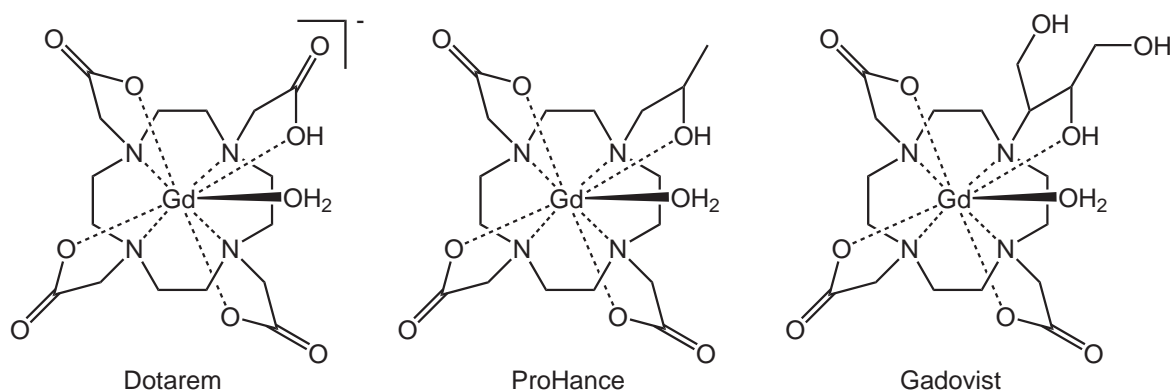


**Figure 4.5: Structure of clinically approved contrast agents based on a tetraazacyclododecanetetraacetic acid ligand.** The chemical compositions of the complexes are  $[\text{Gd}(\text{DOTA})(\text{H}_2\text{O})]^-$  (Dotarem<sup>®</sup>),  $[\text{Gd}(\text{HP-DO3A})(\text{H}_2\text{O})]$  (ProHance<sup>®</sup>) and  $[\text{Gd}(\text{DO3A-butrol})(\text{H}_2\text{O})]$  (Gadovist<sup>®</sup>). Structures from Caravan *et al.* (1999).

structure prevents release of Gd (Tweedle *et al.*, 1995; Gibby *et al.*, 2004). However, the stability of a contrast agent during an *in vivo* application can not only be described by the stability constant of the pure compound but one has also to consider the possibility of transmetallation with endogenous cations such as  $\text{Cu}^{2+}$ ,  $\text{Ca}^{2+}$ ,  $\text{Fe}^{3+}$  and  $\text{Zn}^{2+}$  which can liberate considerable amounts of  $\text{Gd}^{3+}$ . The affinity to transmetallation depends strongly on the used chelator molecule and the portion of free  $\text{Gd}^{3+}$  may be lower than 1% after more than 3 days (Laurent *et al.*, 2006, 2010).

#### 4.2.4.2 Other positive contrast agents

A positive contrast agent can also be obtained from manganese complexes. These complexes contain  $\text{Mn}^{2+}$  and are generally less stable than  $\text{Gd}^{3+}$  ones due to the fact that the body contains biological structures which are able to sequester  $\text{Mn}^{2+}$  as it is an essential ion. The contrast agent Teslascan<sup>®</sup> (active component mangafodipir trisodium) from Amersham was approved by the FDA on November 26, 1997 for hepatic MRI<sup>4</sup> but seems to be discontinued today as it does not figure in the latest FDA listing of approved drugs (fig. 4.7). This contrast agent is the only one which acts by releasing complexed  $\text{Mn}^{2+}$  to endogenous macromolecules. A pronounced effect of the  $\text{Mn}^{2+}$  protein adducts on proton relaxation can be observed (Aime *et al.*, 2005).

#### 4.2.4.3 Negative contrast agents

Iron oxide nanoparticles are the most popular material for generating  $T_2$  contrast (Hahn *et al.*, 2011). Although other types of  $T_2$  contrast agents like paramagnetic

<sup>4</sup>FDA Drug Safety Newsletter, US Food and Drug Administration, online available at <http://www.fda.gov/Drugs/DrugSafety/DrugSafetyNewsletter/ucm142889.htm>

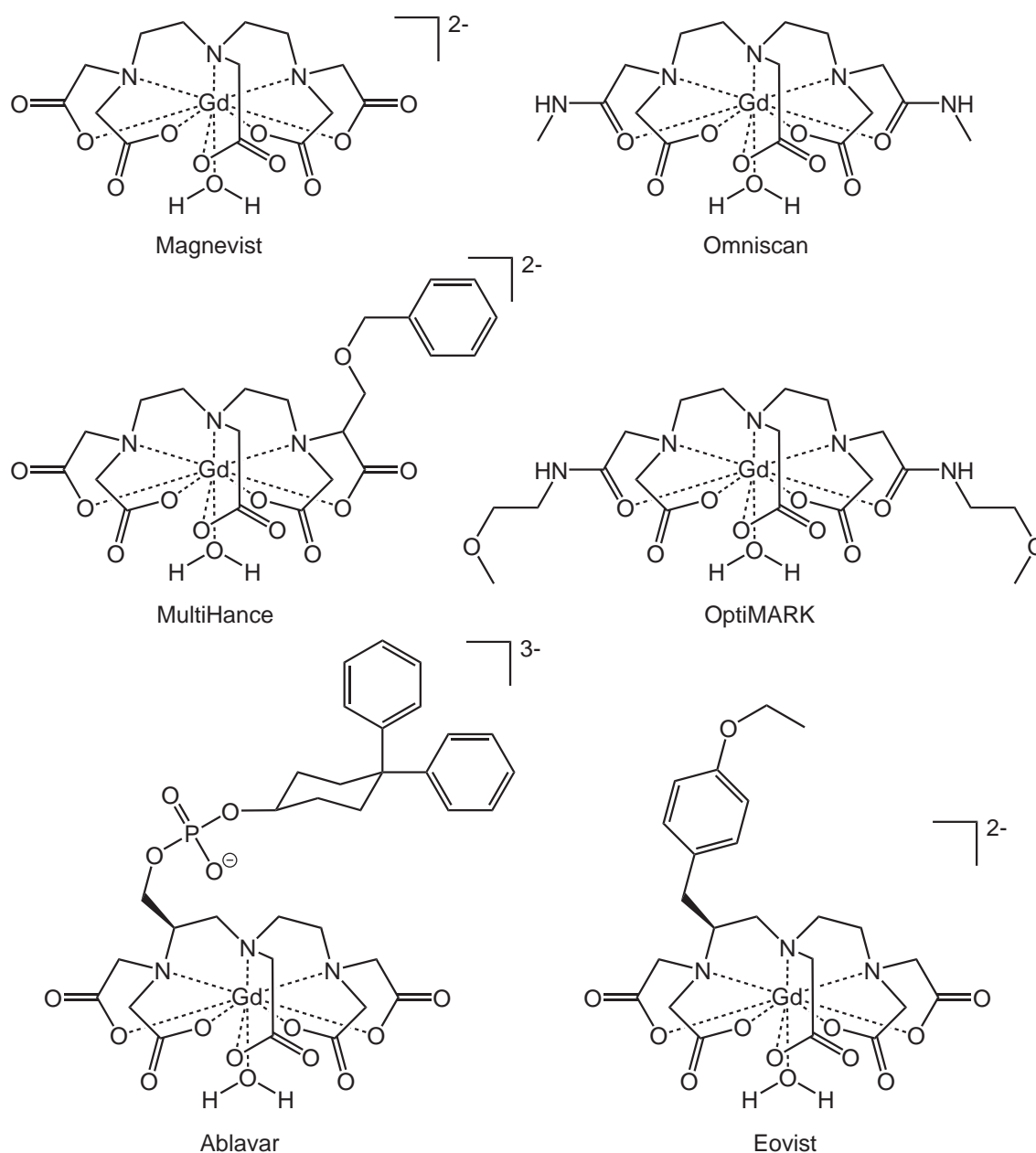


**Figure 4.6: Structure of clinically approved contrast agents based on a diethylenetriaminepentaacetic acid ligand.** The chemical compositions of the complexes are  $[\text{Gd}(\text{DTPA})(\text{H}_2\text{O})]^{2-}$  (Magnevist<sup>®</sup>),  $[\text{Gd}(\text{DTPA-BMA})(\text{H}_2\text{O})]$  (Omniscan<sup>®</sup>),  $[\text{Gd}(\text{BOPTA})(\text{H}_2\text{O})]^{2-}$  (MultiHance<sup>®</sup>),  $[\text{Gd}(\text{DTPA-BMEA})(\text{H}_2\text{O})]$  (OptiMARK<sup>®</sup>),  $[\text{Gd}(\text{MS-325})(\text{H}_2\text{O})]^{3-}$  (Ablavar<sup>®</sup>),  $[\text{Gd}(\text{EOB-DTPA})(\text{H}_2\text{O})]^{2-}$  (Eovist<sup>®</sup>). Structures from Tyeklár *et al.* (2007) for Ablavar<sup>®</sup>, Vander Elst *et al.* (2001) for Eovist<sup>®</sup> and all others from Caravan *et al.* (1999).

liposomes (Terreno *et al.*, 2010) are under development, in 2009 all clinically approved  $T_2$  contrast agents were superparamagnetic iron oxide (SPIO) nanoparticles (Qiao *et al.*, 2009). SPIO nanoparticles are generally made up from maghemite ( $\gamma\text{-Fe}_2\text{O}_3$ ) or magnetite ( $\text{Fe}_3\text{O}_4$ ) and act preferentially on the spin-spin relaxation due to the induced field inhomogeneities (Qiao *et al.*, 2009; Jun *et al.*, 2008). Iron

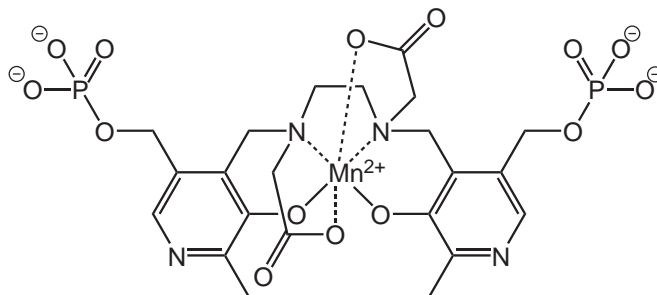


**Figure 4.7: Structure of mangafodipir trisodium.** Mangafodipir is the generic name for  $[\text{Mn}(\text{DPDP})]^{3-}$ . Structure from Aime *et al.* (2005).

oxide nanoparticles can be classified according to their size: magnetic iron oxide nanoparticles (MION) have a diameter in the  $\mu\text{m}$ -range, whereas the size of superparamagnetic iron oxide nanoparticles (SPIO) is situated around hundreds of nm and that of ultra-small superparamagnetic iron oxide (USPIO) in the range  $< 50$  nm. SPIO contrast agents are in clinical use for diagnosis of liver diseases (Semelka and Helmberger, 2001) while USPIO are in development for lymph-node imaging, angiography, and blood-pool imaging (Corot *et al.*, 2006). These contrast agents possess different coating groups to ensure their solubility and allow a targeting to the region of interest. Tab. 4.4 shows an overview of the available  $T_2$  contrast agents for clinical use (Qiao *et al.*, 2009). Due to the approval procedure, the listed products may be available only in certain countries.

**Table 4.4: Approved negative contrast agents.** All listed contrast agents belong to the class SPIO.

brand name	manufacturer	active compound	coating
Abdoscan <sup>®</sup>	GE Healthcare	Ferristen (OMP)	sulfonated styrene-divinylbenzene copolymer
GastroMARK <sup>®</sup>	Advanced Magnetics	Ferumoxil (AMI-121)	Siloxane
Lumirem <sup>®</sup>	Guerbet	identical to GastroMARK <sup>®</sup>	
Resovist <sup>®</sup>	Schering	Ferrixan (SHU 555A)	Dextran
Cliavist <sup>®</sup>	Medicadoc	identical to Resovist <sup>®</sup>	
Feridex <sup>®</sup>	Advanced Magnetics	Ferumoxide (AMI-25)	Dextran
Endorem <sup>®</sup>	Guerbet	identical to Ferridex <sup>®</sup>	

Tab. 4.5 contains the characteristic physical properties of the clinically approved negative contrast agents. The two principal parameters in the design of SPIO are the crystal size and the nanoparticle size. The crystal size corresponds to the extension of the iron oxide core whereas the nanoparticle size is the overall dimension of

the core coated with the surface modifying groups. The large particle size of oral

**Table 4.5: Physical constants of negative contrast agents.** Data were taken from Wang *et al.* (2001). Ferristene data is also found in Matsumura *et al.* (1999). The authors have not determined  $r_2$  quantitatively, but they state that  $r_2 > r_1$ .

compound	$d_{\text{crystal}}$ (nm)	$d_{\text{NP}}$ (nm)	$r_1$ (mM <sup>-1</sup> s <sup>-1</sup> )	$r_2$ (mM <sup>-1</sup> s <sup>-1</sup> )	$r_2/r_1$
Ferristene	< 50	3500	1.4	$r_2 > r_1$	
Ferumoxsil	10	300	3.2	72	22.5
Ferrixan	4.2	62	25.4	151.0	5.94
Ferumoxide	4.8-5.6	80-180	23.9	98.3	4.11

magnetic ferristene particles (OMP) is explained by their structure. These particles contain a latex core with a polymer coating and the iron oxide nanoparticles are bound to the surface of the latex core. The other listed negative contrast agents are composed of an iron oxide core on which the coating is bound.

#### 4.2.5 New positive, inorganic and nanostructured contrast agents

Today all clinically approved  $T_1$  contrast agents are based on Gd<sup>3+</sup> chelated by organic polydentate ligands as we have seen in section 4.2.4. However, recent advances in nanotechnology have resulted in the development of nanoparticles with MRI contrast enhancing properties. Nanoparticles are interesting candidates for contrast agents because of their increased relative surface resulting in a larger interaction zone between the relaxation enhancing ions and the water protons (Na *et al.*, 2009). The existing iron oxide  $T_2$  contrast agents have the disadvantage to show a signal-decreasing effect which renders image interpretation difficult as the resulting dark regions can be confused with other pathogenic conditions. Additionally, the high susceptibility of the iron oxide material introduces distortions of the magnetic field in neighboring tissue, known under the name susceptibility artifact or blooming artifact, that generates obscure images and affects the background around the actual location of the agent (Bulte and Kraitchman, 2004). It is therefore desirable to dispose of nanoparticulate  $T_1$  contrast agents for clinical use, as these are paramagnetic and do not disturb the magnetic field homogeneity over a long range. In addition, molecular  $T_1$  complexes have short life spans in the body so that long-time tracking is difficult and work mostly non-specifically as they remain typically in the blood circulation or within the extracellular matrix.  $T_1$  nanoparticulate contrast agents may be used for visualization of disease-specific biomarkers on a molecular or cellular level as has been demonstrated recently in the case of iron oxide nanoparticles (Na *et al.*, 2009).

Summarizing the present knowledge about molecular and nanoparticulate contrast agents, the new class of nanoparticulate  $T_1$  contrast agents should have the following characteristics:

- Easy surface modification and efficient labeling
- Possibility of intracellular uptake and accumulation
- Favorable pharmacokinetics concerning retention and excretion
- High stability and low transmetallation

Nanoparticulate contrast agents can be made up from an inorganic core structure decorated with binding structures for paramagnetic ions (Na *et al.*, 2009). Use of these particles results in a high local concentration of paramagnetic ions and therefore a strong contrast. However, the maximum number of  $\text{Gd}^{3+}$  ions is limited by the binding sites on the surface. A further drawback is the generally complicated synthesis which involves several steps, at least production of the core structure, addition of the binding sites to the surface and chelating  $\text{Gd}^{3+}$  ions in these binding sites. These drawbacks might be overcome by using paramagnetic inorganic nanoparticles where the paramagnetic ions are an integral part of the core structure. Obviously, synthesis is here limited to the step of the core formation. Many compounds containing transition or lanthanide metals seem to be good candidates but most of the research was devoted to Gd-based nanoparticles doubtlessly because of the extensive data on the properties of Gd complexes.

Fortin *et al.* (2007) reported the synthesis of polyethylene glycol capped ultra-small  $\text{Gd}_2\text{O}_3$  nanoparticles with a small and narrow size distribution (US- $\text{Gd}_2\text{O}_3$ ). Relaxivity measurements showed high  $r_1$  and  $r_2$  values and a  $r_2/r_1$  ratio compatible with a positive contrast agent. Bridot *et al.* (2007) devised the preparation of  $\text{Gd}_2\text{O}_3$  nanoparticles of different core diameters embedded in a polysiloxane shell (GadoSiPEG) which can also carry organic fluorophores for dual magnetic resonance and fluorescence imaging. Predominant positive enhancement was observed particularly for the smallest core size of 2.2 nm. Park *et al.* (2009) synthesized also ultra-small  $\text{Gd}_2\text{O}_3$  nanoparticles of even smaller size and with a D-glucuronic acid coating (GOGA). High relaxivity values compatible with a positive contrast agent were observed.  $\text{GdF}_3$  nanoparticles with a citrate coated surface ( $\text{GdF}_3\text{:cit}$ ) were prepared by Evanics *et al.* (2006). The size of the active core was not measured but the overall particle size was on the order of 100 nm. Hifumi *et al.* (2006) synthesized dextran-coated paramagnetic  $\text{GdPO}_4$  nanoparticles ( $\text{GdPO}_4/\text{dextran}$ ) with a hydrodynamic diameter of 23 nm for the whole construct. Lee *et al.* (2009) reported of layered gadolinium hydrochloride of the composition  $[\text{Gd}_2(\text{OH})_5]\text{Cl}$  (LGdH) in the form of nanosheets with a lateral dimension of about 120 nm and a height of several nanometers. Although the  $r_2/r_1$  ratio is very high, the authors find a positive signal enhancement. Poly acrylic acid stabilized lanthanide fluoride nanoparticle aggregates (LFNPA) of the composition  $\text{NaGdF}_4$  were prepared and characterized by Cheung *et al.* (2010). They observed a  $r_1$  mass relaxivity relative to the composite about 5-times higher than that of Gd-DTPA. Unfortunately, the value was not reported per mole of paramagnetic substance, so that it cannot be compared to the other results. Tab. 4.6 lists all the above mentioned positive nanoparticulate contrast agents in an overview.

**Table 4.6: New nanoparticulate positive contrast agents.** The given diameter  $d$  is either for the active core only (indicated by c) or for the whole particle (indicated by p). For references see text. The Larmor frequency for protons at a magnetic field of 1 T is  $\omega/2\pi = 42.57$  MHz.

name	active core	$d$ (nm)	$r_1$ $r_2$		$r_2/r_1$	$\omega/2\pi$ (MHz)
	compound		(mM <sup>-1</sup> s <sup>-1</sup> )			
US-Gd <sub>2</sub> O <sub>3</sub>	Gd <sub>2</sub> O <sub>3</sub>	3 (c)	9.4	13.4	1.4	63.9
GadoSiPEG	Gd <sub>2</sub> O <sub>3</sub>	2.2 (c)	8.8	11.4	1.3	298
GOGA	Gd <sub>2</sub> O <sub>3</sub>	1 (c)	9.9	10.5	1.1	63.9
GdF <sub>3</sub> :cit	GdF <sub>3</sub>	130 (p)	3.17	3.6	1.1	600
PGP/dextran	GdPO <sub>4</sub>	23 (p)	13.9	15	1.1	20
LGdH	[Gd <sub>2</sub> (OH) <sub>5</sub> ]Cl	120/3 <sup>†</sup>	2.20	6.92	3.1	127.7
LFNPA	NaGdF <sub>4</sub>	20 (p) <sup>‡</sup>	only $r_1$ mass relaxivity			63.9

<sup>†</sup>Nanosheets of 120 nm lateral dimension and a height of 3 nm.

<sup>‡</sup>400 nm for aggregates made up from the particles.

## 4.2.6 Nanoparticles as multimodal agents for imaging and therapy

Nanoparticles are applied in science and medicine in two main fields. They can be employed in imaging where their contrast generating or enhancing properties are exploited. They can also serve in therapy, using as active principle the composition of the nanoparticle itself or a drug linked with the nanostructure. As we will discuss in the following, this is not a "either or" separation but there exist numerous multimodal applications which combine the two fields. The common imaging applications in science and medical diagnosis, where nanoparticles can be used, include magnetic resonance imaging (MRI), optical imaging, positron emission tomography (PET), single-photon emission computed tomography (SPECT), X-ray computed tomography (CT) and ultrasound imaging. Each technique possesses its spatial and temporal resolution limits and has advantages and drawbacks. Depending on the penetration depth, *in vivo* images of parts or entire animals or humans can be acquired (Frullano and Meade, 2007). Multimodal agents allow for the colocalization of the images obtained by multiple imaging techniques and represent a powerful tool for research and diagnosis in animals and humans. When used in therapy, nanostructures can overcome the disadvantages of small molecular drugs like a short blood circulation time and non-specific biodistribution which can cause unwanted side effects (Kim *et al.*, 2009). Nanoparticles for multimodal imaging and, if desired, simultaneous therapy can be obtained by merging different nanostructures or the incorporation of several functionalities within one nanoparticle. Tab. 4.7 lists the major imaging and therapeutic applications for nanoparticles together with their specific target component within the nanostructure.

**Table 4.7: Imaging and therapeutic techniques and their targeting component.** Several targeting components can be combined in a single nanostructure to obtain a construct which is active for all the corresponding techniques. Abbreviations: magnetic resonance imaging (MRI), positron emission tomography (PET), single-photon emission computed tomography (SPECT), X-ray computed tomography (CT). Table adapted from Kim *et al.* (2009) and completed with data from Wadas *et al.* (2010), Pimlott and Sutherland (2011), Gazeau *et al.* (2008) and Le Duc *et al.* (2011).

	Technique	Targeting component	
Imaging	Luminescence	Organic fluorophore Lanthanide atom Quantum dots	
	MRI	Chelated paramagnetic ions ( $\text{Gd}^{3+}$ , $\text{Mn}^{2+}$ ) Paramagnetic nanoparticles ( $\text{Gd}_2\text{O}_3$ , $\text{GdF}_3$ , $\text{GdPO}_4$ , $\text{GdVO}_4$ , $[\text{Gd}_2(\text{OH})_5]\text{Cl}$ , $\text{NaGdF}_4$ ) Superparamagnetic nanoparticles ( $\gamma\text{-Fe}_2\text{O}_3$ , $\text{Fe}_3\text{O}_4$ )	
	PET	$\beta^+$ -emitting radioisotope ( $^{11}\text{C}$ , $^{13}\text{N}$ , $^{15}\text{O}$ , $^{18}\text{F}$ , $^{64}\text{Cu}$ , $^{66}\text{Ga}$ , $^{86}\text{Y}$ , $^{89}\text{Zr}$ , $^{124}\text{I}$ )	
	SPECT	$\gamma$ -emitting radioisotope ( $^{67}\text{Ga}$ , $^{99\text{m}}\text{Tc}$ , $^{111}\text{In}$ , $^{123}\text{I}$ , $^{201}\text{Tl}$ )	
	CT		Iodine Gadolinium
			Gold nanostructure
Therapy	Ultrasound	Microbubble	
	Chemotherapy	Anticancer drug (doxorubicin, paclitaxel, etc.)	
	Surgery	Luminescent dye	
	Photothermal therapy	Nanostructure ( $\text{Au}$ , $\gamma\text{-Fe}_2\text{O}_3$ , $\text{Fe}_3\text{O}_4$ )	
	Radiosensitizing	Nanostructure with heavy element (Gd)	
	Neutron-capture therapy	Gadolinium	

#### 4.2.6.1 Coupling of MRI and optical imaging

The most popular combination of imaging techniques is the coupling of MRI and optical imaging (Frullano and Meade, 2007; Kim *et al.*, 2009). As MRI offers a high penetration depth in tissue, it can overcome the drawback in optical imaging due to the limitation of the penetration depth to about 100 – 300 nm caused by tissue absorption and light scattering. The use of an MRI contrast agent, which possesses also luminescent properties, can simultaneously reduce scanning times by contrast enhancement and allows for screening using rapid optical imaging. As the resolution in MRI is limited to the mm range, but optical detection allows to separate structures which are several hundreds of nm away, the coupling enables also a resolution increase. While typical MRI  $T_1$  contrast agents require millimolar concentrations,

luminescent compounds as well as radioactive tracers can be detected down to the picomolar range and are therefore orders of magnitude more sensitive. Multimodal probes can combine the complementary advantages of optical techniques concerning acquisition speed and sensitivity down to low concentrations with the deep tissue penetration of MRI. The majority of multimodal agents for simultaneous MRI and optical detection are MRI contrast agents coupled with organic dyes (Kim *et al.*, 2009) but luminescent lanthanides can also be used beneficially.

Bridot *et al.* (2007) synthesized  $\text{Gd}_2\text{O}_3$  core nanoparticles of several nanometers diameter which were encapsulated by a polysiloxane shell exposing organic fluorophores covalently bound to the amino groups of APTES ((3-aminopropyl)triethoxysilane). Particles were stabilized by polyethylene glycol grafted to the surface. These nanoparticles showed a positive MRI enhancing effect (GadoSiPEG in tab. 4.6) as well as strong fluorescence from the organic dyes. Injected in mice, the particles were detectable by MRI and fluorescence imaging.

Moreover, the implementation of a fluorescence measurement device in a commercial MRI scanner was recently reported by Mastanduno *et al.* (2011).

#### 4.2.6.2 Coupling of MRI and positron emission tomography or single-photon emission computed tomography

Positron emission tomography (PET) is a technique that uses the  $\gamma$ -radiation produced from the annihilation of positrons from radioisotopes with electrons in the surrounding medium without the need for external excitation (Turkington, 2008). In single-photon emission computed tomography (SPECT), the  $\gamma$ -radiation is produced directly by the decay of an adequate radioisotope (Wadas *et al.*, 2010). As  $\gamma$ -radiation is involved in both cases, the penetration depth is unlimited on the scale of biological samples. Compared to MRI, the resolution is lower and anatomy cannot be resolved but PET and SPECT have the highest sensitivity of all imaging techniques: they enable determination of the local concentration of the radioisotope and can detect a single abnormal cell (Hahn *et al.*, 2011; Pimlott and Sutherland, 2011). PET and SPECT are therefore capable to detect the onset of cancer before any macroscopic changes can be visualized with *e. g.* MRI. The drawback of PET and SPECT is that a cyclotron is needed on site to generate the short-lived radioisotopes.

PET can be coupled to MRI or CT by incorporating radioisotopes suitable for positron emission such as  $^{11}\text{C}$ ,  $^{13}\text{N}$ ,  $^{15}\text{O}$ ,  $^{18}\text{F}$ ,  $^{64}\text{Cu}$ ,  $^{66}\text{Ga}$ ,  $^{86}\text{Y}$ ,  $^{89}\text{Zr}$  or  $^{124}\text{I}$  in the contrast agent and observing the organism in a PET/MRI or PET/CT scanner, respectively. SPECT can also be coupled to MRI or CT when using radioisotopes like  $^{67}\text{Ga}$ ,  $^{99\text{m}}\text{Tc}$ ,  $^{111}\text{In}$ ,  $^{123}\text{I}$  or  $^{201}\text{Tl}$  which emit  $\gamma$ -radiation. The amount of the radioisotope incorporated in the contrast agent must be carefully controlled as sensitivities for PET and SPECT are quite different from those encountered in MRI or CT. For the example of the coupling of PET and MRI and based on the typical volume resolutions of the two techniques, one can calculate that a PET signal may arise from as little as  $10^{-15}$  mol of a tracer in the smallest detection volume while MRI needs at least  $10^{-9}$  mol of a contrast agent in order to have an effect.

Xie *et al.* (2010) covered oleate-coated iron oxide nanoparticles of 15 nm diameter

with dopamine and encapsulated this construct in human serum albumin (HSA). Cy5.5 fluorophores and  $^{64}\text{Cu}$ -DOTA complexes were covalently attached to amino groups of the HSA surface. These composite nanoparticles showed high  $r_2$  relaxivity values and were detectable by tri-modal imaging using PET, MRI and near-infrared fluorescence.

#### 4.2.6.3 Coupling of MRI and X-ray computed tomography

X-ray computed tomography (CT) can provide three-dimensional images with a resolution comparable to that of MRI (Frullano and Meade, 2007). Contrast is generated mainly between bones and other parts of the body but tissue differentiation is poor. CT can therefore furnish complementary information to MRI where contrast is generated between water containing regions, that is between different tissue types. Commonly used CT contrast agents include barium sulfate for gastroenterological imaging as well as highly iodine-substituted organic molecules for intravenous administration. Due to the heavy atom nature of the Gadolinium atom, its high electron density makes it also a well suited element for the design of CT contrast agents. However, considering the commonly used doses for X-ray exams, chelated Gd is not suited due to its high cost. More contrast with a smaller total dose can be obtained by concentration of many Gd atoms in a nanostructure which can be targeted to the intended imaging zone.

Santra *et al.* (2005) reported the synthesis of single-core-multiple-shell nanoparticles composed of a  $\text{SiO}_2$  core with incorporated Ru(bipy) (tris(2,2'-bipyridyl)dichloro ruthenium (II)) which serves as a photostable fluorescent dye. The first shell was composed of silica which served as a base for the anchoring of a  $\text{Gd}^{3+}$ -ethylenediamine triacetic acid complex via a linker. The second shell exposed amino groups from APTES for bioconjugation. X-ray absorption images showed a strong contrast due to the radio-opacity of the nanoparticles. Relaxivity measurements yielded a high relaxation enhancement due to the  $\text{Gd}^{3+}$ -ions.

#### 4.2.6.4 Coupling of MRI and ultrasonography

Examples of agents which can generate simultaneously contrast in MRI and ultrasound examinations are only known to a lesser extent. The problem resides in the different size scales of the contrast agents. Whereas the size of typical nanoparticles is in the ten or hundred nanometer range, ultrasound contrast agents for current imaging practice need to be in the several micrometer range (Hahn *et al.*, 2011). A combination could therefore only be obtained by loading microbubbles with nanoparticles.

Ao *et al.* (2010) devised the preparation of Gd-DTPA-loaded microbubbles. Poly(lactic-co-glycolic acid) (PLGA) was used to fabricate microspheres with a diameter in the micrometer range and filled with fluorocarbon and Gd-DTPA. Injection of the microbubbles in a rabbit yielded an enhanced ultrasound echo intensity in the liver as well as more contrasted MRI images.

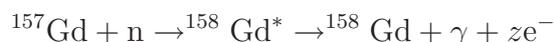
#### 4.2.6.5 Coupling of MRI and chemotherapy

Using nanoparticles simultaneously as MRI contrast agent and as drug transport vehicles has several advantages. First, nanoparticles encapsulating drugs have generally a longer body circulation time than molecular drugs. Second, the nanoparticle as scaffold allows for targeting of the drug by attaching targeting compounds to its surface and avoids therefore undesired side effects in non pathogenic tissue. Third, nanoparticulate drug vehicles can circumvent the multidrug resistance effect of tumor cells where tumor cells can easily pump out drugs by membrane pumps (Kim *et al.*, 2009). Fourth, the accumulation of the drug at the target site can be followed by MRI and doses as well as administration intervals can be adjusted properly for maximal effect.

Piao *et al.* (2008) reported the fabrication of water-dispersible hollow iron oxide nanocapsules composed of magnetite ( $\text{Fe}_3\text{O}_4$ ). In order to increase the colloidal stability and the biocompatibility, the surface was covered with polyethylene glycol. The nanoparticles showed a negative contrasting effect in MRI experiments while the doxorubicin molecules loaded on the surface had a growth-inhibiting effect on cancer cells.

#### 4.2.6.6 Coupling of MRI and neutron-capture therapy

Neutron-capture therapy (NCT) is a noninvasive experimental therapy which can be used for the treatment of glioblastoma multiforme, the most aggressive malignant form of human brain tumors (Hosmane *et al.*, 2011). NCT requires first the administration to the patient of a compound containing an isotope with high absorption cross section for thermal neutrons. Commonly used agents contain either  $^{10}\text{B}$  or  $^{157}\text{Gd}$ . Such a compound may be targeted to the tumor through the blood circulation due to the disruption of the blood-brain barrier. The patient is then exposed to thermal neutrons which induce a nuclear reaction in the compound. In terms of multimodality, the isotope  $^{157}\text{Gd}$  is the most promising. Its huge neutron absorption cross section of 259,000 barn for thermal neutrons of 2,200 m/s is the highest absorption cross section of all stable isotopes. This isotope has also a relatively large natural abundance of 15.7% (Sears, 1992). Upon neutron capture, the  $^{157}\text{Gd}$  nucleus performs a complicated nuclear reaction



which provokes the prompt emission of high energy  $\gamma$ -radiation with an energy up to 7.8 MeV and several mostly Auger electrons from internal conversion with energies  $\leq 41$  keV (De Stasio *et al.*, 2001).  $\gamma$ -radiation and electrons have different action ranges and biological effects. While  $\gamma$ -radiation is only weakly absorbed and passes through the entire body, high energy transfer Auger electrons are highly ionizing over short ranges of tens of nanometers. These electrons can cause DNA double strand breaks in tumor cells and lead to necrosis. Coupling of imaging and therapy is possible when the MRI contrast agent acts simultaneously as a source of  $^{157}\text{Gd}$ .

Bridot *et al.* (2009) synthesized hybrid gadolinium oxide nanoparticles for MRI and NCT. They prepared nanoparticles with a  $\text{Gd}_2\text{O}_3$  core of 3 nm and a polysiloxane

shell which could carry organic fluorophores. Solubility and stability was increased by grafting of PEG to the surface. These particles showed a  $r_1$  value higher than that of Gd-DOTA complexes. Incubation of EL4 cells with the nanoparticles and irradiation by a thermal neutron beam caused cell death whereas incubation without irradiation or irradiation without incorporated nanoparticles had no effect on cell viability.

## 4.3 Materials and methods

### 4.3.1 Sample preparation

Relaxation time measurements were carried out on different nanoparticle dispersions, on dissolved  $\text{Gd}^{3+}$  ions as well as on a commercial  $T_1$  contrast agent. For the nanoparticle dispersions, we indicate the synthesis numbers from tab. 2.4 for nonambiguous identification of the samples. We used nanoparticles composed of pure  $\text{GdVO}_4$  (synthesis number MS4), silica coated pure  $\text{GdVO}_4$  ( $\text{GdVO}_4/\text{SiO}_2$ , MS2Si), Eu-doped  $\text{GdVO}_4$  ( $\text{Gd}_{0.6}\text{Eu}_{0.4}\text{VO}_4$ , MS6R), silica coated Eu-doped  $\text{GdVO}_4$  ( $\text{Gd}_{0.6}\text{Eu}_{0.4}\text{VO}_4/\text{SiO}_2$ , MS19) as well as nanoparticles produced by the citrate route and composed of either pure  $\text{GdVO}_4$  (MS23) or Eu-doped  $\text{GdVO}_4$  ( $\text{Gd}_{0.6}\text{Eu}_{0.4}\text{VO}_4$ , MS24). Core-shell nanoparticles possessing a  $\text{Y}_{0.6}\text{Eu}_{0.4}\text{VO}_4$  core and a  $\text{GdVO}_4$  shell (MS26) were also measured. Dotarem<sup>®</sup> (Guerbet) and  $\text{GdCl}_3$  (Prolabo) were employed for comparison reasons. Ultrapure water is used for all dilutions. Crystalline  $\text{GdCl}_3$  is dissolved to a final concentration of 10 mM based on mass. Dotarem<sup>®</sup> 0.5 M is diluted to a final concentration of 10 mM based on volume. Nanoparticle suspensions are diluted by volume to about 10 mM final vanadate concentration based on the vanadate concentration of the stock solution. For nuclear magnetic resonance dispersion spectroscopy, the samples MS4, MS6R, MS23 and MS24 are diluted by volume to exactly 10 mM final concentration. Due to the size difference, a 10 mM dispersion of nanoparticles produced by the normal route synthesis is generally slightly milky whereas a dispersion of the same concentration of nanoparticles from the citrate route is completely clear. All dilutions except that of MS26 are stable at room temperature for at least several days. Dilutions of the core-shell nanoparticles MS26 show precipitation within minutes and are therefore prepared immediately before the measurement. Sample preparation for luminescence quantum yield determination and hydrogen peroxide detection is carried out as described in sections A.6.3 and 3.2.4.3, respectively.

### 4.3.2 Measurement of relaxation times

Relaxation time measurements are performed on a Bruker NMS 120 minispec relaxometer operating at a proton resonance frequency of  $\omega/2\pi = 20$  MHz and a temperature of 37 °C. In order to avoid confusion between the angular frequency  $\omega$  and the frequency  $\nu$ , we define here that all frequencies given in units of Hz correspond to  $\omega/2\pi = \nu$ . The spectrometer is calibrated using standard water/oil mixtures of known component ratio according to manufacturer's instructions. The

prediluted samples are further diluted directly inside 10 mm NMR tubes to a series containing 10 samples of 1 mL. All dilutions are carried out using ultrapure water. The tubes are sealed and placed in a water bath at 37 °C for at least 10 min prior to measurement.  $T_1$  relaxation times are determined using the inversion recovery pulse sequence (section A.7.6) with a repetition time  $TR = 5$  s. The pulse separation time  $TI$  is adjusted until the condition  $TI \approx 0.6 T_1$  is fulfilled. For the measurement of the  $T_2$  relaxation time, the CPMG pulse sequence (section A.7.6) is employed using a repetition time  $TR = 8$  s. Generally 100 echos with a echo time  $TE$  between 0.5 and 2 ms depending on the concentration of the sample are recorded.  $TE$  is adjusted manually in order to record the complete magnetization decay during the 100 echos. In both cases, the device's software performs the fit of the measured magnetization recovery and displays directly the corresponding relaxation times with error.

### 4.3.3 Relaxivity data analysis

Relaxation times are normalized according to eq. 4.9 in order to obtain the relaxivities. We calculated relaxivities per  $\text{Gd}^{3+}$  ion and per nanoparticle. In the calculation procedure for the ionic relaxivities, only the Gd concentration and not the total rare earth concentration is considered as the other ions should not participate to the relaxivity.  $\text{Eu}^{3+}$  ions in their electronic ground state  ${}^7\text{F}_0$  do not contribute as they have a  $4f^6$  configuration meaning that the orbitals with  $l = -3 \dots +2$  are occupied with one electron of  $s = +1/2$ . The intermediate coupling scheme yields  $J = 0$  for the total spin of the electrons in the  $4f$  shell. However, the first excited electronic state in  $\text{Eu}^{3+}$  having the term symbol  ${}^7\text{F}_1$  lies only about  $400 \text{ cm}^{-1}$  above the ground state (Carnall *et al.*, 1989) and might be partially populated at ambient temperature as  $25 \text{ }^\circ\text{C}$  correspond to  $207 \text{ cm}^{-1}$  (Van Vleck, 1932). This state has a total spin of  $J = 1$  and could therefore contribute to the relaxivity. We note that a reduction from  $\text{Eu}^{3+}$  to  $\text{Eu}^{2+}$  would also generate a total spin as the seventh electron is in the state  $l = +3$  and  $s = +1/2$  and one obtains therefore  $J = 7/2$ . There is no effect from  $\text{Y}^{3+}$  as it possesses only fully occupied orbitals. For reasons of simplicity, we will in a first approximation assume that all  $\text{Eu}^{3+}$  are in the ground state and consider solely the concentration of  $\text{Gd}^{3+}$  during the normalization procedure.

Relaxivities per nanoparticle are estimated by calculating first the volume of one nanoparticle. In order to simplify this approach, nanoparticles are considered being homogeneous in size and spherical with a diameter equal to the number average diameter determined from DLS. In the case of silica coated samples, the diameter of the non-modified pristine material is used. The number of Gd ions per particle is evaluated using the unit size dimensions  $a = b = 7.215 \text{ \AA}$  and  $c = 6.350 \text{ \AA}$  obtained for  $\text{GdVO}_4$  (MS4) for all samples (tab. 1.3), a number of 4 formula units per unit cell and the formula stoichiometry. The relaxivity per nanoparticle is then obtained by multiplying the relaxivity per Gd ion with the number of Gd ions per nanoparticle.

### 4.3.4 Nuclear magnetic resonance dispersion spectroscopy

${}^1\text{H}$  nuclear magnetic resonance dispersion spectroscopy (NMRD) experiments are performed with a Stelar Spinmaster FFC2000 fast field cycling relaxometer at  $25 \text{ }^\circ\text{C}$ .

Spin-lattice relaxation times are measured in the frequency range from  $\omega/2\pi = 10$  kHz to 15 MHz by acquiring 10 data points per frequency decade in equidistant frequency steps on a logarithmic scale. All samples are measured in 10 mm NMR tubes at a vanadate concentration of 10 mM and the obtained data is normalized to the  $\text{Gd}^{3+}$  concentration. The automated measurement procedure consists in the application of first a polarization, second a relaxation and third a acquisition field. The polarization field corresponding to a proton resonance frequency of  $\omega/2\pi = 15$  MHz serves to boost signal intensity and is applied for 2 s. Then the transition to the relaxation field is performed quickly within 2 ms. Magnetization relaxes in the relaxation field of the chosen frequency and for a time span  $\Delta$  which is varied within the interval  $0-5 T_1$ . The scanning of  $\Delta$  is necessary for the measurement of the time-dependent magnetization and the extraction of the corresponding relaxation time  $T_1$  for each defined frequency. The determination of the quantity of magnetization remaining after  $\Delta$  is performed after a quick transition within 1 ms to the acquisition field corresponding to 9 MHz and by applying a  $\pi/2$  detection pulse.

### 4.3.5 Response to hydrogen peroxide

Luminescence properties are characterized as explained in section A.6.2. Measurements of the response to hydrogen peroxide and data analysis are carried out as explained in sections 3.2.4.3 and 3.2.4.7, respectively. In the particular experiment, we have observed a dense layer of spincoated nanoparticles produced by addition of 40  $\mu\text{l}$  of a 120 mM suspension of  $\text{Gd}_{0.6}\text{Eu}_{0.4}\text{VO}_4$  nanoparticles (sample MS6R) or 100  $\mu\text{l}$  of a 94 mM suspension of  $\text{Y}_{0.6}\text{Eu}_{0.4}\text{VO}_4/\text{GdVO}_4$  core-shell nanoparticles (sample MS26) on a glass coverslip. Luminescence is recorded for 10 min during photoreduction and recovery following the addition of hydrogen peroxide. The luminescence intensity per image frame is evaluated in a circular region with homogeneous coverage of nanoparticles.

## 4.4 Results and discussion

### 4.4.1 Relaxation times at 20 MHz

We first determined the relaxation times of the well studied compound Dotarem<sup>®</sup> in order to validate our measurement procedure (fig. 4.8). As expected we find a linear dependence of the relaxation rates  $1/T_1$  and  $1/T_2$  with the concentration of the contrast agent. Furthermore, the transverse relaxation time is always smaller than the longitudinal relaxation time as predicted by the theory (section 4.1.2 and fig. 4.2). The linear fit yields the relaxivities  $r_1 = 3.59 \text{ mM}^{-1} \text{ s}^{-1}$  and  $r_2 = 4.44 \text{ mM}^{-1} \text{ s}^{-1}$  which are in quite good agreement with the literature values of  $r_1 = 3.56 \text{ mM}^{-1} \text{ s}^{-1}$  and  $r_2 = 4.75 \text{ mM}^{-1} \text{ s}^{-1}$  (Caravan *et al.*, 1999). These findings confirm the reliability of our measurement protocol.

In a second step, we determined the relaxation times for free  $\text{Gd}^{3+}$  ions from  $\text{GdCl}_3$  where we obtained the relaxivities  $r_1 = 10.4 \text{ mM}^{-1} \text{ s}^{-1}$  and  $r_2 = 12.1 \text{ mM}^{-1} \text{ s}^{-1}$  (graph not shown). In the literature, relaxivities for  $\text{Gd}^{3+}$  ions are reported for

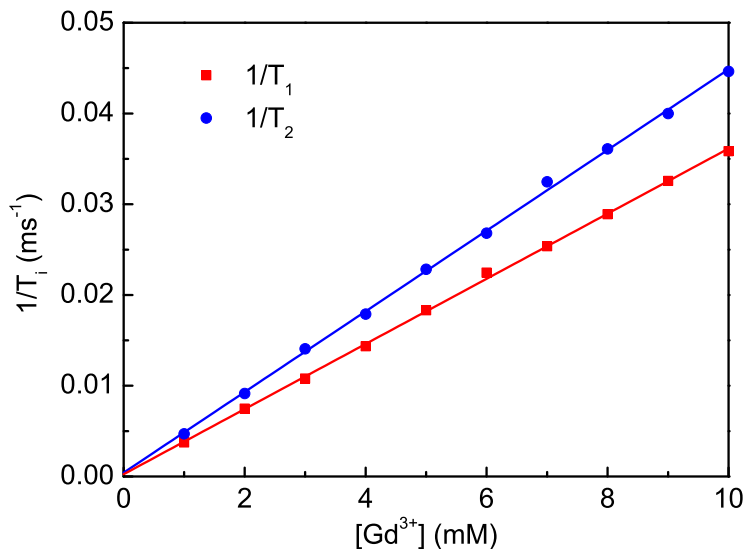


**Figure 4.8: Relaxation times for Dotarem®.**  $T_1$  and  $T_2$  relaxation times were measured at 37 °C. The fit yields relaxivities of  $r_1 = 3.59 \text{ mM}^{-1} \text{ s}^{-1}$  and  $r_2 = 4.44 \text{ mM}^{-1} \text{ s}^{-1}$ .

a variety of magnetic fields and temperatures. Bernheim *et al.* (1959) performed temperature-dependent measurements on  $\text{Gd}^{3+}$  ions at 20 MHz. From their result graph, we can read values of about  $r_1 = 10.8 \text{ mM}^{-1} \text{ s}^{-1}$  and  $r_2 = 12.1 \text{ mM}^{-1} \text{ s}^{-1}$  for 37 °C. Although we must allow for some read-out error, our data is in very good agreement with these values. This confirms once again the suitability of the measurement procedure.

We then applied this measurement protocol to determine the relaxation times of dispersions of several of our rare earth vanadate nanoparticles. We found a linear dependence of the inverse relaxation times with the concentration of Gd contained in the respective particles for all examined samples. Data are only shown for  $\text{Gd}_{0.6}\text{Eu}_{0.4}\text{VO}_4^{\text{cit}}$  nanoparticles (MS24) produced by the citrate route (fig. 4.9) for reasons of clarity. The calculated relaxivities for all studied samples are listed in tab. 4.8.

We will first compare the effect of silica coating on the relaxivities. We remind that MS4 is not the pristine base material of MS2Si but as normal route syntheses are quite reproducible as seen from the diameters of the samples  $\text{GdVO}_4$  (MS4) and  $\text{Gd}_{0.6}\text{Eu}_{0.4}\text{VO}_4$  (MS6R), we assumed that the pristine nanoparticles of MS2Si have a diameter comparable to that of MS4. The silica coated form of pure  $\text{GdVO}_4$  nanoparticles (MS2Si) compared to the raw form MS4 has somewhat higher  $r_1^{\text{ion}}$  and  $r_2^{\text{ion}}$  relaxivities. In contrast, the silica coated sample  $\text{Gd}_{0.6}\text{Eu}_{0.4}\text{VO}_4$  (MS19) shows slightly lower relaxivity values than the non-silica coated form MS6R. The first conclusion that can be drawn from these findings is that silica coating does not impede contact of water molecules with the gadolinium ions and that the silicate layer must therefore be porous. If the silica shell acted as a barrier, the  $r_1^{\text{ion}}$  as well as  $r_2^{\text{ion}}$  values would have decreased dramatically because the inner-shell contribution to the relaxivity which is based on direct contact between the water molecule and the

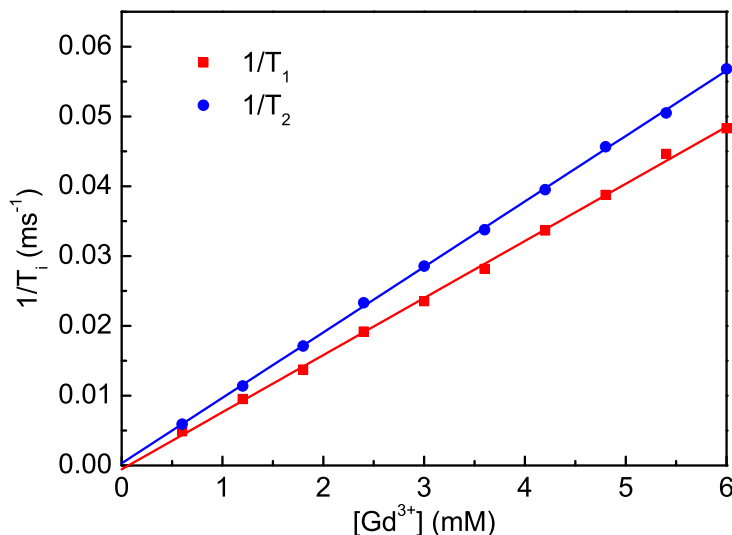


**Figure 4.9: Relaxation times for  $\text{Gd}_{0.6}\text{Eu}_{0.4}\text{VO}_4^{\text{cit}}$  nanoparticles.**  $T_1$  and  $T_2$  relaxation times were measured for the sample MS24 at 37 °C. The fit yields relaxivities of  $r_1 = 8.18 \text{ mM}^{-1} \text{ s}^{-1}$  and  $r_2 = 9.38 \text{ mM}^{-1} \text{ s}^{-1}$ .

paramagnetic ion would have been impeded (section 4.2.3). In this case the entire relaxivity must come from the outer sphere contribution and we would expect a smaller  $r_1^{\text{ion}}$  value (section 4.2.3.2). The apparent contradictory evolution of the relaxivities upon silica coating can be explained when considering two opposite effects. An increase in size of the particle increases the rotational correlation time according to eq. 4.8 which in turn reduces the relaxation time and increases the relaxivity. As  $\tau_R$  depends in the third power on the radius, a factor of about 1.3 in the size of the particles  $\text{GdVO}_4/\text{SiO}_2$  (MS2Si) and  $\text{Gd}_{0.6}\text{Eu}_{0.4}\text{VO}_4/\text{SiO}_2$  (MS19) changes  $\tau_R$  by more than a factor 2 and may have a pronounced effect on the relaxivities. On the other hand, size increase is a result of the thickness of the silica layer as the diameter of the non-silica coated nanoparticles MS4 and MS6R is almost identical. Although the silica shell is porous and does not impede water penetration, a thicker shell hampers the diffusion of the water molecules more than a thinner layer. We would therefore expect more hindrance in the case of the sample MS2Si. Considering our results, we find that the effect of size increase overcompensates the effect of a thicker silica layer. This finding supports further the fact that the silica layer is porous and adds only very little perturbation for the diffusion of water molecules.

The comparison of the samples  $\text{Gd}_{0.6}\text{Eu}_{0.4}\text{VO}_4$  (MS6R) to  $\text{GdVO}_4$  (MS4) and  $\text{Gd}_{0.6}\text{Eu}_{0.4}\text{VO}_4^{\text{cit}}$  (MS24) to  $\text{GdVO}_4^{\text{cit}}$  (MS23) indicates that nanoparticles composed of  $\text{Gd}^{3+}$  and  $\text{Eu}^{3+}$  ions possess higher relaxivity values than the nanoparticles containing only  $\text{Gd}^{3+}$ . In this case, it is better to compare the relaxivities per nanoparticle as these are corrected for the different compositions and represent the performance of the material.  $r_1^{\text{NP}}$  as well as  $r_2^{\text{NP}}$  are, in both cases, about twice as high for the Eu-containing nanoparticles as for the nanoparticles not containing any Eu. We remind that  $\text{Eu}^{3+}$  should, at least in its electronic ground state,

**Table 4.8: Relaxivities for rare earth vanadate nanoparticles.** Particle sizes are given as the number average diameter from dynamic light scattering (DLS).  $r_i^{ion}$  is the relaxivity relative to the molar quantity of  $Gd^{3+}$  ions. The relaxivity for an average nanoparticle is denoted by  $r_i^{NP}$ . In both cases,  $i$  may either be 1 or 2. The superscript cit denotes nanoparticles formed *via* the citrate route. CC stands for coordination complex.

composition	$d_{\langle n \rangle}$ (nm)	sample	$r_1^{ion}$	$r_2^{ion}$	$r_1^{NP}$	$r_2^{NP}$	$r_2/r_1$
			(mM <sup>-1</sup> s <sup>-1</sup> )				
GdVO <sub>4</sub>	41	MS4	0.95	1.31	420,000	570,000	1.38
GdVO <sub>4</sub> /SiO <sub>2</sub>	72 <sup>†</sup>	MS2Si	1.12	2.08	not determined		1.86
Gd <sub>0.6</sub> Eu <sub>0.4</sub> VO <sub>4</sub>	42	MS6R	2.97	3.47	840,000	980,000	1.17
Gd <sub>0.6</sub> Eu <sub>0.4</sub> VO <sub>4</sub> /SiO <sub>2</sub>	57	MS19	2.52	3.03	710,000	860,000	1.21
GdVO <sub>4</sub> <sup>cit</sup>	11	MS23	4.60	5.52	39,000	47,000	1.20
Gd <sub>0.6</sub> Eu <sub>0.4</sub> VO <sub>4</sub> <sup>cit</sup>	14	MS24	8.18	9.38	86,000	98,000	1.15
Y <sub>0.6</sub> Eu <sub>0.4</sub> VO <sub>4</sub> /GdVO <sub>4</sub>	55	MS26	4.0	4.7	$2.5 \cdot 10^6$	$2.9 \cdot 10^6$	1.2
Dotarem <sup>®</sup>	CC	Guerbet	3.59	4.44	–	–	1.24
GdCl <sub>3</sub>	ion	Prolabo	10.4	12.1	–	–	1.16

<sup>†</sup>The comparison of the DLS data (tab. 2.4) for the samples MS2 and MS2Si shows that the pristine material is probably aggregated so that  $r_i^{ion}$  can not be calculated.

not contribute to the magnetic moment and should therefore not increase the relaxivity. Nevertheless, our data confirms the opposite. Although several Eu-doped Gd-containing nanoparticulate systems are reported in the literature (Shi *et al.*, 2010; Wong *et al.*, 2009), a comparison of Eu-containing and non-Eu-containing nanoparticles from the same synthesis pathway, in order to study the effect of Eu-doping on the relaxivity, was never carried out to our knowledge. Considering the large difference in the relaxivities of nanoparticles with and without Eu, the simple partial population of an excited electronic state seems not to be sufficient to explain the origin of the observed relaxivity increase and we conducted thus frequency-dependent relaxation time measurements on these samples in the attempt to study further this phenomenon. The results will be presented in section 4.4.2.

Another finding concerns the size effect for samples without silica coating. When we compare the samples GdVO<sub>4</sub><sup>cit</sup> (MS23) to GdVO<sub>4</sub> (MS4) and Gd<sub>0.6</sub>Eu<sub>0.4</sub>VO<sub>4</sub><sup>cit</sup> (MS24) to Gd<sub>0.6</sub>Eu<sub>0.4</sub>VO<sub>4</sub> (MS6R), we find higher relaxivities values per ion for the smaller particles prepared by the citrate route. This is not a contradiction to the first case where we compared the effect of silica coating. When silicating a sample, the size increases without adding any Gd but results from addition of silica as a magnetically inactive compound. In the present case, different sizes result from a different distribution of the magnetically active Gd-containing compound. As the relaxivities per ion are normalized to the Gd-quantity, a different size of nanoparticles means a different contact surface. For the explanation of this effect, we assume the nanoparticles as spheric for simplicity. The volume of a nanoparticle is proportional to the number of Gd ions contained when dealing with nanoparticles

of one and the same composition. We can therefore consider the relaxivities per concentration as relaxivities per volume of substance. The volume of a sphere is  $V = (1/6)\pi d^3$  and its surface  $S = \pi d^2$ . The surface to volume ratio which specifies the surface per quantity of substance scales then as  $S/V \propto 1/d$ . The ratio of the surfaces between nanoparticles from the normal synthesis route and those from the citrate route is therefore about 3. When we compare the  $r_1^{ion}$  and  $r_2^{ion}$  values for the respective materials, we find also a factor on the order of 3. This finding indicates that the relaxivity is mainly influenced by the active contact surface between the nanoparticle and the water protons. A much larger surface corresponds to more Gd ions which can be exposed to the surrounding water. This change in the number of accessible Gd centers together with the importance of direct contact between water protons and Gd ions for the inner-sphere mechanisms is responsible for the higher relaxivities per ion. The effect of an increased contact surface seems to be more important than the slowing down of the tumbling due to a bigger particle. Assuming that the toxicity of the nanoparticles is only determined by the total Gd quantity administered to the patient, it is preferable to produce more nanoparticles of smaller size for a given quantity of material. The relaxivity per nanoparticle is of course smaller for the nanoparticles from the citrate synthesis route than for those from the normal route as the number of Gd ions per particle as well as the absolute surface area are reduced.

We will now compare the relaxivity of the core-shell nanoparticles  $Y_{0.6}Eu_{0.4}VO_4/GdVO_4$  (MS26) with that of other nanoparticles obtained from the normal synthesis route. As we already mentioned in section 4.3.1, the long-term stability of dispersed core-shell nanoparticles was poor and depending on the time requirement for a measurement, slight precipitation during data acquisition was possible. As precipitation diminishes the concentration of nanoparticles which can act on proton relaxation, the given values of  $r_1$  and  $r_2$  probably underestimate slightly the relaxivities and should be taken as a lower limit. A direct comparison between nanoparticles with core-shell structure and the single component ones  $GdVO_4$  (MS4) and  $Gd_{0.6}Eu_{0.4}VO_4$  (MS6R) is difficult because of the different particle diameters. As bigger particles tend to have higher relaxivities per particle  $r_i^{NP}$ , the higher values for  $Y_{0.6}Eu_{0.4}VO_4/GdVO_4$  may be at least partially explainable by the size increase. However, taking into account our findings about the large effect of the contact surface, it seems plausible that, in the case of nanoparticles of the same size, the core-shell particles are more efficient for relaxation enhancement than the homogeneous  $GdVO_4$  (MS4) or  $Gd_{0.6}Eu_{0.4}VO_4$  (MS6R) nanoparticles. In the core-shell nanoparticles, the magnetically active  $Gd^{3+}$  ions lie close to the surface and can interact with water protons whereas  $Gd^{3+}$  ions in the center of the homogeneous nanoparticles do not have direct contact to water. A more in-depth analysis would demand nanoparticles of the same size for all designs.

The relaxivity ratio  $r_2/r_1$  for Dotarem<sup>®</sup> and free  $Gd^{3+}$  ions is about 1.2. The suspensions of our nanoparticles except those made up from pure and homogeneous  $GdVO_4$  from the normal synthesis route show also this ratio. The behavior of the two latter samples (MS4 and MS2Si) may be explained by the onset of magnetic interaction between the  $Gd^{3+}$  ions in the spatially extended  $GdVO_4$  phase (section 1.3.3). Such an interaction would yield higher  $r_2$  values and the corresponding

material would tend to become a negative contrast agent like superparamagnetic iron oxide nanoparticles. A similar size-dependent behavior of the  $r_2/r_1$  ratio has also been observed by Bridot *et al.* (2007) for their  $\text{Gd}_2\text{O}_3$  nanoparticles.

#### 4.4.2 Frequency-dependent relaxation times

Longitudinal relaxation times were measured by Pierre Levitz from the *Laboratoire de Physique de la Matière Condensée* (LPMC) as a function of the Larmor frequency in the range from  $\omega/2\pi = 10$  kHz to 15 MHz. The corresponding concentration-normalized relaxivities are plotted in fig. 4.10 for  $\text{GdVO}_4$  nanoparticles doped or not with  $\text{Eu}^{3+}$  and from the normal and citrate route syntheses. We observe

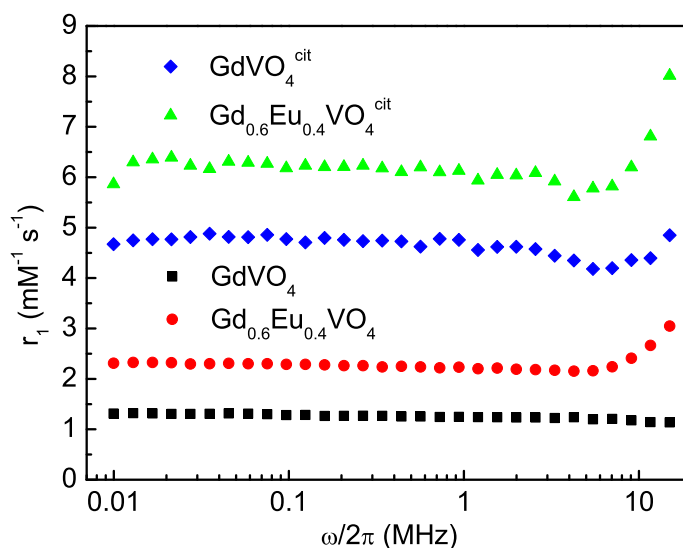


**Figure 4.10: Comparison of the NMRD profiles for several Gd-containing nanoparticles.** Data are shown for nanoparticles composed of  $\text{GdVO}_4$  (MS4) and  $\text{Gd}_{0.6}\text{Eu}_{0.4}\text{VO}_4$  (MS6R) from the normal synthesis route as well for the nanoparticles  $\text{GdVO}_4^{\text{cit}}$  (MS23) and  $\text{Gd}_{0.6}\text{Eu}_{0.4}\text{VO}_4^{\text{cit}}$  (MS24) produced by the citrate route at  $25^\circ\text{C}$ .

that the relaxivities are nearly constant for all samples up to a frequency of about 5 MHz. This behavior is also found for Gd chelates where the constant range extends up to 1-10 MHz depending on the actual contrast agent (fig. 4.11). Over the whole frequency range, the suspensions containing nanoparticles from the citrate route show higher relaxivities than those from the normal synthesis pathway. Furthermore, Eu-containing nanoparticles possess also for all measured frequencies a higher  $r_1$  relaxivity than those not containing Eu. This behavior confirms the trend from the measurements at a fixed frequency of 20 MHz. A direct quantitative comparison at 20 MHz is not feasible as the measurements were not performed at the same temperature and only up to 15 MHz. At the moment, we do not have a comprehensive understanding of the influence of Eu-doping on the relaxivities and further studies will have to be performed in the future to elucidate this problem.

It is interesting to compare the relaxation behavior of our nanoparticles with that of common Gd chelates for higher frequencies when leaving the plateau range.

## Figure withdrawn due to copyright restrictions

**Figure 4.11: NMRD profiles for three clinically approved Gd<sup>3+</sup> contrast agents.** All data are for a temperature of 25 °C. For ligand abbreviations and the corresponding structures see fig. 4.5 and 4.6. Reprinted with permission from P. Caravan *et al.*, Chem. Rev. 99 (9), 2293-2352. Copyright 1999. American Chemical Society.

While the relaxivity decreases dramatically for *e. g.* Dotarem<sup>®</sup> from 1 MHz to 10 MHz, the relaxivities for our Eu-containing nanoparticles (MS6R and MS24) increase steeply (fig. 4.10). The effect is less pronounced in the case of GdVO<sub>4</sub> nanoparticles from the citrate route (MS23) and is not visible because presumably outside the measurement window for nanoparticles of the same composition and from the normal synthesis pathway (MS4). Assuming that the outer-sphere contribution is of about the same magnitude for all samples as discussed in section 4.2.3.2 for the case of small Gd chelates, we can attribute the different behavior between Gd chelates and nanoparticles to a change in the inner-sphere relaxivity. The theoretical analysis of the inner-sphere relaxation process (section 4.2.3.1) and the simulation of the dipolar component (eq. 4.14) for different values of the rotational correlation time as conducted by Caravan *et al.* (1999) allow to explain the different evolution at high frequencies. Eq. 4.14 itself contains two contributions. There is a term dependent on the nuclear precession frequency  $\omega_H$  (nuclear term) and a term which is a function of the electronic precession frequency  $\omega_S$  (electronic term). As the gyromagnetic ratio is much bigger for an electron than for a proton with the ratio being  $\gamma_S/\gamma_H = 658$ , the electronic term is bigger than the nuclear term for low frequencies. At high frequencies, the nuclear contribution becomes important and the electronic contribution approaches zero. Depending on the actual value of  $\tau_{c1}$  which itself is a function of  $\tau_R$  (eq. 4.16), the shape of the dispersion curves changes. A lengthened rotational correlation time  $\tau_R$  produces a bigger value of  $\tau_{c1}$  which can

finally change the shape of the curve from a higher to a lower plateau descent to a marked maximum peak.

We can estimate the influence of the rotational correlation time using eq. 4.8. For spherical nanoparticles with a radius  $a = 6$  nm at  $25^\circ\text{C}$  in water with a viscosity of  $\eta \approx 0.9$  mPa  $\cdot$  s (Sengers and Watson, 1986) we obtain a  $\tau_R = 200$  ns. In contrast,  $\tau_R$  for Dotarem<sup>®</sup> is only about 80 ps (Powell *et al.*, 1996). The factor of about 2,500 can change dramatically the influence of the electronic and nuclear term to the overall relaxation. Due to the complexity of the relaxation mechanism reflected in the number of parameters involved in the Solomon-Bloembergen-Morgan equations, we did not perform a more detailed analysis of the relatively featureless NMRD curves because it would be prone to error (Caravan *et al.*, 1999).

Unfortunately the measurement range of the employed instrument is not sufficient to record the whole peak but the onset of a peak is clearly visible for all samples except the  $\text{GdVO}_4$  (MS4) one. As commercial MRI scanners operate at a magnetic field of 1.5 T or now also 3 T, corresponding to a proton resonance frequency of 64 MHz or 128 MHz, respectively, a contrast agent that shows a marked relaxation maximum in this range is of great interest.

### 4.4.3 Luminescence

The luminescence spectrum of a suspension of  $\text{Gd}_{0.6}\text{Eu}_{0.4}\text{VO}_4$  nanoparticles from the normal route synthesis (MS6R) is shown in fig. 4.12.  $\text{Gd}_{0.6}\text{Eu}_{0.4}\text{VO}_4$  shows

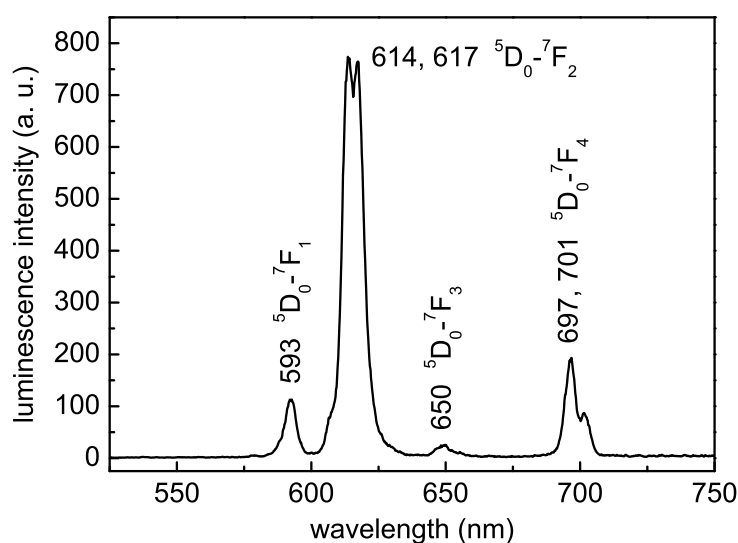


**Figure 4.12: Luminescence emission spectrum for  $\text{Gd}_{0.6}\text{Eu}_{0.4}\text{VO}_4$  nanoparticles.** Data is for sample MS6R. Luminescence was excited at 280 nm. The peak positions as well as the corresponding transitions are indicated.

generally the same emission spectrum as  $\text{Y}_{0.6}\text{Eu}_{0.4}\text{VO}_4$  (fig. 3.7).  $\text{Gd}_{0.6}\text{Eu}_{0.4}\text{VO}_4$  absorbs strongly in the UV range and an efficient energy transfer is possible from the  $\text{VO}_4^{3-}$  ions to  $\text{Eu}^{3+}$  ions (Jin *et al.*, 2008). We find one emission peak at 593 nm

due to the  ${}^5D_0 - {}^7F_1$  transition, the strong principal double emission peak at 616 nm ( ${}^5D_0 - {}^7F_2$ ), a very weak peak at 650 nm ( ${}^5D_0 - {}^7F_3$ ) and another double peak at 699 nm ( ${}^5D_0 - {}^7F_4$ ). The spectrum corresponds to those found for Eu doped  $GdVO_4$  in the literature. Jin *et al.* (2008) reported for ricelike nanoparticles with a length of 120 nm and a width of 50 nm composed of  $Gd_{0.9}Eu_{0.1}VO_4$  the central peak at 616 nm using an excitation at 260 nm. Zheng *et al.* (2011) synthesized  $Gd_{0.95}Eu_{0.05}VO_4$  microstructures with a particle size of 800 nm for which they found the most intense peak at 618 nm following excitation at 277 nm.

Concerning the quantum yield, we have determined a value of 3.8 % for this sample which is about a factor 3 smaller than the quantum yield for the  $Y_{0.6}Eu_{0.4}VO_4$  samples (tab. 3.4). This finding is surprising as Palilla *et al.* (1965) reported that the substitution of  $Y^{3+}$  by  $Gd^{3+}$  provides an equally efficient material with no significant spectral differences. Unfortunately they do not give the Eu concentration in their samples but it seems that the study was carried out using low Eu concentration of a few percent. The photophysical characteristics may change with increasing Eu concentration. A recent study using the compound  $Y_{0.6}Eu_{0.4}VO_4$  showed that the quantum yield depends on the Eu to matrix ion ratio and does not show the same evolution for the bulk material and nanoparticles (Mialon, 2009; Mialon *et al.*, 2009). It is therefore possible that our lower quantum yields for Gd matrices result from a combination of particle size and composition effects. We finally note that the emission spectrum of  $Y_{0.6}Eu_{0.4}VO_4/GdVO_4$  core-shell nanoparticles (graph not shown) displays the same peaks as that of  $Gd_{0.6}Eu_{0.4}VO_4$ .

#### 4.4.4 Hydrogen peroxide detection

Eu-doped nanoparticles were spincoated densely on a coverslip and illuminated at high laser intensity. The corresponding time-dependent luminescence intensity is shown in the upper panel of fig. 4.13 for nanoparticles of the composition  $Gd_{0.6}Eu_{0.4}VO_4$  and in the upper panel of fig. 4.14 for core-shell nanoparticles made up from  $Y_{0.6}Eu_{0.4}VO_4/GdVO_4$ . The decreasing luminescence intensity confirms that photoreduction takes place in both systems. We obtain characteristic decay times of about 10 s and 200 s for the nanoparticles consisting of a Eu-doped  $GdVO_4$  matrix and about 20 s and 120 s for the core-shell particles. The intensity changes upon photoreduction were about 70 % and 40 %, respectively. The values for the first sample are comparable to those obtained for our silica coated  $Y_{0.6}Eu_{0.4}VO_4$  samples as well as to formerly obtained data (Casanova *et al.*, 2009). In contrast, core-shell nanoparticles show a weaker bleaching.

The luminescence recovery relative to the initial intensity after photoreduction was 18 % for the particles with mixed Gd and Eu at 10 mM  $H_2O_2$  and 15 % for core-shell particles at 100  $\mu$ M  $H_2O_2$ . In the first case, the maximum recovery was already achieved after about 2 min although the measurement was conducted for 10 min. The maximum recovery of 18 % for a  $H_2O_2$  concentration of 10 mM seems small compared to values of 200 % obtained for 45  $\mu$ M  $H_2O_2$  by Casanova *et al.* (2009). As discussed in section 3.2.5.1, this difference may be explained by the actual measurement protocols where ensemble detection and not single particle detection was performed. In core-shell particles, the saturation of the luminescence recovery is

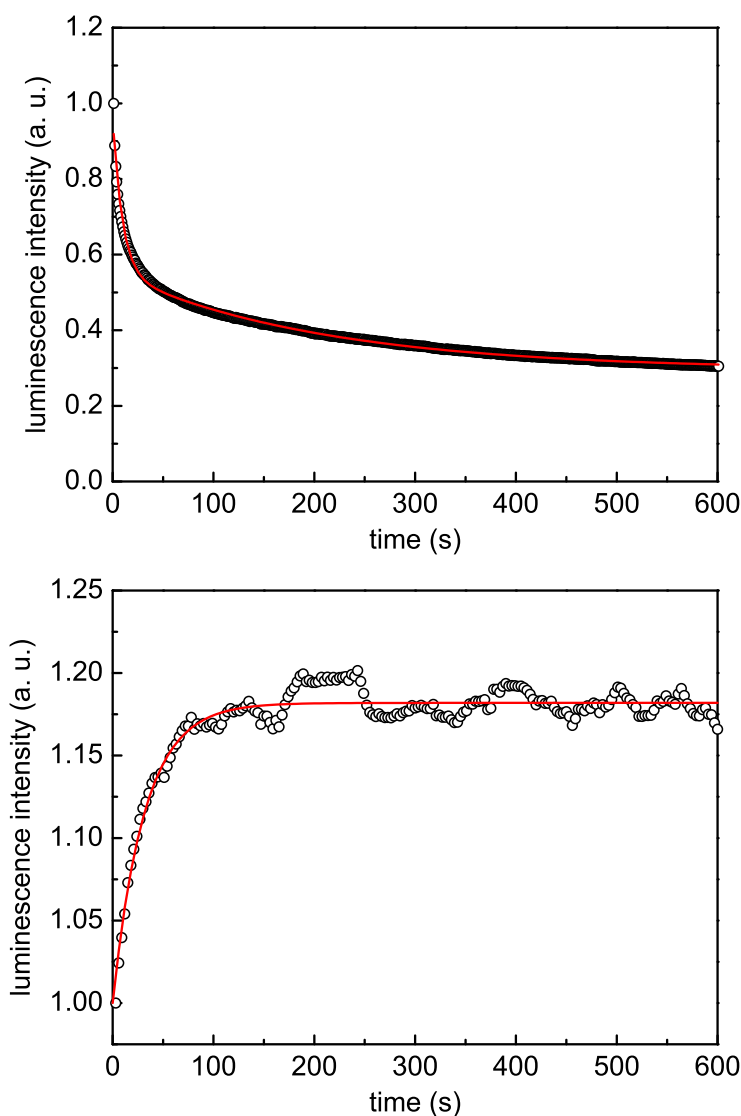


**Figure 4.13:  $\text{Gd}_{0.6}\text{Eu}_{0.4}\text{VO}_4$  nanoparticles as hydrogen peroxide sensors in ensemble detection.**

Data are for sample MS6R. Illumination was performed at 466 nm. Upper graph: Photoreduction. Laser intensity:  $1.6\text{ kW/cm}^2$ . Exposition time: 800 ms. 1 image per s. Data was fit with a biexponential decay function:  $I = I_\infty + a_1 \exp\left(-\frac{t}{\tau_1}\right) + a_2 \exp\left(-\frac{t}{\tau_2}\right)$ . The fit yielded the decay constants  $\tau_1 = 9.6\text{ s}$  and  $\tau_2 = 206\text{ s}$  as well as the remaining intensity  $I_\infty = 30\%$ . Lower graph: Luminescence recovery after adding 10 mM hydrogen peroxide. Laser intensity:  $0.3\text{ kW/cm}^2$ . Exposition time: 800 ms. 1 image per 3 s. Data was fit with a monoexponential growth function:  $I = 1 + \Delta I \cdot \left[1 - \exp\left(-\frac{t}{\tau^*}\right)\right]$ . We obtained a normalized luminescence recovery of  $\Delta I = 18\%$  with a recovery constant  $\tau^* = 31\text{ s}$ .

much slower. This behavior is certainly due to the 100-fold lesser hydrogen peroxide concentration. However, compared to the characteristic constants for silica coated nanoparticles made up from  $\text{Y}_{0.6}\text{Eu}_{0.4}\text{VO}_4$  (section 3.2.5.1) also determined at a hydrogen peroxide concentration of  $100\ \mu\text{M}$ , we find that the total recovery is lower and the characteristic recovery time longer for core-shell particles.

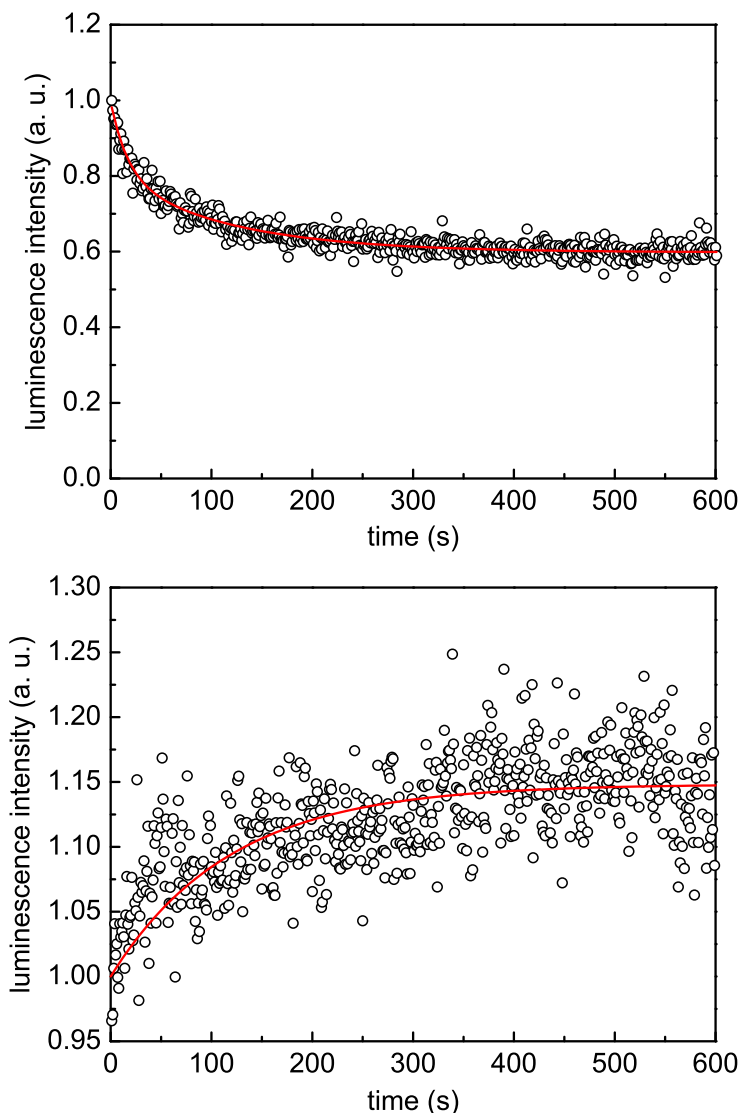


**Figure 4.14:  $\text{Y}_{0.6}\text{Eu}_{0.4}\text{VO}_4/\text{GdVO}_4$  core-shell nanoparticles as hydrogen peroxide sensors in ensemble detection.** Data are for sample MS26. Illumination was performed at 466 nm. Upper graph: Photoreduction. Laser intensity:  $1.6 \text{ kW/cm}^2$ . Exposition time: 100 ms. 1 image per s. Data was fit with a biexponential decay function:  $I = I_\infty + a_1 \exp\left(-\frac{t}{\tau_1}\right) + a_2 \exp\left(-\frac{t}{\tau_2}\right)$ . The fit yielded the decay constants  $\tau_1 = 17 \text{ s}$  and  $\tau_2 = 116 \text{ s}$  as well as the remaining intensity  $I_\infty = 60 \%$ . Lower graph: Luminescence recovery after adding  $100 \mu\text{M}$  hydrogen peroxide. Laser intensity:  $0.3 \text{ kW/cm}^2$ . Exposition time: 400 ms. 1 image per s. Data was fit with a monoexponential growth function:  $I = 1 + \Delta I \cdot [1 - \exp\left(-\frac{t}{\tau^*}\right)]$ . We obtained a normalized luminescence recovery of  $\Delta I = 15 \%$  with a recovery constant  $\tau^* = 119 \text{ s}$ .

The findings of lower photoreduction and recovery as well as of longer characteristic recovery times compared to silica coated  $\text{Y}_{0.6}\text{Eu}_{0.4}\text{VO}_4$  nanoparticles indicate that although the  $\text{GdVO}_4$  shell does not impede the contact between the  $\text{Y}_{0.6}\text{Eu}_{0.4}\text{VO}_4$  core and hydrogen peroxide, it induces more hindrance than a silica layer. To confirm the presence of such an effect, measurements on single particles should be

performed. These were not conducted here as they are more complex and as the aim of this study was a proof of principle of the hydrogen peroxide detection capability of multimodal nanoparticles. The obtained results clearly show that the intensity increase of photoreduced nanoparticles is due to the action of  $\text{H}_2\text{O}_2$ .

## 4.5 Conclusion

In this chapter, we discussed the importance of multimodal imaging and of imaging combined with therapy. We presented the properties of vanadate nanoparticles containing only Gd or simultaneously Gd and Eu in view of their application as multimodal agents. We showed that  $\text{GdVO}_4$  nanoparticles act as a potent positive contrast agent resulting from high relaxivities and a low  $r_2/r_1$  ratio. The relaxivities can even be increased by employing the citrate route synthesis which yields small particles of about 10 nm diameter or by Eu-doping of the particles. Stable dispersions of  $\text{Gd}_{0.6}\text{Eu}_{0.4}\text{VO}_4^{\text{cit}}$  nanoparticles possess relaxivities higher than that of Dotarem<sup>®</sup>, a standard clinically approved positive contrast agent. In addition, due to the presence of Eu, these nanoparticles are multimodal and show also luminescence and have the capability to detect hydrogen peroxide. Our frequency dependent relaxation time measurements indicated that  $\text{Gd}_{0.6}\text{Eu}_{0.4}\text{VO}_4$  and  $\text{Gd}_{0.6}\text{Eu}_{0.4}\text{VO}_4^{\text{cit}}$  nanoparticles probably exhibit a marked relaxivity maximum around the working field strengths of commercial MRI scanners and could therefore be particularly suited for this application. A further increase of the multimodal performances seems to be possible by using core-shell nanoparticles with a core optimized for luminescence and a shell with proton relaxation enhancement potential. We have further demonstrated that the luminescence spectrum does not change significantly upon substitution of Y by Gd in the matrix and that the strong red emission is maintained for  $\text{Gd}_{0.6}\text{Eu}_{0.4}\text{VO}_4$  nanoparticles.  $\text{Gd}_{0.6}\text{Eu}_{0.4}\text{VO}_4$  as well as core-shell nanoparticles show a photoreduction behavior and a luminescence recovery upon addition of hydrogen peroxide which makes the particles suitable for time- and space-resolved  $\text{H}_2\text{O}_2$  detection on a single particle level.

We have thus demonstrated that our nanoparticles can act as contrast agents in MRI, as photostable luminescent dyes and as hydrogen peroxide sensors. Based on reports in the literature, several further applications seem possible. As our particles can be functionalized (Casanova *et al.*, 2007; Giaume *et al.*, 2008), addition of specific targeting moieties to the surface is feasible. A second organic fluorophore may also be grafted to the surface as already shown for  $\text{Y}_{0.6}\text{Eu}_{0.4}\text{VO}_4$  nanoparticles enabling dual color imaging (Casanova *et al.*, 2006). We also expect a contrasting effect in X-ray computed tomography due to the incorporation of heavy atoms with high electron densities. Chemotherapy by coupling nanoparticles to anti-cancer drugs with simultaneous monitoring of the location of the carrier by MRI should also be possible. A very promising application is the use of our Gd-containing nanoparticles in NCT where the positioning of the radiation source could be followed by MRI and/or luminescence imaging. For PET imaging, theoretically nanoparticle syntheses may be carried out with radioactive  $^{86}\text{Y}$  or, perhaps more feasible, the

radio nuclide  $^{64}\text{Cu}$  may be bound to the surface of the nanoparticles by organic chelator molecules.

# Summarizing discussion and outlook

Multimodal imaging techniques are becoming more and more important. The use of a probe or a contrast agent which generates a signal in several imaging techniques is particularly interesting as it provides a wealth of information which cannot be obtained employing only a single imaging method. Additional benefits arise from less toxicity as a lower amount of xenobiotics has to be introduced in the organism examined and a cost reduction as only one instead of several probes have to be administered. In this perspective, we have developed a new type of rare earth vanadate nanoparticles for multiple imaging techniques including luminescence, oxidant detection, and magnetic resonance.

These nanoobjects were designed based on the comprehensive data available on nanoparticles of the general type  $Y_{1-x}Eu_xVO_4$  and in particular  $Y_{0.6}Eu_{0.4}VO_4$  which show a strong, non-blinking and stable luminescence due to the presence of  $Eu^{3+}$  ions. Additionally to the pure application as a luminescence label, this type of particles can serve to detect inside the cell endogenously produced oxidants and especially hydrogen peroxide with temporal and spatial resolution. This ability relies on a reversible change of the oxidation state of  $Eu^{3+}$  ions linked with a modification of the luminescence emission properties. The substitution of  $Y^{3+}$  by the paramagnetic ion  $Gd^{3+}$  confers proton relaxation enhancing properties to the nanoparticles due to the possible interaction between the electronic spin of  $Gd^{3+}$  and the nuclear spins of protons in surrounding water. We have synthesized nanoparticles made up from pure  $GdVO_4$  and in the Eu-doped form of the composition  $Gd_{0.6}Eu_{0.4}VO_4$ . Thanks to the well documented syntheses routes, it was possible to produce for the two compositions nanoparticles of either about 10 nm or 40 nm diameter. Core-shell nanoparticles of about 40 nm were obtained using a new synthesis protocol forming first a core of  $Y_{0.6}Eu_{0.4}VO_4$  which is then surrounded by a  $GdVO_4$  shell.

A crucial information about the nanoparticles, in particular for the application as an MRI contrast agent, is the concentration of rare earth ions or equivalently vanadate in a given aqueous preparation. We have studied in detail a wet chemistry approach relying on the quantification of vanadate by a colorimetric reaction. We have proven that the nature of the rare earth counterions does not influence the absorption constant of the red-brown colored vanadium complex. Precise measurements allowed to define an accuracy limit of this detection principle which was determined to be less than 2%. Another important issue when using these nanoparticles as MRI contrast agents in living organisms is their stability. As free gadolinium as well as vanadate ions in the form of orthovanadate are toxic, a degradation of the nanoparticles must be excluded. We used a colorimetric reaction based on the complexation of free rare earth ions by an organic chelator to determine the concentration of released ions. The measurement showed that the leached rare

earth ion concentration remained below about 20  $\mu\text{M}$  after almost two weeks. The comparison of these data with leached concentrations for other nanoparticle systems from the literature confirmed the stability of our compound and suggests a suitability of our nanoparticle system for *in vivo* applications which has to be confirmed by measurements of the nanoparticle biodistribution.

One of the central questions when dealing with nanoparticles is their morphology expressed in terms of size, shape and if applicable their substructure. At the same time, it is difficult to define a true size as different measurement methods yield results biased by different factors. Dynamic light scattering is a easy and rapid method for routine measurements mainly aiming to compare relative data between different nanoparticle systems. However, assuming that electron microscopy defines dimensions that are closer to the true geometrical ones, light scattering generally overestimates the particle size. The apparently simple conclusion that it is better to determine particle sizes by microscopy is contradicted by the time consuming procedure that is necessary to obtain a reasonable ensemble averaging. We employed a method based on the analysis of the reflection broadening in the X-ray diffraction pattern of powderous dried nanoparticles to gain information about the microstructure of the nanoobjects. The technique is relatively simple, requires, besides the diffraction pattern of a bulk reference material, no further information and allows for the reconstruction of the shape of the smallest crystalline entity in the material, the crystallite. We found that crystallites in 40 nm  $\text{GdVO}_4$  nanoparticles have a shape best described as compressed prolate spheroids or platelets with about 25 nm length and 16 nm height. From the comparison with the electron microscopy dimensions for the entire nanoparticle, it is clear that one nanoparticle consists of several crystallites. This finding enabled us, on the one hand, to tentatively propose a model for the assembly of the crystallites in the nanoparticles, but on the other hand, impedes unfortunately an easy size determination of the entire nanoparticle by X-ray diffraction. Nevertheless, the recourse to microstructural analysis of X-ray data may reduce considerably the amount of electron micrographs needed for a reliable size determination due to the observed shape similarity between crystallites and nanoparticles.

Cellular signaling pathways are generally complex and their elucidation is difficult. Hydrogen peroxide mediated signaling cascades do not constitute an exception to this rule. It is therefore of special interest to possess a tool which enables the detection of hydrogen peroxide with temporal and spatial resolution. Common organic dyes suffer from the fact that hydrogen peroxide induces in most cases a non-reversible change of the molecular structure impeding the detection of decreasing concentrations after an initial burst. We have demonstrated that nanoparticles of the compositions  $\text{Gd}_{0.6}\text{Eu}_{0.4}\text{VO}_4$  and core-shell nanoparticles made up from  $\text{Y}_{0.6}\text{Eu}_{0.4}\text{VO}_4/\text{GdVO}_4$  retain the property of luminescence modulation by the oxidant concentration. Although we have not yet established a quantitative calibration diagram relating luminescence intensity and hydrogen peroxide concentration as done for particles of the composition  $\text{Y}_{0.6}\text{Eu}_{0.4}\text{VO}_4$ , the experiments serve as a proof of principle that gadolinium-containing rare earth vanadate nanoparticles can be used in experiments aiming to

elucidate signaling pathways. Of course, the property of being luminescent renders an application as pure luminescent probe also possible.

The interest of the incorporation of gadolinium in the nanoparticles resides in its property as a proton relaxation enhancing agent. Nowadays, a significant portion of all clinical MRI scans is performed after the administration of a contrast agent to the patient. Commercially available and clinically approved positive contrast agents are at present composed of  $\text{Gd}^{3+}$  ions complexed by an organic chelator with strong affinity in order to prevent the release of toxic free  $\text{Gd}^{3+}$  ions. However, this strong complexation hinders more efficient contact between the  $\text{Gd}^{3+}$  center and the water proton. Gadolinium as integral component of the nanoparticle crystal structure has the advantage of a very low leaching while surface ions can efficiently interact with protons. We found that the relaxivity of pure or Eu-doped  $\text{GdVO}_4$  nanoparticles of about 10 nm diameter as well as of the core-shell nanoparticles is higher than that of the commercial chelate compound Dotarem<sup>®</sup> making them promising candidates for a potential medical application. Our results from frequency-dependent relaxivity measurements demonstrate that the relaxivities for 40 nm as well as for 10 nm nanoparticles are, in the entire frequency range studied, higher if these particles are Eu-doped. Additionally, relaxivities for nanoparticle dispersions seem to increase in the frequency range of interest for medical imaging while those of typical gadolinium chelates decrease steeply.

In order to further study the role and influence of europium, we performed temperature- and field-dependent measurements of the magnetization for bulk  $\text{GdVO}_4$  and pure as well as Eu-doped  $\text{GdVO}_4$  nanoparticle powder samples. Data obtained for the bulk confirmed the paramagnetic behavior according to a Curie-Weiss law in the temperature range from 290 K down to 5 K. The measured Weiss temperature and susceptibility were in agreement with literature values and validate our measurement protocol. The results obtained for the nanoparticles evidenced a decrease in the Weiss temperature as expected from the theory. However, field-dependent magnetization data for particles doped or not doped with europium superimpose exactly so that a magnetization change can be excluded as the reason to explain higher relaxivities for Eu-doped nanoparticles. A consistent interpretation for the influence of the presence of  $\text{Eu}^{3+}$  ions has at the moment not yet been found.

The present data suggest that rare earth vanadate nanoparticles containing simultaneously europium and gadolinium ions either as a mixture or in a core-shell composition are very promising candidates for an application as *in vivo* multifunctional probes. Further research should be devoted to the development of a synthesis protocol for the production of core-shell nanoparticles of 10 nm diameter for which a significant increase in the relaxivity can be predicted. The question of the influence of  $\text{Eu}^{3+}$  ions on the relaxivity merits also to be studied further. It would be useful to obtain a calibration curve linking the observed luminescence recovery to the hydrogen peroxide concentration. This data could then allow to estimate the efficiency of the  $\text{Eu}^{3+}$  luminescence recovery in either a  $\text{GdVO}_4$  or a  $\text{YVO}_4$  matrix. However, one has to be aware that not only the matrix material composition but also the particle morphology influences the kinetic constants.

Another interesting approach would be to study the efficiency of our nanoparticles as a target in gadolinium neutron capture therapy. Data could be obtained

by characterization of the nuclear reaction upon irradiation of a nanoparticle dispersion with thermal neutrons. Irradiation of cancerous cells loaded previously with nanoparticles and determination of the growth inhibition would be another possibility. A probe for positron emission tomography can be obtained by association of the nanoparticles with the necessary isotopes for this technique. Possible designs include the direct incorporation of the isotope in the nanoparticle crystal structure or its binding or chelation to the functionalized particle surface. The introduction of these functionalities seem to be achievable with a reasonable expenditure of time as the involved nuclear reactions rely only on the presence of a specific isotope and are independent from the nanoparticle design.

# Appendix A

## Theory of characterization methods

### A.1 X-ray powder diffraction

#### A.1.1 Bragg-Brentano parafofocussing geometry

The use of the Bragg-Brentano geometry (Aslanov *et al.*, 1998; Louër, 2002) during data acquisition makes possible a parafofocussing of the incident radiation. The sample is illuminated by a divergent beam which allows for higher intensity than a collimated one. However, one introduces an angular error as the incident beam hits the sample at different points and angles. This error may be corrected for first by using a polycrystalline powder without preferential orientation and second by employing a  $\theta$ - $\theta$  geometry where the X-ray tube and the detector are placed at the same angle with respect to the sample plane. The second condition ensures that all diffracted beams are refocused at the detector position.

The underlying geometrical principle is shown in fig. A.1. Divergent X-rays are

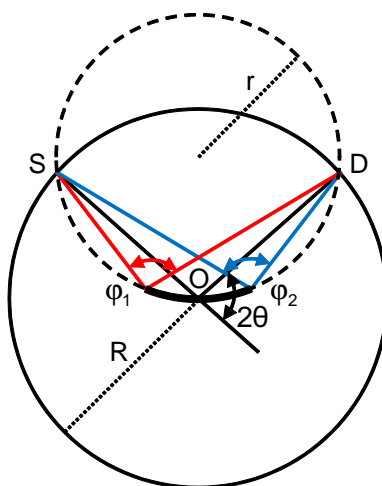


**Figure A.1: Bragg-Brentano parafofocussing geometry.** For further explanations see text.

produced by the source S at the distance  $R$  from the middle of the sample. The latter is fixed in its position O and the source as well as the receiving slit of the detector D move on a common goniometer circle with radius  $R$  according to the  $\theta$ - $\theta$  geometry. S, O and D lie always on a common circle, the focussing circle. Its radius  $r$  varies from  $R/2$  for  $2\theta = 0^\circ$  to  $\infty$  for  $2\theta = 180^\circ$ . The incident radiation hits the

sample on its left limit under the angle  $\varphi_1$  and under the angle  $\varphi_2$  on its right limit. If the Bragg condition is fulfilled, radiation is reflected under the same angle as the respective incident angles. Due to the geometry of the depicted circles, all radiation produced in S and reflected from any point of the sample will arrive exactly in D. However, this refocussing is only achieved if the sample possesses a curvature as shown in the figure which is continuously readjusted as the scattering angle changes. In practice, the sample has a flat surface and refocussing in D is therefore not perfect. This contributes to the observed linewidth. The line broadening effect decreases with increasing  $2\theta$ . Furthermore, the point detector may be replaced by a two-dimensional detector in order to accelerate the measurement, however, one is strictly speaking no longer in the Bragg-Brentano geometry although the results are found similar.

A systematic line shift error arises if the sample surface is not placed exactly in the center of the goniometer circle. In this case, observed reflection positions are shifted about  $\Delta(2\theta)$  in position according to the equation

$$\Delta(2\theta[\text{rad}]) = -\frac{2s}{R} \cos \theta \quad (\text{A.1})$$

with  $R$  being the radius of the goniometer circle and  $s$  the vertical displacement of the sample surface relative to the center of the circle (Wilson, 1963). This systematic aberration is the largest error affecting the line positions in Bragg-Brentano geometry.

Another source of a systematic error is the sample transparency, resulting in that the incident radiation penetrates significantly inside the sample and diffraction is not longer originating only from the sample surface (Wilson, 1963). In the case of rare earth vanadate materials, heavy metals with a high electron density are present leading to high X-ray absorption coefficients.

### A.1.2 Technical data of the X-ray diffractometer

Samples are finely ground prior to measurement in an agate mortar. Silicon powder (purity 99+ %, 325 mesh, Strem Chemicals) for determination of the instrumental resolution is used as received. X-ray powder diffraction (XPD) is performed on a X'pert MPD powder diffractometer (PANalytical) at ambient temperature. The sample is spun during acquisition at a speed of 1 turn/min. Copper  $K_\alpha$  radiation with the two components Cu  $K_{\alpha 1}$  at a wavelength of  $\lambda = 1.540598 \text{ \AA}$  and Cu  $K_{\alpha 2}$  at a wavelength of  $\lambda = 1.544390 \text{ \AA}$  is used. Data acquisition is performed in a Bragg-Brentano parafocussing geometry. The incident beam path contains in the following order after the X-ray tube a 0.02 rad Soller slit, a  $0.5^\circ$  divergence slit, a 10 mm mask and a  $1^\circ$  anti-scatter slit. In the diffracted beam path a 5.5 mm anti-scatter slit corresponding to an angular resolution of  $1^\circ$  and a 0.02 rad Soller slit are used. No monochromator is used in the optic path but a Ni foil placed before or after the Soller slit allow an elimination of the Cu  $K_\beta$  component. Diffracted intensity is monitored on a X'celerator area detector (PANalytical) which covers a scattering angle segment of  $2.546^\circ$  through a nickel filter. The optical path is shown in fig. A.2.

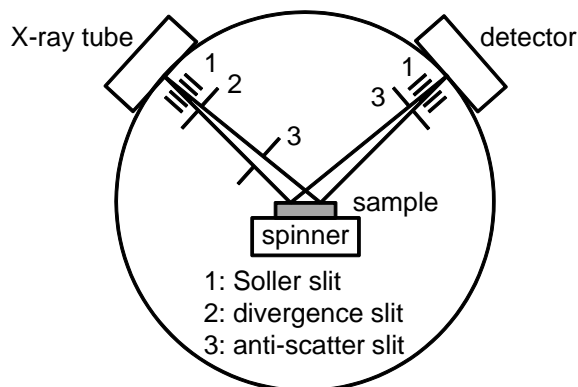


**Figure A.2: Data acquisition in Bragg-Brentano geometry.** The figure depicts the actual geometry used for our experiments. The mask is not shown.

### A.1.3 Calibration for instrumental aberrations

The systematic line shift error (section A.1.1) is assessed from the analysis of the line positions of silicon. 2.21 g  $\text{GdVO}_4$  from the ceramic method are gently mixed with 0.79 g silicon powder (purity 99+ %, 325 mesh, Strem Chemicals). The specified mesh size means that the silicon particles have a diameter smaller than  $44 \mu\text{m}$ <sup>1</sup>. Data acquisition is performed in the  $2\theta$  range from  $10^\circ$  to  $82^\circ$  with a step width of  $0.005^\circ$  and an integration time of 100 s per step. Peaks for silicon are identified by comparing their positions with those given by Hubbard *et al.* (1975). Precise peak positions are determined by fitting a pseudo-Voigt function to each  $\text{Cu } K_\alpha$  doublet using FullProf. The position obtained from  $\text{Cu } K_{\alpha 1}$  radiation is used for the comparison with the literature position and eq. A.1 is employed for calculation of the correction factor.

### A.1.4 Correction factor for sample eccentricity

The correction factor for eccentricity was determined from the Bragg peaks of silicon. Observed peak positions were compared to literature values (Hubbard *et al.*, 1975) and the peak displacement is plotted in fig. A.3 as a function of the peak position from the literature  $\theta_{lit}$ . Using the radius of the goniometer circle of  $R = 200 \text{ mm}$ , we can calculate from eq. A.1 a vertical displacement of the sample surface of  $s = \frac{aR}{2} = (0.22 \pm 0.01) \text{ mm}$ . This displacement is due to a combination of inaccuracies arising from the mechanical calibration of the diffractometer and from the filling height of the sample in the sample holder. As the determined value is very small, we may assume that the sample holder filling procedure is sufficient accurate. In default of a recalibration measurement for each sample studied which would demand mixing of a big sample quantity with silicon powder and subsequently the loss of the sample for further characterizations, we will use the fixed correction factor  $SYCOS = a = 0.0022$  in FullProf for all diffraction pattern refinements. We note that, in

<sup>1</sup>E11-09e1 Standard Specification for Woven Wire Test Sieve Cloth and Test Sieves, American Society for Testing and Materials, West Conshohocken, PA, USA (2009)

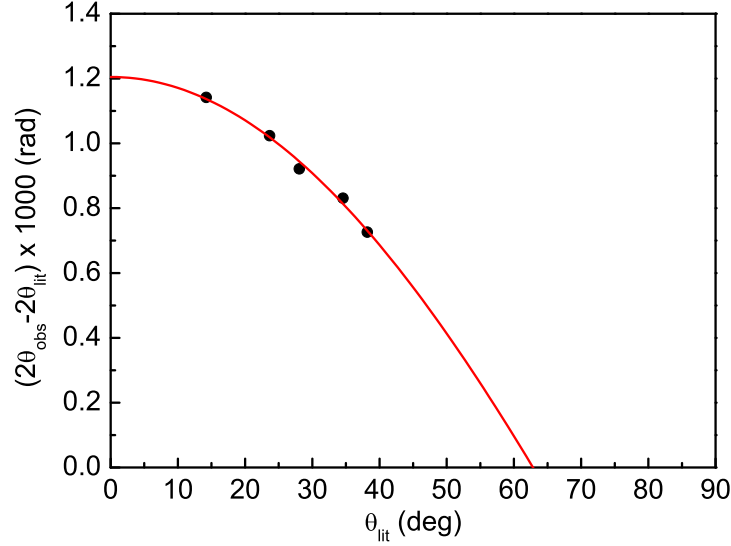


**Figure A.3: Displacement of the reflection positions of silicon.** Data was fitted to the equation  $2\theta_{obs} - 2\theta_{lit} = \Delta(2\theta) = a \cos \theta + b$  where  $b$  allows for a systematic constant shift independent on the scattering angle. The values of  $a = -0.0022 \pm 0.0001$  and  $b = -0.0010 \pm 0.0001$  were obtained.

principle, this factor can also be refined for each individual diffraction pattern as a free parameter but as a strong correlation with the zero shift value can take place, it is preferable to use this determined value as a fixed quantity.

### A.1.5 Profile shape function

Diffraction peaks from Bragg reflections have a finite width due to various physical effects. This width which can either be characterized by the full-width at half maximum (FWHM) denoted as  $\Gamma$  or by the integral peak breadth  $\beta$  which is defined as the width of a rectangle having the height of the peak and the same surface as the integrated peak surface.

Several functions have been proposed in the literature to model X-ray diffraction peak shapes (Young and Wiles, 1982). The Voigt function

$$\begin{aligned} V(2\theta - 2\theta_{\mathbf{H}}) &= L(2\theta - 2\theta_{\mathbf{H}}) \otimes G(2\theta - 2\theta_{\mathbf{H}}) \\ &= \int_{-\infty}^{+\infty} L[(2\theta - 2\theta_{\mathbf{H}}) - \Delta(2\theta)] \cdot G[\Delta(2\theta)] d\Delta(2\theta), \quad (\text{A.2}) \end{aligned}$$

which is defined as the convolution of a Lorentzian  $L(2\theta - 2\theta_{\mathbf{H}})$  with a Gaussian  $G(2\theta - 2\theta_{\mathbf{H}})$ , has been shown to yield good results (Langford, 1978). As the convolution operation is expensive in terms of computation time, the Voigt function can be approximated by the pseudo-Voigt function, a linear combination of a Lorentzian and a Gaussian (Wertheim *et al.*, 1974) of the same FWHM  $\Gamma_L = \Gamma_G = \Gamma$ , which is much easier to calculate:

$$\tilde{V}(2\theta - 2\theta_{\mathbf{H}}, \Gamma) = \eta L(2\theta - 2\theta_{\mathbf{H}}, \Gamma) + (1 - \eta)G(2\theta - 2\theta_{\mathbf{H}}, \Gamma) \quad (\text{A.3})$$

$\eta$  is the mixing factor for which the condition  $0 \leq \eta \leq 1$  holds. Adjustable parameters therein are  $\eta$  and  $\Gamma$ . The relation between  $\Gamma$  and the integral breadth is given by

$$\beta_{pV} = \frac{\pi\Gamma}{2\eta + (2 - 2\eta)\sqrt{\pi \ln 2}}. \quad (\text{A.4})$$

As it is difficult to relate  $\eta$  and  $\Gamma$  to any physical property (Thompson *et al.*, 1987), is often advantageous to calculate the corresponding Lorentzian and Gaussian FWHM as these are linked to physical parameters. The conversion can be done using the numerical expressions given by Hastings *et al.* (1984):

$$\Gamma = \left( \Gamma_G^5 + 2.69269 \Gamma_G^4 \Gamma_L + 2.42843 \Gamma_G^3 \Gamma_L^2 + 4.47163 \Gamma_G^2 \Gamma_L^3 + 0.07842 \Gamma_G \Gamma_L^4 + \Gamma_L^5 \right)^{\frac{1}{5}} \quad (\text{A.5})$$

$$\eta = 1.36603 \frac{\Gamma_L}{\Gamma} - 0.47719 \left( \frac{\Gamma_L}{\Gamma} \right)^2 + 0.11116 \left( \frac{\Gamma_L}{\Gamma} \right)^3 \quad (\text{A.6})$$

A convenient form of the obtained Lorentzian is

$$L(2\theta - 2\theta_{\mathbf{H}}) = \frac{\beta_L}{\beta_L^2 + \pi^2 (2\theta - 2\theta_{\mathbf{H}})^2} \quad (\text{A.7})$$

with the integral breadth

$$\beta_L = \frac{\pi\Gamma_L}{2}, \quad (\text{A.8})$$

while the Gaussian part can be described by

$$G(2\theta - 2\theta_{\mathbf{H}}) = \frac{1}{\beta_G} \cdot \exp \left[ -\frac{\pi (2\theta - 2\theta_{\mathbf{H}})^2}{\beta_G^2} \right] \quad (\text{A.9})$$

with the integral breadth

$$\beta_G = \frac{\Gamma_G}{2} \sqrt{\frac{\pi}{\ln 2}}. \quad (\text{A.10})$$

The angular dependence of the line broadening due to instrumental and sample effects is different resulting in a distinct variation of the width of the Lorentzian and Gaussian component of the reflection (Hastings *et al.*, 1984). A generalized form of the line width variation has been introduced by Thompson *et al.* (1987):

$$\Gamma_G^2 = U \tan^2 \theta + V \tan \theta + W + \frac{P}{\cos^2 \theta} \quad (\text{A.11})$$

$$\Gamma_L = X \tan \theta + \frac{Y}{\cos \theta} \quad (\text{A.12})$$

Herein,  $U$ ,  $V$  and  $W$  are instrumental resolution parameters.  $P$  accounts for isotropic reflection broadening with Gaussian character due to the finite crystallite size and  $Y$  for the corresponding Lorentzian parameter. We note that the parameters  $P$  and  $Y$  cannot be refined simultaneously as they are correlated. Finally,  $X$  is the Lorentzian isotropic strain parameter. Eq. A.11 is a modified form of the initial

Caglioti formula (Caglioti *et al.*, 1958) which concerns only instrumental resolution parameters. In the above equations, it was assumed that no anisotropic effects are present.

Another problem in powder diffraction which has to be corrected for, concerns the asymmetry of the reflection profile. This effect is particularly important for low diffraction angles and is caused by the fact that the detector monitors the intensity in a finite section of the Debye-Scherrer cone (Prince, 1983). The high curvature of the cone at low angles introduces a distortion of the shape and position of the reflection. The effect has been treated theoretically (van Laar and Yelon, 1984) and peak shape functions which correct for axial divergence are available. Finger *et al.* (1994) proposed to treat the asymmetry by convolution of a peak shape function, in our case the pseudo-Voigt function  $\tilde{V}$ , with an axial divergence asymmetry function  $D(\Delta, 2\theta_{\mathbf{H}})$  yielding the new asymmetric peak shape function

$$\Omega(2\varphi, 2\theta - 2\theta_{\mathbf{H}}) = \frac{\int_{2\varphi_{min}}^{2\theta_{\mathbf{H}}} D(\Delta, 2\theta_{\mathbf{H}}) \cdot \tilde{V}(2\varphi - \Delta, 2\theta - 2\theta_{\mathbf{H}}) d\Delta}{\int_{2\varphi_{min}}^{2\theta_{\mathbf{H}}} D(\Delta, 2\theta_{\mathbf{H}}) d\Delta}. \quad (\text{A.13})$$

Herein,  $2\varphi$  is the current detector angle and  $2\varphi_{min}$  the detector position below which no intensity is monitored. Both angles are defined relative to the incident beam in an analogous way to  $2\theta$ . The actual value of  $D$  depends on the position of the Bragg peak and can be calculated quantitatively from the sample-to-detector distance  $L_L$ , the sample slit length  $S_L$  and the detector slit length  $D_L$ . As the extraction of the absolute geometrical dimensions of the slits is not intended during Rietveld refinement,  $S_L$  and  $D_L$  can be normalized to  $L_L$  so that only the slit lengths remain refinable parameters in FullProf.

We note that eq. A.13 is derived for low scattering angles satisfying the expression  $2\theta < 90^\circ$ . A corresponding expression can be obtained for  $2\theta > 90^\circ$  but as asymmetry is generally negligible for  $2\theta > 35^\circ$ , we will limit our considerations to the first case. The convolution cannot be evaluated analytically for useful peak functions and numerical procedures must therefore be used.

## A.1.6 Determination of the instrumental resolution

We investigated which material can best be used to determine the instrumental resolution by comparison of the diffraction patterns of silicon powder of defined grain size and of bulk GdVO<sub>4</sub> (sample MS8). Analysis of the integral peak breadths is performed by selecting each Bragg peak manually and by fitting the  $K_\alpha$  doublet with a pseudo-Voigt function using the corresponding application in FullProf. In the case of the GdVO<sub>4</sub> sample, overlapping peaks are not used for the analysis. The automated procedure allows for the simultaneous output of the integral breadth as well as of the individual breadths of the Lorentzian and Gaussian obtained by deconvolution of the pseudo-Voigt function.

### A.1.7 Material for resolution calibration

We have analyzed the integral peak breadths of silicon powder and of bulk  $\text{GdVO}_4$  from the high temperature ceramic method. The result is plotted as the breadth of a pseudo-Voigt function as well as its deconvoluted Lorentzian and Gaussian breadths in fig. A.4. Several conclusions can be drawn from the comparison of the data for

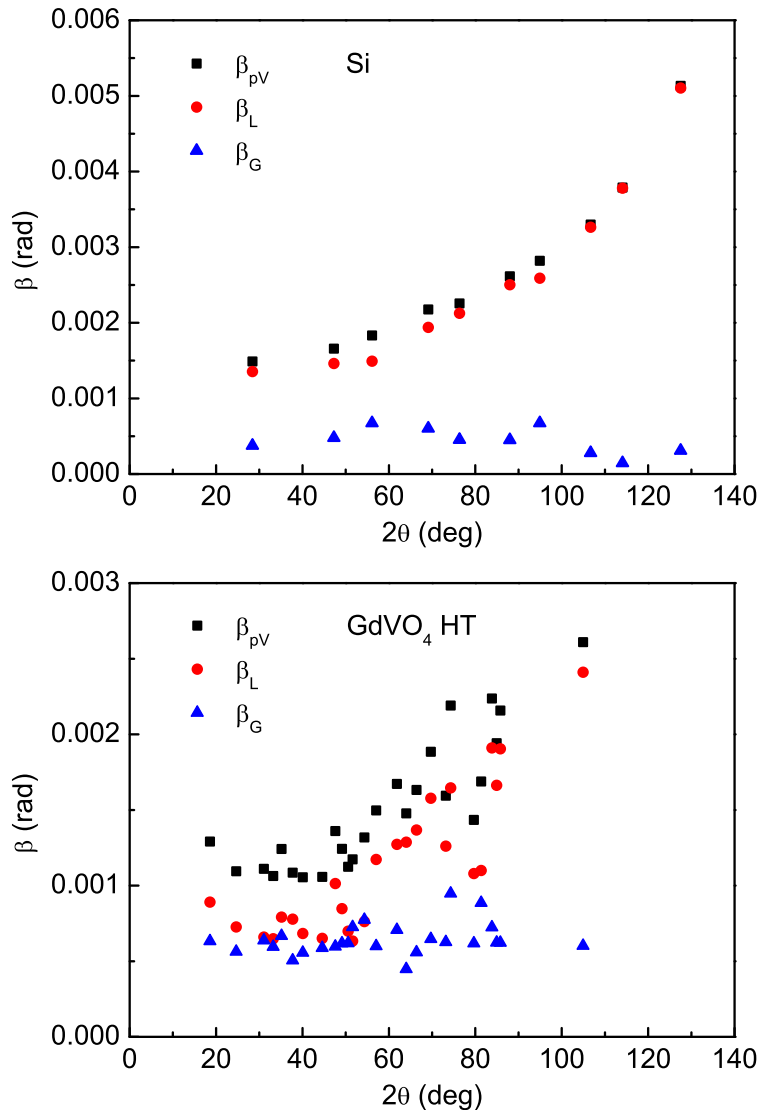


**Figure A.4: Integral breadth of the Bragg peaks of calibration samples.** Upper graph: Integral peak breadths for silicon. Lower graph: Integral peak breadths for bulk  $\text{GdVO}_4$  obtained from the ceramic method (sample MS8). Peaks were fitted to a pseudo-Voigt function.  $\beta_{pV}$  designates the integral breadth of the pseudo-Voigt function and  $\beta_L$  and  $\beta_G$  are the integral breadths of the Lorentzian and Gaussian contributions, respectively, obtained from deconvolution.

the two samples. First, the general trend of larger peaks for increasing diffraction angle is the same for both materials. Second, as silicon crystallizes in the cubic space group  $Fd\bar{3}m$  (Hubbard *et al.*, 1975), a group of higher symmetry than the tetragonal

$I4_1amd$  space group of  $GdVO_4$ , we have fewer peaks and higher resolution at large scattering angles due to reduced overlap. Third, the peak width of silicon increases smoothly with increasing scattering angle while the increase is noisy in the case of the bulk  $GdVO_4$  sample, possibly due to an anisotropy effect. We will discuss this point more in detail for the nanoparticles in section 2.6. A fourth result concerns the deconvolution of the integral peak breadth of the pseudo-Voigt function into its Lorentzian and Gaussian components. While for both samples the Gaussian breadth is low and reaches only values in the order of 0.0005 rad, the Lorentzian component is much larger. Furthermore, we observe that the variation in the values of the Gaussian breadth is on the same order of magnitude as the value itself. As we deal with bulk samples, size effects should not be an issue and we can conclude that the instrumental resolution can mainly be described by a Lorentzian profile with a negligible Gaussian contribution.

From the comparison of the total integral breadth for the silicon powder and that of the bulk  $GdVO_4$  sample (fig. A.5), we observe that the latter yields smaller values. The used silicon powder was characterized by the supplier with 325 mesh meaning

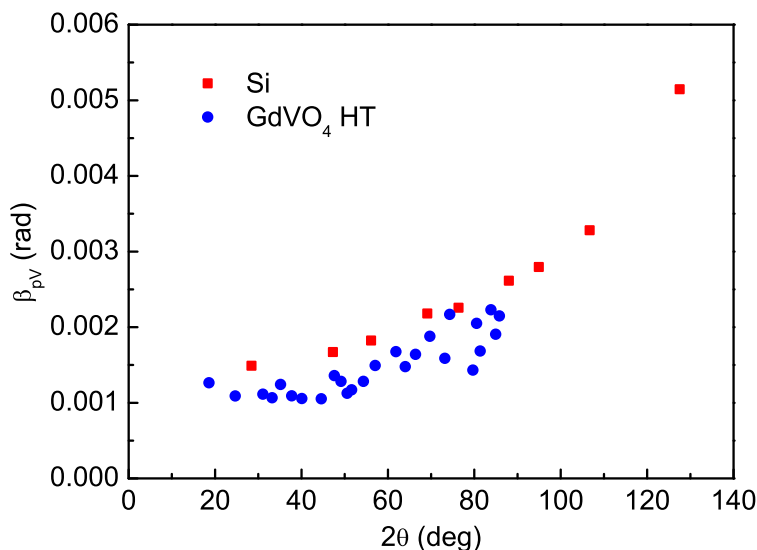


**Figure A.5:** Comparison of the integral breadths of the Bragg peaks for silicon and bulk  $GdVO_4$ . Peaks were fitted with a pseudo-Voigt function.

that all particles passed through a mesh with 44  $\mu\text{m}$  mesh size. It is possible that the grains in our bulk  $GdVO_4$  sample are larger than that size. We will therefore use this sample and not the silicon powder as a calibration standard for the determination of the instrumental resolution parameters by Rietveld refinement of the diffraction pattern (section 1.2.3.3).

## A.1.8 Rietveld refinement

Analysis of individual reflections is possible in small and highly symmetrical crystal systems (Smart and Moore, 2005). For larger and less symmetrical structures, con-

siderable overlap exists between the reflections and impedes the exact measurement of the intensity of an individual reflection peak. Rietveld (1969) devised a method to solve crystal structures from powder diffraction data that does not use individual peak positions and intensities but analyzes the overall intensity in the acquired profile. The principle of the method consists of using a trial structure and its calculated diffraction profile which is compared with the measured profile. The trial structure is then gradually modified until a best match with the measured profile is found. Several parameters like instrument resolution, peak asymmetry and temperature influence considerably the observed intensity profile and have therefore to be taken into account when modeling the trial structure.

### A.1.9 Debye-Waller factor

The Debye-Waller or temperature factor describes the temperature dependency of the intensity of the diffracted radiation (Stout and Jensen, 1989). Thermal motion spreads the electrons of an atom over a larger volume than that found at 0 K resulting in a decreased scattering power. The effect depends on the mass of the atom, on the strength of the interaction between the nucleus and the electrons and increases with increasing temperature. Compared to the scattering power  $f_0$  at 0 K, the elastic coherent scattering  $f$  which generates the Bragg reflections is reduced by the Debye-Waller factor according to the equation

$$f = f_0 \langle \exp(i\mathbf{q} \cdot \mathbf{u}) \rangle^2, \quad (\text{A.14})$$

where  $q = \frac{4\pi \sin \theta}{\lambda}$  is the scattering vector,  $\mathbf{u}$  the thermal displacement vector and  $\langle \dots \rangle$  denotes temporal averaging. Applying statistical mechanics to the assumed isotropic, harmonic vibrations with a temperature dependency according to the Boltzmann law, Debye (1913) and Waller (1923) have shown that eq. A.14 can be reduced to

$$f = f_0 \exp\left(\frac{-q^2 \langle u^2 \rangle}{3}\right) = f_0 \exp\left(-B \frac{\sin^2 \theta}{\lambda^2}\right) \quad (\text{A.15})$$

with the thermal agitation factor  $B = \frac{16\pi^2}{3} \langle u^2 \rangle$ . As the Debye-Waller factor shows a  $\sin^2 \theta$  dependency in the exponential function, the effect is particularly important at high scattering angles. Diffraction data must therefore be acquired up to high scattering angles in order to be able to extract the Debye-Waller factor with accuracy.

### A.1.10 Algorithm for Rietveld refinement

The common observable in X-ray diffraction is the count rate of the detector  $C_i$  where the index  $i$  denotes the  $i$ th position of the detector out of  $n$  total positions in the entire diffraction pattern. The calculated count rate  $C_{c,i}$  of a trial structure can be described as

$$C_{c,i} = S \sum_{\mathbf{H}} I_{\mathbf{H}} \cdot \Omega(2\theta_i - 2\theta_{\mathbf{H}}) + Bk_i \quad (\text{A.16})$$

where  $S$  is the scale factor,  $\mathbf{H}$  is the reciprocal lattice vector which labels the Bragg reflections,  $I_{\mathbf{H}}$  is the integrated intensity arising from the Bragg reflection characterized by  $\mathbf{H}$ ,  $\Omega$  is the peak shape function of the reflection situated at the position  $2\theta_{\mathbf{H}}$  and  $Bk_i$  is the background in the  $i$ th detector position (Pawley, 1981). We note that the integrated intensity itself is a product of several factors depending on the actual experiment and includes among others the Lorentz polarization factor  $L_{\mathbf{H}}$  (eq. A.24). Refining of a crystal structure according to the Rietveld method means that the weighted squared difference between the observed  $C_i$  and calculated  $C_{c,i}(\boldsymbol{\alpha})$  count rates has to be minimized. The calculated count rates depend on a parameter vector  $\boldsymbol{\alpha}$ . The function to minimize may be written as

$$\xi^2 = \sum_{i=1}^n w_i [C_i - C_{c,i}(\boldsymbol{\alpha})]^2 \quad (\text{A.17})$$

with  $w_i = \sigma_i^{-2}$  and  $\sigma_i^2$  being the variance of the count rate  $C_i$  and  $n$  the number of the detector positions used for the measurement. A convenient implementation of the Rietveld method is found in the program FullProf (Rodríguez-Carvajal, 1993, 2001) contained in the suite of programs WinPLOTR (Rodríguez-Carvajal and Roisnel, 1998; Roisnel and Rodríguez-Carvajal, 2001).

### A.1.11 Agreement factors

The agreement between the calculated and the observed pattern is evaluated by a set of agreement factors (Hill and Fischer, 1990; Jansen *et al.*, 1994). These factors may be divided in two classes depending whether they are calculated using all observation points or only those points where Bragg peaks are observed. The common factors include the profile factor

$$R_p = \frac{\sum_{i=1}^n |C_i - C_{c,i}|}{\sum_{i=1}^n C_i} \quad (\text{A.18})$$

and the weighted profile factor

$$R_{wp} = \sqrt{\frac{\sum_{i=1}^n w_i |C_i - C_{c,i}|^2}{\sum_{i=1}^n w_i C_i^2}}, \quad (\text{A.19})$$

which are both calculated from all observation points. The Bragg factor depends only on the observation points contributing to Bragg peaks:

$$R_B = \frac{\sum_{\mathbf{H}} |I_{obs,\mathbf{H}} - I_{c,\mathbf{H}}|}{\sum_{\mathbf{H}} |I_{obs,\mathbf{H}}|} \quad (\text{A.20})$$

The observed integrated intensity  $I_{obs,\mathbf{H}}$  is calculated from

$$I_{obs,\mathbf{H}} = I_{c,\mathbf{H}} \sum_{i=1}^n \frac{\Omega(2\varphi, 2\theta_i - 2\theta_{\mathbf{H}}) \cdot (C_i - Bk_i)}{C_{c,i} - Bk_i}. \quad (\text{A.21})$$

The crystallographic  $R_F$ -factor

$$R_F = \frac{\sum_{\mathbf{H}} |F_{obs,\mathbf{H}} - F_{c,\mathbf{H}}|}{\sum_{\mathbf{H}} |F_{obs,\mathbf{H}}|} \quad (\text{A.22})$$

is obtained according to the Bragg factor but uses the observed structure factor

$$F_{obs,\mathbf{H}} = \sqrt{\frac{I_{obs,\mathbf{H}}}{L_{\mathbf{H}}}} \quad (\text{A.23})$$

with  $L_{\mathbf{H}}$  being the Lorentz polarization factor. The latter is given for random powder samples in Bragg-Brentano geometry by the expression

$$L_{\mathbf{H}} = \frac{m''}{\cos \theta_{\mathbf{H}} \sin^2 \theta_{\mathbf{H}}} \quad (\text{A.24})$$

where  $m''$  is the multiplicity factor for powder methods (Lipson *et al.*, 2006). Another factor describing the quality of the refinement and called goodness of fit is defined by

$$\chi^2 = \frac{R_{wp}}{R_{exp}} \quad (\text{A.25})$$

where  $R_{exp}$  is the expected weighted profile factor given by

$$R_{exp} = \sqrt{\frac{n-p}{\sum_{i=1}^n w_i C_i^2}}. \quad (\text{A.26})$$

Herein,  $n$  is the total number of data points and  $p$  the number of refined parameters. Each of the mentioned factors has a different sensibility to variations in the different refinement parameters and a comprehensive assessment of the quality of the refinement can only be obtained by a combination of several agreement factors.

### A.1.12 Crystal structure refinement of GdVO<sub>4</sub> samples

Crystal structure refinement is performed using the Rietveld code implemented in FullProf. The following general settings are used for all samples:

- Single phase refinement for GdVO<sub>4</sub> in the tetragonal space group  $I4_1/amd$  (No. 141). Gd<sup>3+</sup> ions in the special position  $4a$   $(0, \frac{3}{4}, \frac{1}{8})$ , V<sup>5+</sup> ions in the special position  $4b$   $(0, \frac{1}{4}, \frac{3}{8})$  and O<sup>2-</sup> ions in the position  $16h$   $(0, y, z)$ . As the metal ions are located in special positions, only the  $y$ - and  $z$ -coordinates of the oxide ions are refinable parameters.
- Background treatment by linear interpolation between more than 10 manually chosen points. The region up to  $2\theta = 13^\circ$  without peaks is excluded.
- Peak positions for Cu  $K_\alpha$  radiation with an intensity ratio for  $K_{\alpha 1}$  to  $K_{\alpha 2}$  of 2 : 1.
- Peak shape modeling with Thompson-Cox-Hastings pseudo-Voigt functions convoluted with an axial divergence asymmetry function as treated theoretically in section A.1.5. Asymmetry is only considered for  $2\theta < 35^\circ$ . Peak profile tails are set to zero after  $10\Gamma$ .
- Refinement of the scale factor.

- Refinement of the zero shift of the detector and use of the fixed correction factor  $SYCOS = 0.0022$  (section A.1.4).

Special settings for bulk samples comprise:

- Refinement of the unit cell parameters  $a = b$  and  $c$ .
- Refinement of the instrumental resolution parameters  $U$ ,  $V$  and  $W$  and the peak shape parameters  $X$  and  $Y$ .
- Refinement of the  $y$ - and  $z$ -coordinates of the oxide ions.
- Use of fixed occupation factors according to the formula stoichiometry of the compound except for the case where the stoichiometry of the sample from the ceramic method is tested. Here, isotropic temperature factors are used as obtained from the sample from coprecipitation and thermal treatment and the occupation factors of V and O are refined.
- Refinement of the isotropic temperature factors for all three types of atoms except for the case where the stoichiometry of the sample from the ceramic method is tested.

The quality of the refined diffraction pattern is assessed qualitatively after each refinement step from the difference plot between the measured and the calculated pattern and quantitatively from the calculated agreement factors.

## A.2 Magnetism and magnetometry

Theoretical considerations in this section rely on the textbooks of Crangle (1991), Blundell (2001) and Coey (2010).

### A.2.1 Quantum numbers

Depending on the electronic configuration of an atom or ion, each valence electron may have additionally to its spin an angular momentum. The angular momentum  $\mathbf{L}$  and spin  $\mathbf{S}$  of the ensemble of the electrons in one atom are obtained from the angular momentum  $\mathbf{l}_i$  and spin  $\mathbf{s}_i$  of an individual electron  $i$  by the relations

$$\mathbf{L} = \sum_{i=1}^n \mathbf{l}_i \quad (\text{A.27})$$

$$\mathbf{S} = \sum_{i=1}^n \mathbf{s}_i, \quad (\text{A.28})$$

where  $n$  is the total number of valence electrons. These quantities are linked to the quantum numbers  $L$  and  $S$  of the angular momentum and spin, respectively, by the relations

$$\mathbf{L}^2 = L(L+1)\hbar^2 \quad (\text{A.29})$$

$$\mathbf{S}^2 = S(S+1)\hbar^2. \quad (\text{A.30})$$

In general, angular momentum and spin cannot be considered individually because of spin-orbit coupling. Two coupling schemes for the two extreme cases of coupling are commonly used. The so-called Russel-Saunders or  $L$ - $S$  coupling, where

$$\mathbf{J} = \mathbf{L} + \mathbf{S} \quad (\text{A.31})$$

holds, is the model of choice for light atoms with small spin-orbit interactions compared to the electrostatic interactions between the electrons. With increasing atomic number, electrostatic interactions decrease and spin-orbit coupling becomes more important. In this case, the  $j$ - $j$  coupling scheme, where first the individual moments are coupled according to

$$\mathbf{j}_i = \mathbf{l}_i + \mathbf{s}_i, \quad (\text{A.32})$$

is better suited. The total angular momentum is then obtained by

$$\mathbf{J} = \sum_{i=1}^n \mathbf{j}_i. \quad (\text{A.33})$$

In rare earth ions, the order of magnitude of the electrostatic Coulomb and spin-orbit coupling interaction is the same and none of the above coupling schemes is appropriate (Wybourne, 1965). In this case, one can use a so-called intermediate coupling scheme based on the  $L$ - $S$  scheme. The new quantum number  $J$  obtained from

$$\mathbf{J}^2 = J(J+1)\hbar^2 \quad (\text{A.34})$$

has  $2J+1$  possible values represented by the magnetic quantum number of the total angular momentum  $m_J$ . The transformation of the eigenstates to the intermediate coupling scheme is achieved by mixing the eigenstates from  $L$ - $S$  coupling.

### A.2.2 Paramagnetism

An atom or ion with the total angular momentum  $\mathbf{J}$  of its electrons has a corresponding magnetic moment given by

$$\boldsymbol{\mu} = \gamma_e \mathbf{J}, \quad (\text{A.35})$$

where  $\gamma_e$  is the gyromagnetic ratio of the electrons. The latter is calculated from the electronic Landé factor  $g_J$  in the given coupling scheme, the Bohr magneton  $\mu_B$  and the Planck constant  $h$  with the abbreviation  $\hbar = h/2\pi$  using the expression

$$\gamma_e = \frac{g_J \mu_B}{\hbar}. \quad (\text{A.36})$$

In the case where  $L$  and  $S$  are good quantum numbers, the Landé factor is obtained from

$$g_J = 1 + \frac{J(J+1) + S(S+1) - L(L+1)}{2J(J+1)}. \quad (\text{A.37})$$

This condition is fulfilled for Russel-Saunders and intermediate coupling schemes.

We consider now a magnetic moment in an external magnetic field. The energy of the moment

$$E = -\boldsymbol{\mu} \cdot \mathbf{B} \quad (\text{A.38})$$

is minimized when the moment lies along the field direction. However, as the total angular momentum is a quantum mechanical quantity, the corresponding vector is limited to the discrete absolute values given by

$$|\mathbf{J}| = \sqrt{J(J+1)}\hbar. \quad (\text{A.39})$$

Assuming that the magnetic field is oriented according to  $\mathbf{B} = (0, 0, B)$ , the projection of the vector in the direction of the field  $J_z$  is restricted to the values

$$J_z = m_J \hbar \quad (\text{A.40})$$

where  $m_J = -J, -J+1, \dots, +J$  can only adopt  $2J+1$  values but not a continuum. As the  $z$ -projection reaches a maximal value of  $J\hbar$  but the absolute value of the vector is  $\sqrt{J(J+1)}\hbar$ , a complete alignment in  $z$ -direction is not possible. The magnetic moment in  $z$ -direction is with eq. A.35, A.36 and A.40 expressed as

$$\mu_z = \frac{g_J \mu_B J_z}{\hbar} = g_J \mu_B m_J \quad (\text{A.41})$$

and the saturation magnetic moment  $\mu_\infty$  is obtained for the case  $m_J = J$

$$\mu_\infty = g_J \mu_B J. \quad (\text{A.42})$$

The aligning force of the magnetic field is antagonized by the thermal movement which tends to randomize the orientation of the magnetic moments. The interplay between these two effects is described by the Brillouin function  $B_J(y)$ , which modulates  $\mu_\infty$  according to

$$\mu = \mu_\infty B_J(y) = g_J \mu_B J B_J(y). \quad (\text{A.43})$$

Herein, the Brillouin function is defined as

$$B_J(y) = \frac{2J+1}{2J} \coth\left(\frac{2J+1}{2J}y\right) - \frac{1}{2J} \coth\frac{y}{2J} \quad (\text{A.44})$$

with

$$y = \frac{g_J \mu_B J B}{k_B T}. \quad (\text{A.45})$$

It is often more demonstrative to calculate the magnetic moment of an atom or ion in units of the Bohr magneton:

$$\frac{\mu}{\mu_B} = g_J J B_J(y) \quad (\text{A.46})$$

An interesting limit case is reached if the magnetic field is low and the temperature high meaning that the variable  $y \ll 1$ . Here, the function  $\coth$  can be expanded in its Taylor series  $\coth = \frac{1}{x} + \frac{x}{3}$  so that eq. A.46 is simplified to

$$\frac{\mu}{\mu_B} = g_J J \frac{y(J+1)}{3J} = \frac{\mu_B g_J^2 J(J+1)}{3k_B} \cdot \frac{B}{T}. \quad (\text{A.47})$$

This is the classical Curie law normalized to one atom or ion with the Curie constant

$$C = \frac{\mu_B g_J^2 J(J+1)}{3k_B}. \quad (\text{A.48})$$

### A.2.3 Magnetic susceptibility

So far, we have considered magnetic effects on the level of a single atom. The theory has now to be extended to matter at the macroscopic scale. As two different unit systems are commonly used in electrodynamics, we will specify when necessary if an equation is given in the Gaussian system by the upper index *cgS* or in the SI system by *SI*.

When a paramagnetic substance is placed in a magnetic field  $\mathbf{H}$ , a total magnetic moment  $\sum_i \boldsymbol{\mu}_i$  being the sum of the individual atomic moments  $\boldsymbol{\mu}_i$  can be observed which has in the Gaussian system the unit emu and in the SI system  $\text{Am}^2$ . The specific magnetization is obtained from the total magnetic moment with the sample mass according to

$$\mathcal{M} = \frac{\sum_i \boldsymbol{\mu}_i}{m}. \quad (\text{A.49})$$

This quantity is measured in the Gaussian system in units of emu/g. The magnetization  $\mathbf{M}$  is defined as the total magnetic moment per volume  $V$

$$\mathbf{M} = \frac{\sum_i \boldsymbol{\mu}_i}{V} \quad (\text{A.50})$$

and measured in the Gaussian system in  $\text{emu}/\text{cm}^3$ . In isotropic paramagnets, there exists a linear relation between the magnetization and the magnetic field

$$M = \chi_v H, \quad (\text{A.51})$$

where  $\chi_v$  is the volume susceptibility. In the Gaussian system, the magnetic field is measured in Oersted and  $\chi_v^{cgS}$  has thus the unit  $\text{emu cm}^{-3} \text{Oe}^{-1}$ . In the SI system, the volume susceptibility  $\chi_v^{SI}$  is dimensionless. The conversion between the two systems is achieved with the equation

$$\chi_v^{SI} = 4\pi \chi_v^{cgS} \left[ \frac{\text{emu}}{\text{cm}^3 \text{Oe}} \right], \quad (\text{A.52})$$

where the brackets indicate the units which have to be used. However, as it is easier to determine the mass of a sample than its volume, a convenient definition of the susceptibility uses the mass susceptibility

$$\chi_m = \frac{|\mathcal{M}|}{H}. \quad (\text{A.53})$$

$\chi_m^{cgS}$  is given in the unit  $\text{emu g}^{-1} \text{Oe}^{-1}$  and the conversion to the SI system is achieved by

$$\chi_m^{SI} \left[ \frac{\text{m}^3}{\text{kg}} \right] = 4\pi \cdot 10^{-3} \chi_m^{cgS} \left[ \frac{\text{emu}}{\text{g Oe}} \right]. \quad (\text{A.54})$$

The determination of  $\chi_m^{cgs}$  is directly feasible from the measurement of the total magnetic moment of the sample, its mass and the applied magnetic field. Another important quantity is the molar susceptibility which can be obtained from the mass or volume susceptibility by calculating

$$\chi_{mol}^{SI} = M_W \chi_m^{SI} = \frac{M_W}{\rho} \chi_v^{SI}, \quad (\text{A.55})$$

with  $M_W$  being the molar mass and  $\rho$  the mass density of the measured compound.  $\chi_{mol}^{SI}$  is given in units of  $\text{m}^3/\text{mol}$ .

We must now link the Curie law derived in section A.2.2 with the susceptibility which can be obtained from a measurement. The relation between the magnetic induction  $\mathbf{B}$  and the magnetic field  $\mathbf{H}$  is given in SI units by

$$\mathbf{B}^{SI} = \mu_0 (\mathbf{H}^{SI} + \mathbf{M}^{SI}) \quad (\text{A.56})$$

where  $\mu_0$  is the vacuum magnetic permeability. We will only consider isotropic effects so that the vectors can be replaced by their absolute values. Together with eq. A.51, we can therefore write

$$B^{SI} = \mu_0 (H^{SI} + \chi_v^{SI} H^{SI}) = \mu_0 (1 + \chi_v^{SI}) H^{SI}. \quad (\text{A.57})$$

As generally  $\chi_v^{SI} \ll 1$ , we can further simplify the expression to

$$B^{SI} = \mu_0 H^{SI}. \quad (\text{A.58})$$

The Curie law was derived as the relation between the magnetic moment per atom or ion and the magnetic induction (eq. A.47). Using eq. A.58, we obtain further

$$\left( \frac{\mu}{\mu_B} \right)^{SI} = C^{SI} \frac{H^{SI}}{T}, \quad (\text{A.59})$$

where the vacuum permeability was integrated in the constant  $C^{SI}$ . For better comparison of the obtained values with literature data, we may define molar quantities

$$M_{mol}^{SI} = C_{mol}^{SI} \frac{H^{SI}}{T}, \quad (\text{A.60})$$

where the molar magnetization is calculated by

$$M_{mol}^{SI} = \mu_0 \mu_B N_A \frac{\mu}{\mu_B}. \quad (\text{A.61})$$

We obtain finally for the molar Curie constant

$$C_{mol}^{SI} = \frac{\mu_0 \mu_B^2 N_A g_J^2 J(J+1)}{3k_B}. \quad (\text{A.62})$$

Herein,  $\mu_0 = 4\pi \cdot 10^{-7} \frac{\text{Vs}}{\text{Am}}$ ,  $\mu_B = 9.274 \cdot 10^{-24} \frac{\text{J}}{\text{T}}$  is the Bohr magneton,  $k_B = 1.381 \cdot 10^{-23} \frac{\text{J}}{\text{K}}$  is the Boltzmann constant,  $N_A = 6.022 \cdot 10^{23} \text{mol}^{-1}$  is the Avogadro constant and  $g_J$  is the Landé factor corresponding to the total angular momentum  $J$ . The constants can be summarized in the new constant

$$\frac{\mu_0 \mu_B^2 N_A}{3k_B} = 1.571 \cdot 10^{-6} \frac{\text{K m}^3}{\text{mol}}. \quad (\text{A.63})$$

## A.3 Dynamic light scattering

### A.3.1 Scattering experiment

When light is shed on a dispersion of nanoparticles, the incident radiation is scattered in all directions (Berne and Pecora, 2003; Schärfl, 2007). We want to limit our considerations to the case of Rayleigh scattering where the scattering objects are supposed to be much smaller than the wavelength of the used radiation. This approximation is valid for particle sizes up to the order of  $\lambda/10$  corresponding to 60 nm for a He-Ne laser. Employing a monochromatic and coherent light source like a laser yields a time-dependent fluctuation in the scattering intensity. These fluctuations are due to the thermally induced Brownian motion of the particles in the dispersant which changes constantly the distance between the scattering objects. Depending on the actual position of the nanoparticles, the interference between the radiation scattered by the individual objects is either constructive or destructive which in turn can be observed when measuring the fluctuations in the intensity. The fluctuations contain information about the motion of the scattering objects.

We consider an incident light of wavelength  $\lambda$  with the wave vector  $\mathbf{k}_i = \frac{2\pi}{\lambda}\hat{e}_i$  where  $\hat{e}_i$  is the unit vector pointing in the propagation direction of the incident light. Assuming elastic scattering, that means that the wavelength of the scattered light is the same as that of the incident light, we obtain for the wave vector after the scattering process  $\mathbf{k}_f = \frac{2\pi}{\lambda}\hat{e}_f$  where  $\hat{e}_f$  is the unit vector in the beam direction. The scattering vector is defined as

$$\mathbf{q} = \mathbf{k}_f - \mathbf{k}_i \quad (\text{A.64})$$

and geometry shows that its magnitude is

$$q = \frac{4\pi n}{\lambda} \sin \theta, \quad (\text{A.65})$$

with  $n$  being the refractive index of the dispersant. The detector situated at the angle  $2\theta$  relative to the incident beam monitors the time dependent intensity  $I(t)$  (fig. A.6).

### A.3.2 Hydrodynamic diameter

Dynamic information of the particles can be obtained from the intensity autocorrelation function (Dunn, 2010). The second order normalized autocorrelation function is calculated by multiplying the intensity at the time  $t$  with that at the time  $t + \tau$

$$g^{(2)}(\tau) = \frac{\langle I(t)I(t + \tau) \rangle}{\langle I(t) \rangle^2}. \quad (\text{A.66})$$

Brackets  $\langle \dots \rangle$  indicates temporal averaging. The second order autocorrelation function is connected to the first order autocorrelation function by the Siegert relationship (Schätzl, 1993):

$$g^{(2)}(\tau) = B + \beta [g^{(1)}(\tau)]^2 \quad (\text{A.67})$$

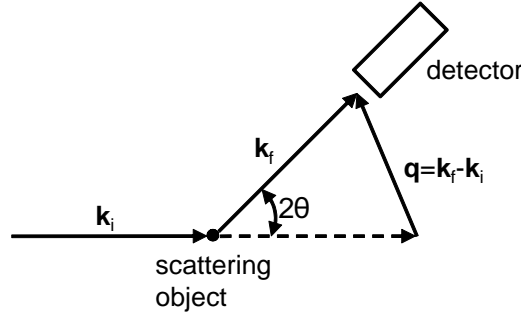


**Figure A.6: Geometry of a scattering experiment.** The incident radiation with the wave vector  $\mathbf{k}_i$  is scattered elastically by a scattering object at an angle  $2\theta$ . The intensity of the scattered radiation with the wave vector  $\mathbf{k}_f$  is monitored on a detector.

Herein,  $B$  is the long-time value of  $g^{(2)}(\tau)$  and usually the expression  $B = 1$  holds. Small differences from unity are due to measurement noise. The factor  $\beta$  accounts for the experimental geometry. We want to limit our theoretical considerations to the case of a monodisperse sample or a sample showing a narrow size distribution which can be treated as pseudo monodisperse. In a monodisperse sample, particles in Brownian motion (Brown, 1828) satisfy the homogeneous diffusion equation also called Fick's second law (Fick, 1855)

$$D\nabla^2\rho(\mathbf{r},t) - \frac{\partial}{\partial t}\rho(\mathbf{r},t) = 0 \quad (\text{A.68})$$

with  $D$  being the diffusion constant and  $\rho(\mathbf{r},t)$  the time and space dependent particle density. The diffusion constant for diffusion of spherical particles in liquids with a low Reynolds number is obtained from the Einstein-Stokes equation (Einstein, 1905)

$$D = \frac{k_B T}{3\pi\eta d}, \quad (\text{A.69})$$

where  $k_B$  is Boltzmann's constant,  $T$  the temperature,  $\eta$  the viscosity of the dispersant and  $d$  the hydrodynamical diameter of a spherical particle. The spatial Fourier transformation of eq. A.68 allows for the calculation of the first order correlation function yielding

$$g^{(1)}(\tau) = \exp(-Dq^2\tau) = \exp(-\psi\tau), \quad (\text{A.70})$$

where we have defined the decay rate  $\psi = Dq^2$ . In the case of a sample with a narrow size distribution, we have to generalize eq. A.70 to

$$g^{(1)}(\tau) = \int_0^\infty G(\psi) \exp(-\psi\tau) d\psi, \quad (\text{A.71})$$

where  $G(\psi)$  is the normalized distribution function of the decay rates for which

$$\int_0^\infty G(\psi) d\psi = 1 \quad (\text{A.72})$$

holds. We note that the special form of eq. A.70 is returned from eq. A.71 for the decay rate distribution  $G(\psi) = \delta(\psi - Dq^2)$ . The method of cumulants (Koppel, 1972; Frisken, 2001) allows finally for the calculation of the second order autocorrelation function which takes the general form

$$g^{(2)}(\tau) = 1 + \beta \exp(-2 \langle \psi \rangle \tau) \left( 1 + \frac{\mu_2}{2!} \tau^2 + \frac{\mu_3}{3!} \tau^3 + \dots \right)^2, \quad (\text{A.73})$$

where  $\mu_m$  are the moments of the  $m$ th order of the mean value

$$\langle \psi \rangle = \int_0^\infty G(\psi) \psi d\psi. \quad (\text{A.74})$$

For the case of a monodisperse sample, we obtain the simplified equation

$$g^{(2)}(\tau) = 1 + \beta \exp(-2Dq^2\tau). \quad (\text{A.75})$$

We have set  $B = 1$  in both cases. It is immediately clear from eq. A.66 and A.75 that the measured intensity can be linked to the diffusion coefficient and further to the hydrodynamic diameter of the scattering object. We note that the hydrodynamic diameter refers to how the scattering object diffuses in the dispersant and is not necessary equal to the geometric diameter. Furthermore, as only spherical objects can be treated, the obtained value of  $d$  corresponds to the hydrodynamic diameter of a sphere with the same diffusion properties as the object actually contained in the dispersion. The diameter is generally overestimated in the case of charged surfaces as an electric double layer moves with the particle and the measured hydrodynamic diameter is therefore that of the core object plus the counter ion layer. Surface modifications such as long chains affect also the diffusion properties.

### A.3.3 Size averages

For dispersions of particles with a narrow size distribution, a single exponential according to eq. A.73 can be fitted to the intensity autocorrelation function (eq. A.66). From the obtained value  $\langle \psi \rangle$ , one can evaluate the mean diffusion coefficient  $\langle D \rangle$  which in turn yields the hydrodynamic diameter as the so-called  $z$ -average diameter with eq. A.69. As this quantity is calculated depending on the scattered intensity, the  $z$ -average diameter is a mean value weighted by intensity. The polydispersity of the dispersion can be characterized by the polydispersity index  $p$  (Koppel, 1972) defined based on the second moment of the mean value by the expression

$$p = \frac{\mu_2}{\langle \psi \rangle^2}. \quad (\text{A.76})$$

A low value close to zero indicates a very narrow size distribution and a quasi-monodisperse dispersion.

When comparing particle sizes obtained from dynamic light scattering, one has to be aware of to which type of size distribution the value refers. Apart from the intensity weighted particle diameter, one can also define volume and number weighted mean values. In each case, the peak shape and the value of the

corresponding mean value changes. For the theoretical explanation of this effect, we consider Rayleigh scattering from a sphere with  $d < \lambda/10$ . Here, the scattered intensity scales as  $d^6$  with the particle size (Bohren *et al.*, 2011). As the volume of a sphere is  $4/3\pi(d/2)^3$ , the volume weighted size distribution can be obtained by dividing the intensity weighted distribution by a factor  $d^3$ . The resulting distribution must be normalized so that the sum of the percentages per size class is equal to 100%. In order to obtain the number weighted size distribution, this process has to be continued by further dividing through  $d^3$  and renormalizing. One finds generally that average size decreases in the order from intensity to volume and number weighting. This effect is illustrated for a simulated sample in fig. A.7. Additionally to the mean

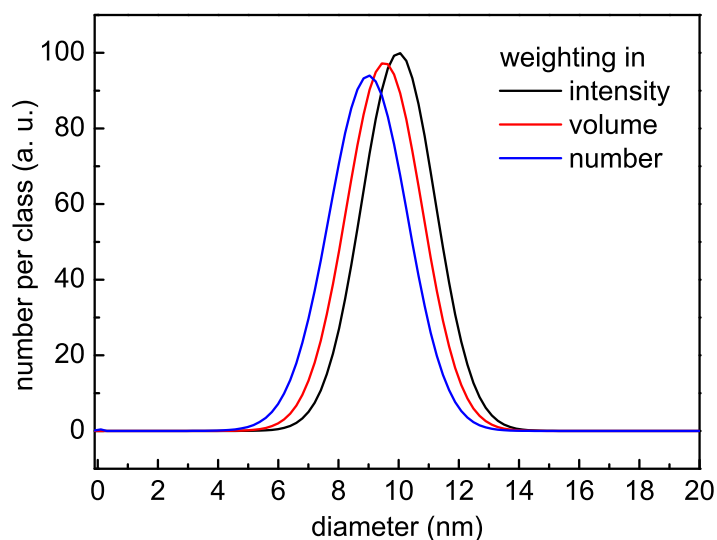


**Figure A.7: Dependency of the average particle size on the weighting method.** The change in the peak shape and position is illustrated beginning from a Gaussian intensity weighted peak centered at  $d = 10$  nm with a FWHM of 2.88 nm and drawn with a finite number of 100 points between 0 and 20 nm. The volume and number weighted peaks are obtained by dividing the initial intensity weighted values through  $d^3$  and  $d^6$ , respectively. In both cases, the peak area was normalized to the same value as for the initial Gaussian peak. In the present case, the maximum of the distribution is situated at 10.0 nm, 9.5 nm and 9.0 nm for intensity, volume and number weighting, respectively.

value, also the peak shape changes. We note that our considerations were made for a sample containing small particles of a narrow size distribution. The transformation of the initially obtained intensity weighted size distribution is more complicated if  $d > \lambda/10$  and Mie scattering theory must therefore be used (Bohren *et al.*, 2011). In the case of polydisperse samples containing several populations of particle sizes, the methods of cumulants cannot be used and another algorithm *e. g.* the CONTIN algorithm must be employed (Provencher, 1982). Here, the different size distributions have also a huge effect on the ratio of each size population.

In summary, particle sizes from DLS can only reliably be compared when the used weighting model is clearly identified and when dealing with dispersions of narrow polydispersity. The intensity weighting uses the least amount of assumptions but the results is not very useful for comparison with other techniques. A more insightful

weighting is based on the number as a number fraction is immediately obvious but one has to critically analyze the result in order to avoid artifacts from the transformation process.

## A.4 Scanning electron microscopy

### A.4.1 General considerations

Scanning electron microscopy (SEM) is a technique allowing for the direct observation of a nanoobject (Goldstein *et al.*, 2002). High energy electrons are produced by field emission and are accelerated in a electric field. The optical path is composed of a combination magnetic and electrostatic lenses which allow to focus the electron beam and enable scanning of the sample surface. The high energy primary electrons interact with the surface of the sample and kick off electrons from the surface atoms. These electrons are called secondary electrons and can be monitored on an Everhart-Thornley detector. Contrast comes from the different ability to release secondary electrons which is closely related to the topography of the surface (Chomel and Rocher, 1989). In general, the secondary electron intensity increases with decreasing angle between the incident electron beam and the surface (fig. A.8). When comparing particle sizes obtained from scanning electron microscopy

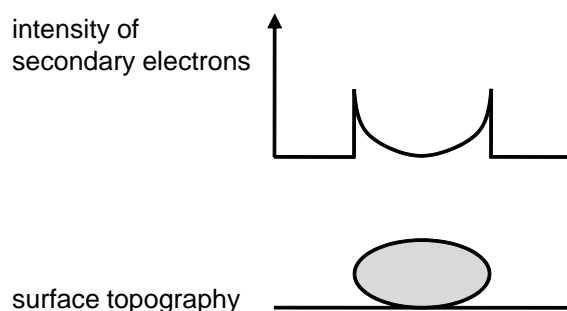


**Figure A.8: Contrast through secondary electron emission.** The emission intensity for secondary electrons is maximal for grazing incidence. In the case of a nanoparticle on a flat surface, maximum intensity is found at the borders of the object.

to sizes from other techniques, one has to be aware of this fact because although a direct visualization of the object is achieved, depending on the shape of the object, the dimensions obtained from microscopy may differ more or less from the actual geometric dimensions. Another important point is that as the sample is under constant electron bombardment, the surface needs to be conducting. Conductive surfaces can be obtained by covering the sample with a thin layer of a heavy metal. In our study, we have chosen a simpler way which avoids the additional step of coating. We used a semiconducting doped silicon wafer on which only a very low density of non-conducting  $\text{GdVO}_4$  nanoparticles was added. Here, the semiconducting support can evacuate the charges and the nanoparticles remain visible although they are isolating.

## A.4.2 Experimental protocol

Samples for scanning electron microscopy are prepared on semiconducting pieces of n- or p-doped silicon wafers of about  $2 \times 2$  cm size. In order to avoid aggregation, silicon surfaces are coated with a thin layer of a polymer possessing an opposite charge to the surface charge of the nanoparticles. The sign of the surface charge of the nanoparticles is determined by measurement of the  $\zeta$ -potential at neutral pH as described in section 2.2.3.3 and is positive for non-modified particles and negative for silica coated ones. For nanoparticles with positive  $\zeta$ -potential, the cationic polymer poly(diallyldimethylammonium chloride) (Sigma Aldrich, average molecular weight 100,000 – 200,000 g/mol, 20 % w/w solution in water) is used while for negative  $\zeta$ -potential the anionic polymer poly(sodium 4-styrenesulfonate) (Sigma Aldrich, average molecular weight  $\sim 70,000$  g/mol, 30 % w/w solution in water) is employed. The structure formulae of the two polymers are depicted in fig. A.9.

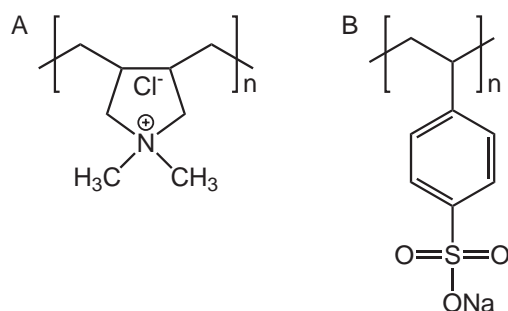


**Figure A.9: Polymers used for surface coating for SEM observation.** A: Cationic polymer poly(diallyldimethylammonium chloride) and B: anionic polymer poly (sodium 4-styrenesulfonate).

The silicon wafers are first cleaned in a piranha mixture freshly prepared from 3 volumes of concentrated sulfuric acid and 1 volume of 30 % hydrogen peroxide for about 30 min. The cleaned wafers are rinsed with ultrapure water and dried under a nitrogen flow. The polymer coating is applied by immersing the wafer in a 10 % (v/v) dilution of one of the upper mentioned polymer stock solutions. The coated wafers are dried under a nitrogen flow and immersed in a dispersion of the nanoparticles to observe at a concentration of about 100  $\mu$ M. After a final drying step under nitrogen flow, the samples are ready for observation. We note that some samples have also been imaged without the previous coating procedure.

Scanning electron microscopy of raw and silica coated GdVO<sub>4</sub> nanoparticles is performed using a Hitachi S-4800 field emission scanning electron microscope. Acceleration voltages from 1 – 10 kV and magnification up to 800,000 are employed. The best resolution is given by the manufacturer to 1 nm at 15 kV acceleration voltage and to 2 nm at 1 kV.

Size analysis is performed using the program Image J (program for image processing and analysis and freely available from the homepage of the U. S. National Institutes of Health under the URL <http://rsbweb.nih.gov/ij/index.html>). A polygon is drawn around the shape of the nanoparticle and the selected area is fitted with an ellipse. Sizes are given as the major and minor axes of the ellipse.

## A.5 Gas adsorption

### A.5.1 Adsorption isotherms

Adsorption is based on the interactions between the solid and the molecules in the gas phase (Rouquerol *et al.*, 1999). Two kinds of forces are involved, which give rise to either physisorption or chemisorption. Physisorption forces have generally a low degree of specificity and adsorption can take place in multilayers. A physisorbed molecule is not altered upon adsorption and returns on desorption to the gas phase in its original form. In contrast, chemisorption is dependent on the reactivity of the adsorbent and adsorbate and is linked to the reactive parts of the surface. Adsorption takes therefore place in monolayers. A chemisorbed molecule undergoes a reaction with the surface or is dissociated on its and cannot be recovered by simple desorption. The determination of the specific surface of a sample requires inert gas molecules such as nitrogen which interacts with the surface by physisorption. The terms adsorption and desorption are usually employed to indicate the direction from which the equilibrium states have been approached. Adsorption hysteresis can be found if the amount adsorbed is not brought to the same level by the adsorption and desorption approach at a given equilibrium pressure. At constant temperature, the relation between the amount adsorbed and the equilibrium pressure is called adsorption isotherm.

Experimental adsorption isotherms recorded in the literature have a wide variety of forms although the majority of these isotherms result from physical adsorption. The International Union of Pure and Applied Chemistry (IUPAC) has established a classification system which allows for a convenient grouping into six main classes (Sing *et al.*, 1985). The typical isotherms of these classes are shown in fig. A.10. Each isotherm type reflects a characteristic adsorption process. Type I signifies adsorption in small micropores with a narrow size distribution which are filled easily at low  $p/p_0$ . The nearly horizontal plateau indicates a very small external surface area. Type II isotherms indicate the formation of an adsorbed layer whose thickness increases progressively with increasing relative pressure. When the equilibrium pressure equals the saturation vapor pressure, the adsorbed layer becomes bulk liquid or solid. The knee at point B is usually considered to represent the completion of the first monolayer and the beginning of the formation of multiple layers. This isotherm type is usually observed for non-porous and macroporous solids. Type III isotherms are found in the case of weak adsorbent-adsorbate interactions and are seldom. Type IV isotherms exhibit a hysteresis loop, which is associated with the filling and emptying of the mesopores by capillary condensation and evaporation. Type V isotherms are found in the case of weak adsorbent-adsorbate interactions in materials where pore filling and emptying can take place. The type VI isotherm, or stepped isotherm, is associated with layer-by-layer adsorption on a highly uniform surface and is rarely found experimentally.

### A.5.2 Brunauer-Emmett-Teller theory

Brunauer *et al.* (1938) devised a theory, nowadays known as the BET theory, which

## Figure withdrawn due to copyright restrictions

**Figure A.10: Main types of gas physisorption isotherms, according to the IUPAC classification.**

The points B in isotherms II and IV represent the completion of the monomolecular layer and the beginning of the formation of the multimolecular layer. Reprinted with permission from F. Rouquerol *et al.*, *Adsorption by Powders and Porous Solids: Principles, Methodology and Applications*, Chapter 1 – Introduction, pp. 1-26. Academic Press, San Diego, CA, USA. Copyright 1999. Elsevier Limited.

allows to relate the gas pressure over the sample to the volume of adsorbed gas. A convenient form of the BET equation is

$$\frac{p}{v_{ads}(p_0 - p)} = \frac{1}{v_m c} + \frac{c - 1}{v_m c} \frac{p}{p_0}, \quad (\text{A.77})$$

where  $p$  is the gas pressure over the sample,  $p_0$  the saturation pressure at which liquefaction of the gas takes place,  $v_{ads}$  the volume of adsorbed gas,  $v_m$  the volume of a monolayer and  $c$  the affinity constant between the gas and the substrate.  $v_{ads}$  and  $v_m$  are generally normalized to the mass of the sample. A plot of  $\frac{p}{v_{ads}(p_0 - p)}$  against  $p/p_0$  in the low relative pressure range is almost linear and corresponds to the region where the formation of the first monolayer takes place. The linear fit of the data points yields the parameters slope  $s = \frac{c-1}{v_m c}$  and intercept  $i = \frac{1}{v_m c}$  which in turn allow for the calculation of the volume of the monolayer

$$v_m = \frac{1}{i + s}. \quad (\text{A.78})$$

The specific surface of the solid is given by the equation

$$A_{BET} = \frac{v_m N_A \sigma}{V_{mol}}, \quad (\text{A.79})$$

where  $N_A$  is Avogadro's number,  $V_{mol}$  the molar volume of the used gas at the measurement temperature, and  $\sigma$  is the average area occupied by a gas molecule

in the completed monolayer. Emmett and Brunauer (1937) proposed that the molecular cross-sectional area  $\sigma$  can be calculated from the density of the solidified gas in a closest-packed state. Thus,

$$\sigma = f \left( \frac{M}{\rho N_A} \right)^{\frac{2}{3}} \quad (\text{A.80})$$

where  $f$  is the packing factor, which for hexagonal close-packing becomes 1.091,  $\rho$  is the density of the solidified gas at the operational temperature, and  $M$  is the molar mass of the adsorbate. The density of the solidified gas can be replaced by that of the liquefied gas at the same temperature. Using eq. A.80, a value of  $0.162 \text{ nm}^2$  for nitrogen can be calculated. A smaller value of  $0.137 \text{ nm}^2$  has also been proposed in literature (Ribeiro Carrott *et al.*, 2001). However, in the present study, we will use the value of  $0.162 \text{ nm}^2$ .

## A.6 Luminescence spectroscopy

### A.6.1 Quantum yield

The quantum yield  $Q$  of a material is defined as the number of emitted photons divided by the number of absorbed photons (Lakowicz, 2006). In terms of rate constants, it may be written as

$$Q = \frac{k_r}{k_r + k_{nr}}, \quad (\text{A.81})$$

where  $k_r$  is the rate constant for transitions from the excited state to the ground state which give rise to luminescence emission and  $k_{nr}$  that for all other non-radiative transitions. It is immediately evident that the expression  $0 \leq Q \leq 1$  holds.

The easiest way to access the quantum yield of a new material is to compare its emission efficiency to that of a molecule with a known value of  $Q$ . A well studied fluorescent molecule which absorbs in the range of the absorption band of vanadate is rhodamine 6G, abbreviated as R6G (fig. A.11). This fluorophore possesses a high quantum yield, reported to be 95% in ethanol at 25 °C (Kubin and Fletcher,

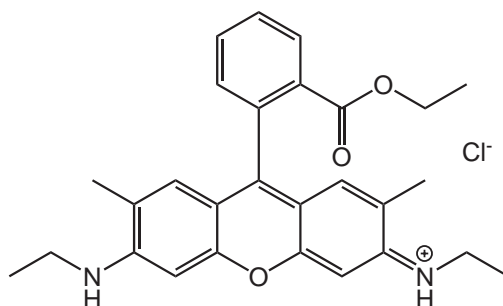


Figure A.11: Structure formula of rhodamine 6G hydrochloride.

1982) and 90% in water at ambient temperature (Magde *et al.*, 2002). The efficient fluorescence emission enables measurements with high precision.

Quantum yield determinations by this method require a calibration curve, which links the fluorescence of a given R6G dilution to its absorption, both measured upon excitation at the wavelength of interest. In the case of our rare earth vanadate nanoparticles, the vanadate band has its absorption maximum at 280 nm and this wavelength must therefore also be used for the calibration. Let us denote with  $S_1$  the integrated fluorescence intensity resulting from an excitation at 280 nm. Within the linearity range of Lambert-Beer's law,  $S_1$  as a function of the absorbance at 280 nm  $A_{280}$  is linear and can be fitted by the expression

$$S_1^{(R6G)} = aA_{280}^{(R6G)}, \quad (\text{A.82})$$

where  $a$  is the proportionality constant and the superscript *R6G* designates data for the calibration sample. We note that the knowledge of the actual R6G concentration of the calibration sample is not necessary. The quantum yield of the nanoparticle dispersion is then calculated by the expression

$$Q = \left( \frac{n^{(NP)}}{n^{(R6G)}} \right)^2 Q_{R6G} \frac{S_1^{(NP)}}{aA_{280}^{(NP)}}, \quad (\text{A.83})$$

where  $n$  is the refractive index of the dispersion medium of the luminophor specified in the superscript,  $Q_{R6G}$  is the known quantum yield of R6G and the superscript *NP* designates data for the nanoparticle sample. For the refractive indices, values of  $n^{(NP)} = 1.33$  for water (Schiebener *et al.*, 1990) and  $n^{(R6G)} = 1.36$  for ethanol (Lide, 2008) were taken. The quantum yield for rare earth vanadate nanoparticles at a wavelength of 280 nm comprises the efficiency of the energy transfer between the vanadate and europium ions as well as the probability of radiative desexcitation of the latter (Huignard, 2001).

## A.6.2 Acquisition of luminescence spectra

The nanoparticle dispersion is prediluted so that it appears almost transparent and transferred into a 2 mm QS 100 quartz cuvette (Helma). Luminescence excitation and emission spectra are recorded using a Hitachi F-4500 fluorescence spectrophotometer. For both measurements, slits of 2.5 nm spectral width are used in the excitation and emission path and scanning is performed at a speed of 240 nm/min. For acquisition of the excitation spectrum, a WG-295 long pass filter (Schott) is placed in the excitation path and a GG-375 long pass filter (Schott) in the detection path. Luminescence is excited in the wavelength range 250 – 600 nm and emission is collected at 617 nm. In the case of the emission spectrum, only a GG-375 long pass filter is placed in the detection path. Luminescence is excited at 280 nm and the emission is recorded in the range 500 – 750 nm.

## A.6.3 Quantum yield determination

For the calibration of the measurement, a tiny quantity of R6G hydrochloride powder (Lambda Physik) is dissolved in about 10 mL absolute ethanol (Carlo Erba). From

this stock solution, 6 dilutions are prepared. Each aliquot is transferred in a 2 mm QS 100 quartz cuvette (Helma). The absorption is measured on a Cary 50 UV-VIS spectrophotometer (Agilent Technologies) in the wavelength range 200 – 800 nm at medium speed and the absorption at 280 nm is read off from the graph. Care is taken that the obtained absorption lies in the range 0.03 – 0.3. The same sample is then transferred to a Hitachi F-4500 fluorescence spectrophotometer. Fluorescence is excited at 280 nm and the emission is recorded from 300 – 800 nm at a scanning speed of 240 nm/min. Slits of 2.5 nm spectral width are used in the excitation and emission path. A WG-295 long pass filter (Schott) is placed in the detection path. The fluorescence intensity is characterized by the integral  $S_1$  of the emission peak in the wavelength range 500 – 750 nm. The calibration equation is obtained by plotting the value  $S_1$  as a function of  $A_{280}$  and fitting the data linearly. This calibration procedure was repeated every several months in order to correct for the intensity decrease due to the aging of the fluorescence spectrometer lamp.

The quantum yield is determined from a nanoparticle dispersion diluted with ultrapure water. The absorption as well as the luminescence are measured using the same instrumental parameters as for the calibration. If the absorbance at 280 nm exceeds 0.3, the sample is further diluted.

#### A.6.4 Instrument calibration

We recorded the fluorescence and absorption spectra of R6G in order to establish a calibration curve for the determination of the quantum yield of the nanoparticle dispersions. The fluorescence emission spectrum of R6G is depicted in fig. A.12. We then plotted the integrated fluorescence intensity as a function of the absorbance

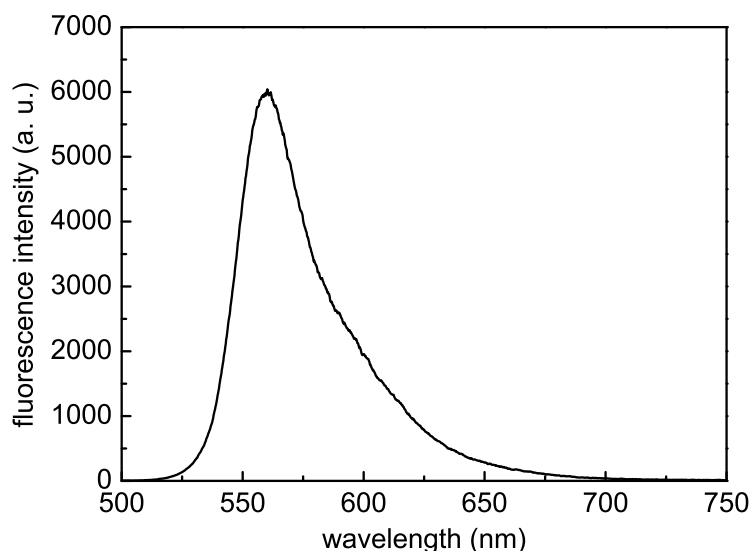


**Figure A.12: Emission spectrum of rhodamine 6G.** Fluorescence was excited at 280 nm and emission was recorded at a speed of 240 nm/min through a WG-295 band pass filter. Slits of 2.5 nm spectral width were used in the excitation and emission path.

at 280 nm in order to calculate the calibration curve (fig. A.13). The linear fit

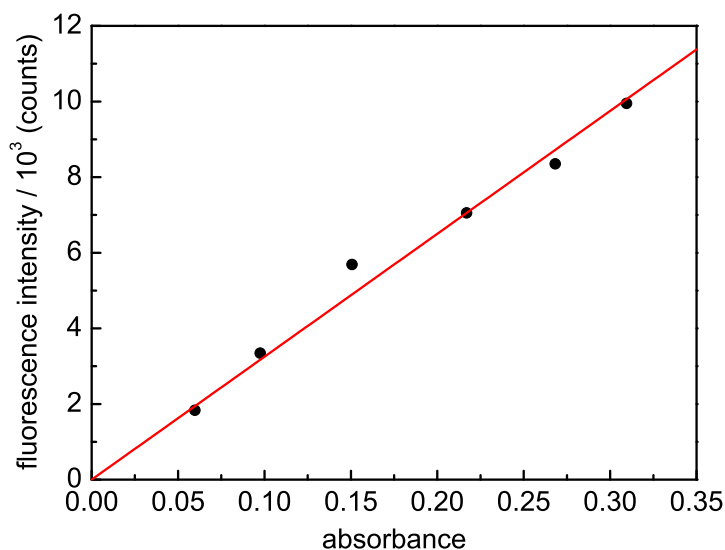


**Figure A.13: Calibration curve for the quantum yield determination.** The data was recorded for rhodamine 6G solutions of different concentrations according to the protocol given in section A.6.3. Data was fitted linearly with the equation  $S_1 = aA_{280}$ .

of the experimental data yields the proportionality constant  $a = (325.1 \pm 7.4) \cdot 10^3$  with a relative error of 2%. In order to estimate the error of the quantum yield determination of a nanoparticle dispersion, we have to add to this error the uncertainty in the determination of the absorbance at 280 nm for the sample. As discussed in section 2.3.1,  $A_{280}$  is obtained from the absorption peak on a background resulting from scattering of the incident light by the nanoobjects. This leads to the extraction of a value with moderate precision. A total error of the quantum yield determination on the order of 5% seems therefore reasonable.

## A.7 Nuclear magnetic resonance

In this introduction to nuclear magnetic resonance, the spin will be treated as a classical quantity whenever possible in order to allow for a simple and concise presentation. Will will recur to quantum mechanics only for the spin quantization conditions. This section relays mainly on the NMR textbooks of Abragam (1983) and Levitt (2008).

### A.7.1 Nuclear spin

Protons and neutrons, together called nucleons, compose the atomic nucleus. Each nucleon carries a spin and the total spin of the nucleus depends on the number of protons and neutrons inside. In order to observe NMR signals, a nucleus with non-vanishing spin  $I$  is needed. Commonly used in NMR are dipole nuclei with  $I = 1/2$

such as  $^1\text{H}$ ,  $^{13}\text{C}$  and  $^{31}\text{P}$  or quadrupole nuclei such as  $^{14}\text{N}$  ( $I = 1$ ). As MRI deals with water protons, we will restrain our theoretical considerations to dipole nuclei and especially to protons.

A nuclear spin gives rise to a quantized angular momentum where both the magnitude as well the orientation are quantized. In order to observe the orientation quantization, a preferred orientation defined by a magnetic field is necessary. This field is usually assumed to point in  $+z$ -direction. If we consider a nuclear spin  $I$  then the magnetic quantum number  $m_I$  can adopt all integer values from  $+I$  to  $-I$  and we get hence  $2I + 1$  possible orientations of the spin vector. In contrast to a classical dipole in a field, the quantum mechanical spin can never align or anti-align with the field but has to respect the  $2I + 1$  orientations. The  $z$ -component  $I_z$  of the angular momentum vector  $\mathbf{I}$  can be expressed as

$$I_z = m_I \hbar \quad (\text{A.84})$$

with  $\hbar = \frac{h}{2\pi}$  and  $h$  being Planck's constant.

### A.7.2 Interaction spin–magnetic field

In the magnetic field, each orientation of the spin vector corresponds to a distinctive magnetic moment. We are mainly interested in the  $z$ -component which is given by

$$\mu_z = \gamma I_z = \gamma m_I \hbar \quad (\text{A.85})$$

with the gyromagnetic ratio  $\gamma$  being a constant for each isotope. In the case of a proton, the nucleus has the two possible spin states  $m_I = +1/2$  and  $m_I = -1/2$ . These are degenerate in absence of a magnetic field but if the nucleus is placed in a magnetic field  $\mathbf{B}_0 = (0, 0, B_0)$ , the degeneracy is broken and the dipole energy depends on the spin state:

$$E = -\boldsymbol{\mu} \cdot \mathbf{B}_0 = -\mu_z B_0 = -\gamma m_I \hbar B_0 \quad (\text{A.86})$$

This splitting of the energy niveaus is called Zeeman effect (fig. A.14). The energy difference between the two states is given by

$$\Delta E = \gamma \hbar B_0 \quad (\text{A.87})$$

and increases with increasing intensity of the magnetic field.

We denote the population of lower energy level as  $n_{+1/2}$  and that of the higher energy level  $n_{-1/2}$ . The population ratio in thermal equilibrium  $n_{-1/2}/n_{+1/2}$  is then defined by the Boltzmann factor

$$\frac{n_{-1/2}}{n_{+1/2}} = \exp \frac{-\Delta E}{k_B T} . \quad (\text{A.88})$$

In a magnetic field of 3 T and at ambient temperature, we obtain a factor  $\frac{\Delta E}{k_B T} \approx 10^{-4}$  and the population difference is therefore small.

As quantization conditions exist only for the magnitude and the  $z$ -component of the spin, each of the  $2I + 1$  orientations corresponds to a mantle of a cone with the

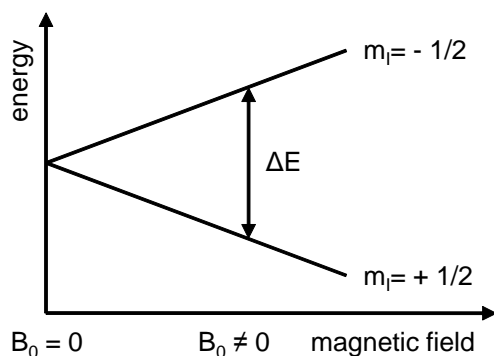


**Figure A.14: Zeeman splitting of the nuclear energy levels in a static magnetic field.** When a nucleus with  $I \neq 0$  is brought into a magnetic field, the energy levels are no longer degenerate and the actual energy of each state depends on the magnetic field intensity. The scheme shows the splitting for a  $I = 1/2$  nucleus.

symmetry axis oriented along the  $z$ -direction on which the spin precesses around the magnetic field direction (fig. A.15). A fixed direction of the spin in space would not be possible because of Heisenberg's uncertainty principle. The frequency of the precession movement is called Larmor angular frequency and can be calculated by

$$\omega = -\gamma B_0. \quad (\text{A.89})$$

The negative sign of the Larmor frequency indicates the sense of precession. For nuclei like  $^1\text{H}$  with a positive gyromagnetic ratio  $\gamma$ , the Larmor precession is counterclockwise around the field direction. For protons, the Larmor frequency has a value of  $\omega/2\pi = 42.57 \text{ MHz/T}$ .

### A.7.3 Macroscopic magnetization

Many spins are contained in a piece of matter and it is convenient not to consider each individual magnetic moment  $\mu_i$  but the sum of all moments. This can be done by defining the macroscopic magnetization vector

$$\mathbf{M} = \frac{\sum_i \mu_i}{V} \quad (\text{A.90})$$

with  $V$  being the volume of the piece of matter. In thermal equilibrium, the  $x$ - and  $y$ -components of the individual precessing spins average out because there is no phase coherence and we obtain therefore for the components of  $\mathbf{M}^{eq}$

$$\begin{aligned} M_z^{eq} &= \frac{\sum_i \mu_{z,i}}{V} \\ M_{xy}^{eq} &= 0. \end{aligned} \quad (\text{A.91})$$

When the spin system is manipulated during a NMR experiment, a non-vanishing component in the  $xy$ -plane may exist. In a coordinate system fixed in the laboratory, this component precesses with  $\omega$  around the  $z$ -axis. It is convenient to define a

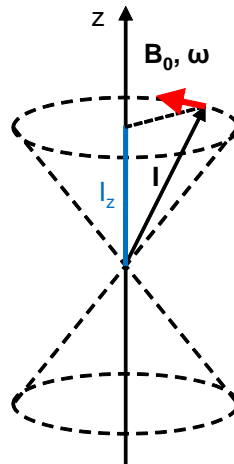


**Figure A.15: Larmor precession of a nuclear spin in a static magnetic field.** The nuclear spin  $\mathbf{I}$  precesses with the Larmor frequency  $\omega/2\pi$  on the mantle of a cone around the field direction (indicated by a red arrow).  $I_z$  is quantized.

rotating reference frame which rotates about the  $z$ -axis with the Larmor frequency. In this reference frame, the description of the  $xy$ -component of the magnetic moment vector becomes easier as it is stationary in the  $xy$ -plane and does not rotate.

#### A.7.4 Resonant energy absorption

Resonant absorption will occur when electromagnetic radiation of the energy  $\hbar\omega = h\nu = \Delta E$  that means of the same frequency  $\nu = \omega/2\pi$  as the Larmor frequency is provided. The actual Larmor frequency of one precise nucleus is not only a function of the isotope but depends also on its surrounding, as the surrounding spins generate a magnetic field additional to the external field  $B_0$ . The resonance condition is therefore not fulfilled for all hydrogen atoms at the same frequency. Nevertheless this so called chemical shift is small and reaches values of several parts per million with respect to the frequency obtained from eq. A.89. The effect of chemical shift will be detailed in section 4.2.1.1 for a MRI relevant exemple.

The resonance frequencies may be determined by scanning the frequency range of interest with a continuous wave. Instead of using this time consuming method of fulfilling resonance conditions successively, a short radio frequency pulse centered at the theoretical Larmor frequency can be used. As the Fourier transformation of a narrow pulse in the time domain gives a large spectrum in the frequency domain, all hydrogen nuclei in the piece of matter can be brought into resonance simultaneously.

For a typical magnetic field strength of several Tesla, the radiation for resonant absorption corresponds to the radio frequency range of the electromagnetic spectrum. Upon absorption, nuclei are transferred from the lower to the higher energy level. In terms of the model of one individual spin in the laboratory reference frame as depicted in fig. A.15, this transition corresponds to a precession on the mantle of the cone oriented downwards. When using the simplified model of the magnetization vector in the rotating reference frame, the transition is equal to a rotation of the

magnetization vector  $M_z$  away from its equilibrium position with a rotation angle dependent on the pulse length (fig. A.16). We note that in thermal equilibrium,

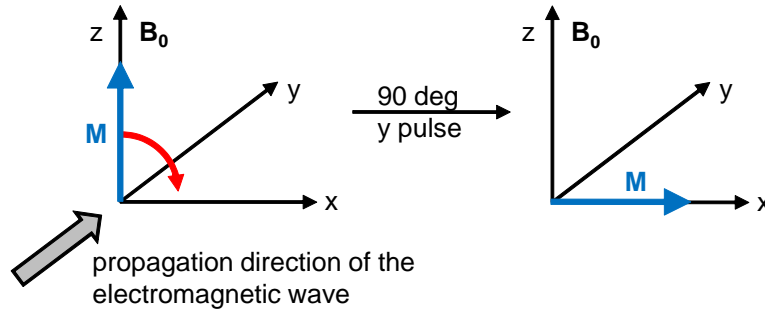


**Figure A.16: Effect of an electromagnetic pulse on the magnetization vector.** We consider the magnetization vector in the rotating reference frame in a static magnetic field in thermal equilibrium (left). The application of a radio frequency pulse propagating in  $+y$ -direction of convenient length (so called "90°-pulse") rotates the magnetization in  $+x$ -direction.

according to eq. A.88, the lower level is always slightly more populated than the higher one. By absorption of electromagnetic radiation, a population inversion is possible *i. e.* the higher level can become more populated than the lower one. Relaxation brings the population back to its thermal equilibrium (section 4.1).

### A.7.5 Signal detection

After application of a 90° pulse to the spin system, the magnetization vector lays in the  $xy$ -plane. In the laboratory reference frame, this vector precesses about the  $z$ -axis. If a receiver coil with effective surface  $A$  is placed in the  $xy$ -plane, the precessing magnetization vector (fig. A.17) generates a time dependent magnetic flux

$$\dot{\Phi} = \frac{d}{dt} (B \cdot A) = \dot{B} \cdot A \quad (\text{A.92})$$

through the the receiver coil and induces therefore an electromotive force  $U_{ind}$  according to Faraday's law:

$$U_{ind} = -\dot{\Phi} \quad (\text{A.93})$$

The induced voltage in the coil corresponds to the NMR signal in the time domain, called the free induction decay (FID). As relaxation takes place, the signal decreases with the time. The reverse Fourier transformation of the FID yields the frequency dependent spectrum from which the resonance frequencies can be read off.

### A.7.6 Pulse sequences

The application of an appropriate pulse sequence instead of only a single pulse (section A.7.4) allows to extract and measure a specific information like the  $T_1$  or  $T_2$  relaxation times (Levitt, 2008). The two major parameters of a pulse sequence are the repetition time  $TR$  and the echo time  $TE$ .  $TR$  is the time between the

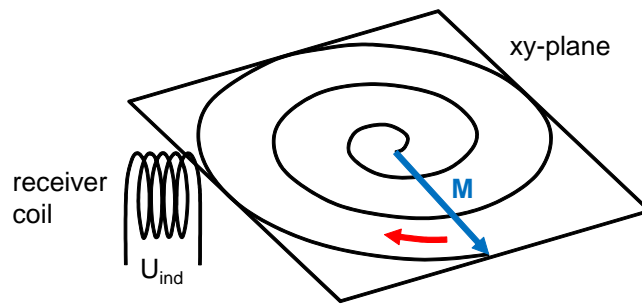


**Figure A.17: NMR signal detection.** The precessing magnetic moment induces an oscillating voltage in the receiver coil which decays with the time.

application of one pulse and the next one and determines the degree of  $T_1$  relaxation that has meanwhile occurred.  $TE$  is the time between two  $180^\circ$  pulses in an echo train where each pulse forms an echo after  $TE/2$ .  $TE$  determines therefore the degree of  $T_2$  relaxation that has occurred.

The inversion recovery pulse sequence allows for the measurement of the  $T_1$  relaxation time. The initial application of a  $180^\circ$  pulse rotates  $M_z$  in  $-z$ -direction. After the inversion time  $TI$  that is the waiting time between the  $180^\circ$  pulse and the following pulse, a further  $90^\circ$  pulse rotates the magnetization recovered in  $+z$ -direction in the  $xy$ -plane where it can be detected. In order to avoid signal loss due to the detector dead time, the signal is refocused by a spin echo sequence after  $TE/2$  and the echo is obtained  $TE$  after the initial  $90^\circ$  pulse (fig. A.18).

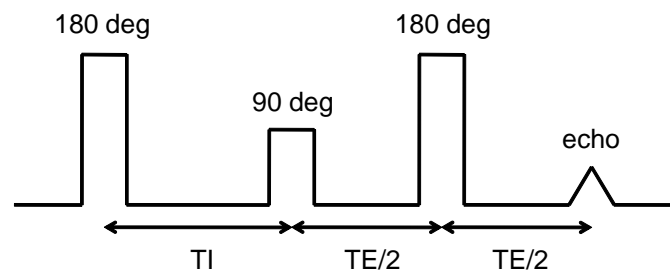


**Figure A.18: Inversion recovery pulse sequence.** The magnetization is inverted by a  $180^\circ$  pulse. After  $TI$ , a  $90^\circ$  pulse rotates the magnetization in the detection direction. The echo is obtained by a spin echo sequence after  $TE$ .

$T_2$  relaxation times can be measured with the Carr-Purcell-Meiboom-Gill (CPMG) pulse sequence (Carr and Purcell, 1954; Meiboom and Gill, 1958). Spins are rotated in  $+x$ -direction by an initial  $90^\circ$  pulse. Due to field inhomogeneities, the Larmor frequency varies slightly for the different spins resulting in a dephasing of the magnetic moments and a loss in total magnetization in the detection direction. The moments can be rephased using a Hahn echo (Hahn, 1950) that is a  $180^\circ$  pulse at the time  $TE/2$ . The echo can be recorded at  $TE$ . Further application of  $180^\circ$  pulses at  $(2n + 1)TE/2$  where  $n \in \mathbb{N}$  yields an echo train at  $2nTE$  (fig. A.19).

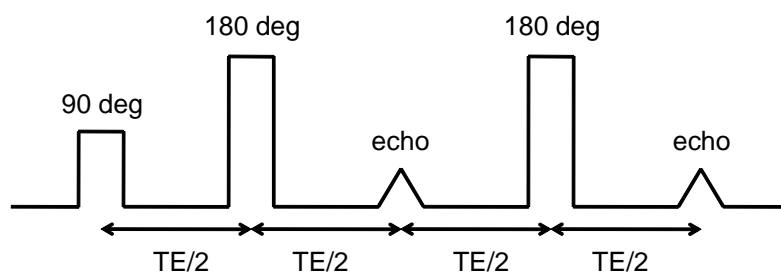


**Figure A.19: CPMG pulse sequence.** The magnetization is rotated in the detection direction by a  $90^\circ$  pulse. Spins dephase in the  $xy$ -plane due to field inhomogeneities. A  $180^\circ$  pulse after  $TE/2$  allows for refocusing and the echo is observed after  $TE$ . The echo sequence can be repeated in order to obtain an echo train.

As we have discussed in section 4.1.1, the directly observable relaxation time after a  $90^\circ$  pulse is  $T_2^*$ . Though we are interested to quantify the pure molecular relaxation time without the effect from field inhomogeneities. This can be achieved using the CPMG sequence. While the envelope of one FID defines  $T_2^*$ , the envelope of the echo train determines the relaxation time  $T_2$  (fig. A.20). We note that the CPMG sequence can only completely compensate the dephasing of spins due to magnetic field inhomogeneities in the case where the spins are not diffusing.

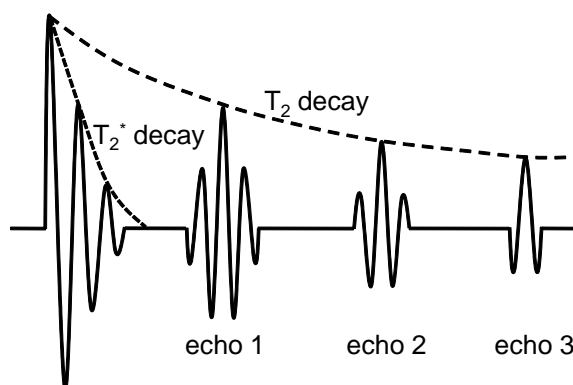


**Figure A.20: Transverse relaxation time measurement.** Due to magnetic field inhomogeneities, the observed signal decays with  $T_2^*$ . The application of a CPMG pulse sequence allows to obtain the  $T_2$  relaxation time due to spin-spin interactions as the envelope of the observed echos.

### A.7.7 Image formation

Nuclear magnetic resonance becomes an imaging technique if one is able to locate the signal of the nuclei in the three spatial directions. This task is performed by linear magnetic field gradients produced by additional coils located inside the main  $B_0$  coil (Westbrook and Kaut, 1998). The magnetic field strength and concomitantly the Larmor frequency of a nucleus is a linear function of its position along the gradient axis. This process is called spatial encoding. In total, there are three gradients

inside the bore of the magnet (fig. A.21). During an image acquisition, each of the

Figure withdrawn due  
to copyright restrictions

**Figure A.21: MRI scanner gradient magnets.** The  $z$ -gradient alters the magnetic field in direction of the field  $B_0$ . The  $x$ -gradient acts on the field strength in the horizontal and the  $y$ -gradient in the vertical direction. The magnetic field strength remains unaltered in the magnetic isocenter located in the middle of the magnet. Image taken from the website of the National High Magnetic Field Laboratory, Florida State University, Tallahassee (<http://www.magnet.fsu.edu>).

three gradients performs one of the following encoding tasks:

- Slice selection that is locating a slice within the patient
- Frequency encoding along the long axis of the anatomy
- Phase encoding along the short axis of anatomy

One of the gradient coils is used to select a slice. As the resonance frequency of the nuclei depends on the field strength in the slice of interest, nuclei therein can be selectively excited by providing a pulse with a band of frequencies coinciding with their Larmor frequencies. The scan plan selected determines which of the three gradient coils is used for slice selection: The  $z$ -gradient is used for axial slices, the  $x$ -gradient for sagittal slices and the  $y$ -gradient for coronal slices. The slice thickness can be varied by the slope of the gradient as well as by bandwidth of the excitation pulse. In spin echo puls sequences, the slice select gradient is switched on during the  $90^\circ$  excitation pulse and during the  $180^\circ$  rephasing pulse (fig. A.22).

After selection of one particular slice, the signal must be located along the both remaining axes. Frequency encoding is usually used along the long axis of anatomy. In coronal and sagittal images, the long axis of anatomy lies along the  $z$ -axis whereas in axial images it lies usually along the horizontal axis except for imaging of the head there it lies along the  $y$ -axis. The frequency encoding gradient is only switched on during the signal reception and is also called readout gradient. In a spin echo sequence, the duration of the frequency encoding gradient is centered in the middle of the echo (fig. A.22). The slope of the frequency encoding gradient determines which part of the anatomy is covered along the frequency encoding axis.

Phase encoding is used to locate the image along the remaining axis. When the phase encoding gradient is switched on, the frequency of the Larmor precession

depends on the position of the nucleus on the gradient axis. A higher precession frequency means that the corresponding nucleus gains a positive phase shift compared to a nucleus in the magnetic isocenter. When the phase encoding gradient is switched off, the precessional frequency of all nuclei returns to that of the magnetic isocenter. However, the accumulated phase difference between the nuclei remains. This difference in phase allows to determine the position of a nucleus along the phase encoding gradient. In a spin echo sequence, the phase encoding gradient is switched on just before the  $180^\circ$  rephasing pulse. Fig. A.22 shows the temporal succession of the three gradients during a spin echo experiment.

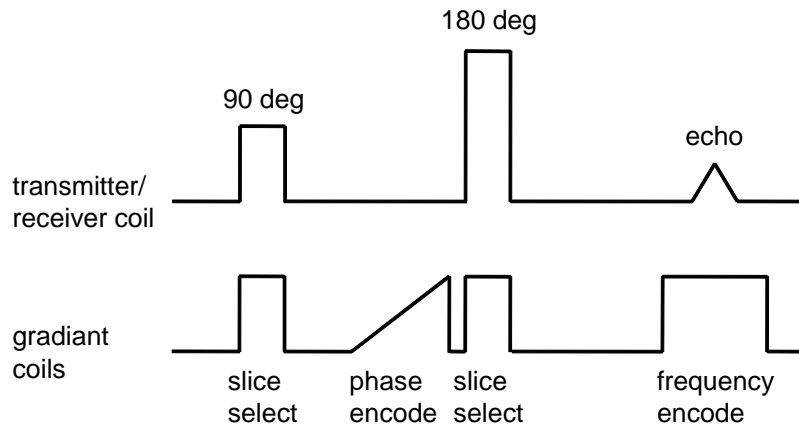


**Figure A.22: Pulse and gradient timing during image acquisition.** The upper curve shows the timing of the  $90^\circ$  detection and  $180^\circ$  rephasing pulse as well as the spin echo. The three types of gradient pulses for image encoding are depicted in the lower panel.

## **Appendix B**

### **Crystallographic and magnetic properties of selected rare earth compounds**

**Table B.1: Crystal structure of selected  $\text{REXO}_4$ .**  $T_T$  is the temperature for crystallographic transitions.

$\text{XO}_4 =$	$\text{PO}_4$		$\text{AsO}_4$		$\text{CrO}_4$		$\text{VO}_4$	
Gd	monoclinic (Thiriet <i>et al.</i> , 2005)	$P2_1/n$	tetragonal (Colwell <i>et al.</i> , 1971)	$I4_1/amd$	tetragonal (Jiménez-Melero <i>et al.</i> , 2006)	$I4_1/amd$	tetragonal (Cashion <i>et al.</i> , 1969)	$I4_1/amd$
Tb	tetragonal (Lee <i>et al.</i> , 1971), 2 close phase transitions $T_{T1} = 2.28$ K (purely magnetic) and $T_{T2} = 2.15$ K (magnetic and crystallographic) (Schwab and Kahle, 1977; Suzuki and Nakajima, 1979; Becker <i>et al.</i> , 1985), $T_{T2}$ distortion to probably monoclinic (Nägele <i>et al.</i> , 1980), magnetic space group $C2'$ (Coing-Boyat <i>et al.</i> , 1975)	$I4_1/amd$	tetragonal $T_T = 27.7$ K Jahn-Teller distortion 1971; Berkhahn <i>et al.</i> , 1973) to orthorhombic, space group $Fddd$ (Göbel <i>et al.</i> , 1972; Schäfer <i>et al.</i> , 1979)	$I4_1/amd$ , Jahn-Teller distortion (Klein <i>et al.</i> , 1971; Berkhahn <i>et al.</i> , 1973) to orthorhombic, space group $Fddd$ (Göbel <i>et al.</i> , 1972; Schäfer <i>et al.</i> , 1979)	tetragonal $T_T = 48$ K Jahn-Teller distortion to orthorhombic, space group $Fddd$ (Buisson <i>et al.</i> , 1976)	$I4_1/amd$ , Jahn-Teller distortion to orthorhombic space group $Fddd$ (Will <i>et al.</i> , 1972), space group $Fddd$ (Kazei <i>et al.</i> , 2005)	tetragonal $T_T = 33$ K Jahn-Teller distortion to orthorhombic space group $Fddd$ (Will <i>et al.</i> , 1972), space group $Fddd$ (Kazei <i>et al.</i> , 2005)	$I4_1/amd$ , Jahn-Teller distortion to orthorhombic space group $Fddd$ (Will <i>et al.</i> , 1972), space group $Fddd$ (Kazei <i>et al.</i> , 2005)
Dy	tetragonal (Fuess <i>et al.</i> , 1971)	$I4_1/amd$	tetragonal $T_T = 11.2$ K Jahn-Teller distortion to orthorhombic (Göbel and Will, 1972a,b), magnetic space group orthorhombic $P_I2_12_12_1$ (Schäfer and Will, 1971)	$I4_1/amd$ , Jahn-Teller distortion to orthorhombic (Göbel and Will, 1972a,b), magnetic space group orthorhombic $P_I2_12_12_1$ (Schäfer and Will, 1971)	tetragonal $T_T = 31.2$ K Jahn-Teller distortion to orthorhombic, space group $Imma$ (Tezuka and Hinatsu, 2001)	$I4_1/amd$ , Jahn-Teller distortion to orthorhombic, space group $Imma$ (Tezuka and Hinatsu, 2001)	tetragonal $T_T = 13.8$ K Jahn-Teller distortion to probably orthorhombic (Cooke <i>et al.</i> , 1970), no evidence but neutron scattering, magnetic space group orthorhombic $Imma$ (Will and Schäfer, 1971)	$I4_1/amd$ , Jahn-Teller distortion to probably orthorhombic (Cooke <i>et al.</i> , 1970), no evidence but neutron scattering, magnetic space group orthorhombic $Imma$ (Will and Schäfer, 1971)

Table B.1 continued.

Ho	tetragonal (Cooke <i>et al.</i> , 1973)	$I4_1/amd$	tetragonal Jahn-Teller (Schwab <i>et al.</i> , 1974)	$I4_1/amd$ , no distortion	tetragonal (Climent-Pascual <i>et al.</i> , 2007)	$I4_1/amd$	tetragonal existence of Jahn- Teller distortion unclear (Battison <i>et al.</i> , 1977), no evidence by neutron scattering (Suzuki <i>et al.</i> , 1984)	$I4_1/amd$
Er	tetragonal (Mangum and Utton, 1975)	$I4_1/amd$	no data		tetragonal (Jiménez <i>et al.</i> , 2002)	$I4_1/amd$	tetragonal (Metcalf and Rosenberg, 1972), no Jahn-Teller distortion (Bleaney, 1999)	$I4_1/amd$
Tm	tetragonal (Kirste <i>et al.</i> , 2003)	$I4_1/amd$	tetragonal $T_T = 6.13$ K distortion to orthorhombic (Bleaney <i>et al.</i> , 1984)	$I4_1/amd$ , Jahn-Teller	tetragonal (Saez-Puche <i>et al.</i> , 2003)	$I4_1/amd$	tetragonal $T_T = 2.15$ K Jahn- Teller distortion to lower symmetry (Cooke <i>et al.</i> , 1972), orthorhombic domains with orthorhombic $a$ axis aligned along either the tetragonal [110] or orthogonal to this direction (Suzuki <i>et al.</i> , 2002)	$I4_1/amd$
Yb	tetragonal (Zhang <i>et al.</i> , 2008)	$I4_1/amd$	tetragonal (Hodges <i>et al.</i> , 1982)	$I4_1/amd$	tetragonal (Jiménez <i>et al.</i> , 2004)	$I4_1/amd$	tetragonal (Fuess and Kallel, 1972), no Jahn-Teller distortion (Radhakrishna <i>et al.</i> , 1981)	$I4_1/amd$

**Table B.2: Magnetic properties of selected REXO<sub>4</sub>.** Antiferromagnetic order is abbreviated with AF and the corresponding Néel temperature of the transition as  $T_N$ . In the case of ferromagnetic order, the abbreviation FM is used and  $T_C$  is the corresponding Curie temperature of the transition. Entries in red font indicate a determination of the magnetic structure by neutron scattering.

XO <sub>4</sub> =	PO <sub>4</sub>	AsO <sub>4</sub>	CrO <sub>4</sub>	VO <sub>4</sub>
Gd	AF, $T_N = 0.8$ K (Thiriet <i>et al.</i> , 2005), no structure determination	AF, $T_N = 1.262$ K, 2 uniaxial sublattices, ordering axis $c$ (Colwell <i>et al.</i> , 1971)	FM, $T_C = 22$ K, moments of Cr <sup>5+</sup> along $c$ -axis forming 24° angle with Gd <sup>3+</sup> moments (Jiménez-Melero <i>et al.</i> , 2006)	AF, $T_N = 2.495$ K, 2 uniaxial sublattices, ordering axis $c$ (Cashion <i>et al.</i> , 1969, 1970)
Tb	AF, $T_N = 2.28$ K, 2 uniaxial sublattices, ordering axis $c$ (Nägele <i>et al.</i> , 1980), below 2.15 K (Nägele <i>et al.</i> , 1980; Lee <i>et al.</i> , 1971) moments canting off $c$ in the (110) plane by 40° (Spooner <i>et al.</i> , 1971) or 20° (Coing-Boyat <i>et al.</i> , 1975), canting temperature dependent (Nägele <i>et al.</i> , 1980)	AF, $T = 1.48$ K (Wüchner <i>et al.</i> , 1972), incommensurable flat spiral or uniaxial sinusoidal, Tb moments in the $ab$ plane, propagation vector [0.041 0.075 0.018] (Kockelmann <i>et al.</i> , 1992)	FM, $T_C = 22.8$ K, Tb <sup>3+</sup> and Cr <sup>5+</sup> spins collinear in basal plane (Buisson <i>et al.</i> , 1976)	AF, $T_N = 0.61$ K (Kahle <i>et al.</i> , 1974), simple 2 sublattice structure (Gehring <i>et al.</i> , 1976), oriented along [110] (Kazei <i>et al.</i> , 2005)
Dy	AF, $T_N = 3.39$ K (Colwell <i>et al.</i> , 1969), antiparallel arrangement of nearest neighbors along $c$ (Fuess <i>et al.</i> , 1971)	AF, $T_N = 2.44$ K (Kahle <i>et al.</i> , 1971), non-collinear, magnetic moments inclined 22° relative to the $b$ axis in the $ab$ plane (Schäfer and Will, 1971)	FM, $T_C = 22.8$ K (Tezuka and Hinatsu, 2001), Dy <sup>3+</sup> and Cr <sup>5+</sup> moments in the $ab$ plane (Steiner <i>et al.</i> , 1979)	AF, $T_N = 3.0$ K, moments aligned in basal plane (Cooke <i>et al.</i> , 1970), anticollinear in $b$ (Will and Schäfer, 1971)

Table B.2 continued.

Ho	AF, $T_N = 1.39$ K, 2 simple sublattice arrangement, ordering axis $c$ (Cooke <i>et al.</i> , 1973)	AF, $T_N = 0.557$ K, 2 sublattices with moments along optical axis (Schwab <i>et al.</i> , 1974)	FM, $T_C = 17.6$ K, $\text{Ho}^{3+}$ and $\text{Cr}^{5+}$ moments in the $ab$ plane (Climent-Pascual <i>et al.</i> , 2007)	AF, $T_N = 4.5$ mK, moments in $aa'$ plane (Suzuki <i>et al.</i> , 1978), 2 equivalent orientations in $a$ and $a'$ direction (Bleaney, 1980; Suzuki <i>et al.</i> , 1984)
Er	AF, $T_N = 100$ mK, ordering axis $c$ (Mangum and Utton, 1975)	no data	FM, $T_C = 15$ K, collinear $\text{Er}^{3+}$ and $\text{Cr}^{5+}$ sublattices, spins probably in $ab$ plane (Saez-Puche <i>et al.</i> , 2003)	AF, $T_N = 0.4$ K, 2 simple sublattice arrangement, ordering axis $c$ (Metcalf and Rosenberg, 1972)
Tm	estimated: AF, $T_N = 6$ $\mu$ K, ordering in (001) plane (Bleaney <i>et al.</i> , 1983)	no cooperative magnetic order (Mangum <i>et al.</i> , 1971)	FM, $T_C = 18$ K, FM sublattices of $\text{Tm}^{3+}$ and $\text{Cr}^{5+}$ aligned antiparallel in $ab$ plane, parallel along $c$ axis (Saez-Puche <i>et al.</i> , 2003)	no cooperative magnetic order by principle (Cooke <i>et al.</i> , 1972), experimentally no order found until 0.1 mK (Suzuki <i>et al.</i> , 1980)
Yb	magnetically ordered at $T < 0.1$ K (Hodges, 1983)	magnetically ordered at $T < 0.3$ K (Hodges <i>et al.</i> , 1982)	ferrimagnetic, $T_C = 25$ K, AF coupling of $\text{Yb}^{3+}$ and $\text{Cr}^{5+}$ , $\text{Yb}^{3+}$ moments in $ab$ plane (Jiménez <i>et al.</i> , 2004)	AF, $T_N = 93$ mK, spins along $c$ , G-type (Radhakrishna <i>et al.</i> , 1981)



# Bibliography

- Abraham, A. (1983). *Principles of Nuclear Magnetism*. International Series of Monographs on Physics. Oxford University Press, Oxford, UK.
- Aime, S., Batsanov, A., Botta, M., Howard, J., Parker, D., Senanayake, K., and Williams, G. (1994). Solution and solid-state characterization of highly rigid, eight-coordinate lanthanide(III) complexes of a macrocyclic tetrabenzylphosphinate. *Inorg. Chem.*, 33(21):4696–4706.
- Aime, S., Botta, M., Fasano, M., and Terreno, E. (1999). Prototropic and water-exchange processes in aqueous solutions of Gd(III) chelates. *Acc. Chem. Res.*, 32(11):941–949.
- Aime, S., Botta, M., and Terreno, E. (2005). Gd(III)-based contrast agents for MRI. *Adv. Inorg. Chem.*, 57:173–237.
- Albers, A., Okreglak, V., and Chang, C. (2006). A FRET-based approach to ratiometric fluorescence detection of hydrogen peroxide. *J. Am. Chem. Soc.*, 128(30):9640–9641.
- Alessio, E. (2011). *Bioinorganic Medicinal Chemistry*. Wiley-VCH, Weinheim, Germany.
- Alloyeau, D., Ricolleau, C., Mottet, C., Oikawa, T., Langlois, C., Le Bouar, Y., Braidy, N., and Loiseau, A. (2009). Size and shape effects on the order-disorder phase transition in CoPt nanoparticles. *Nature Mater.*, 8(12):940–946.
- Alonso, B. and Sanchez, C. (2000). Structural investigation of polydimethylsiloxane-vanadate hybrid materials. *J. Mater. Chem.*, 10(2):377–386.
- Andersson, K. and Hovmöller, S. (1998). The average atomic volume and density of proteins. *Z. Kristallogr.*, 213(7-8):369–373.
- Ao, M., Wang, Z., Ran, H., Guo, D., Yu, J., Li, A., Chen, W., Wu, W., and Zheng, Y. (2010). Gd-DTPA-loaded PLGA microbubbles as both ultrasound contrast agent and MRI contrast agent – a feasibility research. *J. Biomed. Mater. Res. B Appl. Biomater.*, 93B(2):551–556.
- Aslanov, L., Fetisov, G., and Howard, J. (1998). *Crystallographic instrumentation*. IUCr Monographs on Crystallography 7. Oxford University Press, Oxford, UK.
- Bae, Y., Kang, S., Seo, M., Baines, I., Tekle, E., Chock, B., and Rhee, S. (1997). Epidermal growth factor (EGF)-induced generation of hydrogen peroxide. *J. Biol. Chem.*, 272(1):217–221.

- Bagno, A., Conte, V., Di Furia, F., and Moro, S. (1997). *Ab Initio* calculations on water-peroxovanadium clusters,  $\text{VO}(\text{O}_2)(\text{H}_2\text{O})_n^+$  ( $n = 1 - 5$ ). Implications for the structure in aqueous solution. *J. Phys. Chem. A*, 101(25):4637–4640.
- Banci, L., Bertini, I., and Luchinat, C. (1991). *Nuclear and Electron Relaxation: The Magnetic Nucleus-Unpaired Electron Coupling in Solution*. Wiley-VCH, Weinheim, Germany.
- Bánfi, B., Molnár, G., Maturana, A., Steger, K., Hegedûs, B., Demaurex, N., and Krause, K.-H. (2001). A  $\text{Ca}^{2+}$ -activated NADPH oxidase in testis, spleen, and lymph nodes. *J. Biol. Chem.*, 276(40):37594–37601.
- Barber, M. (1983). Finite size scaling. In Domb, C. and Lebowitz, L., editors, *Phase Transitions and Critical Phenomena*. Academic Press, New York, NY, USA.
- Barford, D. (2004). The role of cysteine residues as redox-sensitive regulatory switches. *Curr. Opin. Struct. Biol.*, 14(6):679–686.
- Barge, A., Cravotto, G., Gianolio, E., and Fedeli, F. (2006). How to determine free Gd and free ligand in solution of Gd chelates. A technical note. *Contrast Media Mol. Imaging*, 1(5):184–188.
- Barreswil, M. (1847). Mémoire sur un nouveau composée oxygénée du chrome. *Ann. Chim. et Phys.*, 20(3):364–369.
- Barton, J., Packer, J., and Sims, R. (1973). Kinetics of the reaction of hydrogen peroxide with cysteine and cysteamine. *J. Chem. Soc., Perkin Trans. 2*, (11):1547–1549.
- Bass, M., DeCusatis, C., Enoch, J., Lakshminarayanan, V., Li, G., MacDonald, C., Mahajan, V., and Van Stryland, E. (2010). *Handbook of Optics. Volume IV. Optical Properties of Materials, Nonlinear Optics, Quantum Optics*. McGraw-Hill, Columbus, OH, USA.
- Battle, X. and Labarta, A. (2002). Finite-size effects in fine particles: magnetic and transport properties. *J. Phys. D: Appl. Phys.*, 35(6):R15–R42.
- Battison, J., Kasten, A., Leask, M., and Lowry, J. (1977). Spectroscopic investigation of holmium vanadate,  $\text{HoVO}_4$ . *J. Phys. C: Solid State Phys.*, 10(2):323.
- Becker, P., Kahle, H., and Keller, K. (1985). The phase diagram of  $\text{TbPO}_4$  measured by linear optical birefringence. *Phys. Status solidi b*, 130(1):191–196.
- Bellin, M. and van der Molen, A. (2008). Extracellular gadolinium-based contrast media: An overview. *Eur. J. Radiol.*, 66(2):160–167.
- Belousov, V., Fradkov, A., Lukyanov, K., Staroverov, D., Shakhbazov, K., Terskikh, A., and Lukyanov, S. (2006). Genetically encoded fluorescent indicator for intracellular hydrogen peroxide. *Nature Methods*, 3(4):281–286.

- Berkhahn, W., Kahle, H., Klein, L., and Schopper, H. (1973). The specific heat of terbium arsenate. *Phys. status solidi b*, 55(1):265–271.
- Berne, B. and Pecora, R. (2003). *Dynamic Light Scattering: With Applications to Chemistry, Biology, and Physics*. Dover Publications, Mineola, NY, USA.
- Bernheim, R., Brown, T., Gutowsky, H., and Woessner, D. (1959). Temperature dependence of proton relaxation times in aqueous solutions of paramagnetic ions. *J. Chem. Phys.*, 30(4):950–956.
- Bertini, I. and Luchinat, C. (1996). Proceedings of the 30th Florence NMR school. *Coord. Chem. Rev.*, 150:1–292.
- Bertini, I., Luchinat, C., and Parigi, G. (2005).  $^1\text{H}$  NMRD profiles of paramagnetic complexes and metalloproteins. *Adv. Inorg. Chem.*, 57:105–172.
- Bjerrum, J., Schwarzenbach, G., and Sillen, L. (1957). *Stability Constants. Part I: Organic Ligands*. Spec. Pub. No. 6. The Chemical Society, London, UK.
- Blasse, G. (1966). On the  $\text{Eu}^{3+}$  fluorescence of mixed metal oxides. IV. The photoluminescent efficiency of  $\text{Eu}^{3+}$ -activated oxides. *J. Chem. Phys.*, 45(7):2356–2360.
- Blasse, G. and Grabmaier, B. (1994). *Luminescent Materials*. Springer, Berlin, Germany.
- Bleaney, B. (1980). Properties of  $\text{HoVO}_4$  below 1 K. I. Predictions from nuclear magnetic resonance. *Proc. R. Soc. Lond. A*, 370(1742):313–330.
- Bleaney, B. (1999). The magnetic properties of erbium vanadate. *Appl. Magn. Reson.*, 16(1):19–22.
- Bleaney, B., Gregg, J., Leask, M., and Wells, M. (1984). Optical and magnetic studies of  $\text{TmAsO}_4$ . *Proc. R. Soc. Lond. A*, 394(1806):69–85.
- Bleaney, B., Pasmán, J., and Wells, M. (1983). Nuclear magnetic resonance of  $^{169}\text{Tm}$  (enhanced) and  $^{31}\text{P}$  in  $\text{TmPO}_4$ . *Proc. R. Soc. Lond. A*, 387(1792):75–90.
- Bloch, F. (1946). Nuclear induction. *Phys. Rev.*, 70(7-8):460–474.
- Bloch, F., Hansen, W., and Packard, M. (1946). Nuclear induction. *Phys. Rev.*, 69(3-4):127.
- Bloembergen, N. and Morgan, L. (1961). Proton relaxation times in paramagnetic solutions. Effects of electron spin relaxation. *J. Chem. Phys.*, 34(3):842–850.
- Bloembergen, N., Purcell, E., and Pound, R. (1948). Relaxation effects in nuclear magnetic resonance absorption. *Phys. Rev.*, 73(7):679–712.
- Blundell, S. (2001). *Magnetism in Condensed Matter*. Oxford University Press, Oxford, UK.

- Bohren, C., Clothiaux, E., and Huffman, D. (2011). *Absorption and Scattering of Light by Small Particles*. Wiley-VCH, Weinheim, Germany, 2nd edition.
- Bottrill, M., Kwok, L., and Long, N. (2006). Lanthanides in magnetic resonance imaging. *Chem. Soc. Rev.*, 35(6):557–571.
- Boussières, G., Foex, M., Haïssinski, M., Morette, A., and Rohmer, R. (1958). Tome XII vanadium, niobium, tantale, protactinium. In Pascal, P., editor, *Nouveau traité de chimie minérale*. Masson, Paris, France.
- Bouzigues, C., Gacoin, T., and Alexandrou, A. (2011). Biological applications of rare-earth based nanoparticles. *ACS Nano*, 5(11):8488–8505.
- Bracken, W. and Sharma, R. (1985). Cytotoxicity-related alterations of selected cellular functions after *in vitro* vanadate exposure. *Biochem. Pharmacol.*, 34(14):2465–2470.
- Bracken, W., Sharma, R., and Elsner, Y. (1985). Vanadium accumulation and subcellular distribution in relation to vanadate induced cytotoxicity *in vitro*. *Cell Biol. Toxicol.*, 1(4):259–268.
- Brandt, R. and Keston, A. (1965). Synthesis of diacetyldichlorofluorescein: A stable reagent for fluorometric analysis. *Anal. Biochem.*, 11(1):6–9.
- Brateman, L. (1986). Chemical shift imaging: A review. *Amer. J. Roentgen.*, 146(5):971–980.
- Brecher, C., Samelson, H., Lempicki, A., Riley, R., and Peters, T. (1967). Polarized spectra and crystal-field parameters of  $\text{Eu}^{+3}$  in  $\text{YVO}_4$ . *Phys. Rev.*, 155(2):178–187.
- Bridot, J.-L., Dayde, D., Riviere, C., Mandon, C., Billotey, C., Lerondel, S., Sabattier, R., Cartron, G., Le Pape, A., Blondiaux, G., Janier, M., Perriat, P., Roux, S., and Tillement, O. (2009). Hybrid gadolinium oxide nanoparticles combining imaging and therapy. *J. Mater. Chem.*, 19(16):2328–2335.
- Bridot, J.-L., Faure, A.-C., Laurent, S., Rivière, C., Billotey, C., Hiba, B., Janier, M., Jossierand, V., Coll, J.-L., Vander Elst, L., Muller, R., Roux, S., Perriat, P., and Tillement, O. (2007). Hybrid gadolinium oxide nanoparticles: Multimodal contrast agents for *in vivo* imaging. *J. Am. Chem. Soc.*, 129(16):5076–5084.
- Broch, E. (1933). Die Kristallstruktur von Yttriumvanadat. *Z. Phys. Chem. B*, 20:345–350.
- Brown, R. (1828). A brief account of microscopical observations made in the months of June, July and August, 1827, on the particles contained in the pollen of plants; and on the general existence of active molecules in organic and inorganic bodies. *Phil. Mag.*, 4:161–173.
- Brunauer, S., Emmett, P., and Teller, E. (1938). Adsorption of gases in multimolecular layers. *J. Am. Chem. Soc.*, 60(2):309–319.

- Buissette, V. (2004). *Nanoluminophores d'oxydes dopés par des lanthanides*. Ph. D. thesis, Ecole Polytechnique, Palaiseau, France.
- Buisson, G., Tchéou, F., Sayetat, F., and Scheunemann, K. (1976). Crystallographic and magnetic properties of  $\text{TbCrO}_4$  at low temperature (X-ray and neutron experiments). *Solid State Comm.*, 18(7):871–875.
- Bulte, J. and Kraitchman, D. (2004). Iron oxide MR contrast agents for molecular and cellular imaging. *NMR Biomed.*, 17(7):484–499.
- Burdon, R., Gill, V., and Rice-Evans, C. (1989). Cell proliferation and oxidative stress. *Free Radical Res. Commun.*, 7(3-6):149–149.
- Burns, A., Ow, H., and Wiesner, U. (2006). Fluorescent core-shell silica nanoparticles: towards "lab on a particle" architectures for nanobiotechnology. *Chem. Soc. Rev.*, 35(11):1028–1042.
- Caglioti, G., Paoletti, A., and Ricci, F. (1958). Choice of collimators for a crystal spectrometer for neutron diffraction. *Nucl. Instrum.*, 3(4):223–228.
- Cai, H. (2005). Hydrogen peroxide regulation of endothelial function: Origins, mechanisms, and consequences. *Cardiovas. Res.*, 68(1):26–36.
- Caille, J., Lemanceau, B., and Bonnemain, B. (1983). Gadolinium as a contrast agent for NMR. *AJNR Am. J. Neuroradiol.*, 4(5):1041–1042.
- Cantley, L., Josephson, L., Warner, R., Yanagisawa, M., Lechene, C., and Guidotti, G. (1977). Vanadate is a potent (Na,K)-ATPase inhibitor found in ATP derived from muscle. *J. Biol. Chem.*, 252(21):7421–7423.
- Cantley, L., Resh, M., and Guidotti, G. (1978). Vanadate inhibits the red cell ( $\text{Na}^+$ ,  $\text{K}^+$ ) ATPase from the cytoplasmic side. *Nature*, 272(5653):552–554.
- Caravan, P., Ellison, J., McMurry, T., and Lauffer, R. (1999). Gadolinium(III) chelates as MRI contrast agents: Structure, dynamics, and applications. *Chem. Rev.*, 99(9):2293–2352.
- Carnall, W., Goodman, G., Rajnak, K., and Rana, R. (1989). A systematic analysis of the spectra of the lanthanides doped into single crystal  $\text{LaF}_3$ . *J. Chem. Phys.*, 90(7):3443–3457.
- Carr, H. and Purcell, E. (1954). Effects of diffusion on free precession in nuclear magnetic resonance experiments. *Phys. Rev.*, 94(3):630–638.
- Casanova, D. (2008). *Nanoparticules d'oxyde : développements et applications comme sondes biologiques*. Ph. D. thesis, Ecole Polytechnique, Palaiseau, France.
- Casanova, D., Bouzigues, C., Nguyen, T.-L., Ramodiharilafy, R., Bouzahir-Sima, L., Gacoïn, T., Boilot, J.-P., Tharaux, P.-L., and Alexandrou, A. (2009). Single europium-doped nanoparticles measure temporal pattern of reactive oxygen species production inside cells. *Nature Nanotechnol.*, 4(9):581–585.

- Casanova, D., Giaume, D., Gacoin, T., Boilot, J.-P., and Alexandrou, A. (2006). Single lanthanide-doped oxide nanoparticles as donors in fluorescence resonance energy transfer experiments. *J. Phys. Chem. B*, 110(39):19264–19270.
- Casanova, D., Giaume, D., Moreau, M., Martin, J.-L., Gacoin, T., Boilot, J.-P., and Alexandrou, A. (2007). Counting the number of proteins coupled to single nanoparticles. *J. Am. Chem. Soc.*, 129(42):12592–12593.
- Cashion, J., Cooke, A., Hoel, L., Martin, D., and Wells, M. (1969). Magnetic properties of gadolinium ortho-vanadate. *Colloques Internationaux du CNRS, Les Eléments des Terres Rares*, 180(2):417–426.
- Cashion, J., Cooke, A., Hoel, L., Martin, D., and Wells, M. (1970). Magnetic properties of gadolinium ortho-vanadate. *J. de Phys.*, C6:417–426.
- Chang, C. and Mao, D. (2007). Thermal dehydration kinetics of a rare earth hydroxide, Gd(OH)<sub>3</sub>. *Int. J. Chem. Kinet.*, 39(2):75–81.
- Chang, I., Hwang, K., and Chiang, C.-S. (2008). Preparation of fluorescent magnetic nanodiamonds and cellular imaging. *J. Am. Chem. Soc.*, 130(46):15476–15481.
- Chang, L., Francesconi, L., Malley, M., Kumar, K., Gougoutas, J., Tweedle, M. F., Lee, D., and Wilson, L. (1993). Synthesis, characterization, and crystal structures of M(DO3A) (M = iron, gadolinium) and Na[M(DOTA)] (M = Fe, yttrium, Gd). *Inorg. Chem.*, 32(16):3501–3508.
- Charlot, G. (1966). *Les Méthodes de la chimie analytique : Analyse quantitative minérale*. Masson, Paris, France, 5th edition.
- Chasteen, N., Lord, E., Thompson, H., and Grady, J. (1986). Vanadium complexes of transferrin and ferritin in the rat. *Biochim. Biophys. Acta Gen. Subj.*, 884(1):84–92.
- Chen, C.-H., Cheng, T.-H., Lin, H., Shih, N.-L., Chen, Y.-L., Chen, Y.-S., Cheng, C.-F., Lian, W.-S., Meng, T.-C., Chiu, W.-T., and Chen, J.-J. (2006). Reactive oxygen species generation is involved in epidermal growth factor receptor transactivation through the transient oxidization of Src homology 2-containing tyrosine phosphatase in endothelin-1 signaling pathway in rat cardiac fibroblasts. *Mol. Pharmacol.*, 69(4):1347–1355.
- Chen, X., Tian, X., Shin, I., and Yoon, J. (2011). Fluorescent and luminescent probes for detection of reactive oxygen and nitrogen species. *Chem. Soc. Rev.*, 40(9):4783–4804.
- Cheng, G., Cao, Z., Xu, X., Van Meir, E., and Lambeth, D. (2001). Homologs of gp91phox: cloning and tissue expression of Nox3, Nox4, and Nox5. *Gene*, 269(1-2):131–140.
- Cheng, K. (1963). Determination of zirconium and hafnium with xylenol orange and methylthymol blue. *Anal. Chim. Acta*, 28:41–53.

- Cheung, E., Alvares, R., Oakden, W., Chaudhary, R., Hill, M., Pichaandi, J., Mo, G., Yip, C., Macdonald, P., Stanisz, G., van Veggel, F., and Prosser, S. (2010). Polymer-stabilized lanthanide fluoride nanoparticle aggregates as contrast agents for magnetic resonance imaging and computed tomography. *Chem. Mater.*, 22(16):4728–4739.
- Choi, H.-J., Kim, S.-J., Mukhopadhyay, P., Cho, S., Woo, J.-R., Storz, G., and Ryu, S.-E. (2001). Structural basis of the redox switch in the OxyR transcription factor. *Cell*, 105(1):103–113.
- Chomel, P. and Rocher, A. (1989). Optique électronique et microscopie électronique à balayage. In Ammou, M., editor, *Microcaractérisation des solides: méthodes d'observation et d'analyse*. CRAM-LPSES-CNRS, Sophia Antipolis, Valbonne, France.
- Ciranni, R., Antonetti, M., and Migliore, L. (1995). Vanadium salts induce cytogenetic effects in in vivo treated mice. *Mutat. Res.*, 343(1):53–60.
- Clempus, R. and Griendling, K. (2006). Reactive oxygen species signaling in vascular smooth muscle cells. *Cardiovasc. Res.*, 71(2):216–225.
- Climent-Pascual, E., Romero de Paz, J., Gallardo-Amores, J., and Saez-Puche, R. (2007). Ferromagnetism vs. antiferromagnetism of the dimorphic  $\text{HoCrO}_4$  oxide. *Solid State Sci.*, 9(7):574–579.
- Coey, J. (2010). *Magnetism and Magnetic Materials*. Cambridge University Press, Cambridge, UK.
- Coing-Boyat, J., Sayetat, F., and Apostolov, A. (1975). Caractéristiques cristallographiques, propriétés et structure magnétiques de  $\text{TbPO}_4$  dans la gamme 1,5 – 300 K. *J. Phys. France*, 36(11):1165–1174.
- Colwell, J., Mangum, B., and Thornton, D. (1971). Low-temperature magnetic susceptibility and heat capacity of  $\text{GdAsO}_4$ . *Phys. Rev. B*, 3(11):3855.
- Colwell, J., Mangum, B., Thornton, D., Wright, J., and Moos, H. (1969). Low-temperature magnetic properties of  $\text{DyPO}_4$ : an ideal three-dimensional ising antiferromagnet. *Phys. Rev. Lett.*, 23(21):1245.
- Cook, D. and Cashion, J. (1979). Mössbauer measurements and exchange interactions in antiferromagnetic  $\text{GdVO}_4$ . *J. Phys. C: Solid State Phys.*, 12(3):605–613.
- Cooke, A., Ellis, C., Gehring, K., Leask, M., Martin, D., Wanklyn, B., Wells, M., and White, R. (1970). Observation of a magnetically controllable Jahn-Teller distortion in dysprosium vanadate at low temperatures. *Solid State Comm.*, 8(9):689–692.
- Cooke, A., Swithenby, S., and Wells, M. (1972). The properties of thulium vanadate – an example of molecular field behaviour. *Solid State Comm.*, 10(3):265–268.

- Cooke, A., Swithenby, S., and Wells, M. (1973). Magnetic interactions in holmium phosphate,  $\text{HoPO}_4$ . *J. Phys. C: Solid State Phys.*, 6(13):2209.
- Corot, C., Robert, P., Idée, J.-M., and Port, M. (2006). Recent advances in iron oxide nanocrystal technology for medical imaging. *Adv. Drug Delivery Res.*, 58(14):1471–1504.
- Cortizo, A., Bruzzone, L., Molinuevo, S., and Etcheverry, S. (2000). A possible role of oxidative stress in the vanadium-induced cytotoxicity in the MC3T3E1 osteoblast and UMR106 osteosarcoma cell lines. *Toxicology*, 147(2):89–99.
- Cortizo, A., Saálice, V., Vescina, C., and Etcheverry, S. (1997). Proliferative and morphological changes induced by vanadium compounds on Swiss 3T3 fibroblasts. *BioMetals*, 10(2):127–133.
- Crangle, J. (1991). *Solid State Magnetism*. Van Nostrand Reinhold, New York, NY, USA.
- Czech, M. (1976). Differential effects of sulfhydryl reagents on activation and deactivation of the fat cell hexose transport system. *J. Biol. Chem.*, 251(4):1164–1170.
- Czech, M., Lawrence, J., and Lynn, W. (1974). Evidence for the involvement of sulfhydryl oxidation in the regulation of fat cell hexose transport by insulin. *Proc. Natl. Acad. Sci. USA*, 71(10):4173–4177.
- Dabadie, T., Ayrál, A., Guizard, C., Cot, L., and Lacan, P. (1996). Synthesis and characterization of inorganic gels in a lyotropic liquid crystal medium. 2. Synthesis of silica gels in lyotropic crystal phases obtained from cationic surfactants. *J. Mater. Chem.*, 6(11):1789–1794.
- D'Autréaux, B. and Toledano, M. (2007). ROS as signalling molecules: mechanisms that generate specificity in ROS homeostasis. *Nature Rev. Mol. Cell Biol.*, 8(10):813–824.
- De Stasio, G., Casalbore, P., Pallini, R., Gilbert, B., Sanità, F., Ciotti, M., Rosi, G., Festinesi, A., Larocca, L., Rinelli, A., Perret, D., Mogk, D., Perfetti, P., Mehta, M., and Mercanti, D. (2001). Gadolinium in human glioblastoma cells for gadolinium neutron capture therapy. *Cancer Res.*, 61(10):4272–4277.
- Debye, P. (1913). Interferenz von Röntgenstrahlen und Wärmebewegung. *Ann. Phys.*, 348(1):49–92.
- Debye, P. and Hückel, E. (1923). Zur Theorie der Electrolyte. *Phys. Z.*, 24(9):185–206.
- Derjaguin, B. and Landau, L. (1941). Theory of the stability of strongly charged lyophobic sols and of the adhesion of strongly charged particles in solution of electrolytes. *Acta Physicochim. URSS*, 14:633–662.

- Dexter, D. (1953). A theory of sensitized luminescence in solids. *J. Chem. Phys.*, 21(5):836–850.
- Djordjevic, C. and Vuletic, N. (1980). Peroxo- and hydroxolanthanide(III) complexes of the EDTA family. *Inorg. Chem.*, 19(10):3049–3053.
- Domingo, J. (1996). Vanadium: A review of the reproductive and developmental toxicity. *Reprod. Toxicol.*, 10(3):175–182.
- Domingo, J. (2002). Vanadium and tungsten derivatives as antidiabetic agents. *Biol. Trace Elem. Res.*, 88(2):97–112.
- Dorenbos, P. (2003). Anomalous luminescence of  $\text{Eu}^{2+}$  and  $\text{Yb}^{2+}$  in inorganic compounds. *J. Phys. Condens. Matter*, 15(17):2645.
- Dufourc, E., Mayer, C., Stohrer, J., Althoff, G., and Kothe, G. (1992). Dynamics of phosphate head groups in biomembranes. comprehensive analysis using phosphorus-31 nuclear magnetic resonance lineshape and relaxation time measurements. *Biophys. J.*, 61(1):42–57.
- Dunn, P. (2010). *Measurement and data analysis for engineering and science*. CRC Press, Boca Raton, FL, USA, 2nd edition.
- Einstein, A. (1905). Über die von der molekularkinetischen Theorie der Wärme geforderte Bewegung von in ruhenden Flüssigkeiten suspendierten Teilchen. *Ann. Phys.*, 322(8):549–560.
- Elliott, R., Harley, R., Hayes, W., and Smith, S. (1972). Raman scattering and theoretical studies of Jahn-Teller induced phase transitions in some rare-earth compounds. *Proc. R. Soc. Lond. A*, 328(1573):217–266.
- Emmett, P. and Brunauer, S. (1937). The use of low temperature van der Waals adsorption isotherms in determining the surface area of iron synthetic ammonia catalysts. *J. Am. Chem. Soc.*, 59(8):1553–1564.
- Ermeneux, F., Goutaudier, C., Moncorgé, R., Sun, Y., Cone, R., Zannoni, E., Cavalli, E., and Bettinelli, M. (2000). Multiphonon relaxation in  $\text{YVO}_4$  single crystals. *Phys. Rev. B*, 61(6):3915–3921.
- Evangelisti, M., Sorop, T., Bakharev, O., Visser, D., Hillier, A., Alonso, J., Haase, M., Boatner, L., and Jos de Jongh, L. (2011). Size-dependent magnetic ordering and spin dynamics in  $\text{DyPO}_4$  and  $\text{GdPO}_4$  nanoparticles. *Phys. Rev. B*, 84(9):094408–1–18.
- Evanics, F., Diamente, P., van Veggel, F., Stanisz, G., and Prosser, R. (2006). Water-soluble  $\text{GdF}_3$  and  $\text{GdF}_3/\text{LaF}_3$  nanoparticles physical characterization and NMR relaxation properties. *Chem. Mater.*, 18(10):2499–2505.
- Fick, A. (1855). Ueber Diffusion. *Ann. Phys.*, 170(1):59–86.

- Finger, L., Cox, D., and Jephcoat, A. (1994). A correction for powder diffraction peak asymmetry due to axial divergence. *J. Appl. Cryst.*, 27(6).
- Finkel, T. (2011). Signal transduction by reactive oxygen species. *J. Cell. Biol.*, 194(1):7–15.
- Forman, H., Maiorino, M., and Ursini, F. (2010). Signaling functions of reactive oxygen species. *Biochemistry*, 49(5):835–842.
- Förster, T. (1948). Zwischenmolekulare Energiewanderung und Fluoreszenz. *Ann. Phys.*, 437(1-2):55–75.
- Fortin, M.-A., Petoral, R., Söderlind, F., Klasson, A., Engström, M., Veres, T., Käll, P.-O., and Uvdal, K. (2007). Polyethylene glycol-covered ultra-small Gd<sub>2</sub>O<sub>3</sub> nanoparticles for positive contrast at 1.5 T magnetic resonance clinical scanning. *Nanotechnology*, 18(39):395501.
- Freed, J. (1978). Dynamic effects of pair correlation functions on spin relaxation by translational diffusion in liquids. II. Finite jumps and independent T<sub>1</sub> processes. *J. Chem. Phys.*, 68(9):4034–4037.
- Freundlich, H. (1903). Über die Fällung von kolloidalen Lösungen durch Elektrolyte. *Z. Phys. Chem.*, 44:129–160.
- Friskén, B. (2001). Revisiting the method of cumulants for the analysis of dynamic light-scattering data. *Appl. Opt.*, 40(24):4087–4091.
- Frullano, L. and Meade, T. (2007). Multimodal MRI contrast agents. *J. Biol. Inorg. Chem.*, 12(7):939–949.
- Fuess, H. and Kallel, A. (1972). Refinement of the crystal structure of some rare earth vanadates RVO<sub>4</sub> (R = Dy, Tb, Ho, Yb). *J. Solid State Chem.*, 5(1):11–14.
- Fuess, H., Kallel, A., and Tchéou, F. (1971). Neutron diffraction determination of the magnetic structure of DyPO<sub>4</sub>. *Solid State Comm.*, 9(22):1949–1952.
- Gacoin, T., Malier, L., and Boilot, J.-P. (1997). Sol-gel transition in CdS colloids. *J. Mater. Chem.*, 7(6):859–860.
- Gaur, K. and Lal, H. (1983). Unusual magnetic behaviour of heavy rare earth vanadates at higher temperature. *J. Mater. Sci. Lett.*, 2(12):744–746.
- Gaur, K., Tripathi, A., and Lal, H. (1983). Quasi-ferromagnetism in antiferromagnetic GdVO<sub>4</sub>. *J. Mater. Sci. Lett.*, 2(4):161–162.
- Gazeau, F., Lévy, M., and Wilhelm, C. (2008). Optimizing magnetic nanoparticle design for nanothermotherapy. *Nanomedicine*, 3(6):831–844.
- Gehring, G., Kahle, H., Nägele, W., Simon, A., and Wüchner, W. (1976). Two-level singlet magnetism in TbAsO<sub>4</sub> and TbVO<sub>4</sub>. *Phys. status solidi b*, 74(1):297–309.

- Giannoni, E., Buricchi, F., Grimaldi, G., Parri, M., Cialdai, F., Taddei, M., Raugei, G., Ramponi, G., and Chiarugi, P. (2008). Redox regulation of anoikis: reactive oxygen species as essential mediators of cell survival. *Cell Death Differ.*, 15(5):867–878.
- Giaume, D. (2006). *Nanoparticules d'orthovanadate d'yttrium : Fonctionnalisation et application comme sondes luminescentes pour la biologie*. Ph. D. thesis, Ecole Polytechnique, Palaiseau, France.
- Giaume, D., Poggi, M., Casanova, D., Mialon, G., Lahlil, K., Alexandrou, A., Gacoin, T., and Boilot, J.-P. (2008). Organic functionalization of luminescent oxide nanoparticles toward their application as biological probes. *Langmuir*, 24(19):11018–11026.
- Gibby, W., Gibby, K., and Gibby, W. (2004). Comparison of Gd DTPA-BMA (Omniscan) versus Gd HP-DO3A (ProHance) retention in human bone tissue by inductively coupled plasma atomic emission spectroscopy. *Invest. Radiol.*, 39(3):138–142.
- Giorgio, M., Trinei, M., Migliaccio, E., and Pelicci, P. (2007). Hydrogen peroxide: A metabolic by-product or a common mediator of ageing signals? *Nature Rev. Mol. Cell Biol.*, 8(9):722–728.
- Göbel, H., Müller-Vogt, G., Orlich, R., and Klein, L. (1972). Crystallographic distortion in TbAsO<sub>4</sub> at low temperatures. *Phys. Lett. A*, 41(5):409–410.
- Göbel, H. and Will, G. (1972a). Crystallographic phase transition in DyAsO<sub>4</sub>. *Phys. Lett. A*, 39(2):79–80.
- Göbel, H. and Will, G. (1972b). Low temperature X-ray diffraction and phase transitions in DyVO<sub>4</sub> and DyAsO<sub>4</sub>. *Phys. status solidi b*, 50(1):147–154.
- Goldstein, J., Newbury, D., Joy, D., Lyman, C., Echlin, P., Lifshin, E., Sawyer, L., and Michael, J. (2002). *Scanning Electron Microscopy and X-Ray Microanalysis*. Kluwer Academic Publishers, Dordrecht, The Netherlands, 3rd edition.
- Goldys, E. (2009). *Fluorescence Applications in Biotechnology and Life Sciences*. John Wiley & Sons, Hoboken, NJ, USA.
- Gorodetsky, G., Hornreich, R., and Wanklyn, B. (1973). Statistical mechanics and critical behavior of the magnetoelectric effect in GdVO<sub>4</sub>. *Phys. Rev. B*, 8(5):2263–2267.
- Gough, D. and Cotter, T. (2011). Hydrogen peroxide: A Jekyll and Hyde signalling molecule. *Cell Death Dis.*, 2:e213.
- Grazulis, S., Chateigner, D., Downs, R., Yokochi, A., Quiros, M., Lutterotti, L., Manakova, E., Butkus, J., Moeck, P., and Le Bail, A. (2009). Crystallography open database – an open-access collection of crystal structures. *J. Appl. Cryst.*, 42(4):726–729.

- Greenwood, N. and Earnshaw, A. (1986). *Chemistry of the Elements*. Pergamon Press, Oxford, UK.
- Groeger, G., Quiney, C., and Cotter, T. (2009). Hydrogen peroxide as a cell-survival signaling molecule. *Antioxid. Redox Signal.*, 11(11):2655–2671.
- Guillot-Noël, O., Kahn-Harari, A., Viana, B., Vivien, D., Antic-Fidancev, E., and Porcher, P. (1998). Optical spectra and crystal field calculations of Nd<sup>3+</sup> doped zircon-type YMO<sub>4</sub> laser hosts (M = V, P, As). *J. Phys. Condens. Matter*, 10(29):6491–6504.
- Guinier, A. (1963). *Théorie et technique de la radiocristallographie*. Editions Dunod, Paris, France, 3rd edition.
- Haas, Y. and Stein, G. (1972). Radiative and nonradiative pathways in solutions. Excited states of the europium(III) ion. *J. Phys. Chem.*, 76(8):1093–1104.
- Hahn, E. (1950). Spin echoes. *Phys. Rev.*, 80(4):580–594.
- Hahn, M., Singh, A., Sharma, P., Brown, S., and Moudgil, B. (2011). Nanoparticles as contrast agents for *in vivo* bioimaging: Current status and future perspectives. *Anal. Bioanal. Chem.*, 399(1):3–27.
- Hahn, T. (2005). *International Tables for Crystallography, Volume A: Space-group symmetry*. Kluwer Academic Publishers, Dordrecht, The Netherlands, 5th edition.
- Haley, T., Komesu, N., Colvin, G., Koste, L., and Upham, H. (1965). Pharmacology and toxicology of europium chloride. *J. Pharm. Sci.*, 54(4):643–645.
- Hamaker, H. (1937). The London-van der Waals attraction between spherical particles. *Physica*, 4(10):1058–1072.
- Hartkamp, H. (1959). Notiz zur photometrischen Bestimmung des Vanadiums mit Wasserstoffperoxyd. *Z. anal. Chem.*, 169(5):339–342.
- Hasebroock, K. and Serkova, N. (2009). Toxicity of MRI and CT contrast agents. *Expert Opin. Drug Metab. Toxicol.*, 5(4):403–416.
- Hastings, J., Thomlinson, W., and Cox, D. (1984). Synchrotron X-ray powder diffraction. *J. Appl. Cryst.*, 17(2):85–95.
- Havel, J., Moreno, C., Hrdlička, A., and Valiente, M. (1994). Spectrophotometric determination of rare earth elements by flow injection analysis based on their reaction with xylenol orange and cetylpyridinium bromide. *Talanta*, 41(8):1251–1254.
- Hermann, P., Kotek, J., Kubíček, V., and Lukeš, I. (2008). Gadolinium(III) complexes as MRI contrast agents: Ligand design and properties of the complexes. *Dalton Trans.*, 37(23):3027–3047.

- Hiemenz, P. and Rajagopalan, R. (1997). *Principles of colloid and surface chemistry*. Marcel Dekker, New York, NY, USA, 3rd edition.
- Hifumi, H., Yamaoka, S., Tanimoto, A., Citterio, D., and Suzuki, K. (2006). Gadolinium-based hybrid nanoparticles as a positive MR contrast agent. *J. Am. Chem. Soc.*, 128(47):15090–15091.
- Higuchi, M., Kodaira, K., Urata, Y., Wada, S., and Machida, H. (2004). Float zone growth and spectroscopic characterization of Tm:GdVO<sub>4</sub> single crystals. *J. Cryst. Growth*, 265(3-4):487–493.
- Hill, R. and Fischer, R. (1990). Profile agreement indices in Rietveld and pattern-fitting analysis. *J. Appl. Cryst.*, 23(6):462–468.
- Hillery, A., Lloyd, A., and Swarbrick, J. (2001). *Drug Delivery and Targeting: For Pharmacists and Pharmaceutical Scientists*. Taylor & Francis, New York, NY, USA.
- Hirano, S. and Suzuki, K. (1996). Exposure, metabolism, and toxicity of rare earths and related compounds. *Environ Health Perspect*, 104(Suppl. 1):85–95.
- Hodges, J. (1983). Tm<sup>3+</sup> and Yb<sup>3+</sup> in TmXO<sub>4</sub> and Yb<sub>3+</sub> in YbXO<sub>4</sub> (X = P, V) from <sup>169</sup>Tm and <sup>170</sup>Yb Mössbauer measurements. *J. Phys. France*, 44(7):833–839.
- Hodges, J., Imbert, P., and Jéhanno, G. (1982). Local properties of Tm<sup>3+</sup> and Yb<sup>3+</sup> in TmAsO<sub>4</sub> and ordering in YbAsO<sub>4</sub> from <sup>169</sup>Tm and <sup>170</sup>Yb mössbauer measurements. *J. Phys. France*, 43(8):1249–1254.
- Holleman, A., Wiberg, E., and Wiberg, N. (1995). *Lehrbuch der anorganischen Chemie*. de Gruyter, Berlin, Germany, 101st edition.
- Hosmane, N., Maguire, J., Zhu, Y., and Takagaki, M. (2011). *Boron and Gadolinium Neutron Capture Therapy for Cancer Treatment*. World Scientific, Singapore.
- Hsu, C. and Powell, R. (1975). Energy transfer in europium doped yttrium vanadate crystals. *J. Lumin.*, 10(5):273–293.
- Huang, C.-C., Liu, T.-Y., Su, C.-H., Lo, Y.-W., Chen, J.-H., and Yeh, C.-S. (2008). Superparamagnetic hollow and paramagnetic porous Gd<sub>2</sub>O<sub>3</sub> particles. *Chem. Mater.*, 20(12):3840–3848.
- Hubbard, C., Swanson, H., and Mauer, F. (1975). A silicon powder diffraction standard reference material. *J. Appl. Cryst.*, 8(1):45–48.
- Huignard, A. (2001). *Nanoparticules de vanadate d'yttrium : Synthèse colloïdale et luminescence des ions lanthanides*. Ph. D. thesis, Ecole Polytechnique, Palaiseau, France.
- Huignard, A., Buissette, V., Laurent, G., Gacoin, T., and Boilot, J.-P. (2002). Synthesis and characterizations of YVO<sub>4</sub>:Eu colloids. *Chem. Mater.*, 14(5):2264–2269.

- Huignard, A., Gacoin, T., and Boilot, J.-P. (2000). Synthesis and luminescence properties of colloidal  $\text{YVO}_4\text{:Eu}$  phosphors. *Chem. Mater.*, 12(4):1090–1094.
- Inokuti, M. and Hirayama, F. (1965). Influence of energy transfer by the exchange mechanism on donor luminescence. *J. Chem. Phys.*, 43(6):1978–1989.
- Itoh, H., Fujisawa, M., Ikegami, Y., and Suzuki, Y. (1985). Stability constants of rare earth citrate complex species. *Lanthanide Actinide Res.*, 1:79–88.
- Jansen, E., Schäfer, W., and Will, G. (1994).  $R$  values in analysis of powder diffraction data using Rietveld refinement. *J. Appl. Cryst.*, 27(4):492–496.
- Järvinen, M. (1993). Application of symmetrized harmonics expansion to correction of the preferred orientation effect. *J. Appl. Cryst.*, 26(4):525–531.
- Jiménez, E., Bonville, P., Hodges, J., Gubbens, P., Isasi, J., and Saez-Puche, R. (2004). Influence of the  $\text{Cr}^{5+}$  ion on the magnetic properties of  $\text{YbCrO}_4$  oxide. *J. Magn. Magn. Mater.*, 272-276(Part 1):571–573.
- Jiménez, E., Isasi, J., Fernandez, M. T., and Saez-Puche, R. (2002). Magnetic behavior of  $\text{ErCrO}_4$  oxide. *J. Alloys Compounds*, 344(1-2):369–374.
- Jiménez-Melero, E., Gubbens, P., Steenvoorden, M., Sakarya, S., Goosens, A., de Reotier, P., Yaouanc, A., Rodríguez-Carvajal, J., Beuneu, B., Isasi, J., Saez-Puche, R., Zimmerman, U., and Martínez, J. (2006). A combined study of the magnetic properties of  $\text{GdCrO}_4$ . *J. Phys. Condens. Matter.*, 18(34):7893–7904.
- Jin, D., Yang, H., Ding, G., Yu, X., Wang, L., and Zheng, Y. (2008). Hydrothermal synthesis and photoluminescence behavior of Eu-doped  $\text{GdVO}_4$ . *Inorg. Mater.*, 44(10):1121–1124.
- Jin, H., Heller, D., Kalbacova, M., Kim, J.-H., Zhang, J., Boghossian, A., Maheshri, N., and Strano, M. (2010). Detection of single-molecule  $\text{H}_2\text{O}_2$  signalling from epidermal growth factor receptor using fluorescent single-walled carbon nanotubes. *Nature Nanotechnol.*, 5(4):302–309.
- Judd, B. (1962). Optical absorption intensities of rare-earth ions. *Phys. Rev.*, 127(3):750–761.
- Jun, Y.-W., Seo, J.-W., and Cheon, J. (2008). Nanoscaling laws of magnetic nanoparticles and their applicabilities in biomedical sciences. *Acc. Chem. Res.*, 41(2):179–189.
- Kahle, H., Klein, L., Müller-Vogt, G., and Schopper, H. (1971). Magnetic properties of  $\text{DyAsO}_4$  at low temperatures. *Phys. status solidi b*, 44(2):619–626.
- Kahle, H., Simon, A., and Wüchener, W. (1974). Observation of a cooperative phase transition in  $\text{TbVO}_4$  at 0.61 K. *Phys. status solidi b*, 61(2):K53–K54.
- Kazei, Z., Snegirev, V., Broto, J., and Rakoto, H. (2005). Jahn-Teller magnet  $\text{TbVO}_4$  in a strong magnetic field up to 50 T. *JETP Lett.*, 82(9):609–612.

- Kerr, J. (1966). Bond dissociation energies by kinetic methods. *Chem. Rev.*, 66(5):465–500.
- Kim, J., Piao, Y., and Hyeon, T. (2009). Multifunctional nanostructured materials for multimodal imaging, and simultaneous imaging and therapy. *Chem. Soc. Rev.*, 38(2):372–390.
- Kim, S., Merchant, K., Nudelman, R., Beyer, W., Keng, T., DeAngelo, J., Hausladen, A., and Stamler, J. (2002). OxyR: A molecular code for redox-related signaling. *Cell*, 109(3):383–396.
- Kirste, A., von Ortenberg, M., Demidov, A., Kazei, Z., Kolmakova, N., Platonov, V., Sidorenko, A., and Tatsenko, O. (2003). Crossover in the van Vleck paramagnet  $\text{TmPO}_4$ . *Physica B*, 336(3-4):335–343.
- Klein, L., Wüchner, W., Kahle, H., and Schopper, H. (1971). Study of a phase transition in  $\text{TbAsO}_4$ . *Phys. status solidi b*, 48(2):K139–K141.
- Kockelmann, W., Schäfer, W., and Will, G. (1992). Low temperature neutron diffraction investigation of the complex incommensurate magnetic ordering behaviour of  $\text{TbAsO}_4$ . *J. Phys. Chem. Solids*, 53(7):913–921.
- Koppel, D. (1972). Analysis of macromolecular polydispersity in intensity correlation spectroscopy: The method of cumulants. *J. Chem. Phys.*, 57(11):4814–4820.
- Kowalewski, J., Kruk, D., and Parigi, G. (2005). NMR relaxation in solution of paramagnetic complexes: Recent theoretical progress for  $S \geq 1$ . *Adv. Inorg. Chem.*, 57:41–104.
- Kowalewski, J., Nordenskiöld, L., Benetis, N., and Westlund, P.-O. (1985). Theory of nuclear spin relaxation in paramagnetic systems in solution. *Prog. Nucl. Magn. Reson. Spectrosc.*, 17:141–185.
- Kropp, J. and Windsor, M. (1965). Luminescence and energy transfer in solutions of rare-earth complexes. I. Enhancement of fluorescence by deuterium substitution. *J. Chem. Phys.*, 42(5):1599–1608.
- Kubin, R. and Fletcher, A. (1982). Fluorescence quantum yields of some rhodamine dyes. *J. Lumin.*, 27(4):455–462.
- Lakowicz, J. (2006). *Principles of fluorescence spectroscopy, Volume 1*. Springer, New York, NY, USA.
- Lambeth, D. (2004). NOX enzymes and the biology of reactive oxygen. *Nature Rev. Immunol.*, 4(3):181–189.
- LaMer, V. and Dinegar, R. (1950). Theory, production and mechanism of formation of monodispersed hydrosols. *J. Am. Chem. Soc.*, 72(11):4847–4854.
- Langford, J. (1978). A rapid method for analysing the breadths of diffraction and spectral lines using the Voigt function. *J. Appl. Cryst.*, 11(1).

- Laporte, O. and Meggers, W. (1925). Some rules of spectral structure. *J. Opt. Soc. Am.*, 11(5):459–463.
- Lassègue, B., Sorescu, D., Szöcs, K., Yin, Q., Akers, M., Zhang, Y., Grant, S., Lambeth, D., and Griendling, K. (2001). Novel gp91phox homologues in vascular smooth muscle cells : Nox1 mediates angiotensin II-induced superoxide formation and redox-sensitive signaling pathways. *Circ. Res.*, 88(9):888–894.
- Lauffer, R. (1987). Paramagnetic metal-complexes as water proton relaxation agents for NMR imaging – theory and design. *Chem. Rev.*, 87(5):901–927.
- Laurent, S., Vander Elst, L., Henoumont, C., and Muller, R. (2010). How to measure the transmetallation of a gadolinium complex. *Contrast Media Mol. Imaging*, 5(6):305–308.
- Laurent, S., Vander Elst, L., and Muller, R. (2006). Comparative study of the physicochemical properties of six clinical low molecular weight gadolinium contrast agents. *Contrast Media Mol. Imaging*, 1(3):128–137.
- Lauterbur, P. (1973). Image formation by induced local interactions: Examples employing nuclear magnetic resonance. *Nature*, 242(5394):190–191.
- Lauterbur, P. (1974). Magnetic resonance zeugmatography. *Pure Appl. Chem.*, 40(1-2):149–157.
- Le Duc, G., Miladi, I., Alric, C., Mowat, P., Bräuer-Krisch, E., Bouchet, A., Khalil, E., Billotey, C., Janier, M., Lux, F., Epicier, T., Perriat, P., Roux, S., and Tillement, O. (2011). Toward an image-guided microbeam radiation therapy using gadolinium-based nanoparticles. *ACS Nano*, 5(12):9566–9574.
- LeBel, C., Ischiropoulos, H., and Bondy, S. (1992). Evaluation of the probe 2',7'-dichlorofluorescein as an indicator of reactive oxygen species formation and oxidative stress. *Chem. Res. Toxicol.*, 5(2):227–231.
- Lee, B.-I., Lee, K., Lee, J. H., Lee, I., and Byeon, S.-H. (2009). Synthesis of colloidal aqueous suspensions of a layered gadolinium hydroxide: A potential MRI contrast agent. *Dalton Trans.*, 38(14):2490–2495.
- Lee, J., Moos, H., and Mangum, B. (1971). Magnetic properties of TbPO<sub>4</sub>, a canted antiferromagnet. *Solid State Comm.*, 9(13):1139–1141.
- Levitt, M. (2008). *Spin dynamics : Basics of nuclear magnetic resonance*. John Wiley, Chichester, UK, 2nd edition.
- Lide, D. (2008). *CRC Handbook of Chemistry and Physics*. CRC Press, Taylor and Francis, Boca Raton, FL, USA, 89th edition.
- Lien-Vien, D., Colthup, N., Fately, W., and Grasselly, J. (1991). *The Handbook of Infrared and Raman Characteristic Frequencies of Organic Molecules*. Academic Press, New York, NY, USA.

- Lipson, H., Langford, J., and Hu, H.-C. (2006). Trigonometric intensity factors. In Prince, E., editor, *International Tables for Crystallography*, volume C, pages 596–598. Springer, Dordrecht, The Netherlands.
- Liu, G. and Jacquier, B. (2005). *Spectroscopic properties of rare earths in optical materials*. Springer Verlag, Berlin, Germany.
- Llobet, J. and Domingo, J. (1984). Acute toxicity of vanadium compounds in rats and mice. *Toxicol. Lett.*, 23(2):227–231.
- Lo, L.-C. and Chu, C.-Y. (2003). Development of highly selective and sensitive probes for hydrogen peroxide. *Chem. Comm.*, (21):2728–2729.
- Louër, D. (2002). Laboratory X-ray powder diffraction. In David, W., Shankland, K., McCusker, L., and Baerlocher, C., editors, *Structure Determination from Powder Diffraction data*. Oxford University Press, Oxford, UK.
- Lowe, M. (2002). MRI contrast agents: The next generation. *Aust. J. Chem.*, 55(9):551–556.
- Maeda, H., Fukuyasu, Y., Yoshida, S., Fukuda, M., Saeki, K., Matsuno, H., Yamauchi, Y., Yoshida, K., Hirata, K., and Miyamoto, K. (2004). Fluorescent probes for hydrogen peroxide based on a non-oxidative mechanism. *Angew. Chem. Int. Ed.*, 43(18):2389–2391.
- Magde, D., Wong, R., and Seybold, P. (2002). Fluorescence quantum yields and their relation to lifetimes of rhodamine 6G and fluorescein in nine solvents: Improved absolute standards for quantum yields. *Photochem. Photobiol.*, 75(4):327–334.
- Mangum, B., Lee, J., and Moos, H. (1971). Magnetically controllable cooperative Jahn-Teller distortion in  $\text{TmAsO}_4$ . *Phys. Rev. Lett.*, 27(22):1517.
- Mangum, B. and Utton, D. (1975). Antiferromagnetic ordering in  $\text{ErPO}_4$ . *AIP Conf. Proc.*, 24(1):65–66.
- Mastanduno, M., Davis, S., Jiang, S., diFlorio Alexander, R., Pogu, B., and Paulsen, K. (2011). Combined three-dimensional magnetic resonance guided optical spectroscopy for functional and molecular imaging of human breast cancer. In Lin, L. and Ntziachristos, V., editors, *Molecular Imaging III, Proceedings of the SPIE-OSA Biomedical Optics Conference, Munich, Germany*, pages 80890A–1–80890A–7.
- Matsumura, M., Yamada, K., Fujimaki, M., Sugihara, H., and Nakagami, H. (1999). Proton relaxation caused by magnetic resonance imaging contrast agent, oral magnetic particles. *Chem. Pharm. Bull.*, 47(6):727–731.
- Meiboom, S. and Gill, G. (1958). Modified spin-echo method for measuring nuclear relaxation times. *Rev. Sci. Instrum.*, 29(8):688–691.

- Meng, T.-C., Fukada, T., and Tonks, N. (2002). Reversible oxidation and inactivation of protein tyrosine phosphatases *in vivo*. *Mol. Cell*, 9(2):387–399.
- Metcalfe, M. and Rosenberg, H. (1972). The magnetothermal resistivity of antiferromagnetic crystals at low temperatures. III.  $\text{ErVO}_4$ , a new antiferromagnet. *J. Phys. C: Solid State Phys.*, 5(4):474.
- Meyer, R., Peters, F., Gmelin, L., Pietsch, E., and Becke-Goehring, M. (1966). *Gmelins Handbuch der anorganischen Chemie. System-Nr. 3. Lieferung 7. Wasserstoffperoxid*. Verlag Chemie, Weinheim, Germany, 8th edition.
- Mialon, G. (2009). *Monocristaux  $\text{YVO}_4:\text{Ln}$  à l'échelle nanométrique : Mécanismes de fluorescence et upconversion*. Ph. D. thesis, Ecole Polytechnique, Palaiseau, France.
- Mialon, G., Gohin, M., Gacoin, T., and Boilot, J.-P. (2008). High temperature strategy for oxide nanoparticle synthesis. *ACS Nano*, 2(12):2505–2512.
- Mialon, G., Türkcan, S., Alexandrou, A., Gacoin, T., and Boilot, J.-P. (2009). New insights into size effects in luminescent oxide nanocrystals. *J. Phys. Chem. C*, 113(43):18699–18706.
- Michalet, X., Pinaud, F., Bentolila, L., Tsay, J., Doose, S., Li, J., Sundaresan, G., Wu, A., Gambhir, S., and Weiss, S. (2005). Quantum dots for live cells, *in vivo* imaging, and diagnostics. *Science*, 307(5709):538–544.
- Milan, E. (1929). The dissociation pressure of vanadium pentoxide. *J. Phys. Chem.*, 33(4):498–508.
- Miller, E., Bian, S., and Chang, C. (2007). A fluorescent sensor for imaging reversible redox cycles in living cells. *J. Am. Chem. Soc.*, 129(12):3458–3459.
- Miller, E. and Chang, C. (2007). Fluorescent probes for nitric oxide and hydrogen peroxide in cell signaling. *Curr. Opin. Chem. Biol.*, 11(6):620–625.
- Miller, E., Dickinson, B., and Chang, C. (2010). Aquaporin-3 mediates hydrogen peroxide uptake to regulate downstream intracellular signaling. *Proc. Natl. Acad. Sci. USA*, 107(36):15681–15686.
- Mooney, R. and Toma, S. (1967). Energy transfer from absorbing group to  $\text{Eu}^{3+}$  in  $\text{YVO}_4:\text{Eu}$ . *J. Chem. Phys.*, 46(11):4544–4545.
- Mukherjee, S., Lane, R., and Lynn, W. (1978). Endogenous hydrogen peroxide and peroxidative metabolism in adipocytes in response to insulin and sulfhydryl reagents. *Biochem. Pharmacol.*, 27(22):2589–2594.
- Mukherjee, S. and Mukherjee, C. (1982). Similar activities of nerve growth factor and its homologue proinsulin in intracellular hydrogen peroxide production and metabolism in adipocytes: Transmembrane signalling relative to insulin-mimicking cellular effects. *Biochem. Pharmacol.*, 31(20):3163–3172.

- Na, H., Song, I., and Hyeon, T. (2009). Inorganic nanoparticles for MRI contrast agents. *Adv. Mater.*, 21(21):2133–2148.
- Nägele, W., Hohlwein, D., and Domann, G. (1980). Structural and magnetic phase transitions in  $\text{TbPO}_4$  studied by neutron diffraction. *Z. Phys. B: Condens. Matter*, 39(4):305–310.
- Nechay, B. (1984). Mechanisms of action of vanadium. *Ann. Rev. Pharmacol. Toxicol.*, 24(1):501–524.
- Nguyên, T. (2009). *Détection de peroxyde d'hydrogène résolue en temps à l'aide de nanoparticules  $\text{Y}_{1-x}\text{Eu}_x\text{VO}_4$  luminescentes : Application à la signalisation vasculaire*. Ph. D. thesis, Ecole Polytechnique, Palaiseau, France.
- Ocaña, M., Rodriguez-Clemente, R., and Serna, C. (1995). Uniform colloidal particles in solution: Formation mechanisms. *Adv. Mater.*, 7(2):212–216.
- Ofelt, G. (1962). Intensities of crystal spectra of rare-earth ions. *J. Chem. Phys.*, 37(3):511–520.
- Ohashi, T., Mizutani, A., Murakami, A., Kojo, S., Ishii, T., and Taketani, S. (2002). Rapid oxidation of dichlorodihydrofluorescein with heme and hemoproteins: Formation of the fluorescein is independent of the generation of reactive oxygen species. *FEBS Lett.*, 511(1):21–27.
- Ohyama, T. and Cowan, J. (1995). Calorimetric studies of metal binding to tetracycline. Role of solvent structure in defining the selectivity of metal ion-drug interactions. *Inorg. Chem.*, 34(11):3083–3086.
- Okada, C. and Rechsteiner, M. (1982). Introduction of macromolecules into cultured mammalian cells by osmotic lysis of pinocytotic vesicles. *Cell*, 29(1):33–41.
- Oksendal, A. and Hals, P.-A. (1993). Biodistribution and toxicity of MR imaging contrast media. *J. Magn. Res. Imaging*, 3(1):157–165.
- Onishi, H. and Ishiwatari, N. (1960). Spectrophotometric determination of bismuth with xylenol orange. *Bull. Chem. Soc. Jpn.*, 33(11):1581–1584.
- Overbeek, J. (1982). Colloids, a fascinating subject: Introductory lecture. In Goodwin, J., editor, *Colloidal dispersions*. Royal Society of Chemistry, London, UK.
- Palilla, F., Levine, A., and Rinkevics, M. (1965). Rare earth activated phosphors based on yttrium orthovanadate and related compounds. *J. Electrochem. Soc.*, 112(8):776–779.
- Pannetier, J. (1993). Powder diffraction techniques. In Baruchel, J., Hodeau, J.-L., Lehmann, M., Regnard, J.-R., and Schlenker, C., editors, *Neutron and Synchrotron Radiation for Condensed Matter Studies. Volume 1: Theory, Instruments and Methods*. Springer Verlag, Berlin, Germany.

- Paravicini, T. and Touyz, R. (2006). Redox signaling in hypertension. *Cardiovasc. Res.*, 71(2):247–258.
- Park, J., Baek, M., Choi, E., Woo, S., Kim, J., Kim, T., Jung, J., Chae, K., Chang, Y., and Lee, G. (2009). Paramagnetic ultrasmall gadolinium oxide nanoparticles as advanced T<sub>1</sub> MRI contrast agent: Account for large longitudinal relaxivity, optimal particle diameter, and *in vivo* T<sub>1</sub> MR images. *ACS Nano*, 3(11):3663–3669.
- Parker, D., Dickins, R., Puschmann, H., Crossland, C., and Howard, J. (2002). Being excited by lanthanide coordination complexes: Aqua species, chirality, excited-state chemistry, and exchange dynamics. *Chem. Rev.*, 102(6):1977–2010.
- Pawley, G. (1981). Unit-cell refinement from powder diffraction scans. *J. Appl. Cryst.*, 14(6):357–361.
- Penfield, J. and Reilly, R. (2007). What nephrologists need to know about gadolinium. *Nat. Clin. Pract Neph.*, 3(12):654–668.
- Pepato, M., Khalil, N., Giocondo, M., and Brunetti, I. (2008). Vanadium and its complexes: The renewed interest in its biochemistry. *Lat. Am. J. Pharm.*, 27(3):468–476.
- Perry, M. (2007). *The Chemotherapy Source Book*. Lippincott Williams & Wilkins, Philadelphia, PA, USA, 4th edition.
- Piao, Y., Kim, J., Na, H., Kim, D., Baek, J., Ko, M., Lee, J., Shokouhimehr, M., and Hyeon, T. (2008). Wrap-bake-peel process for nanostructural transformation from  $\beta$ -FeOOH nanorods to biocompatible iron oxide nanocapsules. *Nat. Mater.*, 7(3):242–247.
- Pickardt, J., Schendler, T., and Kolm, M. (1988). Röntgenuntersuchung von Einkristallen ternärer Lanthanoid-Vanadium(III)-Oxide LnVO<sub>3</sub> (Ln = Gd, Dy, Er). *Z. anorg. allg. Chem.*, 560(1):153–157.
- Pimlott, S. and Sutherland, A. (2011). Molecular tracers for the PET and SPECT imaging of disease. *Chem. Soc. Rev.*, 40(1):149–162.
- Poluektov, N. and Gava, S. (1971). Concentration dependence of lanthanide luminescence in yttrium orthovanadate phosphors. *Opt. Spectros. USSR*, 31:45–48.
- Popa, N. (1992). Texture in Rietveld refinement. *J. Appl. Cryst.*, 25(5):611–616.
- Popa, N. (1998). The (hkl) dependence of diffraction-line broadening caused by strain and size for all laue groups in Rietveld refinement. *J. Appl. Cryst.*, 31(2):176–180.

- Powell, D., Dhubhghaill, O., Pubanz, D., Helm, L., Lebedev, Y., Schlaepfer, W., and Merbach, A. (1996). Structural and dynamic parameters obtained from  $^{17}\text{O}$  NMR, EPR, and NMRD studies of monomeric and dimeric  $\text{Gd}^{3+}$  complexes of interest in magnetic resonance imaging: An integrated and theoretically self-consistent approach. *J. Am. Chem. Soc.*, 118(39):9333–9346.
- Powell, R. and Blasse, G. (1980). Energy transfer in concentrated systems. In Dunitz, J., Hemmerich, P., Ibers, J., Jorgensen, C., Neilands, J., Goodenough, J., Reinen, D., and Williams, R., editors, *Luminescence Energy Transfer*, volume 42 of *Structure and Bonding*, pages 43–96. Springer, Berlin, Germany.
- Prince, E. (1983). The effect of finite detector slit height on peak positions and shapes in powder diffraction. *J. Appl. Cryst.*, 16(5).
- Provencher, S. (1982). A constrained regularization method for inverting data represented by linear algebraic or integral equations. *Comput. Phys. Commun.*, 27(3):213–227.
- Purcell, E., Torrey, H., and Pound, R. (1946). Resonance absorption by nuclear magnetic moments in a solid. *Phys. Rev.*, 69(1-2):37–38.
- Qiao, R., Yang, C., and Gao, M. (2009). Superparamagnetic iron oxide nanoparticles: From preparations to *in vivo* MRI applications. *J. Mater. Chem.*, 19(35):6274–6293.
- Radhakrishna, P., Hammann, J., and Pari, P. (1981). Neutron diffraction study of antiferromagnetism in  $\text{YbVO}_4$ . *J. Magn. Magn. Mater.*, 23(3):254–256.
- Reed, E. and Moos, W. (1973). Multiphonon relaxation of excited states of rare-earth ions in  $\text{YVO}_4$ ,  $\text{YAsO}_4$ , and  $\text{YPO}_4$ . *Phys. Rev. B*, 8(3):980–987.
- Ribeiro Carrott, M., Candeias, A., Carrott, P., Ravikovitch, P., Neimark, A., and Sequeira, A. (2001). Adsorption of nitrogen, neopentane, *n*-hexane, benzene and methanol for the evaluation of pore sizes in silica grades of MCM-41. *Microporous Mesoporous Mater.*, 47(2-3):323–337.
- Rietveld, H. (1969). A profile refinement method for nuclear and magnetic structures. *J. Appl. Cryst.*, 2:65–71.
- Riseberg, L. and Moos, H. (1968). Multiphonon orbit-lattice relaxation of excited states of rare-earth ions in crystals. *Phys. Rev.*, 174(2):429–438.
- Rodríguez-Carvajal, J. (1993). Recent advances in magnetic structure determination by neutron powder diffraction. *Physica B*, 192(1-2):55–69.
- Rodríguez-Carvajal, J. (2001). Recent developments of the program FullProf. *Commission for Powder Diffraction, International Union of Crystallography, Newsletter*, 26:12–19.

- Rodríguez-Carvajal, J. and Roisnel, T. (1998). FullProf.98 and WinPLOTR: New Windows 95/NT applications for diffraction. *Commission for Powder Diffraction, International Union of Crystallography, Newsletter*, 20:35–36.
- Roisnel, T. and Rodríguez-Carvajal, J. (2001). WinPLOTR: A windows tool for powder diffraction pattern analysis. In Delhez, R. and Mittemeijer, E., editors, *Materials Science Forum, Proceedings of the European Powder Diffraction Conference (EPDIC 7)*, volume 378-381, pages 118–123. Trans Tech Publications, Dumten-Zürich, Switzerland.
- Rouquerol, F., Rouquerol, J., and Sing, K. (1999). *Adsorption by Powders and Porous Solids: Principles, Methodology and Applications*. Academic Press, San Diego, CA, USA.
- Rousseau, R. (2001). Detection limit and estimate of uncertainty of analytical XRF results. *Rigaku J.*, 18(2):33–47.
- Rumpf, M.-E. (1937). Contribution à l'étude en solution aqueuse de quelques persels obtenus par action de l'eau oxygénée. *Ann. Chim.*, 8:456–527.
- Saez-Puche, R., Jiménez, E., Isasi, J., Fernandez-Diaz, M., and Garcia-Munoz, J. (2003). Structural and magnetic characterization of RCrO<sub>4</sub> oxides (R=Nd, Er and Tm). *J. Solid State Chem.*, 171(1-2):161–169.
- Sage, M.-H. (2006). *Orbital, charge and magnetic order of RVO<sub>3</sub> perovskites*. Ph. D. thesis, Rijksuniversiteit Groningen, Groningen, The Netherlands.
- Sanchez, D., Ortega, A., Domingo, J., and Corbella, J. (1991). Developmental toxicity evaluation of orthovanadate in the mouse. *Biol. Trace Elem. Res.*, 30(3):219–226.
- Santra, S., Bagwe, R., Dutta, D., Stanley, J., Walter, G., Tan, W., Moudgil, B., and Mericle, R. (2005). Synthesis and characterization of fluorescent, radio-opaque, and paramagnetic silica nanoparticles for multimodal bioimaging applications. *Adv. Mater.*, 17(18):2165–2169.
- Schäfer, W. and Will, G. (1971). Neutron diffraction study of antiferromagnetic DyAsO<sub>4</sub>. *J. Phys. C: Solid State Phys.*, 4(18):3224.
- Schäfer, W., Will, G., and Müller-Vogt, G. (1979). Refinement of the crystal structure of terbium arsenate TbAsO<sub>4</sub> at 77 K and 5 K by profile analysis from neutron diffraction powder data. *Acta Cryst. B*, 35(3):588–592.
- Schäferling, M., Grögel, D., and Schreml, S. (2011). Luminescent probes for detection and imaging of hydrogen peroxide. *Microchim. Acta*, 174(1):1–18.
- Schärftl, W. (2007). *Light Scattering from Polymer Solutions and Nanoparticle Dispersions*. Springer, Berlin, Germany.

- Schätzl, K. (1993). Single-photon correlation techniques. In Brown, W., editor, *Dynamic Light Scattering*, pages 76–148. Oxford University Press, Oxford, UK.
- Scherrer, P. (1918). Bestimmung der Grösse und der inneren Struktur von Kolloidteilchen mittels Röntgenstrahlen. *Nachr. Ges. Wiss. Göttingen*, 26:98–100.
- Schiebener, P., Straub, J., Levelt Sengers, J., and Gallagher, J. (1990). Refractive index of water and steam as function of wavelength, temperature and density. *J. Phys. Chem. Ref. Data*, 19(3):677–717. 3.
- Schwab, M., Berkhahn, W., Kahle, H., Simon, A., and Wüchner, W. (1974). Magnetic ordering in  $\text{HoAsO}_4$  investigated by means of specific heat and spectroscopic measurements. *Phys. status solidi b*, 65(2):613–624.
- Schwab, M. and Kahle, H. (1977). Specific heat of  $\text{TbPO}_4$ . *Phys. status solidi b*, 84(1):167–170.
- Schwarz, H. (1963). Die Phosphate, Arsenate und Vanadate der Seltenen Erden. *Z. anorg. allg. Chem.*, 323(1-2):44–56.
- Sears, V. (1992). Neutron scattering lengths and cross sections. *Neutron News*, 3(3):29–37.
- Semelka, R. and Helmberger, T. (2001). Contrast agents for MR imaging of the liver. *Radiology*, 218(1):27–38.
- Sengers, J. and Watson, J. (1986). Improved international formulations for the viscosity and thermal conductivity of water substance. *J. Phys. Chem. Ref. Data*, 15(4):1291–1314.
- Shi, Z., Neoh, K., Kang, E., Shuter, B., and Wang, S.-C. (2010). Bifunctional  $\text{Eu}^{3+}$ -doped  $\text{Gd}_2\text{O}_3$  nanoparticles as a luminescent and  $T_1$  contrast agent for stem cell labeling. *Contrast Media Mol. Imaging*, 5(2):105–111.
- Shionoya, S. and Yen, W. (1998). *Phosphor Handbook*. CRC Press, Boca Raton, FL, USA.
- Sigel, H. and Sigel, A. (1995). Vanadium and its role in life. In Orvig, H., Thomson, M., Batell, M., and McNeill, M., editors, *Metal ions in biological systems*, pages 576–594. Marcel Dekker, New York, NY, USA.
- Sing, K., Everett, D., Haul, R., Moscou, L., Pierotti, R., Rouquerol, J., and Siemieniewska, T. (1985). Reporting physisorption data for gas/solid systems with special reference to the determination of surface area and porosity (recommendations 1984). *Pure Appl. Chem.*, 57(4):603–619.
- Smart, L. and Moore, E. (2005). *Solid State Chemistry*. Taylor and Francis, Boca Raton, FL, USA, 3rd edition.

- Smith, C. and Rayment, I. (1996). X-ray structure of the magnesium(II)–ADP–vanadate complex of the *Dictyostelium discoideum* myosin motor domain to 1.9 Å resolution. *Biochemistry*, 35(17):5404–5417.
- Soh, N., Sakawaki, O., Makihara, K., Odo, Y., Fukaminato, T., Kawai, T., Irie, M., and Imato, T. (2005). Design and development of a fluorescent probe for monitoring hydrogen peroxide using photoinduced electron transfer. *Bioorg. Med. Chem.*, 13(4):1131–1139.
- Solomon, I. (1955). Relaxation processes in a system of two spins. *Phys. Rev.*, 99(2):559–565.
- Spooner, S., Lee, J., and Moos, H. (1971). Configuration of moments in TbPO<sub>4</sub>. *Solid State Comm.*, 9(13):1143–1145.
- Stein, G. and Würzberg, E. (1975). Energy gap law in the solvent isotope effect on radiationless transitions of rare earth ions. *J. Chem. Phys.*, 62(1):208–213.
- Steiner, M., Dachs, H., and Ott, H. (1979). The determination of the magnetic structure of DyCrO<sub>4</sub> by neutron diffraction. *Solid State Comm.*, 29(3):231–234.
- Stezowski, J. and Hoard, J. (1984). Heavy-metal ionophores – correlations among structural parameters of complexed nonpeptide polyamino acids. *Isr. J. Chem.*, 24(4):323–334.
- Stöber, W., Fink, A., and Bohn, E. (1968). Controlled growth of monodisperse silica spheres in the micron size range. *J. Coll. Inter. Sci.*, 26(1):62–69.
- Stohs, S. and Bagchi, D. (1995). Oxidative mechanisms in the toxicity of metal ions. *Free Radic. Biol. Med.*, 18(2):321–336.
- Stout, G. and Jensen, L. (1989). *X-ray structure determination. A practical guide.* John Wiley & Sons, New York, NY, USA, 2nd edition.
- Sucksmith, W. (1932). The gyromagnetic ratio for paramagnetic substances. III. Results on salts of the rare earth group. *Proc. R. Soc. Lond. A*, 135(826):276–281.
- Sugimoto, T. (1987). Preparation of monodispersed colloidal particles. *Adv. Colloid Interface Sci.*, 28:65–108.
- Suh, Y.-A., Arnold, R., Lassègue, B., Shi, J., Xu, X., Sorescu, D., Chung, A., Griendling, K., and Lambeth, D. (1999). Cell transformation by the superoxide-generating oxidase Mox1. *Nature*, 401(6748):79–82.
- Sundaresan, M., Yu, Z.-X., Ferrans, V., Irani, K., and Finkel, T. (1995). Requirement for generation of H<sub>2</sub>O<sub>2</sub> for platelet-derived growth factor signal transduction. *Science*, 270(5234):296–299.

- Suzuki, H., Inoue, T., Higashino, Y., and Ohtsuka, T. (1980). Enhanced nuclear cooling and spin-lattice relaxation time in  $\text{TmVO}_4$ . *Phys. Lett. A*, 77(2-3):185–188.
- Suzuki, H., Naher, S., Shimoguchi, T., Mizuno, M., Ryu, A., and Fujishita, H. (2002). X-ray diffraction measurement below 1 K. *J. Low Temp. Phys.*, 128(1-2):1–7.
- Suzuki, H. and Nakajima, T. (1979). Two phase transitions of  $\text{TbPO}_4$  at low temperatures. *J. Phys. Soc. Jpn.*, 47(5):1441–1445.
- Suzuki, H., Nambudripad, N., Bleaney, B., Allsop, A., Bowden, G., Campbell, I., and Stone, N. (1978). Enhanced nuclear cooling and antiferromagnetism in  $\text{HoVO}_4$ . *J. Phys. Colloques*, 39(C6):800–802.
- Suzuki, H., Ohtsuka, T., Kawarazaki, S., Kunitomi, N., Moon, R., and Nicklow, R. (1984). Neutron diffraction study on the hyperfine-enhanced nuclear spin order of  $\text{HoVO}_4$ . *Solid State Comm.*, 49(12):1157–1160.
- Swanson, H., McMurdie, H., Morris, M., and Evans, E. (1967). Standard X-ray diffraction powder patterns. *Natl. Bur. Stand. Monogr.*, 25(5):30.
- Takac, I., Schröder, K., Zhang, L., Lardy, B., Anilkumar, N., Lambeth, D., Shah, A., Morel, F., and Brandes, R. (2011). The E-loop is involved in hydrogen peroxide formation by the NADPH oxidase Nox4. *J. Biol. Chem.*, 286(15):13304–13313.
- Tanner, J., Parsons, Z., Cummings, A., Zhou, H., and Gates, K. (2011). Redox regulation of protein tyrosine phosphatases: Structural and chemical aspects. *Antioxid. Redox Signal.*, 15(1):77–97.
- Tatiersky, J., Pacigová, S., Sivák, M., and Schwendt, P. (2009). Monoperoxidovanadium(v) complexes: Synthesis, structure and solution properties. *J. Argent. Chem. Soc.*, 97(1):181–198.
- Terreno, E., Castelli, D., Viale, A., and Aime, S. (2010). Challenges for molecular magnetic resonance imaging. *Chem. Rev.*, 110(5):3019–3042.
- Tezuka, K. and Hinatsu, Y. (2001). Magnetic and crystallographic properties of  $\text{LnCrO}_4$  ( $\text{Ln} = \text{Nd}, \text{Sm}, \text{and Dy}$ ). *J. Solid State Chem.*, 160(2):362–367.
- Thiriet, C., Javorsky, P., and Konings, R. (2005). Low-temperature study of magnetic ordering in gadolinium orthophosphate. *Solid State Comm.*, 134(6):409–412.
- Thompson, P., Cox, D., and Hastings, J. (1987). Rietveld refinement of Debye-Scherrer synchrotron X-ray data from  $\text{Al}_2\text{O}_3$ . *J. Appl. Cryst.*, 20(2):79–83.
- Thunus, L. and Lejeune, R. (1999). Overview of transition metal and lanthanide complexes as diagnostic tools. *Coord. Chem. Rev.*, 184(1):125–155.

- Tonosaki, K. and Otomo, M. (1962). Spectrophotometric determination of cerium(III) and some rare earths with xylenol orange. *Bull. Chem. Soc. Jpn.*, 35(10):1683–1686.
- Tóth, E., Helm, L., and Merbach, A. (2001). Relaxivity of gadolinium (III) complexes: Theory and mechanism. In Merbach, A. and Tóth, E., editors, *The Chemistry of Contrast Agents in Medical Magnetic Resonance Imaging*, pages 45–119. John Wiley, Chichester, UK.
- Touboul, M. and Popot, A. (1985). Synthesis, crystal-chemistry and physical-properties of new forms of  $\text{RVO}_4$  (R = In, Fe, Cr, Al, Nd, Y). *Rev. Chim. Min.*, 22(5):610–624.
- Türkcan, S. (2010). *Investigation of the Cell membrane Architecture by single-molecule tracking of peptidic toxins*. Ph. D. thesis, Ecole Polytechnique, Palaiseau, France.
- Turkington, T. (2008). PET physics and PET instrumentation. In Wahl, R. and Beanlands, R., editors, *Principles and Practice of PET and PET/CT*. Lippincott Williams & Wilkins, Philadelphia, PA, USA, 2nd edition.
- Tweedle, M. (1992). Physicochemical properties of gadoteridol and other magnetic resonance contrast agents. *Invest. Radiol.*, 27(Suppl. 1):S2–S6.
- Tweedle, M., Wedeking, P., and Kumar, K. (1995). Biodistribution of radiolabeled, formulated gadopentetate, gadoteridol, gadoterate, and gadodiamide in mice and rats. *Invest. Radiol.*, 30(6):372–380.
- Tyeklár, Z., Dunham, S., Midelfort, K., Scott, D., Sajiki, H., Ong, K., Lauffer, R., Caravan, C., and McMurry, T. (2007). Structural, kinetic, and thermodynamic characterization of the interconverting isomers of MS-325, a gadolinium(III)-based magnetic resonance angiography contrast agent. *Inorg. Chem.*, 46(16):6621–6631.
- van Laar, B. and Yelon, W. (1984). The peak in neutron powder diffraction. *J. Appl. Cryst.*, 17(2):47–54.
- Van Uitert, L. and Johnson, L. (1966). Energy transfer between rare-earth ions. *J. Chem. Phys.*, 44(9):3514–3522.
- Van Vleck, J. (1932). *The Theory of Electric and Magnetic Susceptibilities*. Oxford University Press, Oxford, UK.
- Vander Elst, L., Chapelle, F., Laurent, S., and Muller, R. (2001). Stereospecific binding of MRI contrast agents to human serum albumin: The case of Gd-(S)-EOB-DTPA (Eovist) and its (R) isomer. *J. Biol. Inorg. Chem.*, 6(2):196–200.
- Vander Elst, L., Maton, F., Laurent, S., Seghi, F., Chapelle, F., and Muller, R. (1997). A multinuclear MR study of Gd-EOB-DTPA: Comprehensive preclinical characterization of an organ specific MRI contrast agent. *Magn. Reson. Med.*, 38(4):604–614.

- Venikouas, G. and Powell, R. (1978). Laser time-resolved spectroscopy: Investigations of energy transfer in  $\text{Eu}^{3+}$  and  $\text{Er}^{3+}$  doped  $\text{YVO}_4$ . *J. Lumin.*, 16(1):29–45.
- Verwey, E. and Overbeek, J. (1948). *Theory of the stability of lyophobic colloids*. Elsevier, Amsterdam, The Netherlands, verwey48 edition.
- Wadas, T., Wong, E., Weisman, G., and Anderson, C. (2010). Coordinating radiometals of copper, gallium, indium, yttrium, and zirconium for PET and SPECT imaging of disease. *Chem. Rev.*, 110(5):2858–2902.
- Waller, I. (1923). Zur Frage der Einwirkung der Wärmebewegung auf die Interferenz von Röntgenstrahlen. *Z. Phys. A*, 17(1):398–408.
- Wang, Y.-X., Hussain, S., and Krestin, G. (2001). Superparamagnetic iron oxide contrast agents: Physicochemical characteristics and applications in MRI imaging. *Eur. Radiol.*, 11(11):2319–2331.
- Weisman, G. and Reed, D. (1996). A new synthesis of cyclen (1,4,7,10-tetraazacyclododecane). *J. Org. Chem.*, 61(15):5186–5187.
- Wertheim, G., Butler, M., West, K., and Buchanan, D. (1974). Determination of the Gaussian and Lorentzian content of experimental line shapes. *Rev. Sci. Instrum.*, 45(11):1369–1371.
- Westbrook, C. and Kaut, C. (1998). *MRI in Practice*. Blackwell Publishing, Oxford, UK, 2nd edition.
- Will, G., Göbel, H., Sampson, C., and Forsyth, J. (1972). Crystallographic distortion in  $\text{TbVO}_4$  at 32°K. *Phys. Lett. A*, 38(3):207–208.
- Will, G. and Schäfer, W. (1971). The magnetic structure of antiferromagnetic  $\text{DyVO}_4$ . *J. Phys. C: Solid State Phys.*, 4(7):811.
- Williamson, G. and Hall, W. (1953). X-ray line broadening from fcc aluminium and wolfram. *Acta Metall.*, 1(1):22–31.
- Wilson, A. (1963). *Mathematical theory of x-ray powder diffractometry*. Philips Technical Library, Eindhoven, The Netherlands.
- Wolfbeis, O., Dürkop, A., Wu, M., and Lin, Z. (2002). A europium-ion-based luminescent sensing probe for hydrogen peroxide. *Angew. Chem. Int. Ed.*, 41(23):4495–4498.
- Wong, H.-T., Chan, H., and Hao, J. (2009). Magnetic and luminescent properties of multifunctional  $\text{GdF}_3:\text{Eu}^{3+}$  nanoparticles. *Appl. Phys. Lett.*, 95:022512.
- Wright, E. and Mellon, M. (1937). The peroxide method for vanadium. *Ind. Eng. Chem. Anal. Ed.*, 9(8):375–376.

- Wüchner, W., Bohm, W., Kahle, H., Kasten, A., and Laugsch, J. (1972). Spectroscopic properties of TbAsO<sub>4</sub>. *Phys. status solidi b*, 54(1):273–283.
- Wybourne, B. (1965). *Spectroscopic properties of rare earths*. Interscience Publishers, John Wiley & Sons, New York, NY, USA.
- Xie, J., Chen, K., Huang, J., Lee, S., Wang, J., Gao, J., Li, X., and Chen, X. (2010). PET/NIRF/MRI triple functional iron oxide nanoparticles. *Biomaterials*, 31(11):3016–3022.
- Yatsimirsky, K., Kostromina, N., Sheka, Z., Davidenko, N., Kriss, E., and Ermolenko, V. (1966). *Complex chemistry of rare earth elements (in Russian)*. Naukova Dumka, Kiev, Ukrainian SSR.
- Yim, H., Kent, M., Tallant, D., Garcia, M., and Majewski, J. (2005). Hygrothermal degradation of (3-glycidoxypropyl)trimethoxysilane films studied by neutron and X-ray reflectivity and attenuated total reflection infrared spectroscopy. *Langmuir*, 21(10):4382–4392.
- Young, R. and Wiles, D. (1982). Profile shape functions in Rietveld refinements. *J. Appl. Cryst.*, 15(4):430–438.
- Yu, M., Lin, J., and Fang, J. (2005). Silica spheres coated with YVO<sub>4</sub>:Eu<sup>3+</sup> layers via sol-gel process: A simple method to obtain spherical core-shell phosphors. *Chem. Mater.*, 17(7):1783–1791.
- Zhang, F., Lang, M., Ewing, R., Lian, J., Wang, Z., Hu, J., and Boatner, L. (2008). Pressure-induced zircon-type to scheelite-type phase transitions in YbPO<sub>4</sub> and LuPO<sub>4</sub>. *J. Solid State Chem.*, 181(10):2633–2638.
- Zhao, W. (2009). Lighting up H<sub>2</sub>O<sub>2</sub>: The molecule that is a necessary evil in the cell. *Angew. Chem. Int. Ed.*, 48(17):3022–3024.
- Zheng, F., Wang, W., and Yang, P. (2011). GdVO<sub>4</sub>:Ln<sup>3+</sup> (Ln = Eu, Dy, and Sm) microstructures: Solvothermal and luminescent properties. *Optoelectron. Adv. Mater. Rapid Commun.*, 5(6):596–599.
- Zheng, M., Wang, X., Templeton, L., Smulski, D., LaRossa, R., and Storz, G. (2001). DNA microarray-mediated transcriptional profiling of the *Escherichia coli* response to hydrogen peroxide. *J. Bacteriol.*, 183(15):4562–4570.
- Zhou, M., Diwu, Z., Panchuk-Voloshina, N., and Haugland, R. (1997). A stable nonfluorescent derivative of resorufin for the fluorometric determination of trace hydrogen peroxide: Applications in detecting the activity of phagocyte NADPH oxidase and other oxidases. *Anal. Biochem.*, 253(2):162–168.